The magnetic properties of epitaxial $Fe_{100-x}Ga_x$ thin films: the role of Gallium composition and film thickness

Syamashree Roy

School of Physics and Astronomy

University of Nottingham

A thesis presented for the degree of

Doctor of Philosophy

23.11.2020

Abstract

Magnetostrictive smart materials in the form of thin films hold a lot of promise because of their utilisation in a variety of microelectromechanical (MEMs) and nanoelectromechanical (NEMs) based devices, magnetic memory and logic technology. A promising candidate is Galfenol which is an alloy of Fe and Ga, and has been demonstrated [1] to have a very high magnetostriction coefficient in bulk single crystal form. Recently, the first measurement of magnetostriction in epitaxial thin films was reported by Parkes *et al.* [2] who found that epitaxial thin films of $Fe_{81}Ga_{19}$ show magnetostriction values as large as the bulk material, making the epitaxial layers a prospective candidate for applications. It is therefore important to understand the role of Ga composition and film thickness in determining the magnetic properties of epitaxial Galfenol.

This thesis investigates the structural, magneto-static, magneto-dynamic and magneto-transport properties of epitaxial sputtered grown thin films of Galfenol. An elaborated and detailed study of this material in thin-film form was done by growing $Fe_{100-x}Ga_x$ films with x ranging from 7% to 30% as well as growing $Fe_{79}Ga_{21}$ films with thickness ranging from 5 nm to 95 nm. All the films discussed in this thesis were epitaxially grown on GaAs(001) substrate due to its low misfit in a cube on cube geometry when grown using sputtering.

The presence of a strong crystalline and epitaxial growth of the samples is demonstrated by analysing the structural properties of these samples. This was then observed to be consistent with a strong cubic magnetocrystalline anisotropy in samples with lower Ga concentration revealed by SQUID magnetometry measurements. The samples, apart from having a cubic anisotropy, also presented a weak uniaxial magnetic anisotropy. A clear dependency of anisotropy on Ga concentration is presented in this thesis, which correlates with a reduction of the crystalline structure with increase in Ga concentration. Field rotation transport measurements for current passed along different crystalline direction re-

vealed crystalline and non-crystalline contributions to the anisotropic magnetoresistance (AMR). A closely comparable pattern was observed between the crystalline magneto-transport coefficients and magnetocrystalline anisotropy constants for varying Ga concentration. Also, magnetocrystalline constants obtained from ferromagnetic resonance measurements followed a similar pattern. The Gilbert or intrinsic damping as a function of Ga concentration was also investigated. A low Gilbert damping comparable to previously reported values makes them a competitive candidate for application into microwave devices. An investigation of the ferromagnetic resonance linewidth gives insight into the relative magnitude of the different contributions to the magnetic damping as a function of Ga concentration.

Similar investigations were also performed on $Fe_{79}Ga_{21}$ samples by varying the film thickness. Samples depicted a good crystalline and epitaxial sputtered growth with strong cubic magnetocrystalline anisotropy. The weak uniaxial anisotropy changes in magnitude for thicker samples. The thicker samples tend to deviate from the patterns observed for thinner samples. Field rotation transport measurements represented four different contributions to the AMR with corresponding unique symmetries. The crystalline contributions agreed with the pattern observed for magnetocrystalline anisotropy constants.

Acknowledgements

First and foremost, I would like to express my sincere gratitude to my supervisor Dr Andrew Rushforth, for his continuous support in the completion of this work. He has been very patient and encouraging from the very first day. His guidance and immense knowledge have helped me in all the time of research and writing of this thesis. I would also like to thank our collaborators, Dr Stuart Cavill, Ms Lillian Clarke, without whose efforts the ferromagnetic resonance experiments result discussed in this thesis would not have been possible, and Dr Emily F Smith for the x-ray photoelectron spectroscopy measurements.

I would like to thank Jasbinder Chauhan for the cleanroom training and giving me advice during the fabrication process and Christopher Pallender, Sanjeev Taak for the constant supplies of liquid helium. I would also like to show my sincere gratitude towards Chris Staddon for the x-ray diffraction training and advice during the whole process.

I would also like to extend a thank you to all the members of C26 for making the workplace and especially lunchtime enjoyable. Many thanks to Mohammed, Sonka, Luke, Ollie, Carl, Stu, Debi and Sam. I want to thank other members of the spintronics group Dr Mu Wang, Dr Kevin Edmonds, Dr Peter Wadley and Dr Khalid Omari.

I would like to thank a very significant person in my life, Dhiren, for all his love, patience and support. Thank you for making me a better person. I would also like to thank all people I came across during this PhD, who I became good friends with and supported me in this journey; Dishil, Graham and Surekha.

I would like to thank my family for their incredible support and many sacrifices. I am forever in their debt for giving me this life. I would especially like to thank my mother for her faith and advice. I am nothing without her.

Contents

List of Symbols and Abbreviations

$\mathbf{M}_s$	Saturation magnetisation.
$\boldsymbol{\lambda_{100}}$	Magnetostriction constant along [100] crystal direction.
$\boldsymbol{K_c}$	Cubic anisotropy constant.
$\boldsymbol{K_u}$	Uniaxial anisotropy constant.
$\boldsymbol{H_c}$	Cubic anisotropy field.
$\boldsymbol{H_u}$	Uniaxial anisotropy field.
$\boldsymbol{\mu_B}$	Bohr magnetron.
$\boldsymbol{E_{total}}$	Total magnetic free energy density.
$\boldsymbol{H_{ext}}$	External magnetic field.
$\boldsymbol{\theta}$	The angle between the applied magnetic field and [010] crystal direction.
$\boldsymbol{\phi}$	The angle between the magnetisation and [010] crystal direction.
$\boldsymbol{\vec{H}_{eff}}$	Total effective magnetic field.
$\boldsymbol{\phi_M}$	Azimulthal angle with respect to [010] crytsal direction.
$\boldsymbol{\theta_M}$	Polar angle.
$\boldsymbol{\omega_{res}}$	Angular resonance frequency.
$\boldsymbol{\Delta H}$	Field linewidth.
$\boldsymbol{\alpha}$	Damping constant.
$\boldsymbol{d_{hkl}}$	is the inter-planar spacing.
$\boldsymbol{\theta_i}$	is the angle of incidence of the x-rays.
$\mathbf{a}$	The lattice spacing of the cubic crystal.
$\boldsymbol{\Phi}$	The angle between the current and the magnetisation in the plane of the sample.
$\boldsymbol{\psi}$	The angle between the magnetisation and uniaxial easy axis [110].
$\boldsymbol{R_{xx}}$	Longitudinal resistance.
$\boldsymbol{R_{xy}}$	Transverse resistance.

$\boldsymbol{C_I}$	The non-crystalline anisotropic magnetoresistance coefficient.
$\boldsymbol{C_U}$	The uniaxial crystalline anisotropic magnetoresistance coefficient.
$\boldsymbol{C_C}$	The cubic anisotropic magnetoresistance coefficient.
$\boldsymbol{C_I}$	The crossed non-crystalline and cubic crystalline anisotropic magnetoresistance coefficient.
AMR	Anisotropic magnetoresistance.
XRD	X-ray diffraction.
XRR	X-ray reflectivity.
XPS	X-ray photoelectron spectroscopy.
SQUID	Superconducting QUantum Interference Device.
FMR	Ferromagnetic resonance.

Chapter 1

Introduction and Background

1.1 Magnetostrictive smart materials

Smart material is a common name given to a wide group of different materials which have an inherent ability to transform one form of energy into another. They tend to show a strong coupling between external stimuli and their mechanical properties. Therefore, under a controlled environment, documenting the changes in these materials can be used to transform energy from one form to another and used in numerous practical applications such as in actuators, sensors, energy harvesters and memory storage devices. Due to their multi-functionality and adaptive characteristics, they have already been used in several industries such as defence, aerospace, civil engineering, nano-technology, bio-medical and automotive. Some of the common types of smart materials include piezoelectric, shape memory, thermochromic, photochromic, magnetorheological and magnetostrictive [3–5].

Magnetostrictive materials are a sub-category of smart materials which can change their shape or deform upon the application of an external magnetic field. This phenomenon of deformation is called magnetostriction. Magnetostriction was first discovered by James Prescott Joules in 1842. He observed that a bar of iron sample changed its length when it was magnetised in an external magnetic field [6]. The fractional change in the dimension of a magnetic material caused by a change in its magnetisation was termed as magnetostriction. The strain was measured along the magnetic field direction, and the volume of the mate-

rial was assumed to remain constant. Therefore, it was termed as linear/direct magnetostriction or Joule effect. Depending on the positive or negative magnetostriction constant value, the length of the material will elongate or reduce respectively upon the application of the magnetic field. Joule observed a weak deformation of less than 1 ppm. Later it was observed that almost all ferromagnetic material such as Co and Ni exhibit some amount of magnetostriction [7–10]. Although the deformation was noticeable, it couldn't be used for practical purposes because of the smaller magnetostriction value.

Joule effect also has an inverse effect associated with it known as the Villari effect named after the scientist Emilio Villari who first discovered it in 1865 [10, 11]. Under this effect, there is a change in magnetisation of the sample as a result of the externally applied mechanical stress. The change in the shape of ferromagnetic materials on the application of a magnetic field or vice versa was accounted by magnetoelastic coupling, which is discussed in detail in section 2.2.4. Apart from Joule effect, there were other effects which were related to magnetostriction. The Wiedemann effect (1883) is the formation of shear strain resulting in a torsional motion of a sample as a result of simultaneous application of magnetic field along the longitude and the circumference of a cylindrical ferromagnetic material [12, 13]. While the inverse effect is called the Matteucci effect, that is a mechanical twisting of the sample results in a strain-induced helical magnetisation [14]. The ΔE-effect is the change in Young's modulus of a material as a result of a change in the magnetic field [10, 15]. Another lesser-known magnetostrictive effect is Barrett effect or volume magnetostriction, as the name suggests, the volume of some ferromagnetic material changes via isotropic expansion of the lattice under the application of a high magnetic field [16]. Because the change in volume of the sample is often negligible even under a high magnetic field, this effect never actually found any practical applications. Figure 1.1 gives a schematic diagram for different types of magnetostrictive effects.

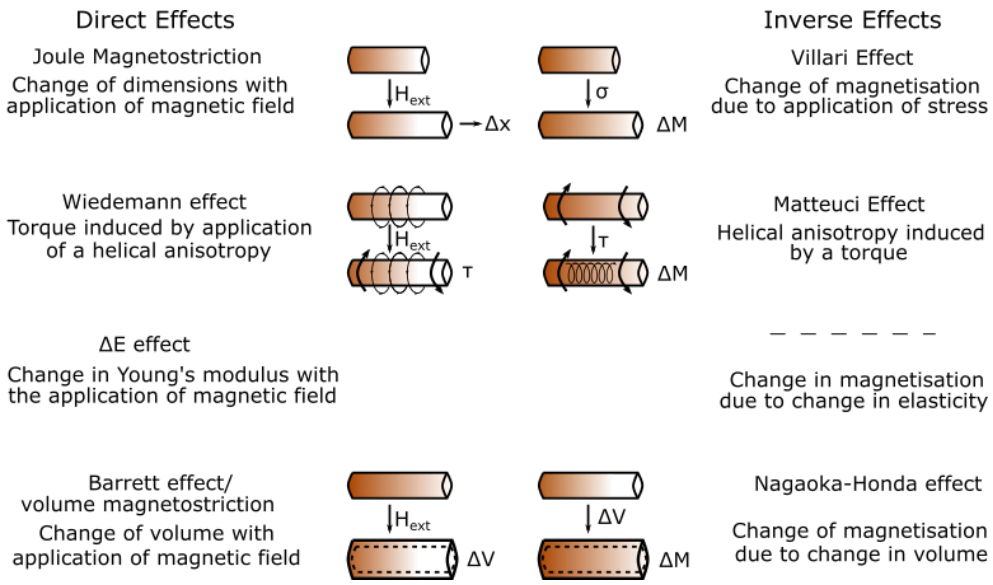

Figure 1.1: Schematic of the magnetostrictive effects.

In 1960, R.C. Hall showed that adding 20% of Al to bcc α-Fe leads to an increase in the value of magnetostriction coefficient by five times that of pure Fe [9, 17]. This led to the study of binary magnetostrictive alloys like Fe-Ni, Fe-Si, Fe-Co, Ni-Co *etc.* [9, 18, 19]. In parallel in the 1960s magnetostriction in rare earth metals was widely studied. The first breakthrough found the largest known magnetostriction in rare earth elements terbium (Tb) and dysprosium (Dy) with the strain of the order of 10000 ppm [20–23]. Nevertheless, this was never put to any practical use because this high magnetostriction was achievable only at cryogenic temperatures. In 1969, the solution to this problem was addressed by Callen suggesting that the addition of transition metals such as iron, with higher Curie temperature, could increase the Curie temperature of rare-earth magnetostrictive elements [24]. Later in 1972, it was discovered that by alloying rare earth elements Dy and Tb with Fe, it was possible to attain magnetostriction value of 433 ppm and 1753 ppm respectively at room temperature [25]. However, they had large magnetocrystalline anisotropy (214.07 kJ/m^3 for $DyFe_2$ and -306.40 kJ/m^3 for $TbFe_2$) at room temperature therefore required a huge magnetic field for deformation. This led to the discovery of the ternary rare-earth-based alloy Terfenol-D. In 1980, Clark *et al.* found that alloying Fe, Dy and Tb together gives a high value of magnetostriction coefficient of 2000 ppm at room temperature and relatively lower magnetic field [20, 26]. It was created and named by the

Naval Ordnance Laboratory. Terfenol-D ($Tb_{0.3}Dy_{0.7}Fe_2$) is named after **Ter**bium, iron-**Fe**, **n**aval **o**rdnance **l**aboratory and **D**ysporosium. However, despite the high magnetostriction value, apart from containing a rare earth element which was not economical, Terfenol-D was particularly tricky to use in mechanical applications and preferred geometries due to its brittle nature with a low tensile strength of roughly 28 MPa [27, 28].

In an effort to develop a rare-earth free, mechanically robust magnetostrictive material, "Galfenol" was discovered through collaborative research between the magnetic materials group at the Naval Surface Warfare Center Carderock Division and the DOE's Ames Laboratory in 1999 [1, 29]. Clark *et al.* found that by alloying Fe with 19 % Ga in single-crystal FeGa yields a large magnetostrictive strain of $3/2\lambda_{100} \geq 400$ppm (will be discussed in more details in section 1.2). The patent holders termed Galfenol at the Etrema Laboratory, USA, where Gal-fenol comes from **Ga**llium, **Fe** and **n**aval **o**rdnance **l**aboratory. It showed excellent mechanical properties with a tensile strength value of ≈ 500 MPa at low fields with high magnetostriction constant making it an ideal candidate to replace Terfenol-D [30, 31]. Table 1.1 shows the saturation magnetisation and the magnetostriction constant along [100] and [111] crystallographic directions. It shows that Galfenol exhibits a high magnetostriction constant when compared to other 3d metals and alloys which do not contain rare earth metals.

Material	M_s (x10^6 Am^{-1})	λ_{100} (x10^{-6})	λ_{111} (x10^{-6})
Fe[7]	1.71	30	-21
Ni[7]	0.49	-46	-24
Co[7]	1.43	-75	50
$Fe_{20}Ni_{80}$[32, 33]	0.86	8	0
$Fe_{81}Ga_{19}$[1]	1.39	395	15
$Tb_{0.3}Dy_{0.7}Fe_2$[34, 35]	0.8	90	1640

Table 1.1: Summarises the values for the saturation magnetisation and magnetostriction constant along [100] and [111] crystal direction of various materials. It gives a comparison between the magnetostrictive properties of Galfenol and other materials.

Since the discovery of magnetostriction in ferromagnetic material in 1842, magnetostrictive materials have found their way into many different types of industrial applications. Initially the Joule effect and its inverse Villari effect were the most widely used for magnetostrictive material applications. However, new research and discovery of new materials have allowed other effects to be used in a variety of different industrial applications.

The Joule effect or linear magnetostriction observed in magnetostrictive material was used for actuation devices, which in the presence of an external magnetic field results in a mechanical movement. One of the very first applications of magnetostrictive material was sonar systems. Nickel and nickel-based alloys were used as a sonar transducer [36], but with time the invention of giant magnetostrictive material like Terfenol-D, replaced Ni for high-performance sonar transducers. For commercial application magnetostrictive materials such as Terfenol-D and Galfenol were made in different geometrical configurations such as linear [27, 37–39], amplified configuration [40, 41], inch-worm [42, 43] *etc.*. The magnetostrictive components are specifically designed considering several factors such as the material's characteristic, attainable dimensions and shapes, coupling among components, energy efficiency, and cost-effectiveness [44–47]. The basic components used in an actuator consists of a smart material such as Terfenol-D or Galfenol, a power coil for inducing the magnetic field, a magnetic circuit for controlling the magnetic field strength and guiding the flux lines, a structural frame to utilise the deformation, and lastly, a sensor for monitoring and feedback. A few examples where bulk magnetostrictive materials were used as actuators are linear motors [48], reaction mass actuators for the purpose geophysical investigation [49], sonar transducers [50], rotational motors [51], electro-hydraulic actuators [40], inch-worm motors [52], flight surface actuators for vibration control [53], dental scalar systems [54], fuel-injection actuator [55], piezoelectric and magnetostrictive hybrid motors [43], acoustic speakers [56] *etc.*. Although limited there are also actuators based on the Wiedemann effect in the form of spring-type magnetostriction actuator such as the optomechanical scanner, step-by-step line motor and high precision vibrational drilling tool [57, 58].

Conversely, the high energy conversion efficiency of magnetostrictive material

enables them to be used for sensors and energy harvesting. For these specific purposes usually the inverse magnetostrictive effects are considered where it can detect a change in magnetic energy for change in the material's mechanical properties such as stress or strain. The most basic design used for sensing is a magnetostrictive material, a mechanical unit exerting strain on the material, pick-up coils surrounding the magnetostrictive material to detect any change in the permeability, and an electronic unit to convert, filter and amplify the signal. The magnetostrictive sensors have different kinds of geometries like rod, wire, ring, ribbon, shaft *etc.* depending on the requirement of the particular application. One of the earliest application was the measurement of torque in the crankshaft of an internal combustion engine, followed by many other applications such as measuring dynamic friction, microphones, phonograph, automotive industry, robotic sensors, biomedical monitoring, magnetoacoustic keyboard, Terfenol-D magnetometer, hearing aid, magnetostrictive fiber optic sensor, linear position sensor, magnetostrictive force sensor, displacement sensor, and non-contact torque sensor [59–72].

Magnetostrictive materials were also used for energy harvesting [73]. Energy harvesting is capturing ambient energy dissipated from a smart material and converting it into electrical energy. Magnetostrictive devices induce a current in the wire coiled around them due to a change in magnetic flux hence, harvesting magnetic energy to electrical energy. The Villari effect was mainly exploited for energy harvesting devices. Energy harvesting from a magnetostrictive material is a two-step process. First, the vibration that is the mechanical energy in the magnetostrictive material is converted into magnetic energy via magneto-mechanical coupling and secondly, the magnetic energy has to be converted into electrical energy via an electro-magnetic coupling. Depending on the requirement of the application magnetostrictive energy harvesters can have various configurations such as the axial type where a rod of magnetostrictive material is used, bending type where the magnetostrictive material is in the shape of a beam or in the form of ribbons [73–77].

So far, all the applications of the magnetostrictive material discussed are in their bulk form. In the era of cutting edge technology miniaturisation of de-

vices to micro and nano systems is crucial. Therefore, materials in the form of thin films are of particular importance. There has been extensive research towards the development of magnetostrictive thin film for decreasing the device dimensions where using a bulk form is not feasible. Thin films based on magnetostrictive materials and their alloys have been studied since the 1970s. Magnetostrictive thin films, apart from being metallic, also offer the advantage of being easily deposited on a conventional semiconductor substrate and device, offering a very cost-effective production for industrial use. Additionally, they are lightweight, have a higher spatial resolution and require small driving magnetic fields in the order of mT. Thin films being sensitive to the magnetic field also allow remote control operation of devices. However, the magnetostriction constant value observed for thin films is usually smaller than that of their bulk counterpart. Therefore, for it to be incorporated in nano and micro-scale technologies efficiently, the same functionality had to be reflected in thin films as well. The need for suitable materials for micro and nano systems drove the development of magnetostrictive films which exhibit high magnetostriction combined with soft magnetic properties. They have been investigated extensively both in the form of single and multilayer films. For single-layer, alloys of 3-d transition metals and rare-earth metals such as TbFe, TbCo, TbDyFe, and SmFeB produced the best results [78–81]. In the case of multilayer films, TbFe/FeCo exhibited the largest magnetostriction of 550 ppm in comparison to single-layer and other multilayer films [82]. In addition, rare-earth free FeGa thin-films were also used for integrating a magnetostrictive material in cost-effective and resilient transducers. To date, magnetostrictive thin films are one of such smart materials which are widely exploited. They have also been used in a variety of microelectromechanical (MEMs) and nanoelectromechanical (NEMs) based devices, for example in microcantilevers, acoustic sensors, vibrational sensors, wireless rotational motors, wireless linear micro-motor, remote-interrogation strain gauge, optical fiber magnetic field sensors, magnetometer, *etc.*. Magnetostrictive thin films apart from being used in MEMs and NEMs based devices found their way into the "spintronics" industry. It is an emerging technology that exploits the intrinsic spin of the electrons and its associated magnetic moment to create functionalities in

solid-state devices [83, 84]. Traditionally, recording data onto a ferromagnetic material consists of a coil of wires attached to some current-sensitive device. As the ferromagnetic material passes under the coil, current is sent through the coil which is proportional to the desired signal as a result generating a magnetic field. The magnetic field then aligns the spins in the ferromagnetic material along a particular direction thus storing the information. Even though charged based or electronically based devices have been around for decades. The retention of information or non-volatile memory is one of the major challenges faced by charged based electronic devices. Furthermore, with an increasing demand to fit more and more electronics devices into smaller and smaller spaces limits the further expansion of the electronic industry.

Ferromagnets are the primary materials used for non-volatile memory storage. The information is stored in the form of binary bits of "0" and "1". Writing in the form of bits requires switching the magnetisation to the desired state using an external agent. Although there are several ways of modifying the magnetisation state, more recently, the use of a hybrid ferromagnetic piezoelectric device is incomparably the most energy-efficient techniques used for logical processing and information storage. This method exploits the Villari effect observed in ferromagnetic materials. A ferromagnetic thin film is mounted on a piezoelectric transducer which induces a strain in that ferromagnetic layer using an electrostatic potential. The electrostatic potential of one polarity will generate a tensile (compressive) strain and will switch the magnetisation to one state to write bit "1" ("0") [85–87].

The foundation of spintronics can be traced back as early as 1856 when Willian Thompson (Lord Kelvin) observed that the resistance of a ferromagnetic material is dependent on the relative orientation between the magnetisation within the material and the current direction. This phenomenon was termed as anisotropic magnetoresistance (AMR) [88]. In 1990s, IBM commercialised AMR-based read heads (IBM 9340 and 9345) and used it in hard disk drives (HDD) [89]. However, the magnitude of areal densities of AMR-based sensors was predicted to be limited to 5 Gb/in^2 [90, 91]. To overcome the increasing demands for higher capacity and improved sensitivity of hard drives, giant magnetoresistance (GMR) was

first discovered independently by Albert Fert and Peter Grunber in 1988 [92–94]. They were also awarded Nobel prize in 2007 for this discovery. As the name suggests, there is a large change in resistivity for a small applied external magnetic field. GMR worked on the principle of Mott's two current model [95–98]. Mott proposed that in ferromagnetic materials, the electrical conductivity occurs using two independent currents, corresponding to the up-spin and down-spin electrons.

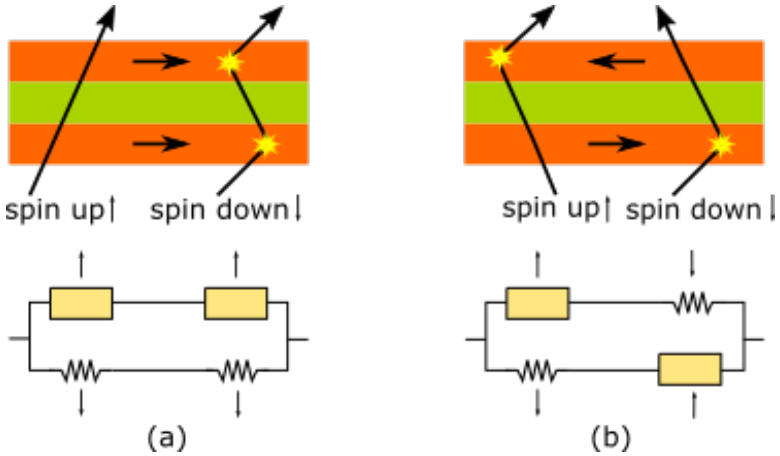

Figure 1.2: Shows a schematic diagram of a simple GMR device, where an non-magnetic spacer layers separate two ferromagnetic layers. (a) the magnetisation in the ferromagnetic layers are parallel to each other that results in lower resistance (b) the magnetisation in the ferromagnetic layers are in anti-parallel configuration that results in high resistance.

Suppose we consider a multilayer system of ferromagnets and non-magnetic metals, assuming that the scattering is strong for electrons with spin anti-parallel to the magnetisation direction, and is weak for electrons with spin parallel to the magnetisation direction. If a current is applied perpendicular to the plane (CPP), for a ferromagnetic arrangement between the layers, one of the spin carries passes through the layer with no scattering, but the other spin carries scatters at both the layers. However, if the layers are in antiferromagnetic configuration, both the spin-up and spin-down electrons scatter. Figure 1.2 shows a depiction of the spin-up and spin-down electrons being scattered for ferromagnetic and antiferromagnetic configuration. In figure 1.2 (a) only the spin-down electrons are scattered by both the layers however figure 1.2 (b) shows that the first layer scatters the spin-down electron and the second layer scatters the spin-up electron.

Therefore, overall the resistance in the antiferromagnetic case will be larger than the ferromagnetic configuration. In 1997, IBM introduced it first commercialised GMR-based HDD with 16.8 GB memory space, which had spin-valve sensors [90, 99, 100].

Soon, in 2004, GMR-based hard drives were replaced by tunnelling magnetoresistance (TMR) based hard drives, first being commercialised by Seagate. By 2006, TMR-HDD had an areal density of 300 Gb/in^2 [101]. TMR effect occurs when a thin insulating layer separates two ferromagnets creating a magnetic tunnel junction (MTJ) and the resistance of the tunnelling current changes with the relative orientation of the two magnetic layers [102]. That is when electrons come across a barrier which it cannot cross over, it can tunnel through the barrier if it is thin enough. The resistance of the structure depends on the relative orientation of the magnetisation of the two ferromagnetic layers. For most of MJTs, the resistance is higher for magnetisation of the ferromagnetic layers aligned anti-parallel to each other than in the case where they are aligned parallel to each other. The TMR-MJT spin-valve technology was used in the read heads of HDD and also in a new type of solid-state memory, a promising contribution towards spintronics, called magnetic random access memory (MRAM) which was a non-volatile memory. The first commercially available MRAM was in the year 2006 [103]. MRAM stood an advantage over regular RAM because of its non-volatile nature; that is a constant supply of power is no longer required to retain information. These devices also had a higher MR ratio, thus enabling a smaller time frame for reading information for the MRAM.

Over the last few decades with the discovery of GMR, TMR [104–106], interest involving ultrathin ferromagnetic structures is ever-increasing. We are currently in an era where ultrathin ferromagnetic structures are incorporated within the magnetoelectronic industry by controlling and manipulating the magnetisation in thin films to store information and for computational purposes. Additionally, recent advancements in materials science research has facilitated more capable magnetostrictive materials in various forms, including polycrystalline and single-crystal thin films. One such non-rare-earth material with moderate magnetostriction constant of 400 ppm is Galfenol which can take the form of bulk as well

as polycrystalline and single-crystal thin films. They have high Curie temperature, low coercivity, low saturation field and excellent mechanical properties making them ideal candidates. This thesis reports detailed studies of its structural, magneto-static and magneto-dynamic properties while varying its composition and thickness in thin-film form.

1.2 Magnetostriction in Galfenol (Fe-Ga)

Galfenol being a single-phase alloy with disordered substitution of Ga in body centred cubic α-Fe exhibits an extraordinary tenfold increase in the magnetostriction constant over pure single-crystal iron [1, 107, 108]. The magnetostriction being the largest in the [100] crystal direction (λ_{100}). $3/2\lambda_{100}$ has a dependence on the Ga concentration achieving 400 ppm at $\approx$ 20% Ga and 440 ppm at $\approx$ 28% Ga for quenched bulk Galfenol along [100] crystal direction. It was a dramatic improvement when compared to the 20 ppm observed in pure single-crystal iron. However, the magnetostriction constant along the rhombohedral [111] direction continued to be relatively unchanged [1].

The magnetostrictive behaviour for the $Fe_{100-x}Ga_x$ alloys for the [100] crystal direction at various Ga concentration can be broadly divided into four groups according to the different lattice structure formation due to disordered substitution of Ga in Fe lattice as the Ga concentration is increased [109]. Figure 1.3 shows the change of $3/2\lambda_{100}$ for bulk Fe-Ga alloys divided into four different regions depending on the concentration of Ga. The figure shows the magnetostriction constant for $Fe_{100-x}Ga_x$ ($4 < x < 35$) prepared by furnace cooling $\approx$10°C/min and by rapid quenching into water at room temperature [109]. The blue solid points represent the alloys prepared under the slow-cooled condition, and the solid red points represent the quenched alloys.

In region I, as the Ga concentration is increased the magnetostriction constant increases monotonically, reaching a maximum value of $\approx$ 320 ppm at $\approx$ 17.9% of Ga for slow-cooled alloys and $\approx$ 390 ppm at 20.6% of Ga for quenched alloys. In region II, as the Ga concentration continues to increases the magnetostriction constant decreases reaching a minimum at 22.5% of Ga for both slow cooled

and quenched alloys. In region III, for Ga concentration between 22.5 to 28.5%, the strain increases again reaching a maximum value of ≈ 380 ppm for slow-cooled alloys and 440 ppm for quenched alloys at 28.5% of Ga. In region IV, for Ga concentration above 28.5%, the magnetostriction constant decreases sharply with the increase in the Ga concentration.

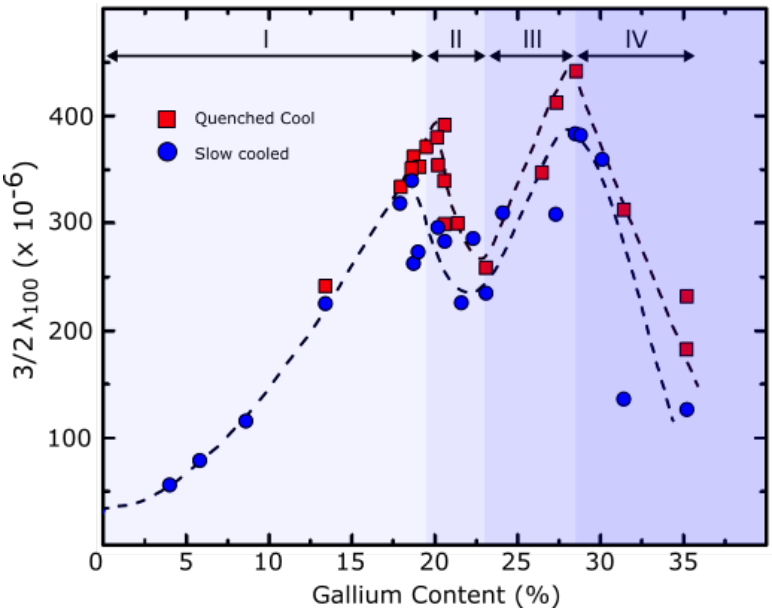

Figure 1.3: Shows the magnetostriction coefficient of bulk Fe-Ga alloy along [100] crystal direction at different Ga concentration. The magnetostriction values have been divided into four different sections, where each section represent a phase formation in Galfenol depending on the Ga concentration. This graph has been adapted from reference [109]. The red points represent the quench cooled samples, and the blue points represent the slow cooled samples.

The origin of an unexpected rise and high enhancement in the magnetostriction of Fe with the addition of Ga has been a subject of research, and numerous theories have been proposed. Comprehensive studies have revealed that the origin of large magnetostriction is structural [110–119]. Figure 1.4 shows the different crystal structures of Fe and $Fe_{100-x}Ga_x$ involved as the Ga concentration is changed. At atmospheric pressure, pure Fe can have three types of allotropes, α-Fe, γ-Fe and δ-Fe. Single crystal iron α-Fe is the most stable form of Fe found at room temperature, and it has a body-centred cubic (bcc) lattice structure, and γ-Fe has a face-centred cubic (fcc) lattice structure as shown in figure 1.4 (a) and

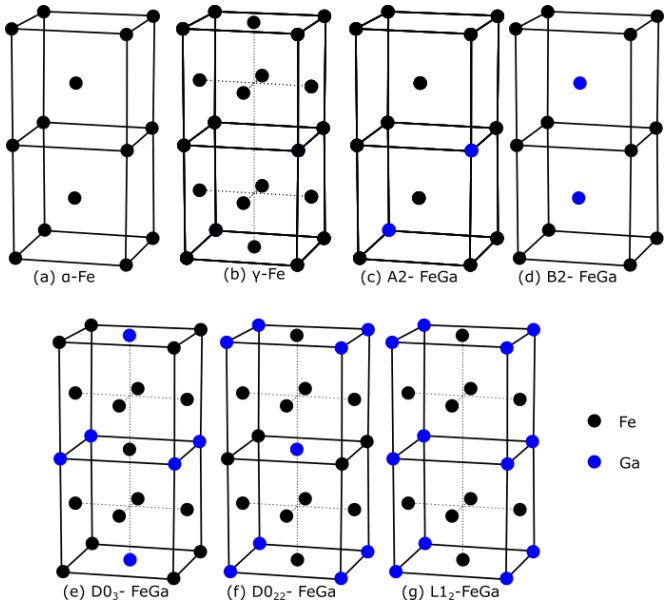

Figure 1.4: Represents the crystal structures of various phase formation of Fe and FeGa. These are the phases formed as the Ga concentration is varied. The black points represent Fe atoms, and the blue points represent Ga atoms. (a) and (b) are the two main allotropes of Fe, α-Fe (body centred cubic) and γ-Fe (face centred cubic) respectively. As Ga is added into Fe, the crystal can take two forms (c) A2-FeGa, where Ga atoms randomly substitute Fe atoms or (d) B2-FeGa, where Ga atoms only occupy the body centred position. As Ga concentration is increased (e) $D0_3$-FeGa structured nano precipitates are formed, and (f) a distorted tetragonal $D0_{22}$ phase is formed. $L1_2$-FeGa, shown in (g) has fcc crystal structure for Ga concentration more than 28%.

(b). When Ga is alloyed with Fe, it can take two forms, an A2 disordered crystal structure where Ga can randomly substitute Fe (figure 1.4 (c)) or Ga will only occupy the body centred sites forming a B2 (ordered bcc) crystal structure (figure 1.4 (d)) [120]. However, B2 ordered structure only exists at temperatures above 650 °C and is not relevant in the current scenario [111]. In region I (fig.1.3), as the Ga concentration is increased, the magnetostriction value increases until it reaches a maximum at $\approx$ 20% Ga, and is attributed to the disordered A2 phase being in metastable equilibrium with an ordered $D0_3$ phase [29, 121–123]. $D0_3$ phase (Fe_3Ga) has Ga at the 4a sites of the face centred cubic structure of γ-Fe, as shown in figure 1.4 (e). A proposed model for the magnetostriction in FeGa

alloys suggested that the $D0_3$ nanoclusters are embedded in an A2 matrix. These $D0_3$ nanoclusters are cubic in nature; however, under the influence of an external magnetic field, they give rise to a magnetic field induced rotation to an intermediate tetragonal $D0_{22}$ phase with Ga-Ga c-axis pairs (shown in figure 1.4 (f)). These tetragonal nano precipitates cause a tetragonal distortion in the A2 cubic structure enhancing the magnetostriction along [100] crystal direction [109, 117–119]. In region III (fig.1.3), the magnetostriction constant peaks again at $\approx 28\%$ Ga concentration, the second peak arises due to the formation of a purely $D0_3$ crystal structure resulting in lattice softening [122–124]. Ultimately in region IV (fig.1.3) as the Ga concentration is increased further, Fe_3Ga existing as a simple fcc $L1_2$ structure starts mixing into the structure resulting in the deterioration of the magnetostriction constant as shown in figure 1.4 (g) [109, 125].

Galfenol on gallium arsenide

For the work presented in this thesis, Galfenol thin films were grown on gallium arsenide (GaAs(001)). GaAs has a cubic zincblende structure. It is an fcc lattice of Ga with another fcc lattice of As displaced by $\sqrt{3}/4$ of the lattice constant along [111] crystal direction [126]. It has a lattice constant of 5.653 Å which almost twice the lattice constant of bcc α-Fe which is 2.866 Å. Therefore, it yields a comparatively low misfit of $\approx$1.4% in a cube on cube epitaxy grown using sputtering.

1.2.1 Early work on Galfenol thin films

Galfenol has been widely studied, and extensive work has been reported on bulk single-crystal and polycrystalline Fe-Ga alloys. They have shown excellent properties characterised by high Curie temperature, low saturation field, low coercivity and high saturation magnetostriction constant. Nevertheless, for it to be incorporated in nano and micro-scale structures, the same functionality had to be reflected in thin films as well [127]. Over the period, efforts have been made to explore the structural, static and dynamic magnetic properties of polycrystalline $Fe_{100-x}Ga_x$ films.

From the bulk work, it is already established that the magnetic properties of

$Fe_{100-x}Ga_x$ alloys strongly depended on the Ga concentration. Therefore, polycrystalline thin films with varying Ga concentration were studied broadly by various groups. Dunlap *et al.* [128] prepared $Fe_{100-x}Ga_x$ films of 800 nm over a wide composition range $0 < x < 36$ grown on Si(100) substrate. The films were grown using the co-sputtering technique where individual targets of Fe and $Fe_{50}Ga_{50}$ were used. The samples were structurally characterised using the x-ray diffraction and Fe Mössbauer effect spectroscopy. They observed a systematic increase in the lattice parameter, a, as the Ga concentration was increased. They have shown that the distribution of Ga atoms in the bcc structure is not random. Ga nanoclusters are formed within the crystal structure before it transitions to the ordered $D0_3$ phase, which confirmed that the short-range ordering plays a vital role in the enhancement of the magnetoelastic properties of Fe-Ga alloys as postulated in previous studies [124]. Javed *et al.* [129] reported polycrystalline $Fe_{100-x}Ga_x$ ($19 < x < 23$) films of thickness 50 nm grown on Si(100) substrate using co-sputtering and evaporation technique. They successfully deposited single-phase bcc FeGa thin films. They also observed a similar trend of increase in the lattice parameter with the increase in the Ga concentration. The films had a weak uniaxial anisotropy at lower Ar pressure and were isotropic with the increase in Ar pressure. Additionally they also reported that the lattice constant was a function of film thickness. Several studies have also reported the saturation magnetostriction constant of these polycrystalline films over a wide range of Ga concentration. They have observed a double peak trend as was seen in bulk $Fe_{100-x}Ga_x$ alloys [130–133]. Apart from Si, other substrates were also used for the growth of polycrystalline Fe-Ga thin films. Lalitha *et al.*[134] grew Fe-Ga thin films on Si, MgO and quartz substrates using RF sputtering and studied the growth and magnetic properties of thin films using x-ray, atomic force microscopy and vibration sample magnetometry measurements. They observed that the MgO substrate favoured higher magnetisation when compared to Si and quartz substrates. Butera *et al.* [135, 136] have grown epitaxial $Fe_{81}Ga_{19}$ films with cubic magnetic symmetry on MgO substrates with dc magnetron sputtering. The cubic magnetocrystalline anisotropy constant was determined to be 1.59 kJ/m^3, and the saturation magnetisation was ≈ 0.15 T. They also observed an

angular variation of the ferromagnetic resonance linewidth suggesting a contribution of two-magnon scattering towards relaxation of the magnetic excitations. Yasushi *et al.* [137] have studied the effect of Ga composition on the static and dynamic properties of $Fe_{100-x}Ga_x$ ($18.5 < x < 33.4$) films of 50 nm thickness onto quartz substrates using dc magnetron sputtering. The saturation magnetisation decreased as the Ga concentration was increased. They observed a maximum saturation magnetostriction constant of 54 ppm. The in-plane effective damping constant decreased up to x =22.3, followed by an increment between 22.3 and 27.2, and decreased further as x was increased. They observed a high value for the in-plane damping constant and associated it with two-magnon scattering and in-plane anisotropy dispersion. The perpendicular (out-of-plane) damping constant showed a similar trend with respect to x but with a lower damping value indicating that the intrinsic damping dominates.

Polycrystalline thin films of Fe-Ga were also studied a function of change in film thickness. Javed *et al.* [138] studied the thickness dependence of the structural and magnetic properties of $Fe_{80}Ga_{20}$ thin films on Si(100) substrate. They varied the thickness of the films between 20 nm to 200 nm. They found that the lattice constant for the films were smaller than the for bulk alloys. As the film thickness was changed, the lattice constant decreased at first and then increased, approaching the bulk value. The surface roughness and grain size increased with film thickness. The saturation magnetostriction constant increased with the increase in the film thickness approaching the bulk isotropic polycrystalline value of 98 ppm. Daniel *et al.* [139] performed measurements of the static and magnetic properties of $Fe_{80}Ga_{20}$ polycrystalline thin films with thickness varying between 20 nm to 80 nm. The films were grown on Si(001) with Cu buffer layer. They observed a lower saturation magnetisation value compared to bulk and epitaxial films. The surface roughness, coercive field, and inhomogeneous broadening tends to increase with the increase in the film. The observed Gilbert damping varied between 0.012 to 0.047 over the thickness range. Yasushi *et al.* [140] also studied the static and dynamic properties of $Fe_{78}Ga_{22}$ polycrystalline thin films with thicknesses between 3 nm to 100 nm grown on soda lime glass substrates. The coercivity increases for increase in the film thickness between 5 nm and 50 nm,

but decreases for the thickness of 100 nm attributed to either the domain wall nucleation or pinning. They observed a damping constant of maximum 0.084, which was much larger than those observed in single-crystal Fe-Ga film. The inhomogeneous broadening also increased with an increase in the film thickness. Nonetheless, the polycrystalline films had a magnetostriction constant value lower than that observed for single and polycrystalline crystal bulk alloys due to the difference in microstructure between films and bulk alloys [141]. Also, the resonant linewidths were large, which was insufficient for microwave applications [136].

Parkes *et al.* [2] reported cubic epitaxial thin film of $Fe_{81}Ga_{19}$ of 21 nm thickness grown by molecular beam epitaxy (MBE) on GaAs(001) substrates. They performed x-ray diffraction to establish the epitaxial growth of the thin film. The magnetostriction was measured using the Villari effect. They observed a magnetostriction constant value of $3/2\lambda_{100} = 395$ ppm, as large as the value reported for single-crystal bulk Fe-Ga alloys. It was also noted that the resonant linewidth was 6.7 mT at 10 GHz and a damping parameter of 0.017 from ferromagnetic resonance studies, lower than those previously reported in the literature. Parkes *et al.* [85] also demonstrated large cubic magnetocrystalline anisotropy in 22.5 nm thick single-crystal $Fe_{81}Ga_{19}$ grown by MBE on GaAs(001) substrates. They demonstrated a strong cubic anisotropy ($K_c = 32.7$ kJm^{-3}) favouring the [100]/[010] easy axis direction and a uniaxial term ($K_u = 8.6$ kJm^{-3}). Bijoy *et al.* [142] reported the growth of single-crystal 20 nm $Fe_{100-x}Ga_x$ ($x = 20, 23, 28$) films on GaAs(001) substrate with a buffer layer of ZnSe by MBE. They observed a narrow FMR linewidth. The FMR linewidth and the Gilbert damping increased with the Ga concentration. The saturation magnetisation of the samples decreased with the increase in Ga concentration.

Even though Fe-Ga alloy is widely studied within its thin-film form, but focus has been mostly on the improvement of the magnetostriction. At the moment, limited research has been carried out on magnetron sputtered epitaxial Fe–Ga films and details about the effect of film composition and film thickness on the magnetic parameters of epitaxial Fe–Ga films are not fully elucidated. In particular, a detailed and elaborated study of the structural, magneto-static and

magneto-dynamic properties of Galfenol thin films grown of GaAs(001) substrate using magnetron sputtering is still not available in literature. Hence, studying the structural and magnetic properties as a function of parameters such as film composition and film thickness could help bring new insight.

1.3 Thesis outline

This thesis has been divided into several chapters presenting an in-depth knowledge about the experimental methodology followed by the analysis undertaken.

Chapter 1 gives a brief overview of the various topic associated with the material under speculation such as a brief history about magnetostriction and magnetostrictive materials, what is Galfenol alloy, the relevant crystal structure of Galfenol, what makes it special, and the motivation.

Chapter 2 is assigned to provide a detailed discussion of the physics behind the basic phenomenon of ferromagnetism, magnetic free energy density and its origin, the process of magnetisation reversal, magnetisation dynamics and magneto-transport effect on thin films. The above mentioned phenomena are the basis of the work presented in this thesis.

Chapter 3 focuses on the materials and the techniques used for the measurement of the structural and magnetic properties of the material. The chapter starts with the growth and fabrication technique used for the samples used in this thesis. Followed by the equipment set-up and measurement techniques that were used on the samples for the collection of the data. In total, five measurements were done on two sets of samples with varying Ga composition and film thickness. Finally, the chapter ends with the steps followed for the simulation and fitting of the experimental data with the simulated data.

Chapter 4 presents the study of the structural properties of the Galfenol thin films obtained by x-ray diffraction (XRD), x-ray reflectivity (XRR) and x-ray photoelectron spectroscopy (XPS).

Chapter 5 focuses on the static magnetic properties of the material which were extracted from the Superconducting QUantum Interference Device (SQUID) magnetometry measurements. It was discussed and compared with similar work

on Fe thin films.

Chapter 6 focuses on the electrical properties of the samples measured by magneto-transport measurements. A direct comparison of the trend observed for magnetocrystalline coefficients and the anisotropy constants were made.

Chapter 7 presents the dynamic properties of Galfenol thin films with varying Ga concentration. The dynamic properties were investigated using the ferromagnetic resonance (FMR) technique. The static properties extracted through FMR measurements were compared with those obtained from the SQUID measurements. The dynamic properties were compared with previously reported results. Unfortunately, due to time constraint, FMR measurements were not performed on the samples with varying film thickness.

Chapter 8 summarises the work that was done and all the conclusions that could be drawn from the experimental results.

Appendix A contains the fitting of the experimental graphs from the SQUID magnetometry measurements with the simulated graph obtained via mathematical calculations.

Chapter 2

Theory

A brief discussion about the background theory of magnetism and the concept behind analysing and understanding the experimental data discussed in this thesis have been presented.

2.1 Ferromagnetism

Ferromagnetic materials show long-range magnetic ordering with a net magnetisation due to the parallel alignment of atomic moments. The net magnetisation is a result of the unpaired spins in the outer d-orbitals interacting with neighbouring atoms via quantum mechanical exchange interaction (explained in section 2.1.2). They carry a spontaneous magnetised state even in the absence of an external magnetic field [143] and can be manipulated using a sufficiently high enough external magnetic field. Iron, cobalt, nickel, alloys such as permalloy, alnico and magnetite are a few examples of these materials possessing ferromagnetism at room temperature, making them essential in industry and modern technological advancement. The electronic configurations at room temperature for these metals are shown in figure 2.1. It gives an idea about the paired and unpaired spin states in the outer d and s orbitals.

Temperature is a critical factor contributing towards the existence of ferromagnetism. When a ferromagnet is heated above a specific critical temperature known as Curie temperature (T_C), the thermal energy within the system begins to exceed the exchange energy. Once the temperature reaches beyond T_C,

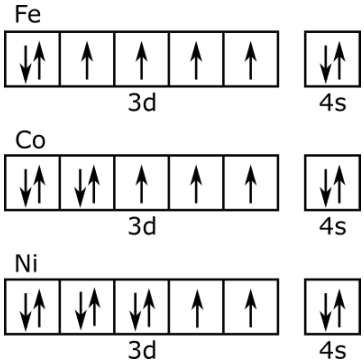

Figure 2.1: The electronic configurations of some ferromagnetic metals at room temperature are shown. The arrows represent the up and down spins. The orbitals are filled using Hund's rule where every orbital is first singly occupied before double occupancy. Hence all the lower energy levels are filled first. It is these unpaired electrons in the d orbitals that interact with neighbouring unpaired d orbital electrons via the exchange interaction resulting in ferromagnetism.

the magnetic moments lose their magnetic ordering producing no net magnetic moment eventually becoming paramagnetic. Figure 2.2 shows the temperature dependence of the magnetisation in a ferromagnetic material. It illustrates the phase transformation from one magnetic state to another. Typically, the Curie temperature for Fe is 1043 K, giving an idea about the amount of thermal energy required to break the long-range ordering in a particular ferromagnetic material.

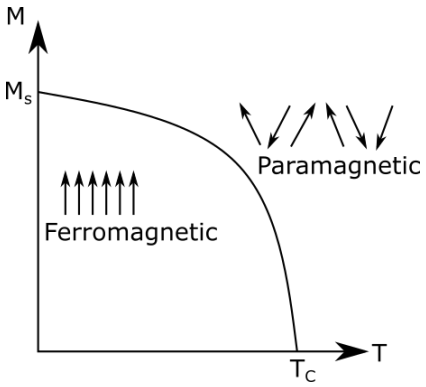

Figure 2.2: The spontaneous magnetisation in ferromagnets at temperature below the Curie temperature is shown. As the temperature approaches absolute zero the spontaneous magnetisation reaches saturation. When the sample is heated above the Curie temperature the thermal motion randomizes the spin orientation and it loses its spontaneous magnetisation thus behaving as a paramagnet.

2.1.1 Spin-orbit Interaction

The magnetic moments expressed in terms of the Bohr magnetron (μ_B) can be represented as,

$$\begin{aligned} \vec{\mu}_L &= -\frac{g_L \mu_B}{\hbar}\vec{L} \\ \vec{\mu}_S &= -\frac{g_S \mu_B}{\hbar}\vec{S} \end{aligned} \tag{2.1}$$

where $\vec{\mu}_L$, $\vec{\mu}_S$ are the magnetic moments associated with orbital angular momentum and spin angular momentum respectively, g_L, g_S are the Landé g-factor with values 1 and 2 respectively, $\vec{L}$ is the orbital angular momentum, $\vec{S}$ is the spin angular momentum, μ_B is the Bohr magnetron quantifying the spin magnetic moment of a single electron, and $\hbar$ is the reduced Planck constant. Suppose we consider the reference frame of the electron and the nucleus is orbiting around the electron creating a positive current loop and a magnetic field $\vec{B}$. Thus, the change of energy of the electron due to the induced torque by the magnetic field $\vec{B}$ on the spin magnetic moment μ_S is given by,

$$\Delta E = -\vec{\mu}_S \cdot \vec{B} \tag{2.2}$$

The relative motion of the nucleus of the atom creating the magnetic field is related to the orbital angular momentum $\vec{L}$ by [143],

$$\vec{B} = \frac{\mu_0 Ze\vec{L}}{4\pi m_e r^3} \tag{2.3}$$

where μ_0 is the permeability in vacuum, Z is the number of protons in the nucleus, and r is the radius of the orbit. If we compare equations 2.1, 2.2 and 2.3 we can establish a relation between spin angular momentum and orbital angular momentum,

$$\Delta E \propto \vec{S} \cdot \vec{L} \tag{2.4}$$

This interaction between the orbital angular momentum of the nucleus and the electron spin angular momentum is known as the spin-orbit coupling. Spin orbit interaction is responsible for many magnetic phenomena such as magnetocrystalline anisotropy and anisotropic magnetoresistance (AMR) [144].

2.1.2 Exchange Interaction

The exchange interaction is the phenomenon behind the existence of long-range magnetic ordering in a ferromagnetic lattice. For a two-electron system, the total Hamiltonian is given by,

$$\hat{H} = \hat{H}_1 + \hat{H}_2 + \hat{H}_{ex} \tag{2.5}$$

where $\hat{H}_1$, $\hat{H}_2$ are the single electron Hamiltonians for electrons 1 and 2 respectively, and $\hat{H}_{ex}$ is the exchange interaction. The exchange energy between the two electrons with spins $\mathbf{S}_1$ and $\mathbf{S}_2$ separated by an angle ϕ_{ex}, is

$$\hat{H}_{ex} = -J_{ex}\mathbf{S}_1 \cdot \mathbf{S}_2 = -2J_{ex}S^2 \cos\phi_{ex} \tag{2.6}$$

where J_{ex} is the exchange integral originating from the overlap of wave functions of the two spins describing the relative proximity of the spins to each other. The exchange interaction is strong enough to orient neighbouring magnetic dipole moments but decays exponentially with distance. The spontaneous ordering of these magnetic moments thus minimises the exchange energy. The spins are oriented parallel or anti-parallel depending on the sign of the exchange integral J_{ex}. In the case of ferromagnets since $J_{ex} > 0$, the exchange energy is minimised when the spins are aligned parallel to each other.

2.2 Magnetic Free Energy Density

The exchange interaction or the exchange energy discussed in the section 2.1.2 describes the interaction between two neighbouring spins in a ferromagnetic material but does not explain why the magnetisation in a ferromagnetic material favours to orient along one particular direction over the other. In the absence of an external magnetic field, the spontaneous magnetisation of the ferromagnet will lie along the easy axis of magnetisation [18, 143]. Hence, when an external magnetic field is applied, there will be an energy expenditure to rotate from the preferred direction of orientation of magnetisation to a required direction of orientation. This energy is called magnetic anisotropy energy. There can be various possible origins for magnetic anisotropy in a material such as the shape or geom-

etry of the sample, crystal symmetry giving the magnetocrystalline anisotropy, and magneto-elastic effects through the strain in the material [18, 144].

The combination of different energies that influence the direction of the magnetisation of a material is the total magnetic free energy density. It is given by equation 2.7.

$$E_{total} = E_{Zeeman} + E_{Exch} + E_{MagAnis} + E_{ME} + E_{Demag} \tag{2.7}$$

where E_{Zeeman} is the energy associated with interaction of the moments with the external applied magnetic field, E_{Exch} is the exchange energy between spins, $E_{MagAnis}$ is the magnetocrystalline energy associated with a crystal lattice, E_{ME} is the magnetoelastic energy associated with the strain in the material, and E_{Demag} is the demagnetising or magnetostatic energy associated with the shape of a ferromagnetic material. Understanding the different energy contributions is important to analyse and understand the experimental data presented in this thesis. The different energy terms that influence the magnetisation of the material studied in this thesis are described in the following sections.

2.2.1 Zeeman Energy

As discussed in section 2.1.1, a ferromagnetic material has ordered magnetic moments hence it has an internal magnetisation. When this ferromagnetic material is placed in an externally applied magnetic field H_{ext}, the energy due to the interaction between the internal magnetisation and the external applied magnetic field is known as Zeeman Energy.

$$E_{Zeeman} = -\mu_0 M_s \int_V (\boldsymbol{H}_{ext} \cdot \boldsymbol{m}) dV \tag{2.8}$$

where μ_0 is the permeability in vacuum, $\boldsymbol{m} = \frac{\mathbf{M}}{|M|}$ is the unit vector along the direction of magnetisation, and the energy is integrated over the entire volume V. In equation 2.8, if we consider no other factors are influencing the magnetisation, H_{ext} will try to align the internal magnetisation parallel to the applied field direction to minimise the total energy.

2.2.2 Magnetocrystalline Anisotropy Energy

In a ferromagnetic material, there are easy and hard axes of magnetisation. Along certain crystallographic directions, it is easy to magnetise the material *i.e* minimum energy is required to achieve saturation along the easy axis and higher energy along others. As a result, the free energy is no longer isotropic. The anisotropic energy introduced by the crystal structure is due to the spin-orbit coupling [143]. This directional dependent anisotropy is known as magnetocrystalline anisotropy, $E_{MagAnis}$.

Magnetocrystalline anisotropy in FeGa/GaAs

The anisotropy energy associated with FeGa thin films grown on GaAs substrate can be represented in terms of direction cosines (α_i) between the magnetisation and the principle crystallographic axes, as shown in figure 2.3. In bulk, Fe has a bcc cubic anisotropy structure with easy axes along crystallographic <100> directions and the hard axes along the <111> directions [143, 145], hence for FeGa thin films grown on [001] oriented GaAs the in-plane cubic easy axes lie along the [010] and [100] directions.

The magnetisation vector as shown in figure 2.3 is represented by the direction cosines,

$$\begin{aligned} \alpha_1 &= \cos\phi_M \sin\theta_M \\ \alpha_2 &= \sin\phi_M \sin\theta_M \\ \alpha_3 &= \cos\theta_M \end{aligned} \tag{2.9}$$

The magnetocrystalline cubic anisotropy energy E_c can be written as [143, 146, 147],

$$E_c = K_{c0} + K_{c1}(\alpha_1^2\alpha_2^2 + \alpha_2^2\alpha_3^2 + \alpha_3^2\alpha_1^2) + K_{c2}(\alpha_1^2\alpha_2^2\alpha_3^2)... \tag{2.10}$$

where K_{ci} is the i^{th} order cubic anisotropy constant, which varies depending on the material. Since the 0^{th} order term has no direction dependence it does not contribute towards the cubic anisotropy energy. The 2^{nd} and higher order terms are usually smaller in magnitude hence can be neglected. Thus, the cubic

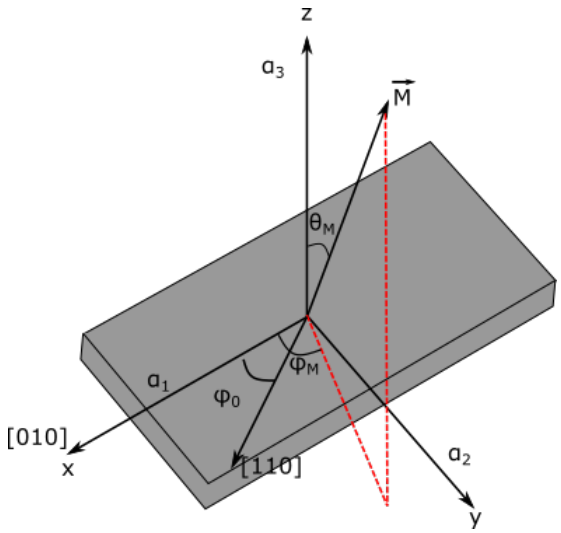

Figure 2.3: The coordinate system of a single layer thin film of FeGa grown on a GaAs substrate is shown. [010] is the cubic easy axis and [110] is the uniaxial easy axis. This coordinate system was used for all the simulations that are included in this thesis.

magnetocrystalline energy term can be simplified to,

$$E_c = K_c(\alpha_1^2\alpha_2^2 + \alpha_2^2\alpha_3^2 + \alpha_3^2\alpha_1^2) \tag{2.11}$$

Substituting the cosines in the above equation we get,

$$E_c = K_c\left(\frac{1}{4}\sin^2(2\phi_M)\sin^2\theta_M + \cos^2\theta_M\right)\sin^2\theta_M \tag{2.12}$$

In thin films the magnetocrystalline energy is different from bulk due to the break in symmetry caused by the thin film geometry [126, 143]. $\theta_M = \frac{\pi}{2}$ since the magnetisation $\vec{M}$ lies in plane of the film due to the demagnetising energy explained in section 2.2.3. Hence the biaxial or cubic anisotropy energy for Fe thin films is

$$E_c = \frac{K_c}{4}\sin^2(2\phi_M) \tag{2.13}$$

For the thin films which are grown on [001] oriented GaAs substrates such as the case for the samples presented in this thesis there is an additional uniaxial anisotropy along [110] due to the interface between the GaAs substrate and the Fe or FeGa thin film [148]. Since the uniaxial anisotropy is confined to the plane of the film, the first order uniaxial anisotropy energy E_u can be expressed as,

$$E_u = K_u\sin^2(\phi_M - \phi_0) \tag{2.14}$$

where $\phi_0 = \frac{\pi}{4}$ for FeGa on [001] GaAs, since the uniaxial anisotropy along [110] lies at an angle $\frac{\pi}{4}$ from the cubic easy axis [010]. Therefore the net magnetocrystalline anisotropy energy for FeGa grown on GaAs can be represented as,

$$\begin{aligned} E_{MagAnis} &= E_c + E_u \\ &= \frac{K_c}{4}\sin^2(2\phi_M) + K_u \sin^2(\phi_M - \frac{\pi}{4}) \end{aligned} \tag{2.15}$$

2.2.3 Demagnetising Energy

When a magnetic material is uniformly magnetised by an external magnetic field, the magnetisation becomes discontinuous or divergent at the edges creating effective magnetic monopoles on either side. But from electrodynamics, we already know magnetic monopoles cannot exist. The magnetic induction $\vec{B}$ thus obeys Gauss's law [145],

$$\begin{aligned} \vec{\nabla} \cdot \vec{B} &= 0 \\ \vec{B} &= \mu_0(\vec{H} + \vec{M}) \\ \vec{\nabla} \cdot \vec{H} &= -\vec{\nabla} \cdot \vec{M} \\ \vec{H} &= \vec{H}_{Demag} \end{aligned} \tag{2.16}$$

As we observe in equation 2.16, a magnetic field $\vec{H}_{Demag}$ is generated in the direction opposite to the magnetisation $\vec{M}$ hence appropriately named as the demagnetising field. The demagnetising energy associated with the demagnetising field is given by,

$$E_{Demag} = -\frac{\mu_0}{2}\int_V \vec{M} \cdot \vec{H}_{Demag} dV \tag{2.17}$$

If the magnetisation of the material is aligned out of the plane of the sample, then the magnetic dipoles will be formed between the upper and lower faces of the sample as shown in figure 2.4 (b) and the demagnetising energy is given by [149];

$$E_{Demag} = \frac{1}{2}\mu_0 M^2 \cos^2\theta \tag{2.18}$$

However, if the magnetisation is aligned in the plane of the sample, the dipoles are formed at opposite edges of the sample (figure 2.4 (a)). For thin films where

sample length >> sample thickness, the demagnetising field can be approximated to 0 due to the long distance between the effective monopoles; therefore, the demagnetising energy induced is 0 [143]. Hence, to reduce the total energy of the system the magnetisation lies in the plane of a thin film.

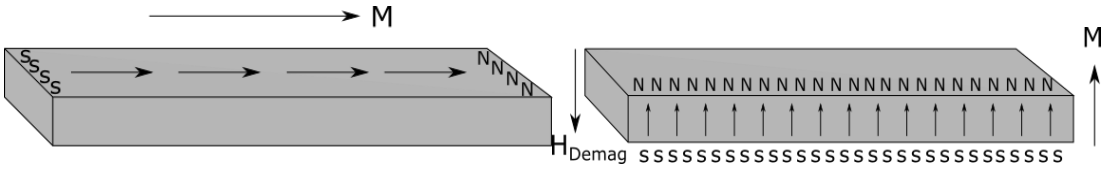

(a) (b)

Figure 2.4: The cross-sectional view of demagnetising field of a magnetic thin film is shown. (a) If the magnetisation lies in the plane of the film, tiny poles are created on the edge. The magnetic field produced at the edge is small comparing to the length of the film hence no demagnetising field is observed. (b) If the magnetisation is perpendicular to the plane of the film as shown a divergence is created on the top and bottom surface of the film, generating a demagnetising field of finite magnitude.

2.2.4 Magnetoelastic Anisotropy Energy

In some ferromagnetic materials, the magnetic properties can change under an application of mechanical deformation (or stress) as a result of a change in the crystal lattice structure. This particular property is defined as the magnetoelastic effect (or inverse magnetostriction or Villari effect). The energy associated with this effect is called the magnetoelastic energy. In elemental ferromagnets it arises through the spin-orbit interaction. In heterogeneous alloys, it can also be associated with inclusion of nanoscale heterogeneities in A2 matrix and is regarded as the structural origin of enhanced magnetostriction in Galfenol, which has been explained previously in section 1.2. Magnetoelastic energy can also be related to the phenomenon of magnetostriction, λ, where a fractional change in length of the sample is observed as it is subjected to a magnetic field. Equation 2.19 gives the mathematical definition of the magnetostriction.

$$\lambda = \frac{\Delta l}{l} \tag{2.19}$$

where l is the length of the material and Δl is the change in length after the application of the magnetic field. Magnetostriction under a saturating magnetic field is denoted by λ_s and can have either a positive or negative value. The sign of these values determines whether the applied magnetic field will cause an elongation (positive) or contraction (negative) along the direction of the applied field. Magnetostriction is an anisotropic property; hence in a crystalline material, the magnetostriction will depend on the angle between the applied magnetic field and the crystal axes. In cubic materials, the magnetostriction is typically measured along the two crystallographic directions [100] and [111].

The magnetoelastic effect can also be described in terms of the magnetoelastic coupling constant, B, corresponding to the magnetic stress causing the magnetostriction. For cubic crystals, the magnetoelastic energy contribution to the free energy is given by the equation 2.20 [144].

$$\begin{aligned} E_{ME} = B_1 \left[\epsilon_{xx}(\alpha_1^2 - \frac{1}{3}) + \epsilon_{yy}(\alpha_2^2 - \frac{1}{3}) + \epsilon_{zz}(\alpha_3^2 - \frac{1}{3}) \right] \\ + B_2 \left[\epsilon_{xy}\alpha_1\alpha_2 + \epsilon_{yz}\alpha_2\alpha_3 + \epsilon_{zx}\alpha_3\alpha_1 \right] \end{aligned} \tag{2.20}$$

where B_1 and B_2 are the magnetoelastic coupling coefficients, α_1, α_2, α_3 are the direction cosines of magnetisation along x, y, z directions respectively, and ϵ_{ij} are the components of the strain tensor. For thin films, with magnetisation only in the plane of the film, α_3 goes to 0 and also assuming the strain terms ϵ_{xy}, ϵ_{yz}, ϵ_{zx} are negligible, equation 2.20 can be simplified to equation 2.21.

$$E_{ME} = B_1 \left[\epsilon_{xx}(\alpha_1^2 - \frac{1}{3}) + \epsilon_{yy}(\alpha_2^2 - \frac{1}{3}) \right] \tag{2.21}$$

The magnetoelastic constant B_1 is given by,

$$B_1 = \frac{3}{2}\lambda_{100}(c_{12} - c_{11}) \tag{2.22}$$

where λ_{100} is the relevant magnetostriction constant and c_{12} and c_{11} are the elastic constants. Hence, the magnetoelastic energy is given by,

$$E_{ME} = \frac{3}{2}\lambda_{100}(c_{12} - c_{11})(\epsilon_{xx} - \epsilon_{xy}) \cos^2 \phi_M \tag{2.23}$$

where ϕ_M is the angle between the magnetisation and the [010] axis. $Fe_{100-x}Ga_x$ has been reported to show high magnetoelasticity at various Ga concentration along [100] direction both in case of bulk as well as in thin films. Galfenol can have large magnetostriction coefficient of up to $3/2\lambda_{100} \approx 350$ ppm at room temperature [1, 107].

2.3 Magnetisation Reversal

Magnetisation reversal is the process of inversion of magnetisation from a positive saturation magnetisation to a negative saturation magnetisation or vice versa by application of a sweeping external magnetic field with sufficient strength to align the magnetisation uniformly with the field direction. The projection of the magnetisation along the sweeping field typically generates a hysteresis loop (figure 2.5).

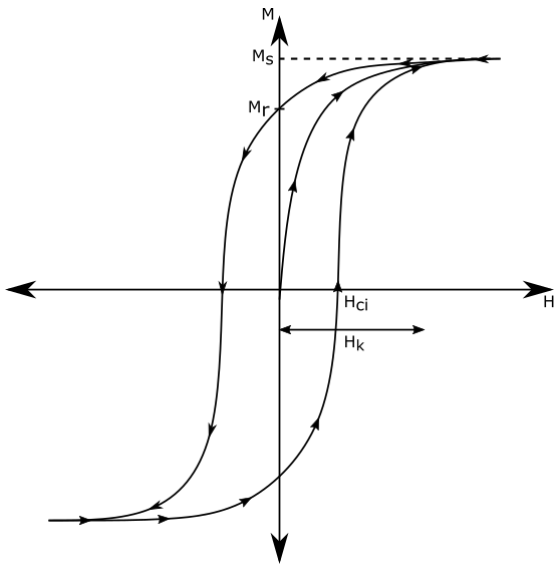

Figure 2.5: An example of a typical hysteresis loop depicting the magnetisation projection along the applied field when the magnetic field is applied along an arbitrary angle with respect to the easy axis. M_s, M_r, H_{ci}, H_k represents the saturation magnetisation, remanent magnetisation, coercive field and anisotropy field respectively.

Figure 2.5 gives a typical example of a hysteresis loop. When a strong positive external magnetic field is applied, the magnetisation will tend to align with the

external field exhibiting a saturation magnetisation (M_s). When the positive applied magnetic field is reduced, the magnetisation retains a positive value at zero applied field, called remanence or remanent magnetisation (M_r) due to the strong exchange interaction and the magnetic anisotropy. In fact, a negative field is required to bring the magnetisation state to zero, known as the coercive field (H_{ci}). H_k represents the anisotropy field, is the field value at the slope break where the magnetisation reaches its saturation value. Upon reduction of the applied field to the opposite direction, the magnetisation undergoes a reversal which occurs due to a combination of magnetisation rotation within domains, and domain wall motion. The main mechanisms involved in magnetisation reversal are described below.

2.3.1 Domain and Domain Walls

In 1907, Weiss discovered that in ferromagnetic materials, uniform magnetic ordering exists within small regions called domains, and different regions with different magnetic orientation coexists, which averages to a zero net magnetisation on a macroscopic scale [143]. These domains are separated by regions, where the magnetic moments rotate coherently, known as domain walls. The magnetisation orientation within a domain and the size of the domain are dependent on various competing energies discussed earlier, ultimately to minimise the free energy of a ferromagnetic material.

Figure 2.6 shows a magnet in the shape of a rectangle in which the magnetisation aligns with the easy axis to minimise the exchange energy and anisotropy energy but at the expense of having high magnetostatic energy due to large stray field. In order to minimise the total free energy density, anti-parallel domains separated by a domain wall reducing the stray fields is formed [143]. However, this anti-parallel alignment of domains leads to a further energy cost due to exchange interaction and anisotropy. But a further decrease in magnetostatic energy can be achieved by the formation of 90° domain walls leading to a full flux closed structure with no magnetostatic energy. The domains are expected to form until the energy required to create a domain wall becomes more significant than the reduction in the magnetostatic energy.

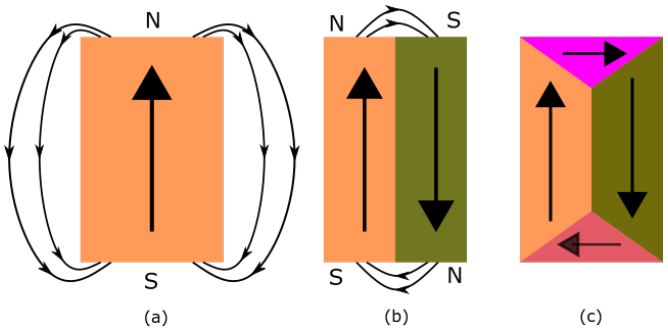

Figure 2.6: Domain formation in a magnet in the shape of a rectangle due to the competition between magnetostatic energy and exchange energy. (a) shows a uniform magnetisation with large stray fields, (b) shows anti-parallel 180° domain with relatively smaller stray fields at the expense of increase in exchange energy and (c) shows formation of closure domain with no stray fields.

Domain Walls

Domain walls separate neighbouring magnetic domains. In order to minimize the total energy of the system, the magnetic moments gradually change direction at the boundaries between neighboring domains. Within a domain wall there is an energy cost related to the exchange energy due to the abrupt change in the orientation of the magnetisation. As the exchange energy increases with the increase in the angle between the spins, it can be reduced by minimising the angle of rotation between the adjacent spins. If the spins rotate over N sites in the domain wall, the angle between adjacent spins becomes π/N. Apart from the exchange energy, since the two domains are oriented to align along the easy axis, which indicates that the spins in the domain wall will lie along the non-easy axis, producing an energy cost associated with it. The exchange energy and the anisotropy energy is combined to govern the total energy per unit area of the domain wall (σ) [18, 144].

$$\sigma = JS^2 \frac{\pi^2}{Na^2} + \frac{NKa}{2} \tag{2.24}$$

where J is the exchange integral, S is the net spin, N is the number of sites over which the spin undergoes π rotation, K is the magnetocrystalline anisotropy constant, and a is the lattice spacing. The first term is due to the exchange energy and is proportional to $1/N$, and tends to make the domain walls wider.

Whereas, the second term is due to the anisotropy energy and is proportional to N, and tends to narrow down the domain wall. The equilibrium wall width is then determined by minimising the sum of these two energies, $d\sigma/dN = 0$.

$$N = \sqrt{\frac{2JS^2\pi^2}{Ka^3}} \tag{2.25}$$

The domain wall thickness is usually expressed by,

$$\delta = Na = \pi S\sqrt{\frac{2J}{Ka}} \tag{2.26}$$

The two common types of 180° domain walls with different spin structures are Bloch and Neél walls [18, 143, 150]. A Bloch wall is shown in figure 2.7(b), it is the transition region between the magnetic domains, where the magnetisation direction rotated in a plane parallel to the plane of the wall. In a Neél (figure 2.7(c)) wall the magnetic moments rotate perpendicular to the plane of the wall. In the case of thin films with magnetisation in the plane of the film, Neél domain walls are preferred because of the extra cost due to the demagnetising energy while Bloch walls are generally found in thicker films.

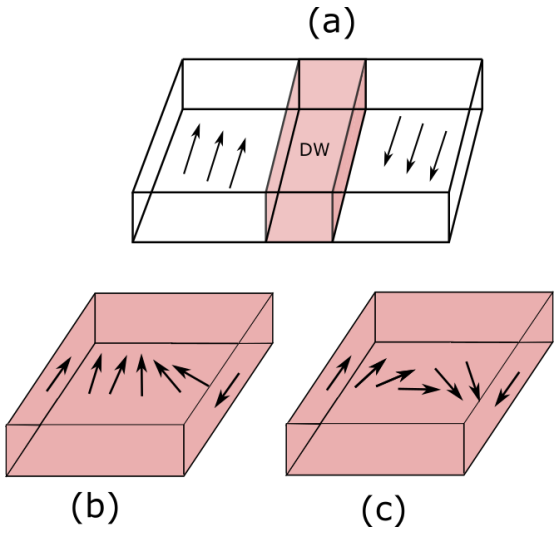

Figure 2.7: Schematic diagram of different types of domain wall (DW) separating anti-parallel or 180° domains in a thin film. (a) shows the DW separating the the 180° domains, (b) Bloch wall (out of plane rotation) and (c) Neél wall (in plane rotation)

2.3.2 Coherent rotation

For materials of smaller dimension, the exchange interaction is dominant hence inducing a uniform magnetisation. The critical size for uniform magnetisation is dependent on the material parameters as well as the shape of the material. Coherent rotation can be described as a process in which a single uniform magnetisation vector undergoes continuous rotation as a result of a competition between the anisotropy energy and Zeeman energy when they are not oriented in the same direction. We consider a particle with uniform magnetisation lying along the easy axis and an external magnetic field is applied along an arbitrary angle, θ, away from the easy axis. For a sufficiently large externally applied magnetic field, the magnetisation vector will be aligned with the applied field. Upon reduction of the strength of the external magnetic field, the torque induced by it to align it along the external field will decrease, and the torque created by the anisotropy field becomes more and more significant, consequently will start rotating the magnetisation vector towards the easy axis. Coherent rotation is a reversible process, that is if the conditions for the initial rotation are kept constant, the magnetisation will rotate back to its initial position through the same configuration.

2.3.3 Magnetisation Switching

Magnetisation switching is the process in which the uniform magnetisation jumps from a local energy minimum to a global energy minimum at a certain external applied field strength when applied in the opposite direction. Magnetisation switching is a discontinuous process; that is the magnetisation vector orientates along with the global energy minimum without passing through the intermediate steps. This magnetisation reversal process is irreversible; that is if the external magnetic field is applied along the initial direction, the magnetisation vector will not switch back through the same steps for the same applied field strength since the free energy has multiple minima.

2.3.4 Stoner-Wohlfarth model

One of the most relevant and simplified cases of magnetisation reversal can be studied for a single domain system. The magnetisation curve for a single domain particle can be calculated using the Stoner-Wohlfarth (SW) model [151, 152]. The model assumes an ellipsoidal particle for a uniform magnetisation throughout the sample. The easy axis is assumed along the elongated axis of the sample hence having a uniaxial magnetic anisotropy as shown in figure 2.8. The total free energy density of the system is given by the exchange energy, anisotropy energy and the Zeeman energy. But for a single domain particle, the exchange energy can be ignored since the exchange energy is always minimised irrespective of the magnetisation vector orientation. Hence the free energy for the SW model is given by,

$$E_{SW} = K_u \sin^2 \phi - MH \cos(\theta - \phi) \tag{2.27}$$

where K_u is the uniaxial anisotropy constant, θ is the angle between the applied magnetic field and the easy axis of the sample, and ϕ is the angle between the magnetisation and the easy axis of the sample. SW model also assumes that the magnetisation vector always lies in the plane of the applied field vector and the easy axis.

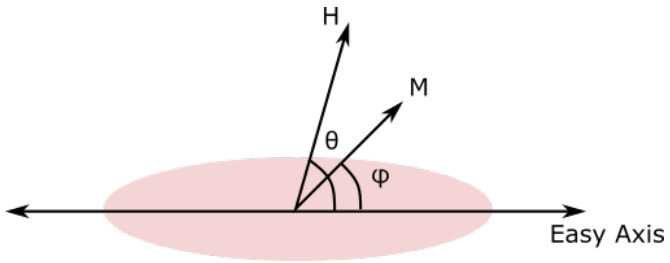

Figure 2.8: Schematic diagram of the SW model where θ is the angle between the applied magnetic field and the easy axis of the sample, and ϕ is the angle between the magnetisation and the easy axis of the sample.

Field applied along the easy axis

When a high saturating positive magnetic field is applied along the easy axis, $\theta = 0°$, the magnetisation vector will lie along with the only energy minimum, $\phi = 0°$, which is the global minimum. When the external magnetic field is removed, two equal energy minima would appear at $\phi = 0°$ and $\phi = 180°$. Nonetheless, the magnetisation will occupy only one of the energy minima, in which it was located previously that is $\phi = 0°$. When a field is applied along $\theta = 180°$, the previous energy minimum at $\phi = 0°$ along which the magnetisation currently lies moves up in energy becoming a local minimum while the minimum at $\phi = 180°$ is further reduced in energy; thus, becoming a global minimum. Thus, at a certain negative field strength, the magnetisation will switch to the new global minimum at $\phi = 180°$. This behaviour is represented by a square hysteresis loop with an abrupt magnetisation reversal if the field is swept between positive and negative saturating fields.

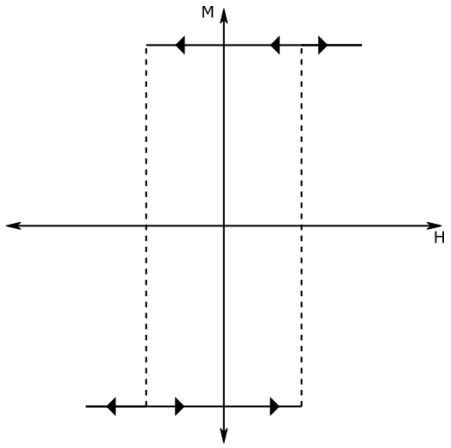

Figure 2.9: Shows the hysteresis loop when the magnetic field is applied along the easy axis as a representation of the SW model.

Field applied along an arbitrary direction away from the easy axis

When the magnetic field is applied along a direction other than the easy axis, such as $\theta = 60°$, for a high positive saturating magnetic field the magnetisation will align along with the energy minimum at $\phi = 60°$. But as the strength of the magnetic field is reduced the position of the energy minimum rotates towards the

easy axis, $\phi = 0°$. This rotation is represented by the reduction in the value of the component of the magnetisation vector measured along the direction of H, as shown in figure 2.10. When a magnetic field is applied in the opposite direction, at certain field strength the magnetisation will switch to the global minimum manifesting a discontinuous jump similar to the field applied along the easy axis.

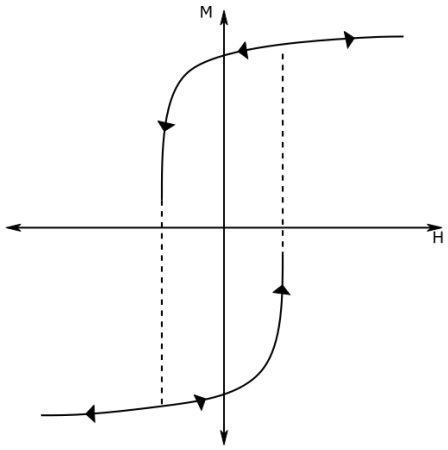

Figure 2.10: Shows the hysteresis loop when the magnetic field is applied at an arbitrary angle away from the easy axis as a representation of the SW model.

Field applied along the hard axis

When the magnetic field is applied along the hard axis, $\theta = 90°$ specific to the sample assumed by the SW model, the magnetisation will always lie along one of the two equivalent global minima. Hence, the magnetisation reversal will not experience any switching or hysteresis behaviour.

The lowest energy state in a thin film at zero applied magnetic field is generally a demagnetised state with multiple domains and domains walls. For a high saturating magnetic field, the samples can be assumed having a single domain with a uniform magnetisation vector achieved by domain wall motion. The domains which are parallel to the applied field will grow at the expense of anti-parallel domains. As the strength of the magnetic field is increased to achieve saturation, there is a coherent rotation of domains towards the applied magnetic field direction. Upon application of the magnetic field in the reverse direction, the magnetisation reversal involves coherent rotation followed by domain nucleation and eventually propagating through the domain wall motion.

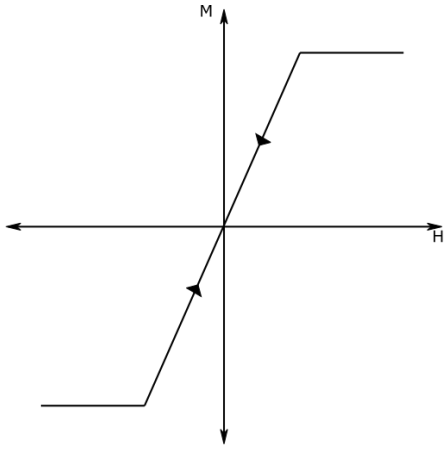

Figure 2.11: Shows the hysteresis loop when the magnetic field is applied along the hard axis as a representation of the SW model.

2.4 Magnetisation dynamics in thin films

Technological advancements in the field of high-quality thin films demand an understanding of the dynamic response of magnetic materials to high-frequency magnetic fields. The precession of the magnetisation under the influence of a time-varying magnetic field in GHz frequency range is governed by the physics of magnetisation dynamics. This section gives a brief introduction to the magnetisation dynamics, and the phenomenon of ferromagnetic resonance.

2.4.1 Larmor precession

As already established in equation 2.1, the magnetic moment of a single electron is related to the spin angular momentum, $\vec{S}$,

$$\vec{\mu}_S = -\gamma \vec{S} \tag{2.28}$$

where γ is the gyromagnetic ratio given by $\gamma = g_S e/2m_e$. However, the static magnetic field will exert a torque on the magnetic moment given by [153, 154],

$$\vec{\tau} = \vec{\mu}_S \times \vec{H} \tag{2.29}$$

Since torque is equal to rate of change of angular momentum, therefore from equation 2.29 we can write,

$$\frac{d\vec{\mu}_S}{dt} = -\gamma \vec{\mu}_S \times \vec{H} \tag{2.30}$$

This torque will cause a precession of the magnetic moment around the magnetic field $\vec{H}$. Thus the precession frequency, ω_L, called Larmor frequency is given by,

$$\omega_L = \gamma H \tag{2.31}$$

γ is a constant quantity with approximate value of $1.75 \times 10^{11}\,\mathrm{rad\,s^{-1}\,T^{-1}}$ or $\gamma/2\pi$ as $28.02\,\mathrm{GHz\,T^{-1}}$.

2.4.2 The Landau-Lifshitz-Gilbert Equation

If we approach the ferromagnetic system from a classical point of view, it can be approximated as a macrospin *i.e* the sum of individual spins, as a result equation 2.30 takes the form,

$$\frac{d\vec{M}}{dt} = -\gamma \vec{M} \times \vec{H} \tag{2.32}$$

where $\vec{M}$ is the magnetisation of the ferromagnetic system. Using the macrospin model and adding a dissipative or damping force to equation 2.32, the magnetisation dynamics can be described by the Landau-Lifshitz-Gilbert (LLG) equation [155, 156],

$$\frac{d\vec{M}}{dt} = -\gamma \vec{M} \times \vec{H}_{eff} + \frac{\alpha}{M_s}\left(\vec{M} \times \frac{d\vec{M}}{dt}\right) \tag{2.33}$$

where α is the dimensionless Gilbert damping parameter, and H_{eff} is the total effective magnetic field acting on the magnetic moments given by,

$$\vec{H}_{eff} = \vec{H}_{Zeeman} + \vec{H}_{Exch} + \vec{H}_{MagAnis} + \vec{H}_{ME} + \vec{H}_{Demag} \tag{2.34}$$

$$\vec{H}_{eff} = -\frac{1}{\mu_0} \nabla_{\vec{M}} \epsilon_{tot} \tag{2.35}$$

where $\vec{H}_{eff}$ is the derivative of the total energy density ϵ_{tot} with respect to the magnetisation, $\vec{M}$, $\vec{H}_{Zeeman}$ is the magnetic field originating due to the interaction of the magnetic moments with the external applied magnetic field, $\vec{H}_{Exch}$ is the field due to the exchange energy, $\vec{H}_{MagAnis}$ is the field due to the anisotropy energy, $\vec{H}_{ME}$ is the field due to the magnetoelastic energy, and $\vec{H}_{Demag}$ is the field due to the demagnetising energy.

The first term in equation 2.33 describes the precessional motion of the magnetisation, $\vec{M}$, around the effective magnetic field, $\vec{H}_{eff}$, and the second term is

the damping included through the Gilbert damping parameter which forces the magnetisation precession to decay towards the direction of the effective magnetic field, H_{eff}. Figure 2.12 shows a schematic diagram of precession of the magnetisation vector, $\vec{M}$, around the effective magnetic field, $\vec{H}_{eff}$, as well as the damping parameter trying to force the magnetisation to be along the magnetic field direction.

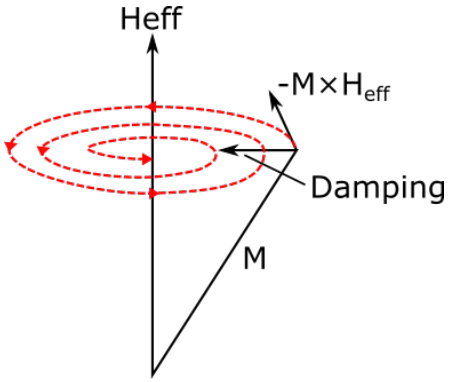

Figure 2.12: Schematic diagram showing the torque acting on magnetisation described by LLG equation. Magnetisation, M, precesses around the effective magnetic field, H_{eff}, and the damping pushes the magnetisation to align along H_{eff}.

2.4.3 Ferromagnetic resonance

Ferromagnetic resonance (FMR) spectroscopy is a highly sensitive technique to investigate both the static and dynamic magnetic properties of ferromagnetic thin films. By performing angle, frequency, and field-dependent FMR measurements it can provide essential parameters such as magnetocrystalline anisotropy constants, saturation magnetisation and the damping parameter [157, 158]. In this section, a brief introduction to the FMR technique is discussed.

The principle behind FMR spectroscopy is based on the precessional motion of the magnetisation in an external magnetic field. As described in section 2.4.1 when a static magnetic field is applied to a magnetic material, the magnetisation starts precessing around the effective magnetic field, H_{eff}. This precessing magnetisation is perturbed when an alternating microwave field, $\vec{H}_{Rf}$, is applied. Figure 2.13 shows a schematic diagram of this precessional motion occurring in

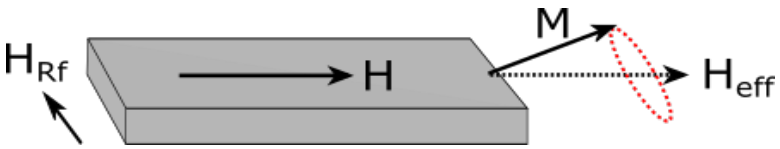

Figure 2.13: A schematic diagram of the FMR effect on a ferromagnetic thin film. When a microwave field, H_{Rf}, is applied normal to the external magnetic field, it perturbs the precession of the magnetisation, M, around the effective magnetic field, H_{eff}.

a ferromagnetic thin film when microwave field, $\vec{H}_{Rf}$, is applied transverse to the external applied magnetic field, $\vec{H}$. It generates a resonance condition when the frequency of the alternating microwave field matches the Larmor frequency [159, 160]. At this resonance condition, the magnetic component of the microwave is absorbed by the spin system having a maximum microwave power absorption observed as a Lorentzian line shape, as shown in figure 2.14.

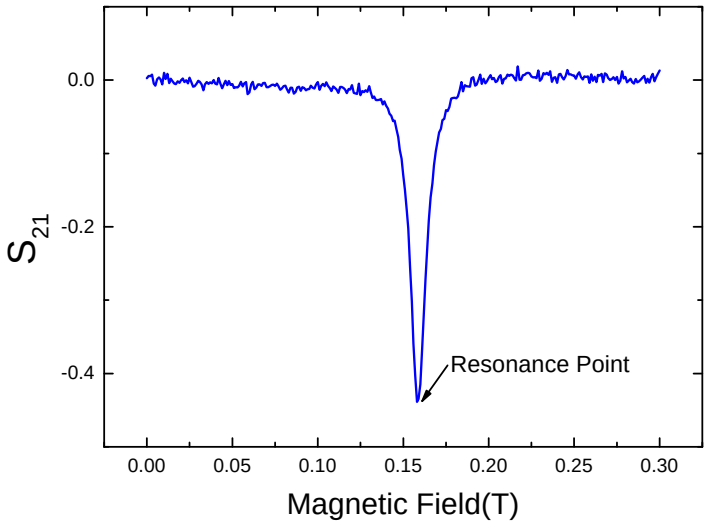

Figure 2.14: S_{21} transmission spectra for sample S534 ($Fe_{86}Ga_{14}$) at 15 GHz, when the magnetic field is applied along [110] direction. A Lorentzian line shape is observed when there is maximum microwave power absorption at the point of resonance.

The resonance condition can be obtained by solving the LLG equation since it gives the time evolution of the magnetisation of a ferromagnet in an external magnetic field [156]. The LLG equation for resonance condition can be solved

using the Kittel approach [159], but since it is based on specific geometries, this restricts the formulae in many ways. In 1955, Smit, Suhl and Beljers [161, 162] obtained a simple form for the resonance condition for any ferromagnet in terms of second derivatives of the total free energy density, E, with respect to polar angle, θ_M, and azimuthal angle, ϕ_M. In this thesis, the method proposed by Smit, Suhl and Beljers is used to obtain the resonance condition.

A magnetic system reaches equilibrium when the total magnetic free energy density (E) is minimum. This equilibrium condition is therefore achieved by,

$$\frac{\partial E}{\partial \theta_M} = 0 \quad \text{and} \quad \frac{\partial E}{\partial \phi_M} = 0 \tag{2.36}$$

As long as microwave field, $\vec{H}_{Rf}$, has a component perpendicular to magnetisation, $\vec{M}$, it will disturb the equilibrium. In principle, the LLG equation should be used but for simplicity the LLG equation without the damping (LL equation) is used since the damping doesn't affect the resonance condition. Thus, the LL equation is given by,

$$\frac{d\vec{M}}{dt} = -\gamma \vec{M} \times \vec{H}_{eff} \tag{2.37}$$

Representing the above equation using the polar coordinate system gives,

$$\frac{d\vec{M}}{dt} = -\gamma (M_s \hat{r}) \times (H_s \hat{r} + H_\theta \hat{\theta} + H_\phi \hat{\phi}) \tag{2.38}$$

where M_s is the magnitude of the magnetisation. Writing 2.37 in matrix form,

$$\begin{bmatrix} \frac{dM_s}{dt} \\ M_s \frac{d\theta_M}{dt} \\ M_s \sin\theta_M \frac{d\phi_M}{dt} \end{bmatrix} = -\gamma \begin{vmatrix} \hat{r} & \hat{\theta} & \hat{\phi} \\ M_s & 0 & 0 \\ H_r & H_\theta & H_\phi \end{vmatrix} \tag{2.39}$$

The total free energy density is,

$$E = -\vec{M} \cdot \vec{H}_{eff} = -\gamma (M_s \hat{r}) \cdot (H_s \hat{r} + H_\theta \hat{\theta} + H_\phi \hat{\phi}) \tag{2.40}$$

Now, if the magnetisation is rotated by a small angle, $\Delta\theta$, the free energy density becomes,

$$E_{rot} = -\gamma [M_s (\hat{r} + \Delta\theta_M \hat{\theta})] \cdot (H_s \hat{r} + H_\theta \hat{\theta} + H_\phi \hat{\phi}) \tag{2.41}$$

Therefore the change in free energy density is,

$$\Delta E = E - E_{rot} = -M_s H_\theta \Delta\theta_M \tag{2.42}$$

Thus, H_θ can be expressed as

$$H_\theta = -\frac{1}{M_s}\frac{\partial E}{\partial \theta_M} \tag{2.43}$$

Similarly, H_ϕ can be expressed as

$$H_\phi = -\frac{1}{M_s \sin\theta_M}\frac{\partial E}{\partial \phi_M} \tag{2.44}$$

Substituting equation 2.43 and 2.44 into 2.39 yields,

$$\begin{bmatrix} \frac{dM_s}{dt} \\ M_s\frac{d\theta_M}{dt} \\ M_s \sin\theta_M \frac{d\phi_M}{dt} \end{bmatrix} = -\gamma \begin{vmatrix} \hat{r} & \hat{\theta} & \hat{\phi} \\ M_s & 0 & 0 \\ H_r & -\frac{1}{M_s}\frac{\partial E}{\partial \theta_M} & -\frac{1}{M_s \sin\theta_M}\frac{\partial E}{\partial \phi_M} \end{vmatrix} \tag{2.45}$$

Equating the above equation gives us,

$$\begin{aligned} \frac{dM_s}{dt} &= 0 \\ -\frac{M_s}{\gamma}\sin\theta_M \frac{d\theta_M}{dt} &= \frac{\partial E}{\partial \phi_M} \\ \frac{M_s}{\gamma}\sin\theta_M \frac{d\phi_M}{dt} &= \frac{\partial E}{\partial \theta_M} \end{aligned} \tag{2.46}$$

The small magnetic field generated by $\vec{H}_{Rf}$ will try to disturb the magnetisation from the equilibrium position. Hence to solve the above set of equations we need to first find the equilibrium position. Assuming, that the deviation of θ_M and ϕ_M from the equilibrium position of $\theta_{M,eq}$ and $\phi_{M,eq}$ is small [163],

$$\begin{aligned} \theta_M &= \theta_{M,eq} + \delta\theta_M \\ \phi_M &= \phi_{M,eq} + \delta\phi_M \end{aligned} \tag{2.47}$$

If we do a Taylor series expansion of $\frac{\partial E}{\partial \theta_M}$ and $\frac{\partial E}{\partial \phi_M}$ keeping only the linear terms from the expansion and substituting 2.47 into 2.46 yields,

$$\begin{aligned} -\frac{M_s}{\gamma}\sin\theta_M \frac{d\delta\theta_M}{dt} &= \frac{\partial^2 E}{\partial\phi_M \partial\theta_M}\delta\theta_M + \frac{\partial^2 E}{\partial\phi_M^2}\delta\phi_M \\ \frac{M_s}{\gamma}\sin\theta_M \frac{d\delta\phi_M}{dt} &= \frac{\partial^2 E}{\partial\theta_M \partial\phi_M}\delta\phi_M + \frac{\partial^2 E}{\partial\theta_M^2}\delta\theta_M \end{aligned} \tag{2.48}$$

The above equations are a pair of homogeneous equations and will have a periodic solution $\delta\theta_M$, $\delta\phi_M \approx e^{i\omega t}$, where ω is the frequency of the microwave magnetic field. If the determinant of the system of equation is equated to 0 this will give us the

resonance frequency of oscillation also known as the Smit Suhl Beljers equation as [161],

$$\left(\frac{\omega_{res}}{\gamma}\right)^2 = \frac{1}{M^2 \sin^2\theta_M}\left[\frac{\partial^2 E}{\partial\theta_M^2}\frac{\partial^2 E}{\partial\phi_M^2} - \left(\frac{\partial^2 E}{\partial\theta_M \partial\phi_M}\right)^2\right]_{\theta_{M,eq},\phi_{M,eq}} \tag{2.49}$$

And the field linewidth which is related to the damping is given by the equation [164],

$$\Delta H = \frac{\alpha}{|\partial\omega_{res}/\partial H_{ext}|}\frac{\gamma}{M_s}\left[\frac{\partial^2 E}{\partial\theta_M^2} + \frac{1}{\sin^2\theta_M}\frac{\partial^2 E}{\partial\phi_M^2}\right]_{\theta_{M,eq},\phi_{M,eq}} \tag{2.50}$$

2.4.4 Ferromagnetic resonance damping

As the magnetisation precesses around the applied magnetic field, it experiences resistance to its precessional motion represented by the rate of energy dissipation of the system. This is known as magnetic damping [155, 165]. The FMR linewidth (ΔH) discussed in the previous section arises from the magnetic damping as well as the imperfections and inhomogeneities within the material. The sources of damping contributing towards FMR linewidth can be divided into intrinsic effects called Gilbert damping, and extrinsic effects often attributed to two magnon scattering, eddy current damping, spin pumping *etc.* [165–168]. Since eddy currents are proportional to the square of the film thickness, hence in thin films such as in case of the samples discussed in this thesis, its contribution can be ignored towards damping. In ferromagnetic thin films, the contributions towards damping mainly come from Gilbert, two magnon scattering, mosaicity and dragging effects which will be discussed in the following section. Attempts have been made to separate these contributions from the measured FMR linewidths.

2.4.4.1 Intrinsic damping

Intrinsic (Gilbert) damping originates from the phenomenological spin relaxation of magnetisation precession. Usually, the itinerant electron behaviour is the dominant cause of intrinsic damping [169, 170]. The origin of this damping is due to the spin-orbit coupling within the crystal lattice structure [155, 171]. Although the mechanism by which damping arises is still a matter of debate, however, the most widely accepted model for intrinsic damping effect is achieved using the

breathing Fermi surface model [172, 173]. The model describes the transfer of angular momentum from the Fermi level electrons to the crystal lattice due to spin orbit coupling effect. In a ferromagnetic crystal lattice the itinerant s-electrons couple with neighbouring non-itinerant d-electrons. As a result of this coupling both s and d electrons undergo precessional motion upon application of a magnetic field. However, the finite mean free path of itinerant electrons leads to a phase lag between the two moments as they attempt to align along the effective magnetic field. This phase lag leads to a transfer of angular momentum [174].

The contribution of the Gilbert damping towards the resonance linewidth is given by,

$$\Delta H_{in} = \alpha \frac{\omega}{\gamma} \tag{2.51}$$

where α is the Gilbert damping parameter, ω is the angular frequency, and γ is the gyromagnetic ratio. In a sample with a perfect crystal structure, the general form of damping terms of the resonance linewidth is given by,

$$\Delta H = \Delta H_0 + \Delta H_{in} \tag{2.52}$$

where ΔH is the field linewidth, ΔH_{in} describes the intrinsic damping behaviour originating due to spin orbit coupling and is a fundamental property of the material, and ΔH_0 is the extrinsic effects originating from the disparity of the magnetic properties within the sample due to structural defects [175].

2.4.4.2 Two-magnon scattering

Two magnon scattering is one of the extrinsic contributions towards FMR damping. The two magnon scattering originates from the coupling between uniform magnetisation precession (FMR mode) and the non-uniform magnetisation precession (spin-wave mode). This could arise from various reasons like local defects, inhomogeneity, boundary conditions, grain size, *etc.* identified as the scattering centres. At resonance, excited magnons precesses as a wave defined by the wave number, $\mathbf{k}$. If the precession is uniform then $\mathbf{k} = 0$, known as the FMR mode. If these uniform spin waves are scattered at the scattering centres to lead the energy transfer from uniform magnetisation precession into degenerate non-uniform spin-waves, $\mathbf{k} \neq 0$, dissipating energy into the lattice. Two-magnon scattering imposes

non-linearity in the FMR damping and is given by [165, 176],

$$\Delta H_{2m} = \Gamma \sin^{-1} \sqrt{\frac{\sqrt{\omega^2 + (\omega_0/2)^2} - \omega_0/2}{\sqrt{\omega^2 + (\omega_0/2)^2} + \omega_0/2}} \tag{2.53}$$

where Γ is a dimensionless parameter describing the magnitude of the two magnon scattering, and ω_0 is given by,

$$\omega_0 = 4\pi\gamma \mathbf{M}_{eff} \tag{2.54}$$

where $\mathbf{M}_{eff}$ is the effective magnetisation. If the two magnon scattering is dominant over the intrinsic damping, the resonance linewidth no longer remains linear and is given by,

$$\Delta H = \Delta H_0 + \Delta H_{in} + \Delta H_{2m} \tag{2.55}$$

Since FMR damping is strongly dependent on the structure of the magnetic material and determines the dynamic behaviour of the material, hence, measuring the damping of the material gives a crucial understanding of the magnetisation dynamics within the material to be used as spintronic devices. For some applications, a low damping parameter is preferred to have a low critical switching current for magnetic switching. Conversely, a higher damping parameter gives faster switching such as required in case of memory devices.

2.4.4.3 Mosaicity and Dragging effect

The mosaicity within thin films structure is one of the sources of enhanced relaxation contributing towards extrinsic damping (ΔH_0). Mosaicity may occur if the crystalline structure, internal fields or the thickness of the film vary from one region to another within the thin film subtly shifting the resonance fields by introducing a range of spin alignments among these individual regions causing a broadening in the linewidth.

Dragging effect is associated with the fact that the magnetisation at lower field may not be collinear with the applied field [177, 178]. Since the linewidth is inversely depended on the cosine of the angle between the magnetisation and the magnetic field, the linewidth is enhanced whenever the magnetisation is not aligned with the magnetic field. In order to minimise the dragging effect, it is

a good practice to use higher values of the applied magnetic field during FMR experiments. However, these terms are usually small; so no further consideration will be given henceforth. For samples which have mosaicity driven line-width broadening shows a eightfold angular dependency. Their is also a eightfold angular dependency in case of samples with a strong field-dragging contribution towards the Gilbert damping.

2.5 Magneto-transport Properties

Magneto-transport is the study of coupling between the transport of electrons through metal or semiconductors and a magnetic field. The resistivity of these metals changes on application of the external magnetic field; this effect is defined as magnetoresistance. It is one of the fundamental properties in the development of data storage, sensors and logic devices [179–181]. In general, magnetoresistive devices are based on ferromagnets, therefore making it a topic of interest. There are several effects that relate the magnetic state of a material to its resistivity. The ordinary Hall effect or ordinary magnetoresistance depends on the applied magnetic field whereas, the anomalous Hall effect is related to magnetisation in the material. Anisotropic magnetoresistance is when the magnetoresistance is affected by both the direction of current and the magnetisation with respect to the crystalline axes. These important concepts and theories have been discussed in this section, which was later used to gain a better understanding and analysis of the experimentally obtained data presented in this thesis.

2.5.1 Ordinary Hall effect

Discovered in 1879 by E.H. Hall [182], if an electric current flows through a conductor and a magnetic field is applied perpendicular to it, a Lorentz force normal to both the directions is exerted on the carriers. Charge starts to accumulate on the edge of the conductor in the course of deflection until a transverse electric field (Hall field) balances the Lorentz force. For example, if we consider a 2D electrically conducting bar of thickness, t, and apply a magnetic field with magnetic flux density, B_z, along the z-direction and current, I_x, along the x-direction, the

resulting electric field will lie in x-y plane hence giving a transverse (R_{xy}) Hall resistance. The Hall voltage, V_H, and Hall resistance, R_{xy}, are given by,

$$V_H = \frac{I_x B_z}{ne} \quad \text{and} \quad R_{xy} = \frac{E_y}{j_x B_z} = \frac{V_H t}{I_x B_z} = -\frac{1}{ne} \tag{2.56}$$

where n is the charge carrier density, e is the charge of electron, E_y is the induced electric current and j_x is their current density. As evident from equation 2.56 the ordinary Hall effect is linear to the applied magnetic applied.

2.5.2 Anomalous Hall effect

In a ferromagnetic material, an additional type of Hall effect called the anomalous Hall effect (AHE) occurs along with the ordinary Hall effect (OHE). When an electric current is applied through a ferromagnetic material, spin-dependent scattering occurs due to the spin-orbit coupling, however, as there is an uneven number of up and down spins in a ferromagnet more carriers deflect towards one side of the bar than the other, generating a net electric field. Thus in Hall bar geometry generating a finite transverse resistance, R_{xy}, proportional to the out of plane component of the magnetisation. R_{xy} due to AHE is usually smaller than the OHE, but depending on certain applied field strengths can exceed as well. A saturating external magnetic field is applied to make sure that OHE R_{xy} contribution dominates over the AHE R_{xy} contribution. The total effect is given by [183–185],

$$R_{xy} = R_{xy}^{OHE} + C R_{xx}^{n} M_z \tag{2.57}$$

where n usually takes a value between 1 and 2, C is a material specific constant and M_z is the out of plane component of the magnetisation. The anomalous part of the equation 2.57 depends both on material specific parameters as well as the longitudinal resistance, R_{xx}.

AHE can originate from three different types of contributions: intrinsic, skew scattering and side-jump. Intrinsic contribution, as the name suggests depends only on the band structure and is independent of any scattering impurities. The intrinsic AHE is observed to yield a contribution proportional to R_{xx}^2. Skew or asymmetric scattering contribution is due to the scattering from impurities caused by the spin-orbit interaction and is proportional to R_{xx}. AHE current can also

have a contribution from side-jump experienced by carriers upon scattering from spin-orbit coupled impurities. Side-jump scattering also being proportional to R_{xx}^2, cannot be separated from the intrinsic contribution by dc Hall measurements.

2.5.3 Anisotropic Magnetoresistance

The resistance of a magnetic material changes depending on the angle between the applied magnetic field and the current flowing through the sample *i.e.* the longitudinal (R_{xx}) resistance and transverse (R_{xy}) resistance of a magnetic material change as the orientation of the magnetisation changes. This effect was first discovered by W. Thomson in 1856 in Fe and Ni [186]. This was understood to arise as a result of spin-orbit interaction. AMR can be described using the equation 2.58 [187],

$$\frac{\Delta\rho}{\rho_{ave}} = \frac{\rho_{||} - \rho_{\perp}}{\rho_{ave}} \tag{2.58}$$

where $\Delta\rho/\rho_{ave}$ is the AMR ratio with $\Delta\rho$ being the change in resistivity of the sample due to AMR effect, ρ_{ave} is the average value of the resistivity for the magnetisation rotated 360° in the plane of the sample, $\rho_{||}$ is the resistivity when the current is parallel to the magnetisation, and $\rho_{\perp}$ is the resistivity when the current is perpendicular to the magnetisation.

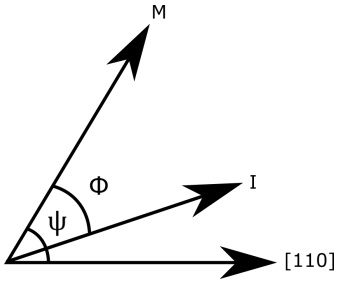

Figure 2.15: The angles between the magnetisation, current, and uniaxial easy axis [110] with respect to each other as defined and used in this thesis.

AMR has contributions from both crystalline and non-crystalline terms. The crystalline term appears due to its dependency on the angle between the magnetisation and the crystalline axes. The non-crystalline term is due to the angle between the magnetisation and the applied electric current. The crystalline terms are typically much smaller than the non-crystalline term. Phenomenologically, it

has been shown in reference [188] that the form of AMR in an anisotropic single crystal ferromagnetic sample is given as,

$$\begin{aligned}\frac{\Delta\rho_{xx}}{\rho_{ave}} &= C_I \cos 2\Phi + C_U \cos 2\psi + C_C \cos 4\psi + C_{I,C} \cos\left(4\psi - 2\Phi\right) \\ \frac{\Delta\rho_{xy}}{\rho_{ave}} &= C_I \sin 2\Phi + C_{I,C} \sin\left(4\psi - 2\Phi\right)\end{aligned} \tag{2.59}$$

where $\Delta\rho_{xx} = \rho_{xx} - \rho_{ave}$, ρ_{ave} is the average value of the resistivity ρ_{xx} for the magnetisation rotated 360° in the plane of the sample, C_I is the non-crystalline coefficient, C_U is the uniaxial crystalline coefficient, C_C is the cubic crystalline coefficient, $C_{I,C}$ is the crossed non-crystalline and cubic crystalline coefficient, Φ is the angle between the current and the magnetisation in the plane of the sample, and ψ is the angle between the magnetisation and uniaxial easy axis [110] as shown in the figure 2.15. Figure 2.16 shows longitudinal AMR along different crystalline directions for sample S642 (5 nm).

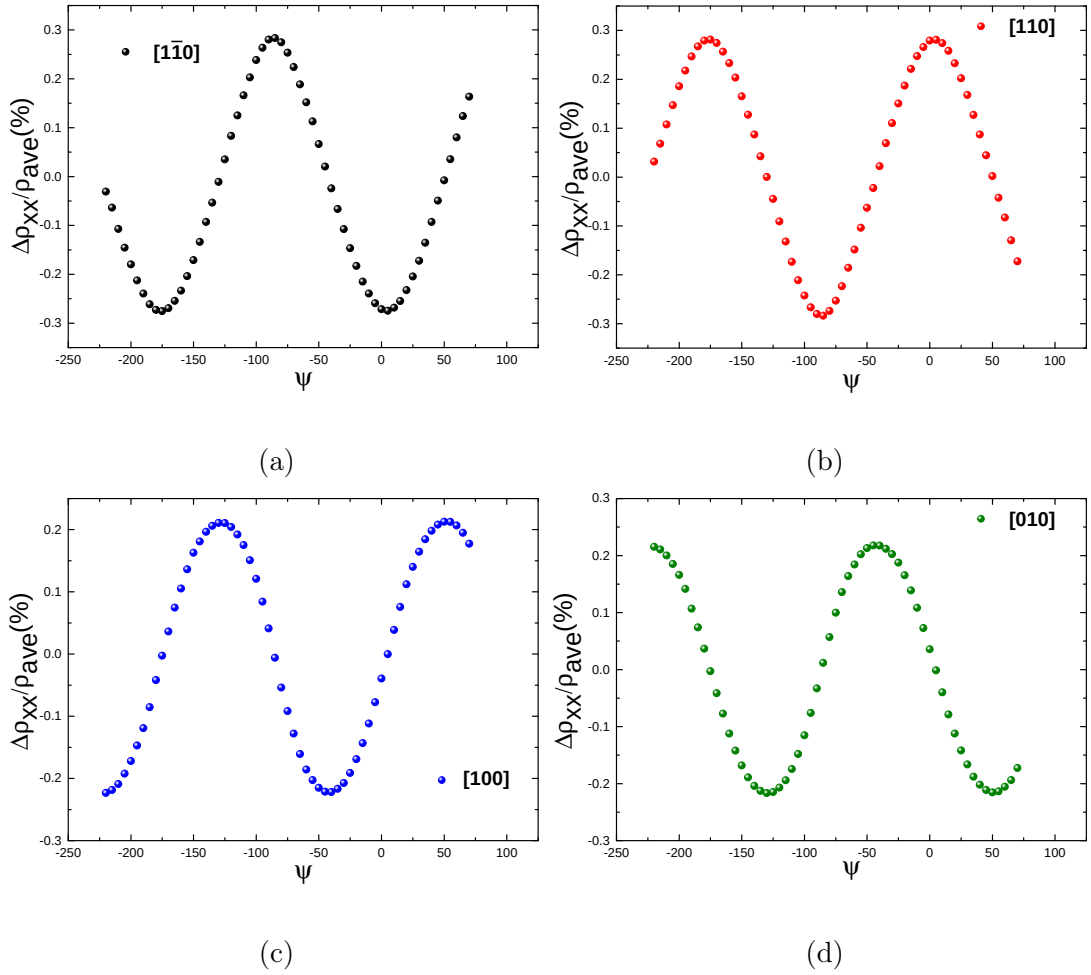

Figure 2.16: Longitudinal AMR for sample S642 along the crystalline direction (a) [1$\bar{1}$0] (b) [110] (c) [100] and (d) [010]. A constant dc current of 1 mA is passed along different crystal direction. ψ is the angle between the magnetisation and uniaxial easy axis [110].

Chapter 3

Materials and Techniques

This chapter describes the growth, experimental and computational techniques used in this thesis.

3.1 Materials Used

The materials used in this thesis are single layers of ferromagnetic Galfenol (Fe-Ga) thin films grown on semiconductor gallium arsenide (GaAs) substrates. All the samples were grown on GaAs(001) substrates of thickness 450 µm and a capping layer of chromium (Cr) of thickness 2 nm was deposited to prevent the samples from oxidising. Two sets of samples were grown which are enumerated in table 3.1 and 3.2. For the first set of samples, the Ga concentration was varied keeping the film thickness as a constant. For the second set, the thickness of the films was varied keeping the composition of the alloy as a constant.

Sample name	Nominal Sample Composition	Growth Rate ($Å s^{-1}$)		Argon Pressure (mTorr)
		Fe	FeGa	
S529	$Fe_{70}Ga_{30}$	0.10	0.32	1.18
S530	$Fe_{76}Ga_{24}$	0.20	0.32	1.18
S531	$Fe_{80}Ga_{20}$	0.30	0.32	1.16
S532	$Fe_{82}Ga_{18}$	0.40	0.32	1.18
S533	$Fe_{85}Ga_{15}$	0.50	0.32	1.21
S534	$Fe_{86}Ga_{14}$	0.60	0.32	1.21
S535	$Fe_{88}Ga_{12}$	0.70	0.32	1.09
S536	$Fe_{90}Ga_{10}$	0.70	0.25	1.12
S537	$Fe_{91}Ga_{09}$	0.70	0.20	1.21
S538	$Fe_{93}Ga_{07}$	0.70	0.15	1.21

Table 3.1: List of the samples used in this thesis for the purpose of studying the role of Ga composition in ferromagnetic Fe-Ga samples as described in the experiments later. All the samples have a film thickness of 20 nm and a Cr capping of 2 nm.

Sample name	Nominal Thickness (nm)	Argon Pressure (mTorr)
S642	5	1.34
S643	7.5	1.15
S641	10	1.15
S640	20	1.26
S644	29	1.24
S646	56.5	1.17
S645	95	1.30

Table 3.2: List of the samples used in this thesis for the purpose of studying the role of thickness variation of ferromagnetic Fe-Ga thin films as described in the experiments later. The above samples have a nominal composition of $Fe_{79}Ga_{21}$ with growth rate of Fe(99.99%) and $Fe_{50}Ga_{50}$ targets being $0.25\,Å\,s^{-1}$ and $0.15\,Å\,s^{-1}$ respectively. All the samples have 2 nm Cr capping layer.

3.1.1 Growth

The thin film layers prepared and studied in this thesis have been grown by the magnetron sputtering technique using the Mantis QPrep500 high vacuum sputter deposition system in the Spintronics Group at the University of Nottingham. The surface of the substrate was prepared by cleaning in 1:1 HCl ($\approx 37\%$) to water solution for 2 minutes. This step was done to ensure that all the native surface oxides and contaminants were well removed [189, 190]. Then the substrate was annealed in the vacuum chamber of the sputtering machine at 550°C for 1 hour and was allowed to cool down to room temperature naturally. It helps to improve the crystal quality of the film by ensuring epitaxial growth as well as a larger grain size [191, 192].

First, a series of $Fe_{100-x}Ga_x$ thin films on GaAs(001) were grown to calibrate the sputter system. Calibration was necessary since the $Fe_{100-x}Ga_x$ films were grown by co-sputtering a composite $Fe_{50}Ga_{50}$ target along with a pure Fe(99.99%) target. Hence, calibrating both the growth rates of FeGa and Fe, along with knowing the composition of the composite target was required. The thicknesses of these samples were monitored in-situ using the crystal quartz monitor (QCM) as well as ex-situ by x-ray reflectivity measurement. The x-ray reflectivity measurements were performed and fitted by myself. The results were used to set the tooling factor on the sputter machine.

Sputtering

Sputtering is a physical vapour deposition (PVD) technique where high energy ion strikes the target, physically ejecting the atoms and molecules from the surface transferring them onto a substrate for deposition. Sputtering is a plasma-based process which is achieved by applying an electric potential to argon gas at low pressure to increase the rate of ionization. Electrons present near the target (cathode) will get accelerated towards the anode (figure 3.1), on the way colliding and ionising the neutral argon atoms resulting in a plasma. The resulting Ar^+ atoms will then be attracted towards the target. Thus, due to momentum transfer, target surface atoms gain sufficient energy for outward motion and get sputtered

onto the substrate. During magnetron sputtering, the plasma is kept confined near the target by applying a magnetic field, increasing the plasma density, the sputtering rate and subsequently increasing the deposition rate.

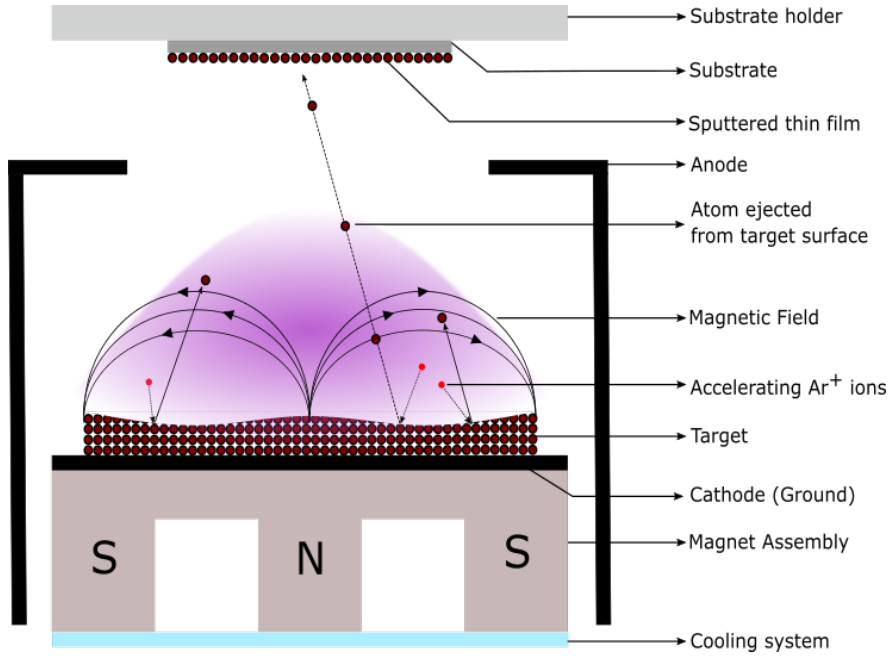

Figure 3.1: Schematic diagram of the magnetron sputtering system used to grow the samples investigated in this thesis. The substrate holder is being rotated at 20 rpm to ensure uniform thin film growth. The magnetic field lines are seen as a cross-section from the side.

Sputtering is among the most widely used deposition techniques due to its high deposition rate at the same time providing high purity uniform thin films at a lower cost. Depending on the material that is being used as a sputtering target, there are two types of magnetron sputtering, DC and RF sputtering. Usually, during DC sputtering a constant electric field is used to ionize argon, for targets that have good electrical conductivity. However, for insulating targets, RF sputtering is used where an radio frequency power supply is used. The vacuum chamber was pumped down to 1×10^{-9} Torr before sputtering; thus, removing any gas contaminants present in the chamber as well as ensuring an increase in the mean free path. When the argon gas is fed into the chamber during sputtering the pressure drops down to roughly 1×10^{-3} Torr. The samples were also rotated at 20 rpm speed in vacuum chamber to ensure uniform thin film deposition.

3.1.2 Fabrication

3.1.2.1 Photo-lithography

Photo-lithography is an optical fabrication process to fabricate micrometer scale device patterns onto thin films using photoresist layers. The sample is prepared by cleaning in acetone and isopropyl alcohol (IPA) to remove any kind of contamination aiding to better adhesion of the photoresist. Then, a thin uniform coating layer of photoresist is achieved by spin-coating. A photoresist is a photosensitive material. There are two types of photoresist positive and negative. A positive photoresist becomes more soluble in a developer on exposure to light, whereas a negative photoresist becomes less soluble. The sample fabrication presented in this thesis was done using a negative photoresist. After spin coating, the sample is baked on a hot plate to dry the photoresist by removing the excess solvent. Then UV light exposure was used to transfer a geometric pattern on to the film by using a photomask, only allowing a specific design to be exposed to light. Once exposed, the photoresist has to be developed using a developing agent which removes the photoresist, leaving behind the exposed pattern. The thin film layer is then removed in the areas that are not protected by photoresist by Ion milling explained later in details in section 3.1.2.2. Finally, the samples are cleaned using acetone and IPA leaving behind the desired device pattern. Figure 3.2 gives a sequence of steps followed during the photo-lithography process for a typical negative photoresist. However, in order to use the samples for magneto-transport measurements, a electrical contact pad is required on the pattern for making necessary connection with the header. Table 3.3 gives a summary of all the steps involved in fabrication procedure after Ion milling for the samples to be used for magneto-transport measurements.

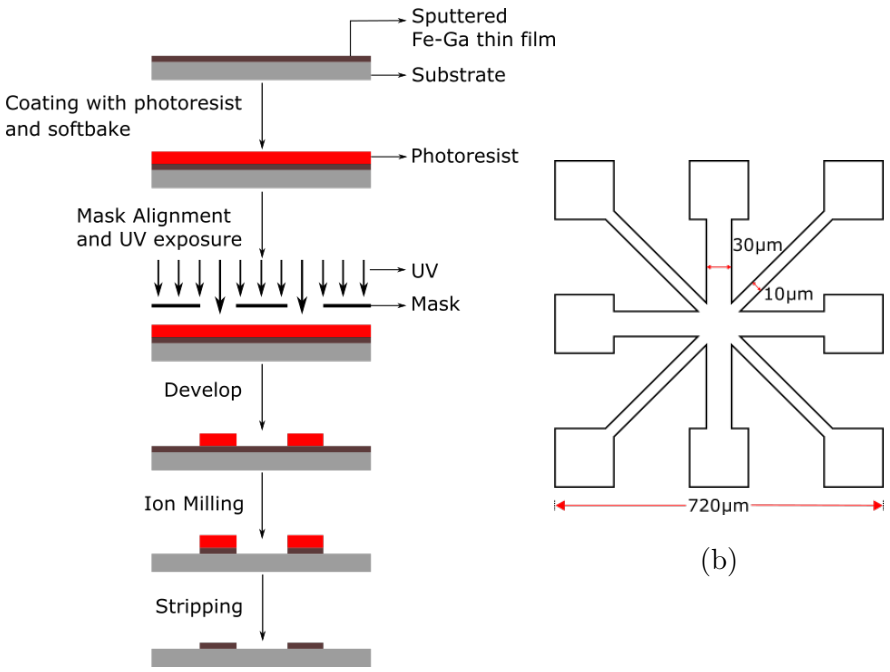

(a) (b)

Figure 3.2: Schematic diagram demonstrating the process involved in photo-lithography (a) shows a detail schematic diagram of the UV exposure onto a mask and photoresist after development. These steps were followed for a negative photoresist which was used for all the samples in this thesis (b) shows a schematic diagram of the union jack device pattern used for the magneto-transport measurements.

Step name	Process name
Spin Coat	BPRS 150 , 4k rpm, 30 seconds
Soft Bake	Hot plate, 90°C, 60 seconds
Expose	UV exposure, 75 J/cm^2 , 6 seconds
Develop	AZ400K:H_2O(1:90), 6 seconds
Metallisation	Thermal evaporator(Ti(20 nm) & Au(100 nm))
Lift off	Warm Acetone

Table 3.3: List of steps used to fabricate samples for the magneto-transport measurements after photo-lithography and ion milling. The sample preparation as well as the fabrication steps were carried out in the clean room facility at University of Nottingham.

3.1.2.2 Ion Milling

Ion milling is a physical etching technique under ultra-high vacuum conditions. Ion beams can be used to etch or erode the surface of the sample after photo-lithography removing all the film layer around the masked device pattern (as shown in figure 3.2) leaving behind just the device pattern. A broad, energetic beam of accelerating ions typically Ar^+ is bombarded at the sample surface; thus etching the sample. The ion source is a helical coil wrapped around a ceramic discharge tube which is then enclosed by a pair of concentric high transparency grids. An RF power at 13.56 MHz is applied as the gas is introduced into the discharge tube thus generating a plasma. A voltage is applied to the inner grid generating the ion beam with the required energy to erode the sample surface, and the outer grid is at ground potential creating a potential difference. As a result of this, ions from the plasma are drawn through the holes in the outer grid, forming a broad ion beam.

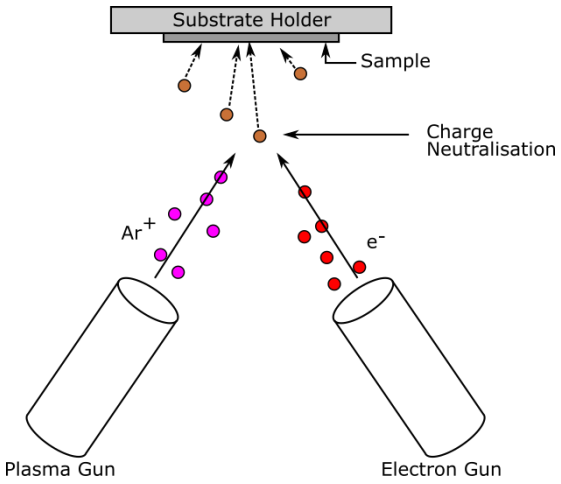

Figure 3.3: Schematic diagram of ion milling used to etch the surface of the sample after photo-lithography to remove the metal layer around the device pattern.

The samples mentioned in this thesis were milled using the Mantis RFMax60 ion source system in the Spintronics Group at the University of Nottingham. An argon (Ar^+) plasma gun and an electron (e^-) gun were co-sputtered at a power of 100 W and 200 W respectively on to the surface of the sample rotating at 20 rpm at a pressure of 1×10^{-3} Torr. A Faraday cup was used to validate that the resulting current is neutralised so that the sample doesn't get charged. Ion

milling is the preferred method of etching since it gives precise and crisp edges leaving behind good quality device pattern.

3.1.2.3 Thermal Evaporation

Thermal evaporation is a physical deposition process where the pure metal source material is evaporated using high heat and deposited onto a substrate under vacuum. The source metals are placed on a boat or a coil of wire with the substrate suspended above it (figure 3.4). The chamber is then pumped down to a pressure of 2×10^{-7}mbar. A current is passed through the boat high enough so that the source material is heated above its melting point, producing some vapor pressure. The evaporated atoms then travel ballistically and accumulate on the substrate surface, forming a thin film. For the samples used in magneto-transport measurement, the electrical contact pads were made using the thermal evaporation process. First, a thin film of Ti (20 nm) and then Au (100 nm) were deposited on the surface of the device.

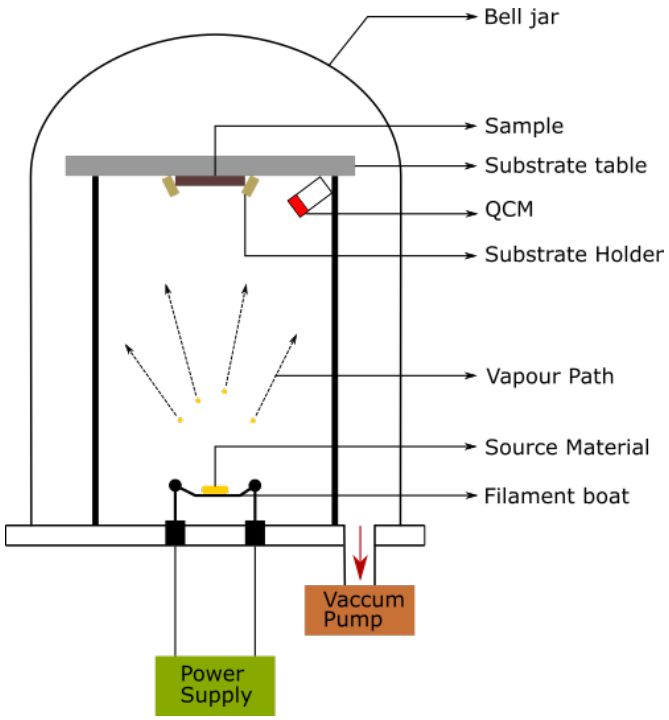

Figure 3.4: Schematic diagram of the thermal evaporator used to create thin metal films on the device pattern to be used as a electrical contact pad for magneto-transport measurements.

3.2 Measurement Techniques

The experimental techniques that have been used to characterise and understand the two sets of samples with varying Ga concentration and varying film thickness are discussed in this chapter. Several measurements techniques were involved in gaining a better understanding of the structural, electrical and magnetic properties of the magnetic thin films.

3.2.1 X-ray Diffraction

X-ray diffraction is a non-destructive technique to determine the structural and physical properties of a material. Structural characterisation of the samples is essential to get an understanding of the crystallinity of the samples as well as the growth quality of the samples. It also gives a better understanding of the behaviours and trends observed during the magnetic characterisation of the samples. When a wave propagates through a medium, it undergoes scattering as long the incident angle (θ_i) is greater than the critical angle (θ_c) which is dependent on refractive index of the material. When a wave is incident on a periodic structure, the scattered waves add up constructively along few specific directions determined by Bragg's law. The Bragg's law for a cubic system is given by equation 3.1.

$$\begin{aligned} n\lambda &= 2d_{hkl}\sin\theta_i \\ \sin^2\theta_i &= (h^2+k^2+l^2)\lambda^2/4a^2 \end{aligned} \tag{3.1}$$

where the integer n is the order of diffraction, λ is the x-ray wavelength, d_{hkl} is the inter-planar spacing, θ_i is the angle of incidence of the x-rays, h, k and l are the Miller indices of the Bragg plane and a is the lattice spacing of the cubic crystal. The diffraction of x-ray waves off a periodic crystal structure is demonstrated in figure 3.5

3.2.1.1 Equipment Set-up

The x-ray diffraction measurements mentioned in this thesis were performed using a Philips X'Pert PANlytical Material Research Diffractometer (MRD), at the

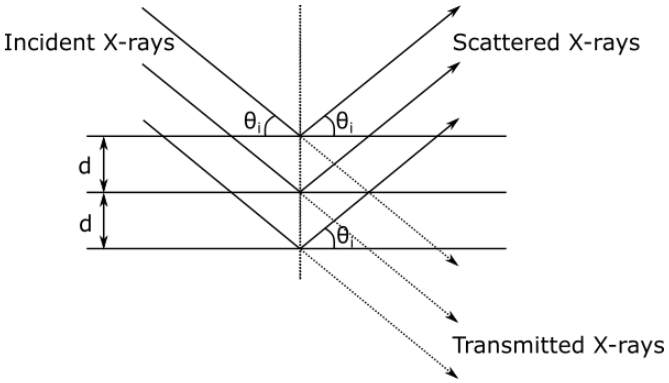

Figure 3.5: Schematic diagram demonstrating Bragg's diffraction. The x-rays with identical wavelength and phase are incident at an angle θ_i onto the planes separated by distance d. The incident rays are scattered off by two different atomic planes within the crystal.

University of Nottingham. A schematic diagram of the Philips X'Pert PANlytical MRD for x-ray diffraction characterization is shown in figure 3.6. The system comprises of a $CuK_{\alpha 1}$ source with a wavelength of 0.154 nm when the generator is at 45 kV and 40 mA. The beam is then placed through a $\frac{1}{2}^{\circ}$ slit to limit divergence which is then projected onto a parabolic mirror to get rid of any residual divergent beams. The beam is then passed through soller slits to get rid of any axial divergence. A Bartels symmetric Ge(220) 4 crystal monochromator is used, which works using the Bragg's law for $CuK_{\alpha 1}$ wavelength. The set-up also contains an open Eularian cradle along with two detectors.

3.2.1.2 Measurement technique

The sample is mounted on the open Eularian cradle which is capable of movement along x, y and z cartesian coordinate direction. Along with this, it is also capable rotation around the axis perpendicular to the plane of the sample (ϕ) and rotation about an axis parallel to the plane of the sample (ψ) allowing freedom for alignment along any preferred orientation. $2\theta - \omega$ continuous specular scan was done on the samples mentioned in this thesis. The angle between the detector and the source is called 2θ, the angle between the detector and the sample surface (tilt) is called ω, and the source position is fixed. The specular scan is achieved by varying both 2θ and ω simultaneously, once the desired crystallographic plane is

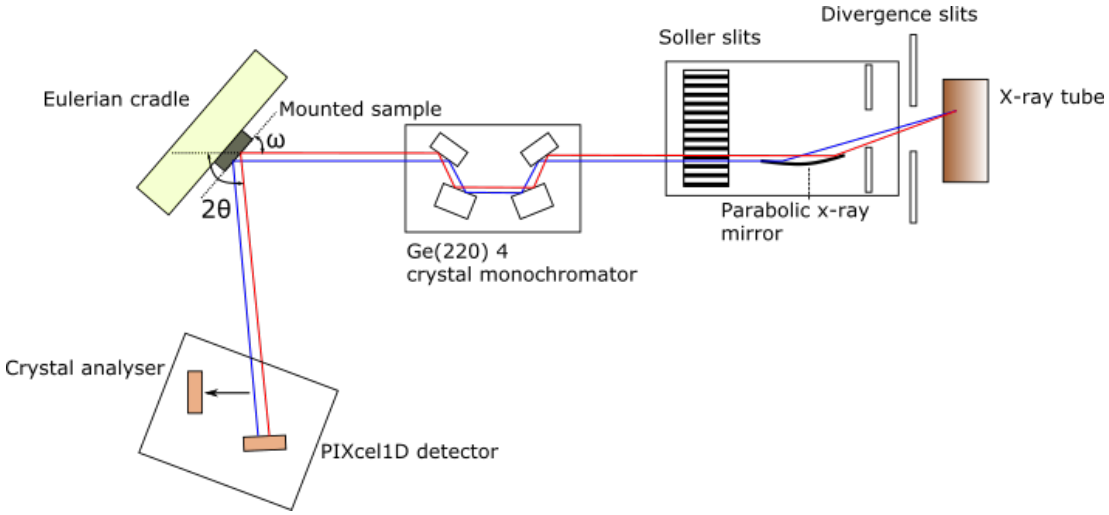

(a)

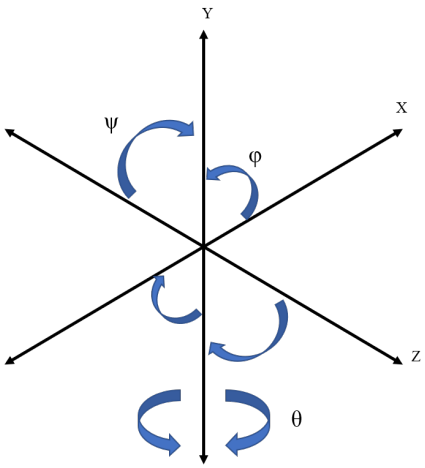

(b)

Figure 3.6: (a) Schematic diagram of XRD measurement using the Philips X'Pert PANlytical MRD. The sample is mounted on the open Eularian cradle which is capable of adjusting along x, y, z, ϕ and ψ. The angle and alignment between the source, sample, and the detector is shown. The x-rays go through the beam conditioner allowing it to collimate and monochromate. (b) Shows the operation of the Eularian cradle with the incident beam along the x-direction.

set after alignment, hence the name. The angular resolution that can be achieved using the Phillips PANlytical X'Pert MRD are 0.0003° for rotation along ω and 2θ, and 0.01° along ϕ and ψ.

3.2.2 X-ray Reflectivity

X-ray reflectivity (XRR) is a non-destructive and fast characterisation technique with a high precision for thin films and multilayers. One can extract information about film thickness, interface roughness, densities *etc.*. Internal structural properties are crucial to understand how these structures and interfaces among different layers affect the magnetisation of the corresponding material.

When a beam of x-rays is incident onto an interface between two mediums with different refractive index at grazing incidence angles, it undergoes specular reflection from the sample. Classically, when an electron experiences an oscillating electromagnetic field, it can absorb the x-rays and re-emit them with the same energy and frequency. At the interface between two mediums the electron density changes as a result part of the x-ray beam is reflected. The interference of these partially reflected x-ray beams creates the oscillation pattern observed in reflectivity experiments. Hence by studying these scattered frequencies, it is possible to gain an understanding of the structural properties. Typically, θ_c, is smaller than $\approx 1°$, but the exact value is dependent on the material properties refractive index and density of that particular material. The net reflectivity using the Fresnel's equation in a single layer thin films is given by,

$$R^2 = \left| \frac{r_1 + r_2 e^{(-2ik_z t)}}{1 + r_1 r_2 e^{(-2ik_z t)}} \right|^2 \tag{3.2}$$

where r_1 and r_2 are the Fresnel reflectivity coefficients of the film and the substrate respectively, k_z is the vertical component of the incident wave vector, and t is the film thickness. Reflectivity maximises when the exponential term goes to 1, which occurs when the difference between the path lengths is an integer multiple of the wavelength (λ) given by,

$$m\lambda = 2t(\sin^2\theta - \sin^2\theta_c)^{\frac{1}{2}} \tag{3.3}$$

where m is an integer. As observed from the figure 3.7 the intensity reduces by

few orders of magnitude after a particular θ_c and then oscillates with decreasing intensity every single time. The interference pattern called the Kiessig fringes is due to the combination of the total internal reflection from the film and substrate. As shown in the figure, the gradient of the reflectivity profile is related to the surface roughness, the amplitude of the fringes is related to the film density, and the width of the fringes is related to the film thickness. Since the fringes are dependent on film thickness, for thick samples (> few hundred nanometers) the fringes become so close to each other almost becoming indistinguishable.

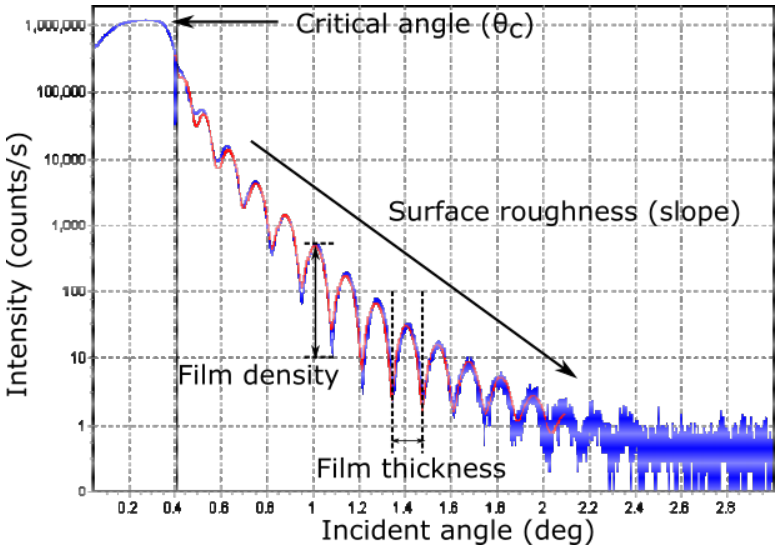

Figure 3.7: Shows an example fit of the reflectivity measurement of sample S644, where the blue line represents the experimental data, and the red line represents the fitting.

3.2.2.1 Equipment Set-up

The x-ray reflectivity measurements mentioned in this thesis were performed using the Philips X'Pert PANlytical Material Research Diffractometer (MRD), at the University of Nottingham, as mentioned in 3.2.1.1. A set-up similar to XRD measurements is used; however, the Bartels symmetric Ge(220) 4 crystal monochromator is replaced with the flat graphite monochromator to improve the peak to background ratio for the measurements. A thin film attachment that is a fine slit of 0.1 mm is required between a parallel plate collimator and the flat graphite monochromator to improve the 2θ resolution for the low angle reflectivity

measurements.

3.2.2.2 Measurement technique

The monochromatic x-ray beam is incident on the sample surface at an angle ω and the reflected intensity at an angle 2θ is recorded by the detector. However, 2θ always kept equal to 2ω in case of reflectivity measurements. Alignment of the x-ray source and detector is crucial for reflectivity measurement, more than x-ray diffraction due to the small glazing angle of incidence. In order to achieve it, the source and the detector were aligned to $\omega = 2\theta = 0°$ in the absence of the sample and 2θ scan was recorded, and peak intensity of the scan was calibrated to 0° to achieve the maximum intensity of the beam path. The sample was then inserted in the beam path by moving the Eulerian cradle in the z-direction until the count rate of the beam intensity is half of its maximum value. This step was done to ensure that the beam reaches the substrate after being reflected from the sample surface. Then, a ω scan was done to ensure that the sample is aligned at the peak intensity, if the sample is slightly misaligned this would result in a shift of the peak and is then recalibrated. To ensure a perfect alignment, the above step was repeated until the sample is aligned with the beam giving the maximum intensity peak during the ω scan. The samples mentioned in this thesis were measured with the range of incident angle ω between 0.25° and 6°, and only the film thickness were extracted.

3.2.3 X-ray Photoelectron Spectroscopy

X-ray photoelectron spectroscopy (XPS) is based on the photoelectric effect. In 1914, Rutherford presented a basic equation for XPS given by;

$$E_k = h\nu - (E_b - \phi_0) \tag{3.4}$$

where E_k is the kinetic energy associated with the photoelectrons, $h\nu$ is the energy required to excite a photon, E_b is the binding energy of an electron before ionisation, and ϕ_0 is the work function of the spectrometer. According to the photoelectric effect, an electron can be excited and eventually ejected from an atomic orbital upon application of sufficient energy. XPS utilises hard x-rays to

excite electrons and measures the kinetic energy of the emitted electrons. Generally, x-rays having energy in 1-2 keV range generate photons with enough energy to excite core electrons. In order for the resultant emitted photoelectrons to be detected, they must escape from the surface without interacting with overlaying atoms. This process may lead to unwanted inelastic scattering. Therefore, XPS is termed as a surface phenomenon. The thickness of the sample to avoid unnecessary inelastic scattering depends on the material density as well as the kinetic energy of the electron being emitted. The photoelectrons that are emitted from the core of the atom are bound to orbitals with energy characteristic to that particular element. Thus by analysing the electron binding energies, it is possible to identify the elements present in that sample.

The XPS provides a spectrum with a series of photoelectron peaks plotted versus the binding energy. The peaks in an XPS spectrum take the form of a convoluted Gaussian-Lorentzian curve. The position of the binding energy gives the specific element and their respective oxidation state. The area of the peak can be utilised to determine the elemental composition of the sample.

3.2.3.1 Equipment Set-up

Typically a XPS setup is equipped with photon source, sample manipulation with different linear and rotational degrees of freedom, an electron optic, an electron energy analyser and an electron detector. It must be carried out under ultra-high vacuum conditions in order to avoid inelastic scattering of electrons ejected from the sample to reach the detector. A metal anode is bombarded with electrons generating x-rays. These x-rays are then monochromated using an electron optic, ensuring that the photons used are quantised. Core electrons with lower binding energy than the incident photon gets ejected. A hemispherical analyser at a fixed potential is used, allowing only certain photoelectrons to pass through it. These electrons then go through the detector which records the number of electrons with corresponding energies. A hybrid magnetic/electrostatic lens mode is used for maximum electron signal. Electrostatic lens mode was used because the sample responded to the magnetic field when tested. Finally, a spectrum is produced using the Kratos VISION II software.

3.2.3.2 Measurement technique

All XPS analysis presented and completed as part of this work was performed by Dr Emily F Smith using the Kratos AXIS ULTRA present at the nanoscale and microscale research centre (NMRC), University of Nottingham. Samples were mounted on a standard Kratos sample bar (13 cm $\times$ 1.5 cm), using double-sided tape. They were pumped down in the instrument airlock overnight and placed on the sample stage at $\approx 3.75 \times 10^{-6}$ mTorr pressure for analysis. The charge neutraliser filament was used to prevent sample surface charging. Samples were analysed using a monochromatic Al k_α x-ray source (1.5 keV) operated at 10 mA emission current and 12 kV anode potential. Spectra were acquired with the Kratos VISION II software. The measurement was done on a sample area of $\approx 300 \times 700$ μm. For each sample, three different areas were analysed to verify the uniformity of the measurement. A wide scan at low resolution was used to estimate the total atomic percentage of the detected elements. Furthermore, a high-resolution spectrum was acquired for photoelectron peaks from the detected elements, and these were used to model the chemical composition. Data sets were exported and processed using CasaXPS.

3.2.4 SQUID Magnetometry

A Superconducting QUantum Interference Device (SQUID) magnetometer is used to measure the magnetisation of materials as a function of an externally applied magnetic field and/or temperature. SQUID magnetometry is a powerful technique because of its sensitivity towards detecting extremely weak magnetic signals [193].

3.2.4.1 Equipment Set-up

A SQUID magnetometer works using the principle of flux quantisation and Josephson effect. It was found that a tunnelling current flows between two superconductors when separated by an insulating medium, in the absence of any externally applied voltage. This separation junction was called Josephson junction (JJ). As established by Brian David Josephson (1962), the current flowing through the

insulating medium between the two superconductors depends on the phase difference ($\Delta\phi_{ph}$) of the two superconducting wave functions. Hence, the current flowing (i_s) through a Josephson junction is given by the equation 3.5.

$$i_s = i_c \sin(\Delta\phi_{ph}) \tag{3.5}$$

where i_c is the critical current below which the cooper pairs of the superconducting region can tunnel through the junction and $\Delta\phi_{ph}$ is the phase difference between the two pairs of superconductors on either side of the Josephson junction. $\Delta\phi_{ph}$ is also influenced by the change in magnetic flux in the superconducting ensemble. The quantisation of magnetic flux makes SQUID magnetometer such a sensitive device.

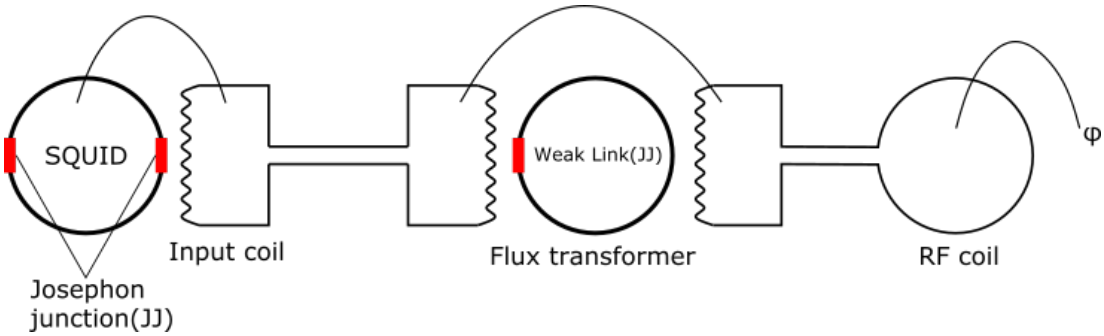

Figure 3.8: Circuit diagram showing the pick up coils and samples inductively coupled to the Josephson junction and rf circuit.

Depending on the number of Josephson junction, SQUID can be of two types, RF (single JJ) and DC (two JJs). The SQUID magnetometer at the University of Nottingham used for magnetometry measurements presented in this thesis is an RF SQUID. The sample is sinusoidally oscillated up and down through the detection coils along the axis of the gradiometer, perpendicular to the plane of the coils. This motion of the sample generates current within the detection coils as the flux keeps on changing. The detection coils are inductively coupled with the Josephson junctions. The induced current is then passed through to the RF circuit from the superconducting Josephson junction, thus changing the amplitude and frequency of the RF oscillations. A feedback loop is added to the RF circuit to measure these changes in the amplitude and frequency more accurately. This feedback loop finds the longitudinal moment of the magnetisation from the

current required to counteract the change produced by the detection coil. The schematic diagram of a rf SQUID is shown in figure 3.9 which has been taken from reference [193].

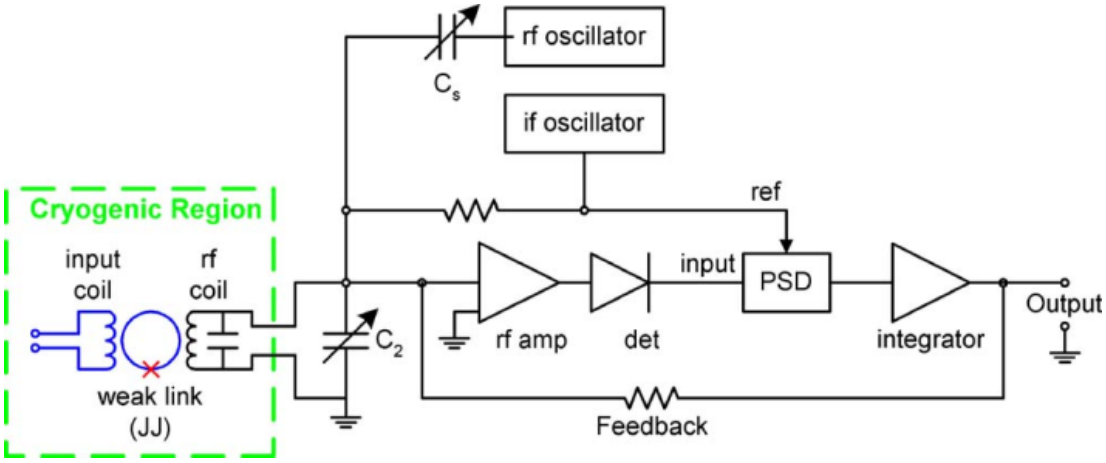

Figure 3.9: Circuit diagram showing a typical rf SQUID. The input circuit diagram as well as the electronics is shown. The input coil is inductively coupled with the pick up coils.

3.2.4.2 Measurement technique

The SQUID magnetometry measurements discussed in this thesis were performed using the Quantum Design MPMS XL SQUID magnetometer in the Spintronics group at the University of Nottingham. A schematic diagram of Quantum Design MPMS XL SQUID is shown in figure 3.10. All the superconducting elements of the system are immersed in liquid Helium. The sample is placed in the central sample space whose temperature can be varied between 1.9 K-400 K. The superconducting magnets provide magnetic field up to 1 T with uniformity of 0.01% over 4 cm.

The samples to be measured were scribed to a dimension of $\approx 4\,\text{mm} \times 5\,\text{mm}$ and attached to a high purity silver wire using GE varnish and placed inside a straw for in-plane measurements. The straw is then attached to the bottom of a non-magnetic sample rod mechanically driven by a servo motor. This rod is then placed within the superconducting detection coil and centred. The SQUID magnetometry measurements were performed in reciprocal sample oscillation (RSO). The magnetic field was swept between ± 0.2 T and the sample was kept at room

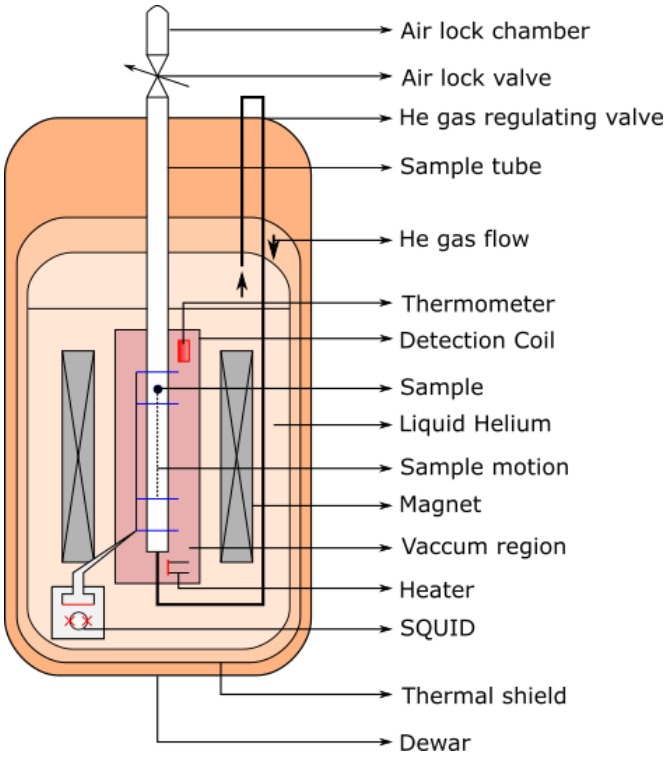

Figure 3.10: The schematic diagram of magnetic property measurement system (MPMS) is shown. All the superconducting elements are emerged in liquid He and the sample sits in the central sample space. The detection coils are inductively coupled with the SQUID.

temperature. The magnetisation measured along the direction of oscillation as mentioned earlier, is called longitudinal moment. To measure the magnetisation along different crystal direction, the sample has to be physically remounted in other crystallographic direction.

3.2.5 Ferromagnetic Resonance Spectroscopy

Ferromagnetic resonance spectroscopy (FMR) is one of the most widely used techniques to measure both magnetisation dynamic properties such as magnetic damping and static properties like anisotropy in ferromagnetic materials. FMR spectroscopy uses the principle discussed in section 2.4. The FMR experiments discussed in this thesis were performed in collaboration with Dr S.A. Cavill and Ms L.E. Clarke at the University of York, department of physics.

3.2.5.1 Equipment Set-up

The two most widely used FMR spectroscopy techniques are vector-network analyser FMR (VNA-FMR) and modulated FMR. While both of them use the same basic principle of FMR they differ slightly in the method of radio-frequency (rf) generation and signal measurement. Typically, a VNA-FMR is used for samples with stronger resonance signals, while modulated FMR being more sensitive is used to detect smaller resonance signals. For the FMR measurements of samples discussed in this thesis, VNA-FMR was used. A schematic diagram of VNA-FMR outlining the basic design of the spectrometer is shown in the figure 3.11.

The spectrometer uses two large Helmholtz coils and a soft iron pole is provided at the centre of each coil to focus the field to the centre of the coil which can be used to provide a magnetic field up to 2 T. This whole set up is placed on a turntable to achieve azimuthal plane rotation of the magnetic field. The VNA is then used to provide an rf signal of a variable frequency to the ferromagnetic samples using non-magnetic SMA port ending coaxial cables. VNA works by comparing the rf frequency of the input and the output signals between the SMA ports connected to either side of the device. The VNA fundamentally measures the scattering parameter (S-parameters) as a ratio of the input signal and output reflected/transmitted signal. For this particular VNA set-up transmission coefficient was used, *i.e.* the ratio of the power of the transmitted to the incident signal, given by the equation 3.6.

$$S_{21} = \frac{b_2}{a_1} \tag{3.6}$$

where 1 and 2 are identified as the input and output port respectively, S_{21} is the forward transmission coefficient, a_1 is the incident wave at port 1 and b_2 is the transmitted wave at port 2.

3.2.5.2 Measurement technique

As shown in figure 3.11, the sample is mounted approximately at the centre of the coils on to a coplanar waveguide (CPW) which is non-magnetic. The sample is mounted such that the sample growth side faces the stripline of the waveguide to maximise the coupling between the sample magnetisation and rf field. This is

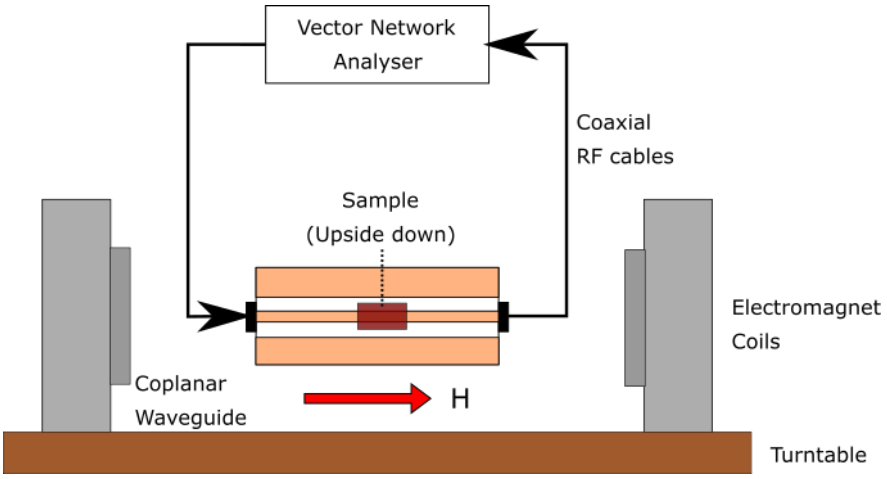

Figure 3.11: A schematic diagram of the FMR spectrometer operating in VNA-FMR mode.

known as the 'flip-chip' geometry [194]. The CPW serves two purposes, one as a sample mount and secondly transmitting the rf signal. An externally varying rf signal ranging between 1 GHz to 20 GHz was provided through the coaxial cables using the VNA in order to provide the rf excitation signal required to generate FMR as discussed in the section 2.4.3. The external applied in-plane magnetic field was varied from 0 T to 0.3 T along different crystalline directions of the sample achieved by rotating the sample in steps of 5°, and the forward transmission signal S_{21} was measured. All the FMR measurements discussed in this thesis were performed at room temperature.

3.2.6 Magneto-transport

Magneto-transport measurements are used to measure the anisotropic magnetoresistance (AMR) in a ferromagnetic film.

3.2.6.1 Equipment Set-up

The magneto-transport measurements discussed in this thesis were performed using the helium-cooled cryostat system at room temperature in the Spintronics group at the University of Nottingham. An electromagnet is positioned outside surrounding the cryostat and is capable of being rotated around a 200° range so that the angle of the sample with respect to the field can be altered. The

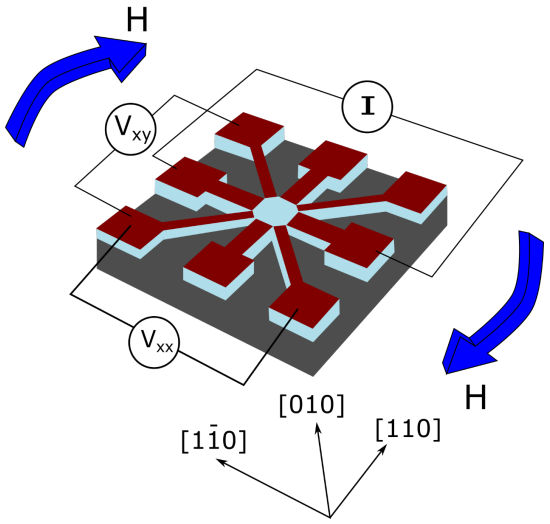

Figure 3.12: Schematic diagram of a union jack device pattern for magneto-transport measurements. The magnetic field is being rotated in the plane of the sample and the measurement geometry for longitudinal and transverse resistances are indicated.

electromagnets are capable of applying a field up to $\pm 0.4\,\mathrm{T}$. The system also comprised of a Keithley 2400 source meter operated in constant current mode and two Keithley 2000 multimeters for measurement of the resistances.

3.2.6.2 Measurement technique

For the magneto-transport measurement for measuring anisotropic magnetoresistance, the sample was first fabricated into the union jack device pattern as discussed in section 3.1.2. The sample was then mounted on a non-magnetic header using GE varnish and attached to a sample probe which can be connected to the source meter and multimeters mentioned above and placed inside the sample space of the cryostat. An in-plane magnetic field of $0.3\,\mathrm{T}$ was provided using the electromagnets. A constant current supply of $1\,\mathrm{mA}$ was passed along the crystal direction whose longitudinal (R_{xx}) and transverse (R_{xy}) resistances are to be measured. The electromagnets were rotated in steps of 5° to change the relative oriented between the sample and the magnetic field. Figure 3.12 shows a schematic diagram of a union jack device pattern for magneto-transport measurements.

3.3 Simulations

3.3.1 Simulating MH loops from the free energy equation

Fitting the hysteresis curves obtained from the SQUID magnetometry data yields the magnetic anisotropy constants. The equation of the total free energy density used for simulation of the hysteresis loops is stated below in equation 3.7.

$$E = -M \cdot H_{ext} \cos(\theta - \phi) + K_u \sin^2(\phi - \frac{\pi}{4}) + \frac{K_c}{4} \sin^2 2\phi \tag{3.7}$$

where E is the magnetic free energy density, M is the magnetisation, H_{ext} is the external applied magnetic field, K_u and K_c are the uniaxial and cubic anisotropy coefficients respectively, θ is the angle between the applied magnetic field and the easy axis of the sample, and ϕ is the angle between the magnetisation and the easy axis of the sample (the model takes into account the angle between [010] and the magnetisation).

All the loops were simulated at a magnetic field value ranging in between $\pm 0.2\,\mathrm{T}$. The field was swept from a large saturating positive ($0.2\,\mathrm{T}$), to large negative ($-0.2\,\mathrm{T}$) and back to large positive field, essentially to make sure that the sample is saturated with the magnetisation vector along the applied magnetic field, eventually generating a complete set of M vs H hysteresis loop at room temperature. Energies were then generated using the equation 3.7 for ϕ ranging from 0 to 2π. The direction of the magnetisation is then determined by the corresponding ϕ value which gives the minimum magnetic free energy represented by ϕ_{min}. When H_{ext} is decreased by a small amount, ϕ_{min} is changed by $\pm\delta\phi$ and scanned to obtain the local minimum. Once the new minimum ϕ value for the given external magnetic field is determined, it is then converted into magnetisation using the equation 3.8.

$$M = M_s \cos(\theta - \phi) \tag{3.8}$$

where M_s is the saturation magnetisation and ϕ is the angle obtained after minimisation of the magnetic free energy.

In order to obtain the magnetic anisotropy constants, hysteresis curves were generated using a range of K_u and K_c along [110] and [1$\bar{1}$0] crystalline direction

using the above method. Then the difference between the simulated curves and the experimentally collected data is found using the cost function (C) given by the equation 3.9. The curves were considered only up to the 0 T external field in order to be consistent with the SW model explained in section 2.3 and to ensure that that the effects of domain wall nucleation is not included during fitting. The cost function value along [110] and [1$\bar{1}$0] direction were summed and the K_u and K_c values with the minimum total cost function were determined as the best fit for that experimental SQUID loop.

$$C = \sum_{i=1}^{n} (x_i - y_i)^2 \tag{3.9}$$

where n is the number of points on both the simulated and experimental curves, x_i is the point i on the simulated curve and y_i is the point i on the experimental curve.

In order to estimate the uncertainties, K_u and K_c were determined by changing the θ value by $\pm 5^\circ$ to represent a reasonable error in the angle in which the sample was mounted. For example, the crystalline axis along [110] is at an angle 45° with respect to the easy axis along [010], so the best fit value for K_u and K_c is taken along this direction. The error is the difference between the best fit value and the value obtained for K_u and K_c at $45^\circ \pm 5^\circ$. This is demonstrated in figure 3.13 showing the experimentally collected data, the best fit value and the MH loop taken into consideration for estimation in error bars for K_u and K_c for sample S536.

3.3.2 Simulating Ferromagnetic resonance conditions

Fitting the data obtained from the ferromagnetic angular resonance at a fixed saturating in-plane external magnetic field yields the saturation magnetisation, the magnetic anisotropy constants, and the damping parameter. It also provides a comparison between the anisotropy constants obtained from SQUID magnetometry. For fitting the FMR data discussed in this thesis, the approach of Smit, Suhl and Beljers was used [162, 195] as discussed in section 2.4.3. In this approach, a simple form for the resonance condition is determined in terms of the second derivative of the total free energy density of magnetisation in an external

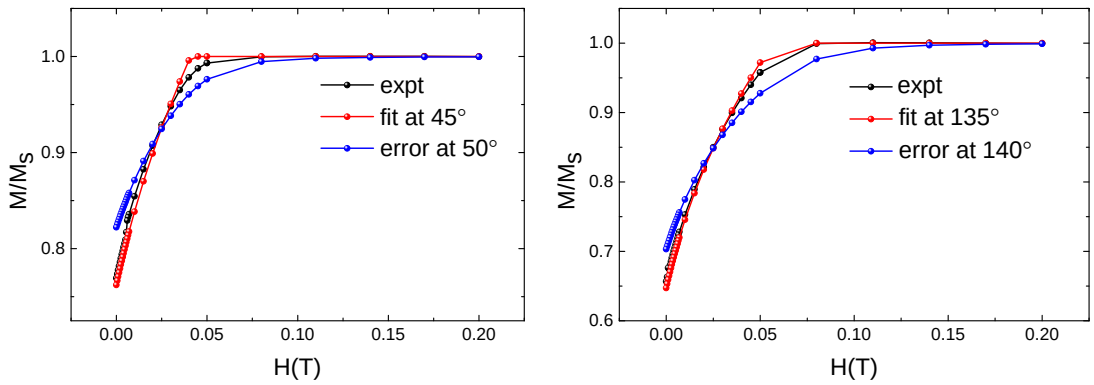

(a) MH loop along [110] (b) MH loop along [1$\bar{1}$0]

Figure 3.13: Modelled MH loops for SQUID along with the experimentally collected data as well as MH loop for estimation of the error bars for K_u and K_c is demonstrated. In (a) MH loop along the crystalline direction [110] is demonstrated and in (b) MH loop along [1$\bar{1}$0] crystalline direction. The MH loops were fitted in the region shown in the above figure.

magnetic field for any ferromagnet. The derivative was done with respect to the polar angle, θ_M, and the azimuthal angle, ϕ_M.

The ferromagnetic resonance frequency is expressed by equation 3.10.

$$\left(\frac{\omega_{res}}{\gamma}\right)^2 = \frac{1}{M^2 \sin^2\theta_M}\left[\frac{\partial^2 E}{\partial\theta_M^2}\frac{\partial^2 E}{\partial\phi_M^2} - \left(\frac{\partial^2 E}{\partial\theta_M \partial\phi_M}\right)^2\right]_{\theta_{M,eq},\phi_{M,eq}} \tag{3.10}$$

where ω_{res} is the resonant angular frequency, γ is the gyromagnetic ratio , M is the magnitude of the magnetisation vector, E is the total free energy density of magnetisation. The field line width is given by the equation 3.11

$$\Delta H = \frac{\alpha}{(\partial\omega_{res}/\partial H_{ext})}\frac{\gamma}{M}\left[\frac{\partial^2 E}{\partial\theta_M^2} + \frac{1}{\sin^2\theta_M}\frac{\partial^2 E}{\partial\phi_M^2}\right] \tag{3.11}$$

where ΔH is the field linewidth, α is the damping parameter.

As we can see from both the equation 3.10 and 3.11 in order to obtain the angular resonance frequency and field linewidth first we need to find the double derivative of the total free energy density equation in polar coordinates. A new demagnetising energy term is added to the total free energy equation density (eq. 3.7). The precessing magnetisation around the effective magnetic field generates an additional stray field in the perpendicular direction, hence the demagnetising energy comes into picture. The total free energy density in polar coordinates is

given by equation 3.12.

$$\begin{aligned} E = & -H_{ext}M_s[\sin\theta_H \sin\theta_M \cos(\phi_H - \phi_M) + \cos\theta_H \cos\theta_M] \\ & + \frac{1}{2}H_u M_s \sin^2\theta_M \cos^2(\phi_M - \phi_0) \\ & + \frac{1}{8}H_c M_s(\sin^4\theta_M \sin^2 2\phi_M + \sin^2 2\theta_M) \\ & + \frac{1}{2}4\pi M_s^2 \cos^2\theta_M \end{aligned} \tag{3.12}$$

where E is the total free energy density, H_{ext} is the external applied magnetic field, M_s is the saturation magnetisation, θ_M is the polar angle, ϕ_H is the angle between the applied magnetic field and the easy axis of the sample, ϕ_M is the azimuthal angle, $H_u = 2K_u/M_s$ is the uniaxial anisotropy field, ϕ_0 is the angle between in-plane uniaxial easy axis and the cubic easy axis, and $H_c = 2K_c/M_s$ is the cubic anisotropy field. The coordinate system used for finding the resonance frequency condition is shown in figure 2.3 in section 2.2.2. Equation 3.13 gives the first derivative of the free energy equation.

$$\begin{aligned} \frac{\partial E}{\partial \theta_M} = & -H_{ext}M_s[\sin\theta_H \cos\theta_M \cos(\phi_H - \phi_M) - \cos\theta_H \sin\theta_M] \\ & + \frac{1}{2}H_u M_s \sin 2\theta_M \cos^2(\phi_M - \phi_0) \\ & + \frac{1}{8}H_c M_s(2\sin^2\theta_M \sin 2\theta_M \sin^2 2\phi_M + 2\sin 4\theta_M) \\ & - \frac{1}{2}4\pi M_s^2 \sin 2\theta_M \\ \frac{\partial E}{\partial \phi_M} = & -H_{ext}M_s \sin\theta_H \sin\theta_M \sin(\phi_H - \phi_M) \\ & - \frac{1}{2}H_u M_s \sin^2\theta_M \sin 2(\phi_M - \phi_0) \\ & + \frac{1}{4}H_c M_s \sin^4\theta_M \sin 4\phi_M \end{aligned} \tag{3.13}$$

In order to find the equilibrium condition, the first derivative of the free energy equation is equated to 0. With the polar angle of the external magnetic field fixed at $\theta_H = \frac{\pi}{2}$ the equilibrium conditions are derived to be

$$\theta_M = \frac{\pi}{2} \tag{3.14}$$

and,

$$- H_{ext}M_s \sin(\phi_H - \phi_M) - \frac{1}{2}\sin 2(\phi_M - \phi_0) + \frac{1}{4}H_c \sin 4\phi_M = 0 \tag{3.15}$$

Hence the second derivative of the total energy density using the equilibrium condition becomes,

$$\begin{aligned}
\frac{\partial^2 E}{\partial \theta_M^2} &= H_{ext}M_s \cos(\phi_H - \phi_M) \\
&\quad - H_u M_s \cos^2(\phi_M - \phi_0) \\
&\quad + H_c M_s \cos^2 2\theta_M \\
&\quad + 4\pi M_s^2 \\
\frac{\partial^2 E}{\partial \phi_M^2} &= H_{ext}M_s \cos(\phi_H - \phi_M) \\
&\quad - H_u M_s \cos 2(\phi_M - \phi_0) \\
&\quad + H_c M_s \cos 4\phi_M \\
\frac{\partial^2 E}{\partial \theta_M \partial \phi_M} &= 0
\end{aligned} \tag{3.16}$$

Substituting equation 3.16 in equation 3.10 yields the resonance condition,

$$\begin{aligned}
\left(\frac{\omega_{res}}{\gamma}\right)^2 &= [H_{ext}M_s \cos(\phi_H - \phi_M) \\
&\quad - H_u \cos^2(\phi_M - \phi_0) + \frac{1}{2}H_c \cos^2 2\theta_M + 4\pi M_s] \\
&\quad \times [H_{ext} \cos(\phi_H - \phi_M) \\
&\quad - H_u \cos 2(\phi_M - \phi_0) + H_c \cos 4\phi_M]
\end{aligned} \tag{3.17}$$

As we can see from the above equation that resonance angular frequency depends both on the uniaxial and cubic anisotropy fields. Hence, the anisotropy constants and the saturation magnetisation can be obtained by fitting the in-plane angular resonance frequency at a constant external field. Sum of least square method was used to fit the simulated data with the experimentally obtained data. Saturation magnetisation and anisotropy fields were kept as free parameters to vary.

Substituting equation 3.16 in equation 3.11 yields the field linewidth. Fitting the simulated linewidth with the experimental data using the same approach as discussed above results in the extrinsic, ΔH_0, and intrinsic, α, damping parameter and two magnon scattering was excluded while fitting since it gave unrealistic fit.

The equation for the field line width is given by

$$\Delta H = \Delta H_0 + \frac{2\alpha\omega_{res}}{\gamma}\frac{1}{\cos\left(\phi_H - \phi_M\right)} \tag{3.18}$$

The slope of the graph yields the intrinsic Gilbert damping and the intercept gives the extrinsic parameter. Figure 3.14 shows an example fit to the resonance frequency and field linewidth for sample S536, where the black solid points represent the experimentally obtained data and the red line represents the fit to the data using equations 3.17 and 3.18 respectively.

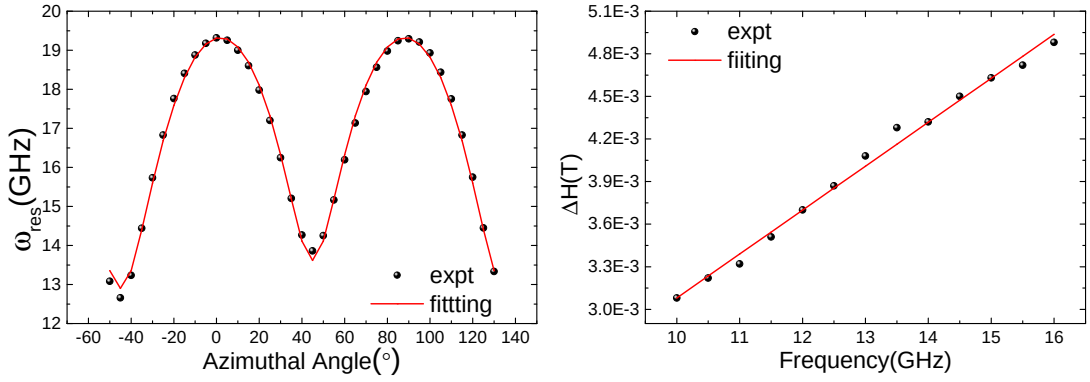

(a) (b)

Figure 3.14: Example for fitting of resonance frequency and linewidth for sample S536 is shown. (a) shows the fitting of the experimental data for resonance frequency at 0.15 T to equation 3.17 (b) shows the fitting of the experimentally obtained linewidth to equation 3.18.

Chapter 4

Structural properties investigated using XRD, XRR and XPS

In this chapter, the structural properties of the samples discussed in this thesis are investigated using x-ray reflectivity, x-ray diffraction, and x-ray photoelectron spectroscopy. The structural properties of the samples are investigated as the Ga concentration is changed in $Fe_{100-x}Ga_x$ thin films, and as the film thickness is changed in $Fe_{79}Ga_{21}$ thin films.

4.1 X-ray reflectivity analysis

The first stage of characterisation was done using x-ray reflectivity. As discussed earlier in section 3.2.2, x-ray reflectivity (XRR) is a popular technique used for characterisation of magnetic thin films. In this section, information about the film thickness, interface roughness and density of the films was extracted from the reflectivity curves obtained for the samples mentioned in this thesis.

4.1.1 X-ray reflectivity analysis of $Fe_{100-x}Ga_x$ thin films with varying Ga concentration

The XRR measurements were carried out using the X'Pert materials research diffractometer system, as discussed in section 3.2.2. The samples were measured with an incident angle (θ) ranging between 0.1° to 3.0°. The data were simulated using the X'Pert reflectivity fitting tool by PANalytical. Although the incident

angle for obtaining the reflectivity curve ranged between 0.1° to 3.0°, the incident angle range for the fitting tool was chosen such that it only fits the curve with minimum background noise. To fit the experimental data, the simulated curve was generated by considering three layers in the sample; originally, at the start of fit, the substrate layer of GaAs(001) is considered of thickness 450 nm, the sample layer ($Fe_{100-x}Ga_x$) is considered of thickness 20 nm, and the capping (Cr) is considered of thickness 2 nm. The thickness of the sample layer and capping layer, the density of the sample layer and capping layer, and the roughness between the substrate and the sample layer as well as the roughness between the sample layer and capping layer were allowed to vary, making it six parameters of fitting for the simulated graph. All the parameters of the substrate layer are fixed to a constant value because of its high quality.

Figure 4.1 presents an example fit of the experimental curve for sample S536 ($Fe_{90}Ga_{10}$). All the simulated curves had a similarly good fitting except for sample S535 ($Fe_{88}Ga_{12}$) where the simulated curve did not fit the experimental data despite varying all the possible parameters. The exact reason for this ambiguity was not understood; one of the reasons could be that something went wrong during the sputter deposition. This ambiguous behaviour of sample S535 was consistent with other measurements discussed later on in this thesis. Therefore, it has been excluded. Table 4.1 shows the value for the film thickness obtained from the fitting as compared to the 20 nm film thickness expected from the growth parameters. The average thickness of the samples were determined to be 26.20 ± 1.1 nm. It also presents the density of the films varying with the Ga concentration but there is no clear relationship between density and Ga concentration and most samples have the same density within the experimental error. During the fitting, the density of the film was initialised as the density of iron that is 7.83 g/cm^3 and kept as a varying parameter. The density of polycrystalline bulk Galfenol ($Fe_{81.6}Ga_{18.4}$) quoted by the patent holders ETREMA Products, Inc is 7.80 g/cm^3. The errors on the parameters were calculated using the error analysis function in the X'Pert Reflectivity software. The software gives an error percentage of ±5% of the original fit value.

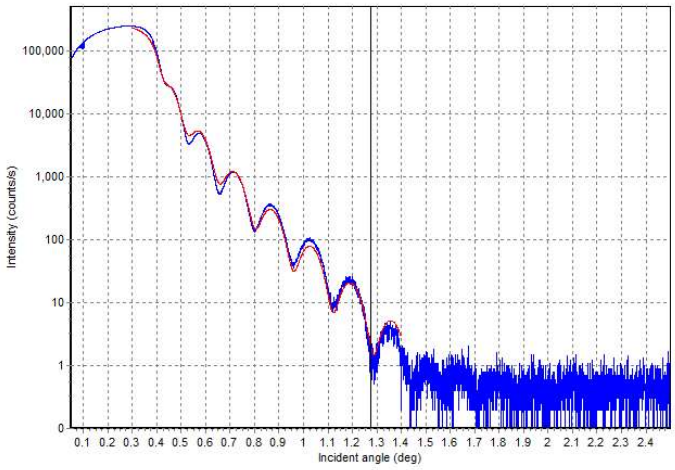

Figure 4.1: Shows the result of fitting between the simulated XRR specular scan represented by the red curve and the experimentally obtained data represented by the blue curve for sample S536 ($Fe_{90}Ga_{10}$).

Nominal Sample Composition	Film thickness from XRR measurement (nm)	Interface-roughness between GaAs(001) and $Fe_{100-x}Ga_x$ (nm)	Density of $Fe_{100-x}Ga_x$ film (g/cm^3)
$Fe_{70}Ga_{30}$	24.84±0.10	2.06±1.14	7.81±0.21
$Fe_{76}Ga_{24}$	27.22±0.09	0.52±0.56	6.88±0.08
$Fe_{80}Ga_{20}$	26.06±0.05	3.22±1.722	7.74±0.11
$Fe_{82}Ga_{18}$	25.97±0.06	0.57±0.29	7.68±0.07
$Fe_{85}Ga_{15}$	26.11±0.10	0.002±0.00	7.14±0.03
$Fe_{86}Ga_{14}$	26.03±0.07	1.72±0.78	7.81±0.19
$Fe_{90}Ga_{10}$	25.33±0.06	1.01±0.01	8.00±0.09
$Fe_{91}Ga_{09}$	27.04±0.11	1.23±0.02	7.77±0.20
$Fe_{93}Ga_{07}$	27.20±0.06	1.44±0.01	8.02±0.07

Table 4.1: Tabulates the samples with the corresponding Galfenol film thickness, surface roughness between Galfenol, and the substrate and the density of the film obtained from the simulation using X'Pert Reflectivity software. All samples had a film thickness of 20 nm at the time of growth.

4.1.2 X-ray reflectivity analysis of $Fe_{79}Ga_{21}$ thin films with varying film thickness

A similar approach was followed to fit the experimental curve with the simulated curve for the samples of $Fe_{79}Ga_{21}$ with varying film thickness using the X'Pert Reflectivity software. To fit the experimental data and the simulated curve, the only initial parameter that was varied was the nominal film thickness, the rest of the fitting parameters were the same for all the samples; that is the substrate layer is considered to be 450 nm thick, and the capping (Cr) is considered of thickness 2 nm. All the parameters associated with the substrate layer are fixed to a constant value because of its high quality. Figure 4.2 represents an example fit for sample S644 (30 nm). The red curve represents the simulated result of the XRR specular scan, and the blue curve represents the experimental data. All the samples had a similarly good fit to the simulated data. Table 4.2 shows the value for the film thickness obtained from the fitting as compared to the nominal film thickness expected from the growth, the film density, and the interface-roughness between the Galfenol film and the substrate. The x-ray reflectivity measurements were never performed for samples S642 (5 nm) and sample S643 (7.5 nm); therefore, they are not mentioned in the table. It can be observed that for films with smaller thickness, the thickness obtained by fitting the experimental data to the simulated XRR specular scan was close to the nominal thickness expected during the growth. However, the thicker samples deviated from the expected growth thickness by a more significant margin. One of the possible reason could be because thicker samples take a longer time to grow. During that time, the internal sputtering parameters may vary slightly.

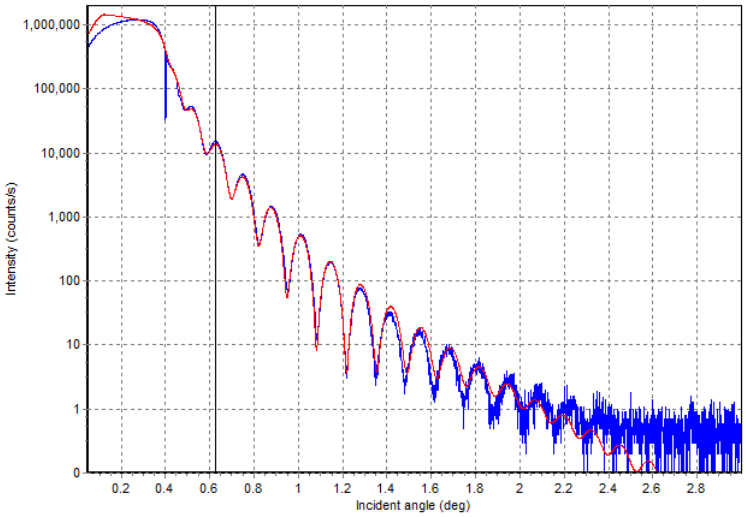

Figure 4.2: Shows the fitting between the simulated curve and the experimentally obtained curve. The red curve represents the simulated curve and the blue curve represents the experimentally obtained data for sample S644 with nominal film thickness of 30 nm.

Sample name	Nominal film thickness (nm)	Film thickness from XRR measurement (nm)	Interface-roughness between GaAs(001) and $Fe_{79}Ga_{21}$ (nm)	Density of $Fe_{79}Ga_{21}$ film (g/cm^3)
S641	10	9.79±0.38	1.50±0.01	7.37±0.96
S640	20	19.80±0.14	1.49±0.79	7.82±0.25
S644	30	29.02±0.09	0.49±0.10	8.36±0.08
S646	60	56.51±0.17	1.25±0.31	7.58±0.29
S645	100	95.07±0.10	0.003±0.00	7.64±0.18

Table 4.2: Tabulates a comparison between the nominal film thickness and that obtained by fitting the data to simulated curve using X'Pert Reflectivity software for $Fe_{79}Ga_{21}$ thin films. The surface roughness between Galfenol and the substrate and the density of the film are also presented.

4.2 X-ray diffraction analysis

Another technique used for characterisation of the samples discussed in this thesis was x-ray diffraction (XRD). The XRD line scans were performed for the ferromagnetic thin films to ascertain the lattice parameters of the crystal. It was performed using the PANalytical X'Pert materials research diffractometer present at School of Physics and Astronomy, University of Nottingham.

4.2.1 X-ray diffraction analysis of $Fe_{100-x}Ga_x$ thin films with varying Ga concentration

XRD measurements were done in order to find the lattice parameter, as well as to monitor change in structure of the thin films as the Ga concentration is gradually varied in the Galfenol films. Figure 4.3 shows the $2\theta - \omega$ scan for the samples as the Ga concentration is gradually increased. It can be clearly seen that for samples up to $Fe_{82}Ga_{18}$ with lower Ga concentration there are two significant peaks, a narrow peak corresponding to the GaAs(004) substrate reflection and a weaker broader (002) peak for the Galfenol film layers. The presence of a single peak indicates that the films are crystalline in nature. However, sample $Fe_{88}Ga_{12}$ was an exception where no sample peak was observed. We are assuming that something went wrong during the growth of $Fe_{88}Ga_{12}$ (S535) sample beyond the capacity of interpretation, which is consistent with the ambiguous results for other measurements carried out on this sample as a part of this thesis. For samples with Ga concentration 20% and higher we observe no sample peak, indicating that with the increase in the impurities in the crystalline Fe structure, the samples becomes random polycrystalline or amorphous in nature. The graphs were fitted to a Gaussian function to determine the sample and substrate peak position, and as well as the FWHM of the peaks. From the graphs, the peak for the film was $\approx 63.85°$ at $Fe_{100-x}Ga_x(002)$, and the peak for the substrate was at $\approx 65.45°$. By using the Bragg's law discussed in section 3.2.1 the lattice parameter (a) along the growth direction was determined to be 0.2953±0.0008 nm which agrees with previously reported values [2]. The average crystallite size was also determined using the Scherrer equation to be 9.55±0.06 nm. These parameters

were calculated using the XRD scan of $Fe_{93}Ga_{07}$. The lattice mismatch was calculated as well using $(a - a_0)/a_0$, where a is the lattice parameter along the growth axis of the film and a_0 corresponds to half the GaAs substrate lattice parameter. a_0 was determined to be 0.284 nm. Therefore the lattice mismatch was established to be $\approx 4\%$.

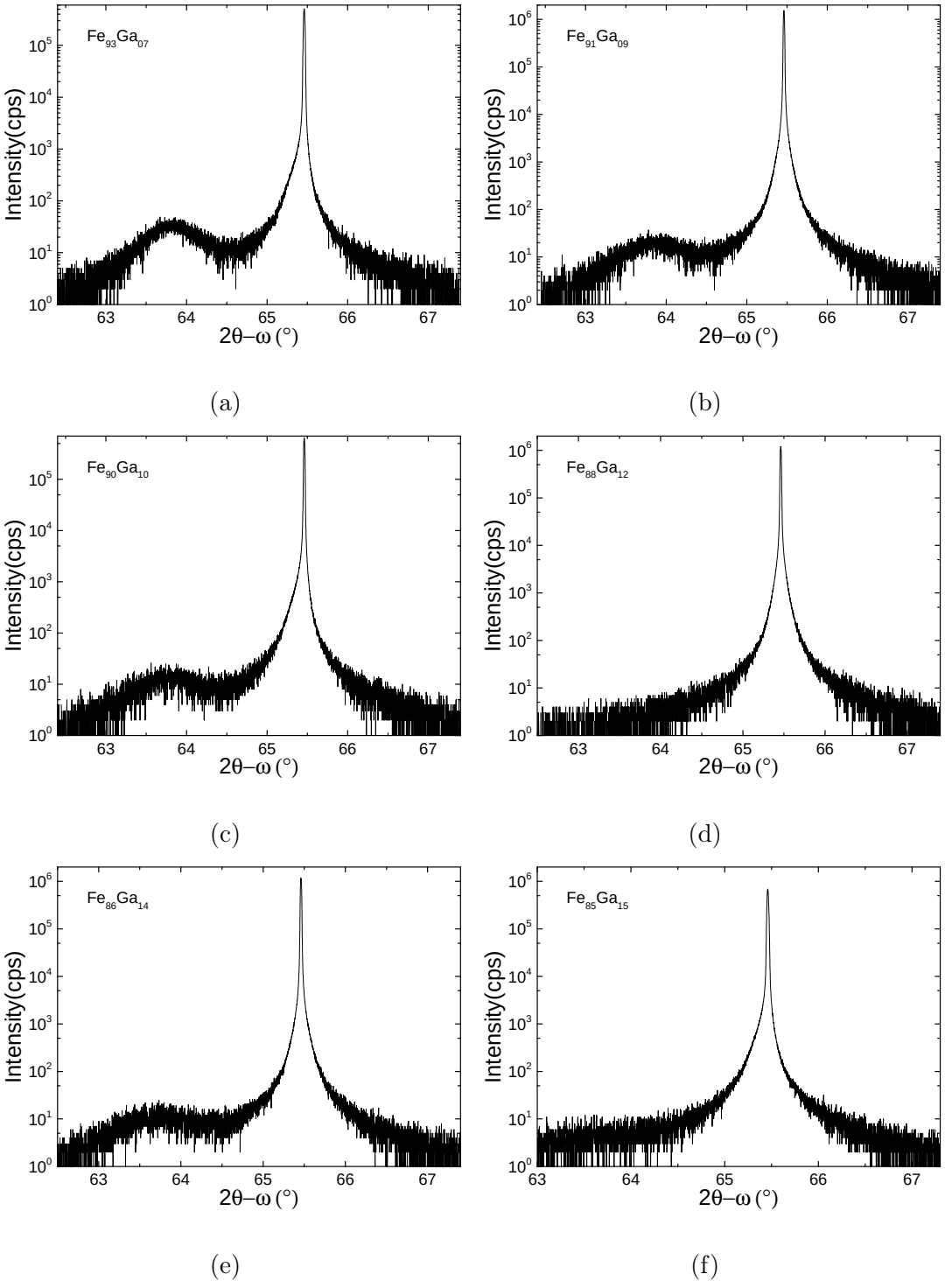

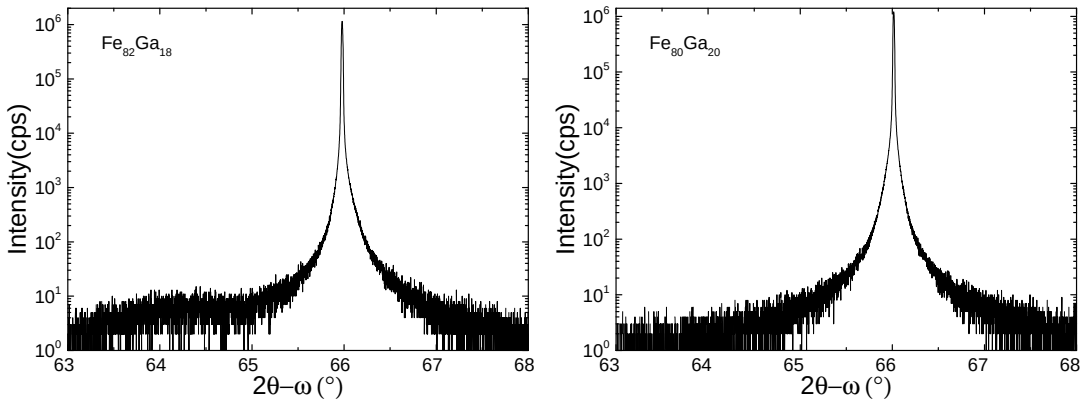

(g)

(h)

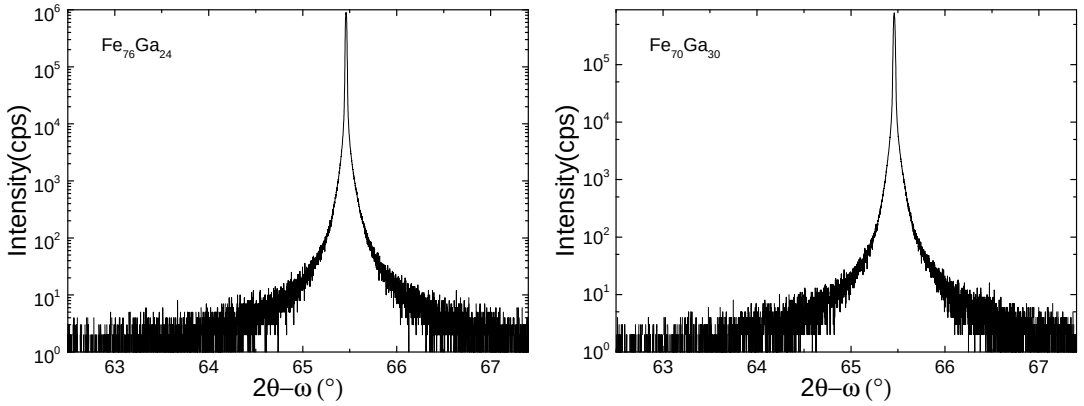

(i) (j)

Figure 4.3: Shows the x-ray diffraction $2\theta - \omega$ scans for the samples with varying Ga composition. The peak for the film was at around 63.81° and the peak for the substrate was at around 65.45°. The sample showed a trend of slowly transitioning from being crystalline for smaller Ga concentration to amorphous or polycrystalline samples for higher Ga concentration.

Figure 4.4 shows the plot for the lattice parameter as the Ga concentration is varied. As the Ga concentration is increased lattice parameter decreases. But the lattice parameter for bulk Galfenol increases linearly with Ga concentration [196]. The contradicting trend between thin film form and bulk Galfenol is due to the stress in the thin films grown on substrates.

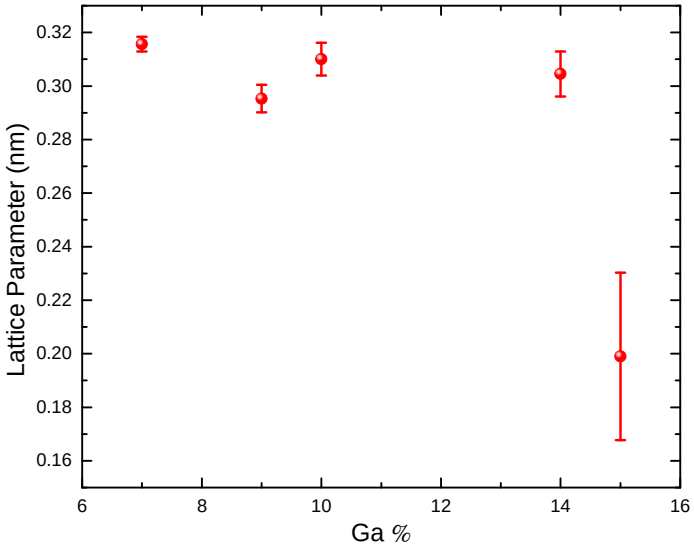

Figure 4.4: Shows the plot for the lattice parameter as a function of Ga concentration.

4.2.2 X-ray diffraction analysis of $Fe_{79}Ga_{21}$ thin films with varying film thickness

Figure 4.5 shows the $2\theta - \omega$ scan for the $Fe_{79}Ga_{21}$ thin films with varying film thickness. Similar to as discussed for samples with varying Ga concentration, these samples also have two peaks, a narrow peak corresponding to the substrate(004) at $\approx 66.05°$and a broad sample peak(002) at $\approx 64.35°$. The sample peak is not that prominent for thinner samples (5 nm and 10 nm), as the thickness of the samples are gradually increased the sample peak also gradually increases and becomes more prominent. The sample peak confirms that the samples are crystalline in nature. This is because the diffraction intensity directly depends on the film thickness, and thinner films have a lower signal to noise ratio; therefore,

smaller peaks are not distinguishable. By using Bragg's equation the lattice parameter (a) for sample S646 (56.5 nm) along the growth direction was determined to be 0.2163±0.0002 nm and the average crystallite size was also determined to be ≈ 10.27 ±0.07 nm. The lattice parameter for the sample S645 (95 nm) is slightly smaller with 0.1931±0.0002 nm. The lattice parameter was difficult to extract for other samples since the sample peak was closer to the substrate peak; therefore, the sample peak was not so prominent for fitting. The lattice parameter for these samples were smaller than the lattice parameter of samples with varying Ga concentration as well as from previously determined value [2]. Increase in the film thickness give rise to compressive strain in the film plane, thereby resulting in tensile strain in the film growth direction. Therefore, the lattice parameter decreases with increase in film thickness. The lattice constant of these films were smaller than bulk single crystal (0.29 nm [197]). Javed *et al.* [138] studied polycrystalline thin films of Galfenol with varying film thickness. They observed that the lattice constant first decreased and then increased toward the bulk value with increasing film thickness.

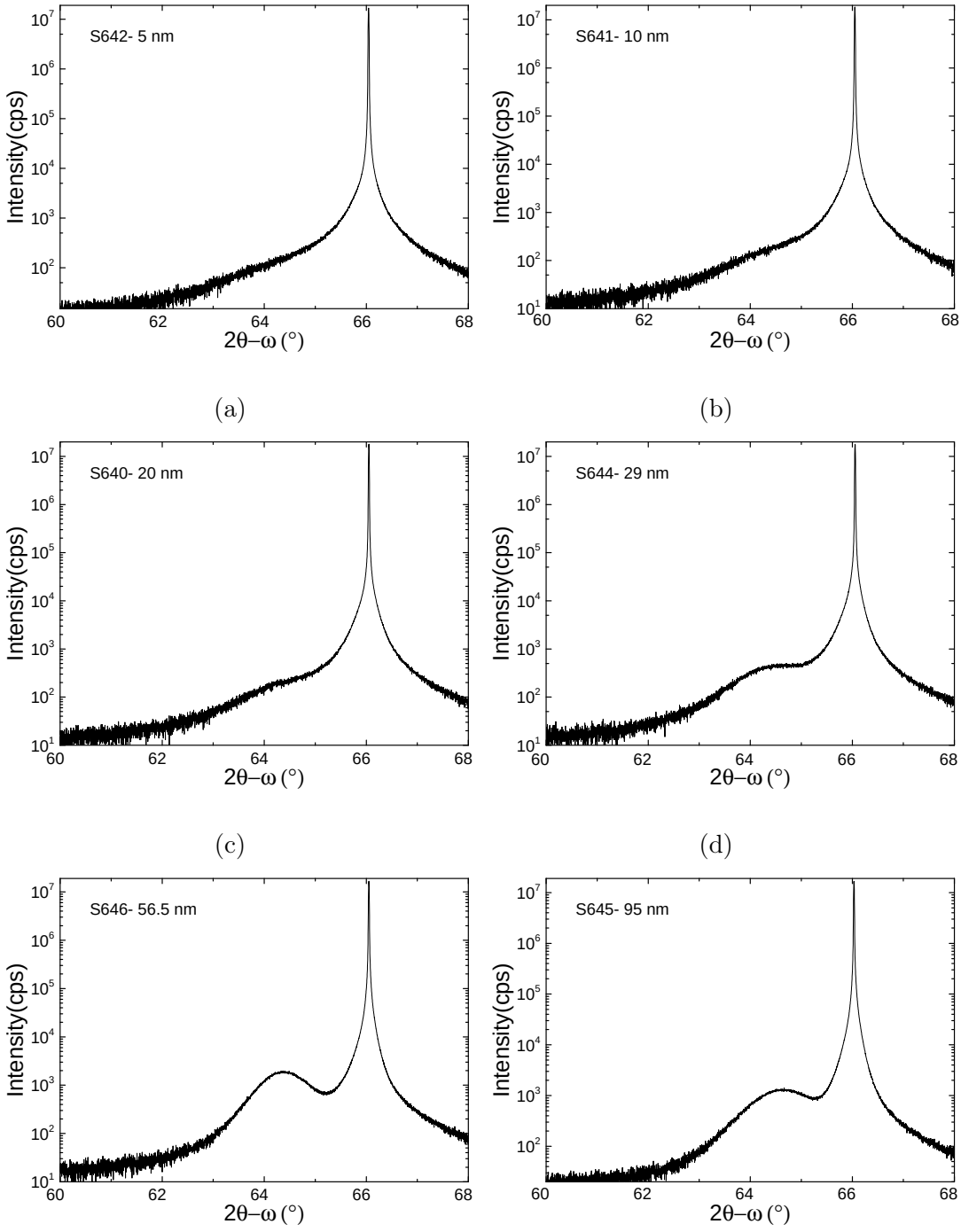

Figure 4.5: Shows the x-ray diffraction $2\theta - \omega$ scans for the $Fe_{79}Ga_{21}$ thin films with varying film thickness. As the film thickness is increased a more prominent sample peak is observed. A narrow peak corresponding to the substrate is observed at $\approx 66.05°$and a broad sample peak is observed at $\approx 64.35°$.

4.3 X-ray photoelectron spectroscopy analysis

X-ray photoelectron spectroscopy (XPS) also known as electron spectroscopy for chemical analysis (ESCA) is a surface analytical technique that provides information about the elemental composition and chemical state of an atom in a material of the top few nanometers of a sample [198, 199]. XPS is based on photoemission process of electrons that is the photoelectric effect [200]. It is a result of interaction between x-rays and electrons in an ultra-high vacuum environment. When x-rays are incident on a sample, they collide with the core electrons and photoelectrons are ejected from the electronic shell of the atoms. The electron is ejected with a certain kinetic energy, directly related to the binding energy of the electron to the atom. Since the core electron is unstable because of the hole in the electronic shell, a valance electron then fills the newly formed hole. Since the binding energy is unique for every element, this can be used to identify the elements in the sample, given by the peaks of the XPS spectrum. The intensity of the peak varies with the concentration of that element at the surface, providing a quantitative determination of the composition. The binding energy of the core electron is also sensitive to the chemical environment of that element, such as bonding to different elements, therefore applied to study the chemical state of the elements present at the surface of the film. Although x-rays can penetrate a material, XPS is a surface-sensitive phenomenon as a consequence of the elastic mean free path of electrons within solids. The unscattered electrons can only escape from roughly 4 nm.

XPS measurements were done on the samples with varying Ga concentration to obtain the composition of the magnetron sputtered grown thin films. Samples were analysed using the Kratos AXIS ULTRA with a monochromatic Al k_α x-ray source present at the nanoscale and microscale research centre (NMRC), University of Nottingham. The XPS spectra and data processing of the spectra were acquired by Dr Emily F Smith. Two samples with extreme Ga concentrations that is S538 with 7% Ga and S529 with 30% Ga were selected for the measurement so that the in-between samples can be assumed to have relevant composition. The samples were etched with a 20 kV ion beam over an area of 1.2 mm square. For

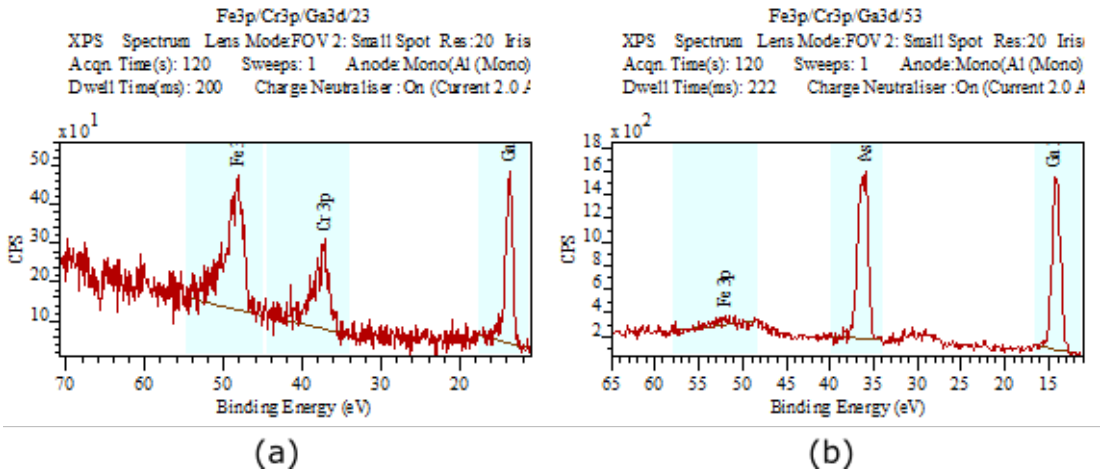

Figure 4.6: Shows the region of binding energy of sample S529($Fe_{70}Ga_{30}$) containing Fe 3p, Cr 3p, As 3d and Ga 3d peaks. (a) in thin film of Fe-Ga with Cr still present from the capping layer after etching (b) in GaAs substrate layer.

the $Fe_{70}Ga_{30}$ sample a 93 s etch removed enough Cr to see peaks for Fe and Ga underneath, leaving some Cr on top. Although the most common peaks used in XPS analysis are Fe 2p, Cr 2p and Ga 3d, the comparison of a low KE electron peak with a much higher KE one when attenuated by an overlayer will affect the quantification. Therefore a higher KE Fe and Cr 3p peaks were selected as they are a closer KE to the Ga 3d and As 3d from the substrate. Although Cr 3p and As 3d peaks are overlapping, because of depth profiling, the Cr is gone by the time it reaches the GaAs layer.

Quantification of the Fe to Ga ratio was directly obtained from Fe 3p and Ga 3d peaks as they are very close in kinetic energies therefore will be attenuated in similar amounts by the overlying Cr metal. XPS spectra of solid-state samples always have a background due to inelastic scattering of the photoelectrons, which needs to be subtracted first to estimate the Stoichiometry of that material. CasaXPS software was used for the analysis to determine the elements and the composition of the samples. Both the samples had composition comparable to what was expected from the growth. Sample S529 ($Fe_{70}Ga_{30}$) had 70±1 % of Fe and 30±1 % of Ga, and sample S538 ($Fe_{93}Ga_{07}$) had 93±1 % of Fe and 7±1 % of Ga. The composition of the $Ga_{50}As_{50}$ substrate for sample S529 was also measured. According to the measurement, the substrate was Ga enriched with 57±1 % of Ga to 43±1 % of As. One of the possible reason could be that there

is Ga enrichment at the interface of the layers. Figure 4.6 shows the spectra for sample S529 ($Fe_{70}Ga_{30}$). Figure 4.6 (a) shows the elements present in the film. Figure 4.6 (b) shows spectra for the substrate layer.

4.4 Summary

This chapter investigated the structural properties of the samples discussed in this thesis. The structural properties covered three areas, firstly monitoring the thickness of the samples grown using magnetron sputtering by using x-ray reflectivity (XRR); secondly, x-ray diffraction (XRD) was done to get an idea about the crystallinity of the samples; lastly, x-ray photoelectron spectroscopy (XPS) measurements were done on the samples with extreme Ga composition ($Fe_{70}Ga_{30}$ and $Fe_{93}Ga_{07}$) to compare with the expected composition during growth. The samples grown with varying Ga composition had the average thickness of 26.20 nm when compared with the as-expected growth thickness of 20 nm. For the samples with varying thickness, the obtained thicknesses remained close to those expected for thinner samples, the deviation from expected thickness increased with the increase in the film thickness because of the prolonged growth time. From the XRD, it was confirmed that the samples remained crystalline for lower Ga concentration, but as the Ga concentration was increased the crystallinity of the samples gradually started to reduce. For the films with varying thickness, it was observed that the thicker films showed prominent crystalline peaks as expected, but for the ultra-thin films the peaks were not distinguishable because of the low signal to noise ratio. From the XPS, it was confirmed that the samples had a composition close to what was expected from the growth initially. In later chapters, a comparison between the structural data and the magnetic properties are made to recognise the agreement of the magnetic properties with respect to the internal structure of the films.

Chapter 5

Static properties investigated using SQUID magnetometry

In this chapter, the effects of altering Ga concentration as well as the film thickness on the static magnetic properties of the sputter grown epitaxial $Fe_{100-x}Ga_x$ thin films on GaAs(001) substrates were characterised using the Superconducting QUantum Interface Device (SQUID) magnetometry. SQUID magnetometry was performed at room temperature using the Quantum Design MPMS XL SQUID magnetometer in the Spintronics group at the University of Nottingham. The longitudinal moment measured by the SQUID gives a measure of the total magnetisation differentiating the crystallographic easy and hard axes additionally giving the corresponding anisotropy energies.

5.1 SQUID magnetometry of $Fe_{100-x}Ga_x$ thin films with varying Ga concentration

SQUID magnetometry measurements were performed at room temperature on 26.20 nm thick $Fe_{100-x}Ga_x$ thin films with x being in the range of 7 to 30 grown on GaAs(001) substrates. The thin films were grown using the sputter deposition technique. The measurements were carried out following the procedure described in section 3.2.4.2. Static magnetic properties such as saturation magnetisation, uniaxial and cubic magnetocrystalline anisotropies, coercivity, and remanence were investigated.

Magnetic hysteresis loops were generated by sweeping the external applied magnetic field from 0.2 T to −0.2 T and back at room temperature. A high magnetic field was used to make sure that the samples are fully saturated in each field direction. The magnetic field was applied along [010]/[100], [110] and [1$\bar{1}$0] directions. The SQUID magnetometry measurements for samples discussed in the table 3.1 are presented in figures 5.1 (a) to (j), demonstrating MH loops for 26.20 nm thick samples with varying Ga concentration. It shows the plot of the longitudinal moment versus the applied magnetic field as the field is varied along different crystallographic directions.

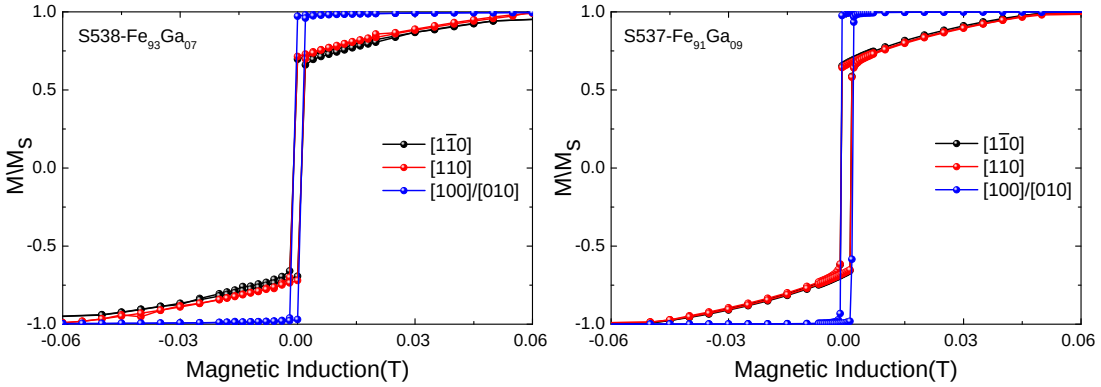

(a) (b)

(c) (d)

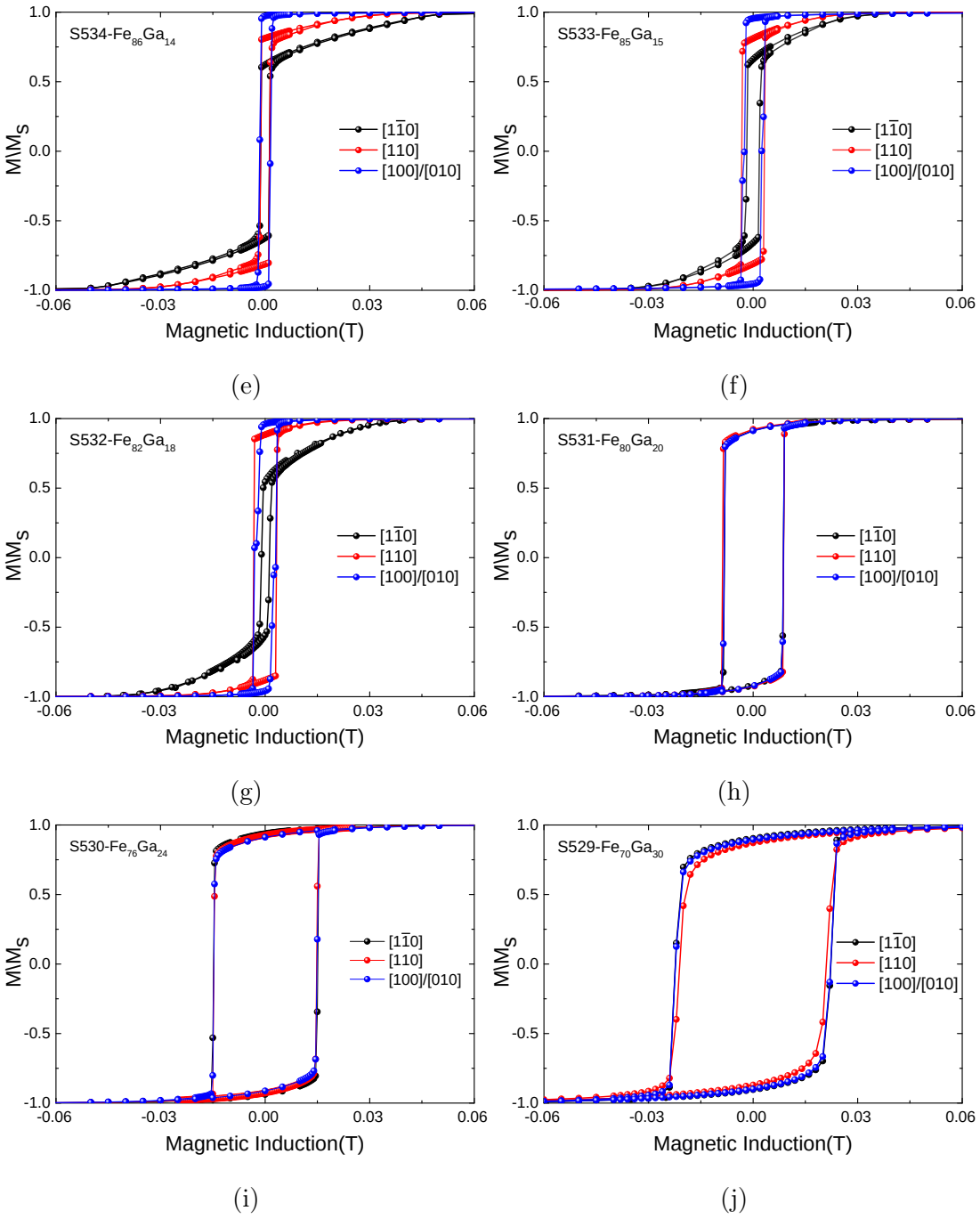

Figure 5.1: Hysteresis loops for 26.20 nm $Fe_{100-x}Ga_x$ thin films grown on GaAs(001) substrate. The hysteresis loops are normalised by saturation magnetisation as a function of magnetic field. The longitudinal magnetic moment along three crystalline direction [1$\bar{1}$0], [110] and [100]/[010] are shown. The hysteresis loop along [1$\bar{1}$0] is represented by the black points, [110] is represented by the red points and [100]/[010] is represented by blue points.

It has been well established for Fe thin films (thickness 8.9 nm, 9.6 nm, 26.20 nm and 32.9 nm) grown on GaAs(001) substrate that [$\bar{1}$10] was harder than [110], while [100] and [010] were magnetically equivalent [126, 201]. The study suggested that the in-plane magnetic anisotropy of these thin films is given by a uniaxial anisotropy (K_u) with an easy axis parallel to [110] superimposed on the cubic anisotropy (K_c) with easy axis along [010] and [100]. It has also been established that epitaxial single-layer thin films of $Fe_{100-x}Ga_x$ grown on GaAs(001) substrate has a net in-plane anisotropy that is a combination of uniaxial and cubic anisotropy [2, 85]. By looking into the experimental SQUID loops of figure 5.1 (a) to (g) as the field is swept along [010]/[100], [110] and [1$\bar{1}$0] directions the difference in the anisotropies is clearly evident. As the magnetic field is swept along [010]/[100], the magnetisation saturates for the smallest external magnetic field value and the remanent magnetisation is largest making it the easy direction of magnetisation. Hence, [010]/[100] direction is established as the easy axis among all the other directions in which the magnetic field was applied. Similarly, if we compare the MH loops along [110] and [1$\bar{1}$0] direction it can be concluded that it is much harder to saturate the magnetisation along the [1$\bar{1}$0] axis, making [110] direction a relatively easier axis of magnetisation. This clearly indicates that there is a strong cubic anisotropy along [010]/[100] directions and weaker uniaxial anisotropy along [110] direction.

By looking into the SQUID loops in figure 5.1 (a) to (g) a qualitative analysis of the trends in the cubic and uniaxial anisotropy constants as well as the coercive fields can be provided. Observing the hysteresis loop of the easy axis along [010]/[100] direction in figure 5.1 (a) for sample S538 with 7 % Ga concentration, it is a square loop with high squareness indicating a significant value for the cubic anisotropy constant. However, as the Ga concentration is gradually increased the squareness of the loop decreases eventually becoming isotropic, indicating a reduction in the value of the cubic anisotropy constant, which is confirmed in later sections. Similarly, the hysteresis loop for the uniaxial axis along [110] becomes harder with the increase in the Ga concentration eventually becoming saturated, indicating an increase in the uniaxial anisotropy constant. The intrinsic coercive field increases as well with increase in the Ga concentration.

Sample name	Fe Content %	M_s $\times 10^6$ Am^{-1}
S529	70	0.826±0.048
S530	76	1.25±0.073
S531	80	1.23±0.075
S532	82	1.38±0.080
S533	85	1.42±0.084
S534	86	1.48±0.089
S535	88	1.48±0.089
S536	90	1.52±0.088
S537	91	1.53±0.089
S538	93	1.53±0.089

Table 5.1: Shows the saturation magnetisation of the sputtered grown thin films as obtained from SQUID measurements.

Table 5.1 presents the saturation magnetisation for epitaxial thin films grown using the sputtered deposition as obtained from SQUID measurements. In a saturated material, the value of the saturation magnetisation can be equated to the total number of magnetic moments present per unit volume. In a $Fe_{100-x}Ga_x$ sample we assume that the magnetic moment contribution will only arise from the Fe concentration. The experimental saturation magnetisation, M_s, was calculated by taking the average of the longitudinal moment at saturation for all the three crystallographic directions in which SQUID was measured initially and dividing it per volume of the sample. The average magnetic moment per Fe atom, $<\mu_{Fe}>$, in Bohr magnetron, μ_B, can be calculated from the saturation magnetisation by dividing the saturation magnetisation by atomic density of Fe. The atomic density of Fe was adjusted accordingly to account for the reduction in Fe concentration when Ga is added. The atomic density of pure Fe is 85.5 atoms/nm^3 [145]. Figure 5.2 shows the average magnetic moment per Fe atom at room temperature as a function of Fe concentration. In order to achieve a gradual increase in Ga concentration, the growth rate of pure Fe(99.99%) target was reduced progressively. The average magnetic moment per Fe atom decreases

as the Fe content decreases. For sample S529 with 70% Fe concentration the average magnetic moment per Fe atom shows a significant deviation. It has been previously reported that for Ga concentration greater than or equal to 30% the magnetic moment of Fe decreases almost linearly with Ga concentration [202]. In another study, they observed that the average magnetic moment per Fe atom decreases with a linear dependency on the Ga content up to 20%. However, this dependency was no longer linear for 25% of Ga. The average magnetic moment per Fe atom had a sudden drop for 25% of Ga. The average magnetic moment per Fe atom reduced from $\approx 2.15\ \mu_B$ for 20% Ga to $\approx 1.83\ \mu_B$ for 25% Ga at 300 K which rounds up to a 15 % change in the average magnetic moment per Fe atom [197]. This was due to the hybridisation of Fe and Ga states and attributed to the formation of $D0_3$ precipitates which is consistent with the samples discussed in this thesis [203, 204]. The average magnetic moment per Fe atom for 10% and 20% Ga sample discussed in this thesis and reference [197], the magnetic moment in case of our samples are systematically lower when compared to the work presented in the reference [197]. One of the possible explanation for the lower magnetic moment could be because of the magnetically dead layer formation of ≈ 1 nm at the interface layer of the film with the substrate (GaAs) and capping layer (Cr). Thus, the average magnetic moment increased by $\approx 5\%$ to account for a possible magnetically dead layer.

Mathematically, the anisotropy energies can be determined by solving the free energy equation which is discussed in details in section 3.3.1,

$$E = -M \cdot H_{ext} \cos(\theta - \phi) + K_u \sin^2(\phi - \frac{\pi}{4}) + \frac{K_c}{4} \sin^2 2\phi \tag{5.1}$$

where E is the magnetic free energy, M is the magnetisation, H_{ext} is the external applied magnetic field, K_u and K_c are the uniaxial and cubic anisotropy coefficients respectively, θ is the angle between the applied magnetic field and the easy axis of the sample, and ϕ is the angle between the magnetisation and the easy axis of the sample. By convention θ for [010] direction is assigned 0°, for [100] direction as 90°, for [110] as 45° and for $[1\bar{1}0]$ as 135° as shown in figure 5.3.

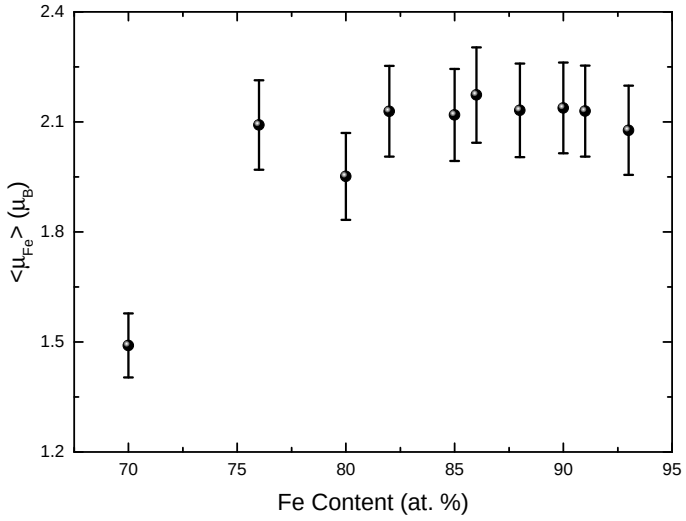

Figure 5.2: Shows average magnetic moment per Fe atom, $<\mu_{Fe}>$, at room temperature as a function of Fe content (at. %) in Galfenol thin films.

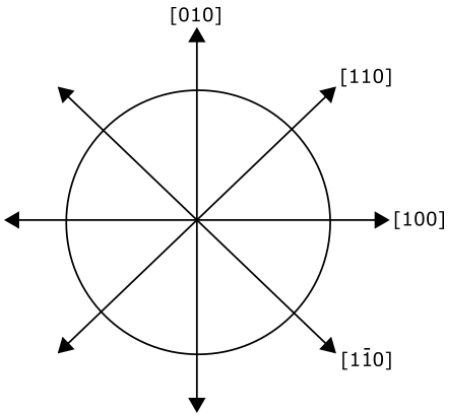

Figure 5.3: Shows the crystallographic directions with respect to one another with respect to a GaAs(001) substrate. The hysteresis loops were simulated by considering the angle between the applied magnetic field and [010] direction as 0°.

From figure 5.1, hysteresis loops for samples (h)-(j), that is the samples with higher Ga concentration, the hysteresis loops in all crystalline directions are alike and hardly distinguishable. The samples have lost their anisotropic nature and have become entirely isotropic. The exact reason behind this behaviour has been explained in details in later sections. Since the samples have become isotropic in nature, equation 5.1 used for simulating hysteresis loops along different crystalline

directions is no longer valid and gives unrealistic results. Hence, samples S531, S530 and S529 will be excluded from further studies about anisotropy constants and will be labelled as isotropic samples wheresoever required.

The hysteresis loops were generated, and the anisotropy constants along with their associated errors were extracted by fitting the hysteresis loops along [110] and [1$\bar{1}$0] using the method described in details in section 3.3.1. The uniaxial and cubic anisotropy constants of these samples were extracted from the hysteresis loops obtained by SQUID experiment at room temperature using the fitting model discussed in section 3.3.1. Figure 5.4 shows an example of this fitting where the hysteresis loop for S536 sample collected during SQUID experiment at room temperature is represented by the black points, and the results from the fitting program is shown in the red line. The fit to the magnetic hysteresis loop is demonstrated for two crystalline directions [110] and [1$\bar{1}$0]. The fitting was focused in the region up to 0 T to ensure that the effects of domain wall nucleation were not included during the fitting procedure to agree with the single domain model. A full set of all the fits to the SQUID magnetometry experimental data can be found in Appendix A.

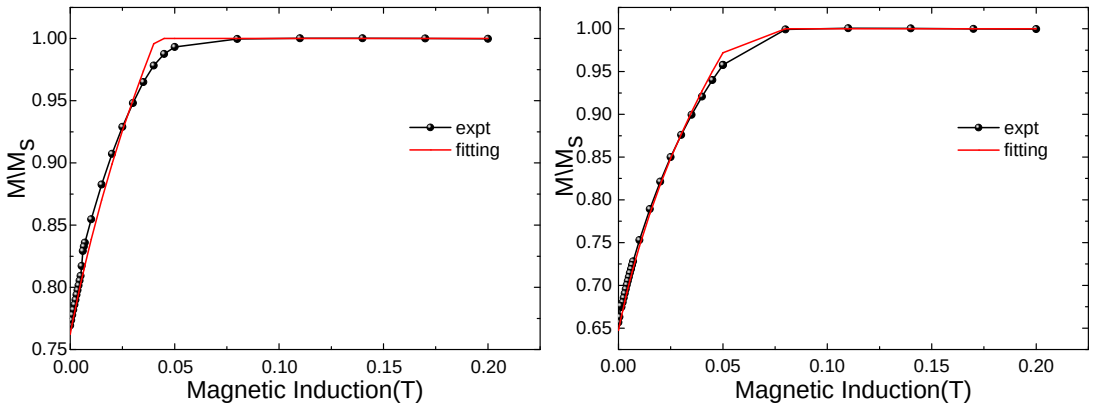

(a) [110] (b) [1$\bar{1}$0]

Figure 5.4: Demonstrates the fitting of the experimental data obtained via SQUID magnetometry with the simulated data for sample S536. The experimental data is represented by the black points and the fitted curve is shown by the red line. Fitting along both the crystalline axes [110] and [1$\bar{1}$0] considered while extracting the anisotropy constants are shown respectively in (a) and (b).

The extracted values of K_c and K_u along with the associated errors for

$Fe_{100-x}Ga_x$ thin film samples with varying Ga composition are shown in table 5.2. The values obtained for sample S535 is deliberately omitted because it gave ambiguous and unrealistic values for the anisotropy constants; one of the possible reason could be the growth parameters during sputtering didn't go as intended. The anomalous nature of this sample was later confirmed during other experimental data discussed in later chapters. Hence, the results will be excluded henceforth.

Sample name	% Ga	K_c (kJ/m^3)	K_u (kJ/m^3)
S532	18	17.0±2.6	7.6±2.3
S533	15	16.8±4.5	3.3±1.3
S534	14	31.4±6.4	8.3±3.0
S536	10	41.7±9.1	6.8±2.6
S537	9	35.5±7.3	4.4±1.7
S538	7	50.5±14.6	0.7± 0.2

Table 5.2: Values of the cubic anisotropy constant, K_c, and uniaxial anisotropy constant, K_u, in kJ/m^3 for $Fe_{100-x}Ga_x$ thin films grown at room temperature. The values were determined by fitting numerically simulated data with the experimental data obtained from SQUID experiment. The percentage of Ga concentrations are represented as it was expected during the growth.

The resulting graph for the K_c anisotropy constant values as a function of Ga composition is shown in figure 5.5. Figure 5.5 shows that the cubic anisotropy initially reduces as the Ga concentration is increased and then saturates. When the Ga concentration is further increased samples become completely isotropic. The primary source for four-fold cubic magnetocrystalline anisotropy in Fe and its alloys is spin-orbit coupling which links the magnetic properties to the crystal symmetry via the electronic orbitals. In section 4.2.1, where the XRD measurements indicated that as the Ga concentration was increased in the $Fe_{100-x}Ga_x$ thin films, the crystallinity of the samples gradually decreased to a point where no sample peak was observed. In the $Fe_{100-x}Ga_x$ thin films, as we keep adding the second element, Ga, reduction in the crystalline quality results in a decrease

in cubic anisotropy eventually becoming completely isotropic.

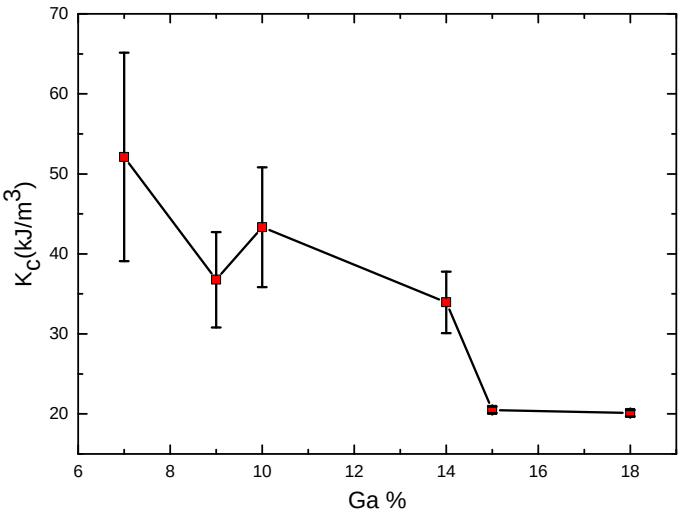

Figure 5.5: Values of the cubic anisotropy constant, K_c, as obtained by fitting experimental SQUID hysteresis loop with the simulated loops for $Fe_{100-x}Ga_x$ thin films with varying Ga composition.

The resulting graph for the K_u anisotropy constant values as a function of Ga composition is shown in figure 5.6. From the figure, it is apparent that the uniaxial anisotropy, K_u, increases up to a certain point and then saturates as the Ga concentration is increased. Above 18 % Ga the magnetic behaviour is isotropic. It has been well studied that the origin of uniaxial anisotropy in thins films of Fe and its alloys is an interface phenomenon between the film and the GaAs substrate [126, 148, 205]. Although the origin of uniaxial anisotropy in Fe/GaAs thin films has been studied vastly, there has not been any conclusive answer to its existence. Some studies have shown that the p states in the As atoms hybridises with the d states in the Fe atoms resulting in a quenching of magnetic moments along the hard axis $[1\bar{1}0]$ producing a uniaxial anisotropy along the [110] axis making it a relatively easier axis than $[1\bar{1}0]$ [206, 207]. However, to determine the exact phenomenon behind this behaviour and the trend observed is still an enigma.

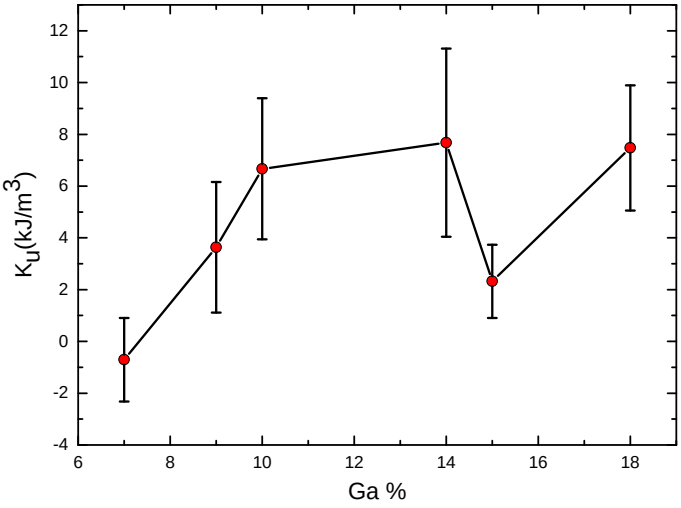

Figure 5.6: Values of the uniaxial anisotropy constant, K_u, as obtained by fitting experimental SQUID hysteresis loop with the simulated loops for $Fe_{100-x}Ga_x$ thin films with varying Ga composition.

Magnetic anisotropy strongly affects the shape of the hysteresis loops and affects the coercivity, and remanence. Figure 5.7 shows the change in the coercive field as the Ga concentration is increased in $Fe_{100-x}Ga_x$ thin films. As discussed earlier, coercivity is the reverse field required to completely demagnetised a material, and this reversal magnetisation process proceeds via domain wall motion. As the Ga concentration increases, impurities increases in the thin film. These defects may act as pinning sites for some domain walls in addition to nucleating them. Hence, as the impurity content increases a larger reversal field is required to demagnetise the material; therefore, increasing the coercivity [145]. This could be reconfirmed from the XRD measurements in section 4.2.1 where the crystallinity of the samples decreased with the increase in the impurity added in the form of Ga.

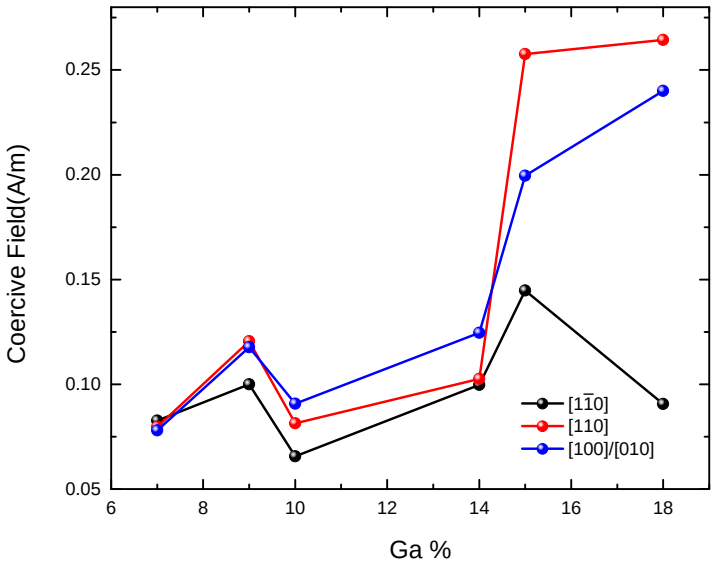

Figure 5.7: Shows the variation of the coercive field as the Ga concentration is varied in three crystallographic directions.

If we consider the free energy equation with no external applied magnetic field, the total energy of the system will only depend on the cubic and uniaxial anisotropy energy.

$$E = K_u \sin^2(\phi) + \frac{K_c}{4} \sin^2(2\phi) \tag{5.2}$$

Therefore, energy minimisation ($dE/d\phi = 0$) will yield the angle where the magnetisation will lie due to the competition between the uniaxial and cubic anisotropies when no magnetic field is applied as shown in figure 5.8.

$$\phi = \frac{1}{2} \arccos(-\frac{K_u}{K_c}) \tag{5.3}$$

The projection of the saturation magnetisation along different crystallographic direction will give the magnetisation along that particular direction. For example,

$$M_{010} = M_s cos\phi \tag{5.4}$$

and,

$$\frac{M_{010}}{M_s} = cos\phi \tag{5.5}$$

gives the remanence ratio. The remanence ratio can also be extracted from the MH loop obtained from the SQUID magnetometry measurements given by the

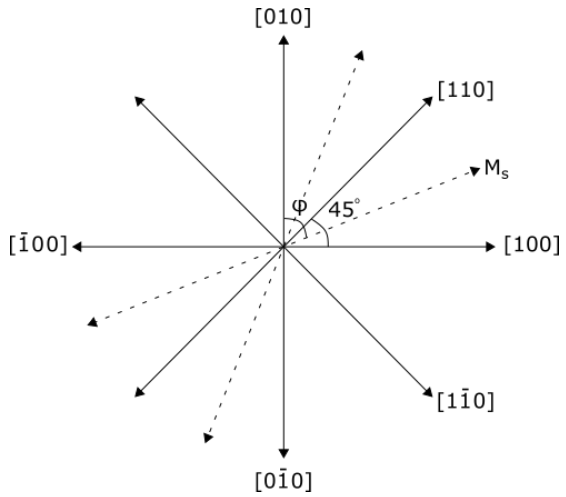

Figure 5.8: The magnetisation will lie at an angle ϕ from one of the cubic easy axes such that it lies inbetween the cubic easy axis and the uniaxial relatively easy axis due to the competition between the uniaxial and cubic anisotropies.

ratio between the remanent magnetisation along a particular crystal direction and the saturation magnetisation along one of the cubic easy axes. Consequently, the anisotropy constants obtained using the least squares fit analysis discussed in earlier sections can be checked with the experimental MH loops from SQUID magnetometry for the consistency of the fitting method. Figure 5.9 shows the remanence ratio along [110] and [1$\bar{1}$0] direction extracted from the MH loop as well as from the remanence ratio obtained from the anisotropy values from the fitting program. The black data points with the error bars are the remanence ratio obtained from the fitting program and the red points gives the remanence ratio obtained from the MH loop.

In figure 5.9 we see that the values obtained via both the method are roughly equal. The sample with 9 % Ga concentration is an exception along [110] direction. A possible reason behind this deviation could not be established. The differences in values are within the boundaries of reasonable error. This indicates that the values of the anisotropies extracted by fitting the MH loops from the SQUID magnetometry experimental data is accurate.

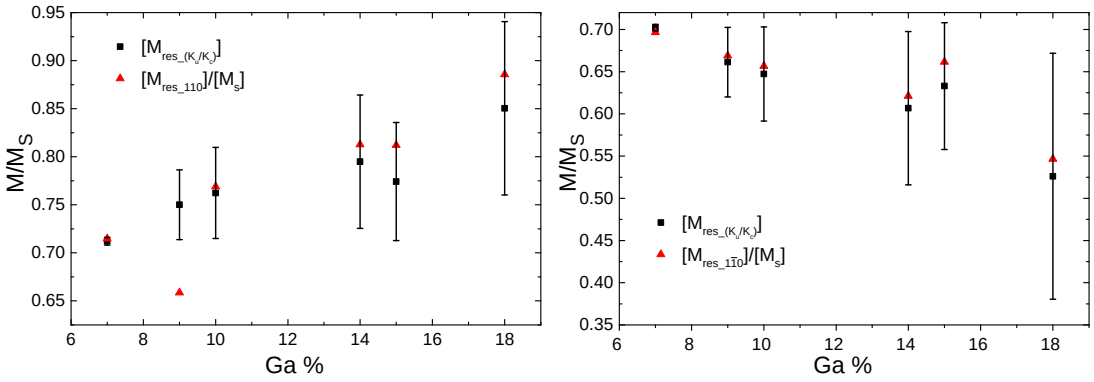

(a) [110] (b) [1$\bar{1}$0]

Figure 5.9: Shows the variation of the remanence magnetisation ratio as the Ga concentration. The graph shows the comparison between the remanence ratio obtained from the MH loops collected during the SQUID experiment and the remanence ratio extracted via indirect process from the anisotropies obtained from the fitting process discussed earlier (a) shows the remanence ratio along [110] and (b) shows the remanence ratio along [1$\bar{1}$0]

5.2 SQUID magnetometry of $Fe_{79}Ga_{21}$ thin films with varying film thickness

SQUID magnetometry measurements were performed at room temperature on $Fe_{79}Ga_{21}$ thin films with increasing film thickness varying between 5 nm to 95 nm grown on GaAs(001) substrates. The measurements were carried out following the procedure described in section 3.2.4.2.

Similar parameters to as discussed in the earlier section were used to generate the hysteresis loops along [010]/[100], [110] and [1$\bar{1}$0] directions. The SQUID magnetometry measurements for samples presented in table 3.2 are demonstrated in figure 5.10. All samples have a nominal composition of $Fe_{79}Ga_{21}$. The longitudinal magnetic moment along [1$\bar{1}$0] direction is represented by black points, along [110] direction is represented by red points and [100]/[010] direction is represented by blue points.

A recognisable distinction between the cubic easy axis along [100]/[010], relatively easy uniaxial axis [110], and the hard axis [1$\bar{1}$0] is observed for most of the samples. For sample S642 with 5 nm film thickness the [100]/[010] and [110]

axes are approximately equivalent and are easy axes. As the film thickness is increased, [100]/[010] and [110] axes start to separate into cubic easy axis and relatively easy uniaxial axis respectively. However, as the sample becomes thicker, S646 and S645 with sample thickness 56.5 nm and 95 nm respectively uniaxial [110] axis almost becomes equivalent to the cubic axes. For samples S646 and S645, the magnetisation reversal is a combination of more prominent coherent rotation of magnetisation and magnetisation switching. There is also a striking similarity between the shape of the hysteresis loop along the hard axis, $[1\bar{1}0]$, for samples S642, S646 and S645.

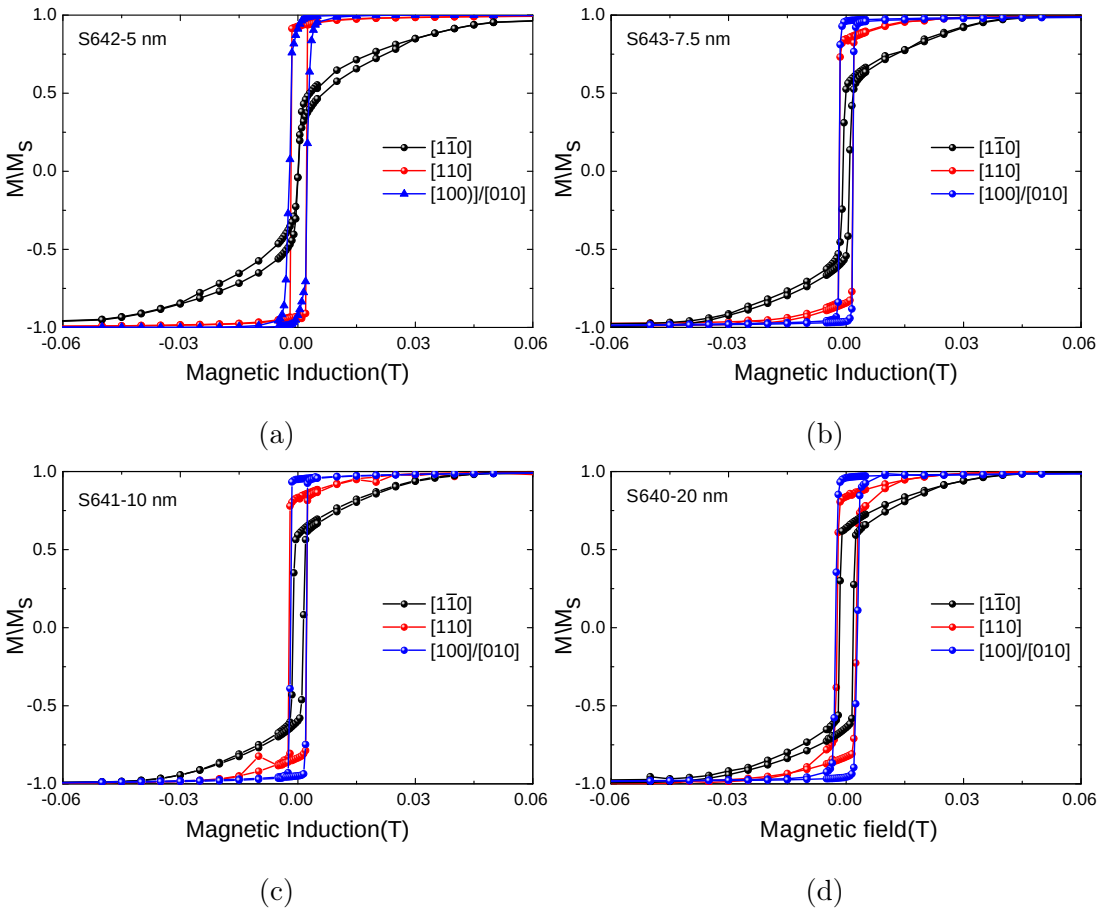

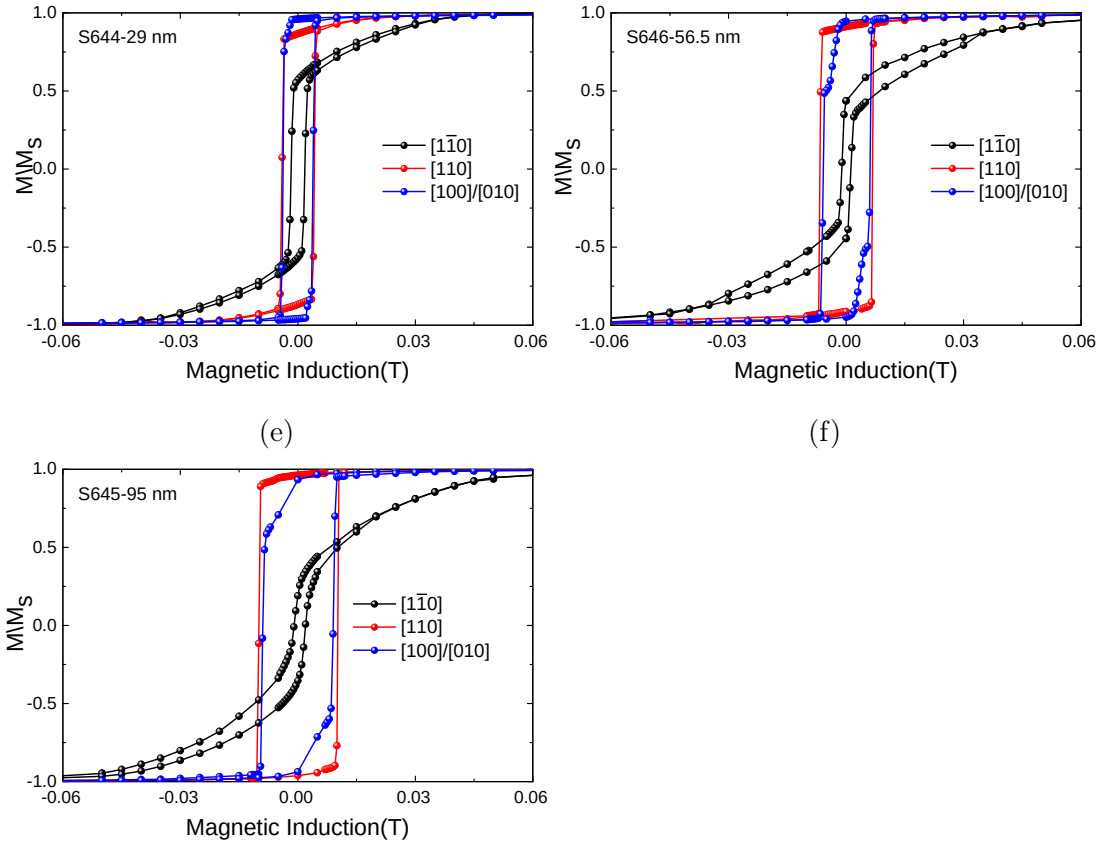

(e) (f)

(g)

Figure 5.10: Hysteresis loops for $Fe_{79}Ga_{21}$ thin films grown on GaAs(001) substrate with varying film thickness are shown. The loops were taken by sweeping the external magnetic field between $\pm 0.2\,\mathrm{T}$. The hysteresis loops are normalised by saturation magnetisation as a function of magnetic field. The longitudinal magnetic moment along three crystalline direction [1$\bar{1}$0], [110] and [100]/[010] are represented by the black, red and blue points respectively.

The fitting procedure was repeated using the same method used for samples with varying Ga composition in order to extract the values of the uniaxial, K_u, and cubic, K_c, anisotropy constants. The extracted values of K_c and K_u along with the associated errors for $Fe_{79}Ga_{21}$ thin film samples with varying film thickness are shown in table 5.3. An example fit to the SQUID magnetometry data of sample S640 is shown in figure 5.11, the black points represent the experimental data, and the fit is shown using the red line. A full set of all the fits to the SQUID magnetometry experimental data can be found in Appendix A.

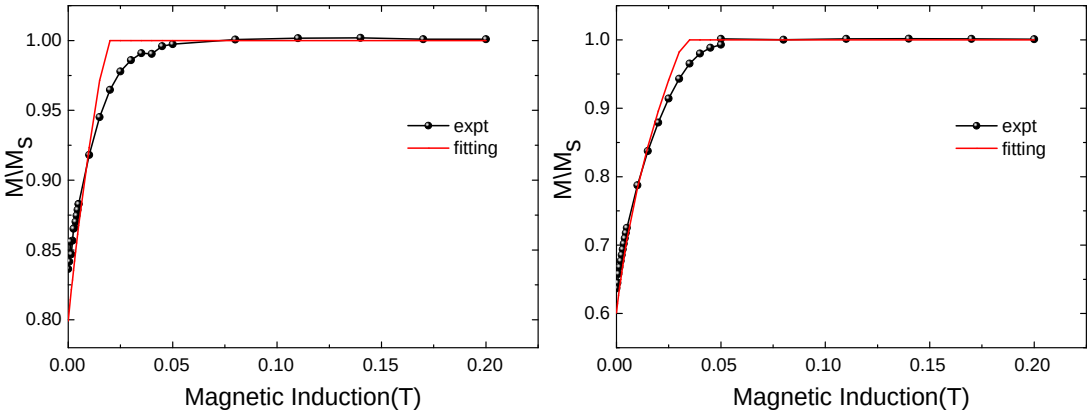

(a) [110] (b) [1$\bar{1}$0]

Figure 5.11: Demonstrates the fitting of the experimental data obtained via SQUID magnetometry with the simulated data for sample S640. The experimental data is represented by the black points and the fitted curve is shown by the red line. Fitting along both the crystalline axes [110] and [1$\bar{1}$0] considered while extracting the anisotropy constants are shown respectively in (a) and (b).

The extracted values of K_c and K_u along with their associated errors for $Fe_{79}Ga_{21}$ thin film samples with varying film thickness are shown in table 5.3. A graphical representation of the anisotropy constants are presented in figure 5.12 and 5.13.

The cubic anisotropy increases with increase in film thickness within the boundaries of reasonable error with a significant spike for sample S646 with a nominal film thickness of 56 nm. In section 4.2.2, the sample peak observed for sample S646 was sharper and clearer than other samples, agreeing with the observation concluded for the cubic anisotropy constant. Both samples S646 and sample S645 had much more distinctive sample peak compared to other sam-

Sample name	Thickness (nm)	K_c (kJ/m^3)	K_u (kJ/m^3)
S642	5	17.4±2.4	12.9±0.4
S643	7.5	19.4±1.2	7.7±2.2
S641	10	19.1±2.2	6.2±1.8
S640	20	17.5±0.4	4.9±2.0
S644	29	17.9±0.6	7.0±2.4
S646	56.5	25.2±2.6	14.3±2.4
S645	95	20.1±5.6	18.8±2.1

Table 5.3: Values of the cubic anisotropy constant, K_c, and uniaxial anisotropy constant, K_u, in kJ/m^3 for $Fe_{79}Ga_{21}$ thin films with varying film thickness are shown. The values were determined by fitting numerically simulated data with the experimental data obtained from SQUID experiment.

ples, which was later reflected on the cubic anisotropy constant being higher for these two samples than other ones. The trends observed for the cubic and uniaxial anisotropies for $Fe_{79}Ga_{21}$ thin films agrees with that observed for epitaxial Fe/GaAs(001) thin films for a wider range of thicknesses (3.53 - 210.92 nm) in references [126, 207–210]. Their results indicated that in addition to an increase in uniaxial anisotropy with decreasing film thickness, cubic anisotropy significantly reduces in the thinnest films. A similar trend was observed for the samples with film thickness 20 nm and below discussed in this thesis. We can also see that the uncertainty in the K_c value in sample S645 (95 nm) is relatively large. The behaviour of the uniaxial anisotropy for samples above film thickness of 20 nm was not exactly understood.

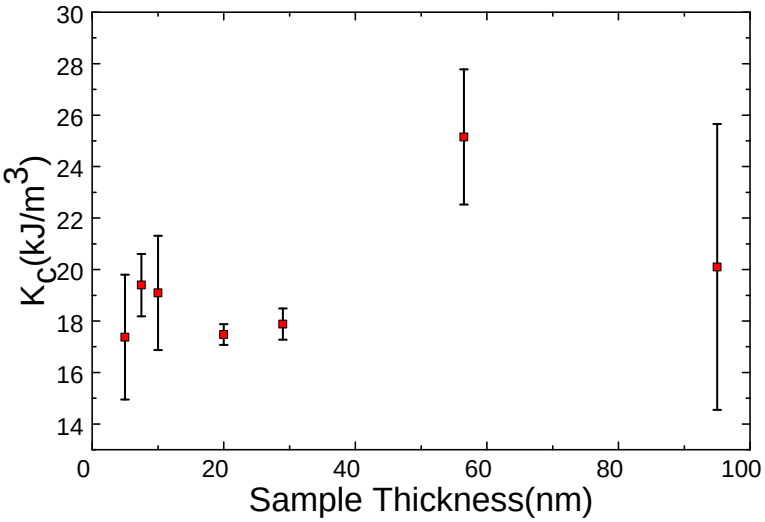

Figure 5.12: Values of the cubic anisotropy constant, K_c, as obtained by fitting experimental SQUID hysteresis loop with the simulated loops for $Fe_{79}Ga_{21}$ thin films with varying nominal film thickness.

The uniaxial anisotropy constant (figure 5.13) decreases as the film thickness is increased being the lowest for 20 nm thick sample (S640). However for films thicker than 20 nm K_u starts rising again well within the error limits. From previous studies of Fe thin films grown on GaAs(001) substrate, the uniaxial anisotropy is an effect of interface interaction since the interfacial Fe atoms are electronically in a different environment compared to those in the rest of the film. Although the Fe (bcc) and GaAs (zincblende) crystal structures are both cubic in nature, their electronic structures and bonding geometries are different. Therefore, the interfacial Fe atoms will not only have to adapt to a different bonding partner but also a different bonding geometry. Consequently, the thickness (t) dependence of the uniaxial anisotropy in Fe thin films is established to be $1/t$ [126, 207, 208]. It has been observed to decrease as the thickness increases in Fe/GaAs samples [207, 208] where films of thickness ranging between 1.0 nm to 8.6 nm were used. The samples discussed in this section deviates from this behaviour for films thicker than 20 nm. However, the reason for the increase in K_u for thicker samples is not known.

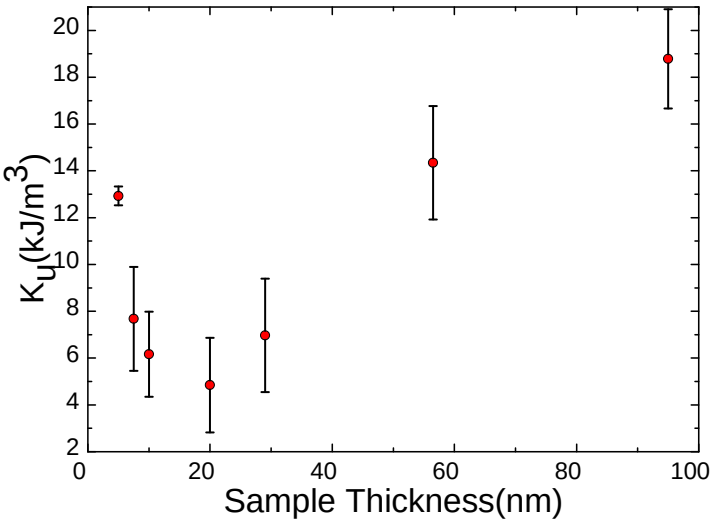

Figure 5.13: Values of the uniaxial anisotropy constant, K_u, as obtained by fitting experimental SQUID hysteresis loop with the simulated loops for $Fe_{79}Ga_{21}$ thin films with varying nominal film thickness.

Figure 5.14 shows the variation in the coercive field as the thickness of $Fe_{79}Ga_{21}$ sample changes. The coercive field along $[1\bar{1}0]$ increases in the beginning as the thickness increases but for the most part remains almost constant. The coercive field along [110] and [100] axes are moderately consistent with each other for samples which are less than 30 nm thick; however, samples thicker than 30 nm seems to have a divergence in their coercive field value. As the thickness increases, the defects in $Fe_{79}Ga_{21}$ films increases as well due to the relaxation of the lattice growth strain. As discussed earlier in section 5.1, as the number of defects increase, they become pinning site for domain walls as well as becoming domain nucleation cites. Therefore, as the film thickness increases the coercivity increases as well.

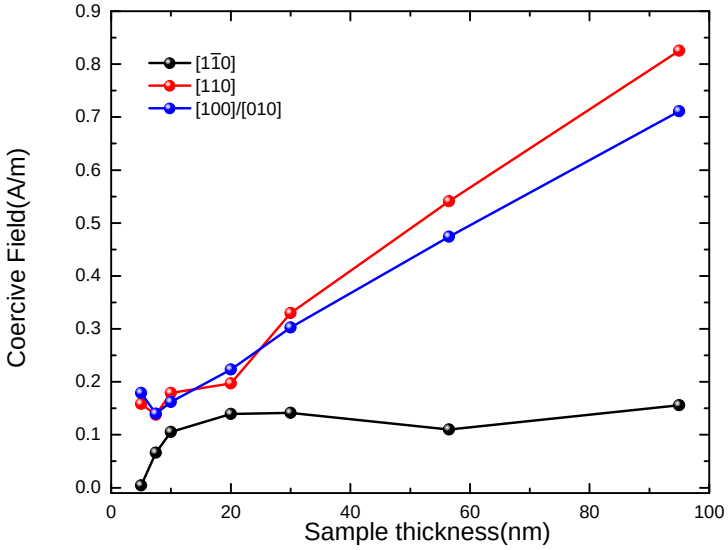

Figure 5.14: Shows the variation of the coercive field as the film thickness is varied in three crystallographic direction.

Similar to the remanence ratio discussed earlier for samples with varying Ga composition, figure 5.15 shows a comparison between the remanence ratio along [110] and [1$\bar{1}$0] direction extracted from the MH loop as well as from the remanence ratio obtained from the anisotropy values from the fitting program. The black data points with the error bars are the remanence ratio obtained using the anisotropy values obtained from the fitting program and the red points gives the remanence ratio obtained from the MH loop acquired by SQUID magnetometry. In figure 5.15 we see that the values obtained via both the method are approximately comparable, indicating that the values of the anisotropies extracted by fitting the MH loops from the SQUID magnetometry experimental data is accurate and confirming that the fitting method is reliable.

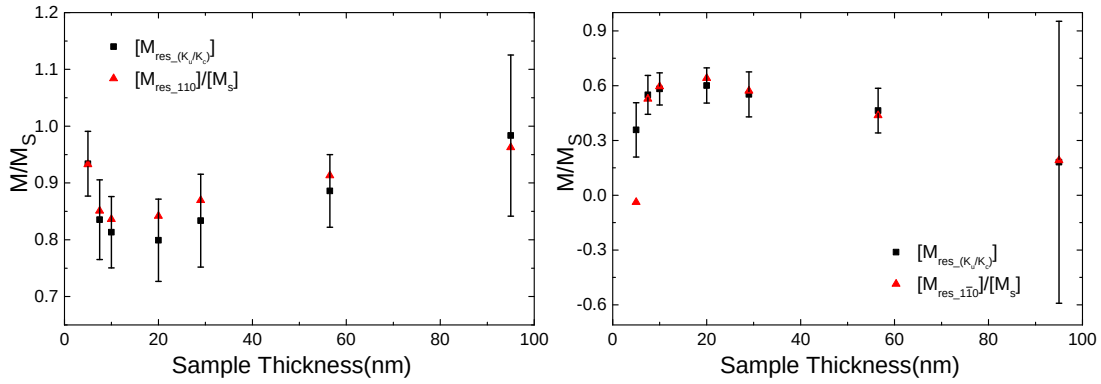

(a) [110] (b) [1$\bar{1}$0]

Figure 5.15: Shows the variation of the remanence magnetisation ratio as a function of sample thickness. The graph shows the comparison between the remanence ratio obtained from the MH loops collected during the SQUID experiment and the remanence ratio extracted using the anisotropies values obtained from the fitting process discussed earlier (a) shows the remanence ratio along [110] and (b) shows the remanence ratio along [1$\bar{1}$0].

5.3 Summary

This chapter investigated the static magnetic properties of $Fe_{100-x}Ga_x$ thin films with a nominal thickness of 26.20 nm and x ranging between 7 to 30 as well as the static properties of $Fe_{79}Ga_{21}$ thin films with thickness ranging between 5 nm to 95 nm. The films were grown on GaAs(001) substrate by magnetron sputter deposition. The static properties were characterised using the SQUID magnetometry technique. The work presented in this chapter highlights the anisotropies associated with Galfenol samples grown on GaAs substrates. The films exhibited a cubic anisotropy along [010]/[100] direction and a uniaxial anisotropy along [110] direction which was evident from the shape of the MH loops along different directions.

For the samples with varying Ga composition, the anisotropic nature tends to disappear above 18 % Ga concentration. There was no clear distinction between the MH loops obtained by SQUID magnetometry when the magnetic field was applied along the different crystalline direction, therefore becoming completely isotropic. The saturation magnetisation obtained from the SQUID MH loops

seems to be in close agreement with the calculated values obtained using the thin film thickness. The MH loops obtained from the SQUID magnetometry are consistent with those generated using the model program; hence the values for the anisotropy constants can be assumed to be reliable. The cubic anisotropy constant tends to decrease with the increase in the Ga concentration. Whereas, the uniaxial anisotropy increases initially but eventually saturating with the increase in the Ga concentration.

For samples with varying film thickness, the cubic and uniaxial anisotropy constants of these films demonstrated a similar relation to thickness as was reported for studies of Fe films grown on GaAs substrate. The cubic anisotropy constant increases with the increase in the film thickness and the uniaxial anisotropy constant decreases with the increase the film thickness but increases for film thicknesses greater than 20 nm.

The parameters extracted and investigated in this chapter will be used to compare with the static magnetic properties that will be extracted from the ferromagnetic resonance experiment in chapter 7.

Chapter 6

Electrical properties investigated using magneto-transport measurements

In this chapter, the magneto-transport measurements on union jack devices fabricated from Galfenol thin films have been described. The effects of altering the Ga concentration on different contributions towards the anisotropic magnetoresistance (AMR) of $Fe_{100-x}Ga_x$ thin films have been studied and discussed. Similarly, the effects of changing the film thickness on the AMR of $Fe_{79}Ga_{21}$ thin films have been considered as well.

6.1 Magneto-transport measurements of $Fe_{100-x}Ga_x$ thin films with varying Ga concentration

Magneto-transport measurements were performed at room temperature on $Fe_{100-x}Ga_x$ thin films grown on GaAs(001) substrates with x ranging between 7 to 30, using the helium-cooled cryostat system in the Spintronics group at University of Nottingham. The union jack devices were fabricated on the sputtered grown thin films using the method described in section 3.1.2, and the magneto-transport measurements were performed using the technique described in section 3.2.6. Magneto-

transport measures the magnetoresistive response of conducting ferromagnetic thin films placed in an external magnetic field. One of such responses is AMR. Phenomenologically AMR has contributions from crystalline and non-crystalline components [188]. The crystalline component arises from the underlying crystallographic structure of the thin film, hence yielding a trend for the behaviour of the uniaxial and cubic magnetocrystalline anisotropies as the Ga composition is altered. In this section, I have described and analysed both the crystalline and non-crystalline contributions towards the AMR from the magneto-transport measurements carried out on thin films with varying Ga concentration.

The magneto-transport measurements for measuring the AMR were done by aligning the union jack device mounted on a non-magnetic header in a saturating magnetic field of 0.3 T such that the magnetic field was in the plane of the sample. The longitudinal and transverse voltages were collected as a function of the angle of the saturating magnetic field. Figure 6.1 (a) to (d) shows an example of longitudinal AMR as a function of angle between the sample and the magnetic field with respect to the [110] crystal direction for sample S534 obtained when a constant dc current of 1 mA passed along different crystalline directions. The AMR is calculated by dividing the voltages recorded from the magneto-transport measurements with the constant dc current being supplied. The measurements were recorded in 5° intervals as the relative orientation between the magnetic field and the sample is being changed. The data points represented in figure 6.1 (a) to (d) have been normalised. This involved finding the average value of ρ_{xx}, subtracting it from each data point and then dividing each data point with the average ρ_{xx} value.

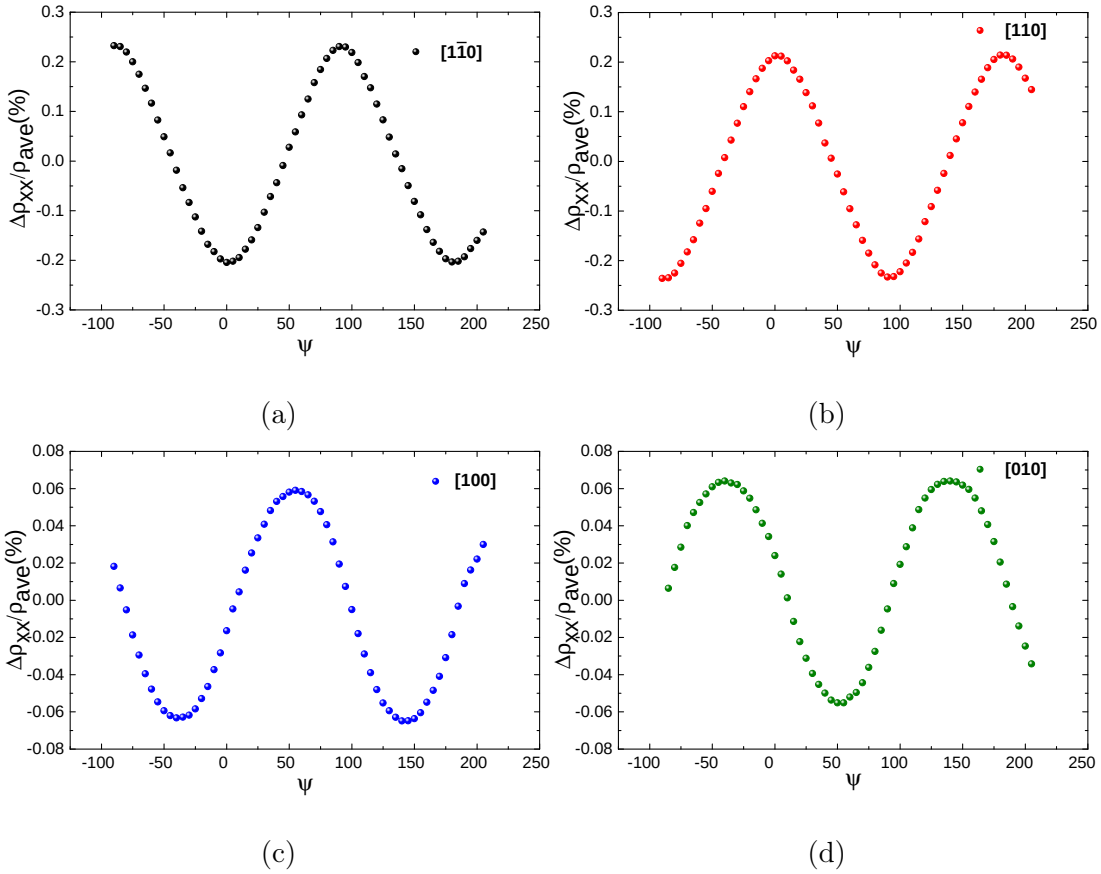

Figure 6.1: Longitudinal AMR for sample S534 along the crystalline direction (a) [1$\bar{1}$0] (b) [110] (c) [100] and (d) [010]. A constant dc current of 1 mA is passed along different crystal direction. ψ is the angle between the magnetisation and uniaxial easy axis [110].

As discussed earlier in section 2.5.3, for ferromagnetic materials which have an ordered crystalline structure, the AMR is largely a function of the angle between the crystalline axes and the magnetisation. Hence, the AMR obtained for the samples discussed in this thesis comprises of two parts, the crystalline AMR due to the crystallographic structure of the material and the non-crystalline AMR due to the lowering of symmetry due to the current along certain specific direction. In order to extract each crystalline and non-crystalline contributions individually accounting for the various allowed symmetries of the observed AMR a more detailed approach is required which was adapted from reference [188]. In the impressive work of reference [188], four different contributions C_C, C_U, C_I, $C_{I,C}$ to AMR in (Ga,Mn)As were individually identified. Each component has a unique symmetry that depends on the magnetisation orientation with respect to

the current direction and the crystalline axes. The form of AMR in an anisotropic single-crystal ferromagnetic sample is given as,

$$\begin{aligned}\frac{\Delta\rho_{xx}}{\rho_{ave}} &= C_I\cos 2\Phi + C_U\cos 2\psi + C_C\cos 4\psi + C_{I,C}\cos\left(4\psi - 2\Phi\right)\\ \frac{\Delta\rho_{xy}}{\rho_{ave}} &= C_I\sin 2\Phi + C_{I,C}\sin\left(4\psi - 2\Phi\right)\end{aligned} \tag{6.1}$$

where $\Delta\rho_{xx} = \rho_{xx} - \rho_{ave}$, ρ_{ave} is the average value of the resistivity ρ_{xx} for the magnetisation rotated 360° in the plane of the sample, C_I is the non-crystalline coefficient, C_U is the uniaxial crystalline coefficient, C_C is the cubic crystalline coefficient, $C_{I,C}$ is the crossed non-crystalline and cubic crystalline coefficient, Φ is the angle between the current and the magnetisation in the plane of the sample, and ψ is the angle between the magnetisation and uniaxial easy axis [110].

In order to extract the different AMR coefficients mentioned in equation 6.1, we consider the magnetisation rotation magneto-transport experiment discussed in section 3.2.6. A constant dc current is supplied along a specific crystal direction, thus defining Φ. An in-plane saturated rotating magnetic field is provided. The magnetic field is rotated in steps of 5° and the respective longitudinal and transverse resistances were measured.

For current along crystalline axis [110], $\Phi = \psi$;

$$\begin{aligned}AMR_{xx,[110]} &= \frac{\Delta\rho_{xx}}{\rho_{ave}}\\ &= C_I\cos 2\psi + C_U\cos 2\psi + C_C\cos 4\psi + C_{I,C}\cos 2\psi\\ AMR_{xy,[110]} &= \frac{\Delta\rho_{xy}}{\rho_{ave}}\\ &= C_I\sin 2\psi - C_{I,C}\sin 2\psi\end{aligned} \tag{6.2}$$

For current along crystalline axis [1$\bar{1}$0], $\Phi = \psi + \frac{\pi}{2}$;

$$\begin{aligned}AMR_{xx,[1\bar{1}0]} &= \frac{\Delta\rho_{xx}}{\rho_{ave}}\\ &= -C_I\cos 2\psi + C_U\cos 2\psi + C_C\cos 4\psi - C_{I,C}\cos 2\psi\\ AMR_{xy,[1\bar{1}0]} &= \frac{\Delta\rho_{xy}}{\rho_{ave}}\\ &= -C_I\sin 2\psi + C_{I,C}\sin 2\psi\end{aligned} \tag{6.3}$$

For current along crystalline axis [100], $\Phi = \psi + \frac{\pi}{4}$;

$$\begin{aligned} AMR_{xx,[100]} &= \frac{\Delta\rho_{xx}}{\rho_{ave}} \\ &= -C_I \sin 2\psi + C_U \cos 2\psi + C_C \cos 4\psi + C_{I,C} \sin 2\psi \\ AMR_{xy,[100]} &= \frac{\Delta\rho_{xy}}{\rho_{ave}} \\ &= C_I \cos 2\psi + C_{I,C} \cos 2\psi \end{aligned} \tag{6.4}$$

For current along crystalline axis [010], $\Phi = \psi - \frac{\pi}{4}$;

$$\begin{aligned} AMR_{xx,[010]} &= \frac{\Delta\rho_{xx}}{\rho_{ave}} \\ &= C_I \sin 2\psi + C_U \cos 2\psi + C_C \cos 4\psi - C_{I,C} \sin 2\psi \\ AMR_{xy,[010]} &= \frac{\Delta\rho_{xy}}{\rho_{ave}} \\ &= -C_I \cos 2\psi - C_{I,C} \cos 2\psi \end{aligned} \tag{6.5}$$

Combining the above four longitudinal AMR equations along various crystallographic directions cancels out certain coefficients from each equation due to symmetry, such as:

$$\begin{aligned} \frac{AMR_{xx,[110]} + AMR_{xx,[1\bar{1}0]}}{2} &= C_U \cos 2\psi + C_C \cos 4\psi \\ \frac{AMR_{xx,[100]} + AMR_{xx,[010]}}{2} &= C_U \cos 2\psi + C_C \cos 4\psi \\ \frac{AMR_{xx,[110]} - AMR_{xx,[1\bar{1}0]}}{2} &= C_I \cos 2\psi + C_{I,C} \cos 2\psi \\ \frac{AMR_{xx,[100]} - AMR_{xx,[010]}}{2} &= -C_I \sin 2\psi + C_{I,C} \sin 2\psi \end{aligned} \tag{6.6}$$

Figure 6.2 (a) shows the overlap of AMR graph along [110] direction to the graph along $[1\bar{1}0]$ direction such that the non-crystalline terms drop out by symmetry and just the crystalline components are left for fitting. The red points represent the AMR along [110] direction, and the black points represent the AMR along $[1\bar{1}0]$ direction. Similarly, in figure 6.2 (b) shows how the AMR along [100] and [010] cancels out to give the crystalline components. The blue points represent the graph along [100] direction, and the dark green points represent the graph along [010] direction. The measured AMR ratios also show a difference more than one order of magnitude for different current directions. In single crystalline ferromagnetic systems, the AMR is related to both the direction of the

magnetisation and the orientation of the current with respect to the crystal axes [211–214]. As a result, the AMR in single crystalline films deviates from the regular $\cos 2\Phi$ dependence, particularly an additional four-fold symmetry could be observed as a result of the spin-orbit coupling, which reflects the effect of the crystalline axes. By combining and fitting the experimentally obtained longitudinal AMR data with equations 6.6 yields the respective AMR coefficients.

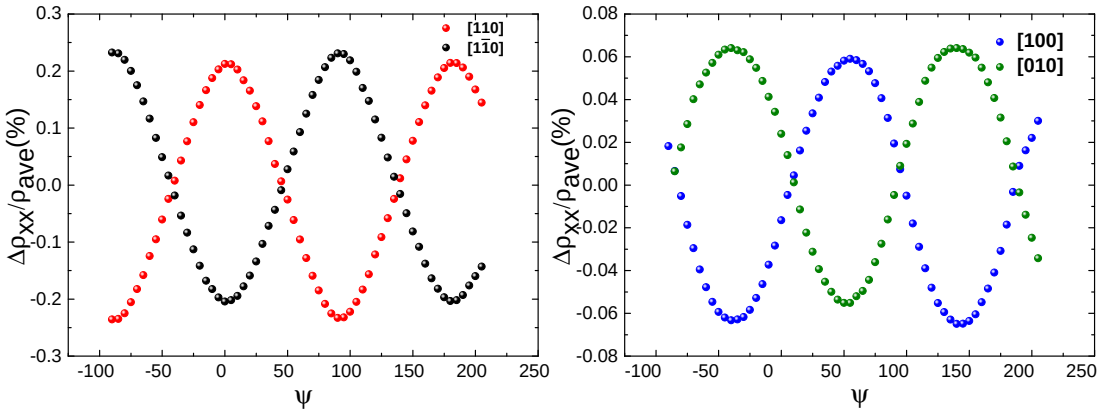

(a) (b)

Figure 6.2: Shows the overlap the longitudinal AMR graphs along the crystalline direction such that the non-crystalline terms drop out of symmetry. (a) Overlap of longitudinal AMR for sample S534 along [1$\bar{1}$0] and [110] crystallographic direction (b) overlap of longitudinal AMR along [100] and [010] crystal direction.

Figure 6.3 shows an example of fitting of the combined experimental data with equation 6.6 for sample S534. The legend on the graphs represent the crystal directions which were considered to determine experimental data points for fitting. As presented earlier the data points along different crystal direction were added or subtracted to satisfy equation 6.6. The black solid points represent the experimental data, and the red line represents the fitting. Figure 6.3 (a) and (c) are dependent on both $cos2\psi$ and $\cos 4\psi$ therefore, the fitting to these curves had two independent parameters. Figure 6.3 (b) and (d) is dependent only on $cos2\psi$ therefore, the fitting to these curves had only one independent parameter which gives a combination of two linear equation for C_I and $C_{I,C}$ coefficients. C_I and $C_{I,C}$ were was then extracted by solving these equations.

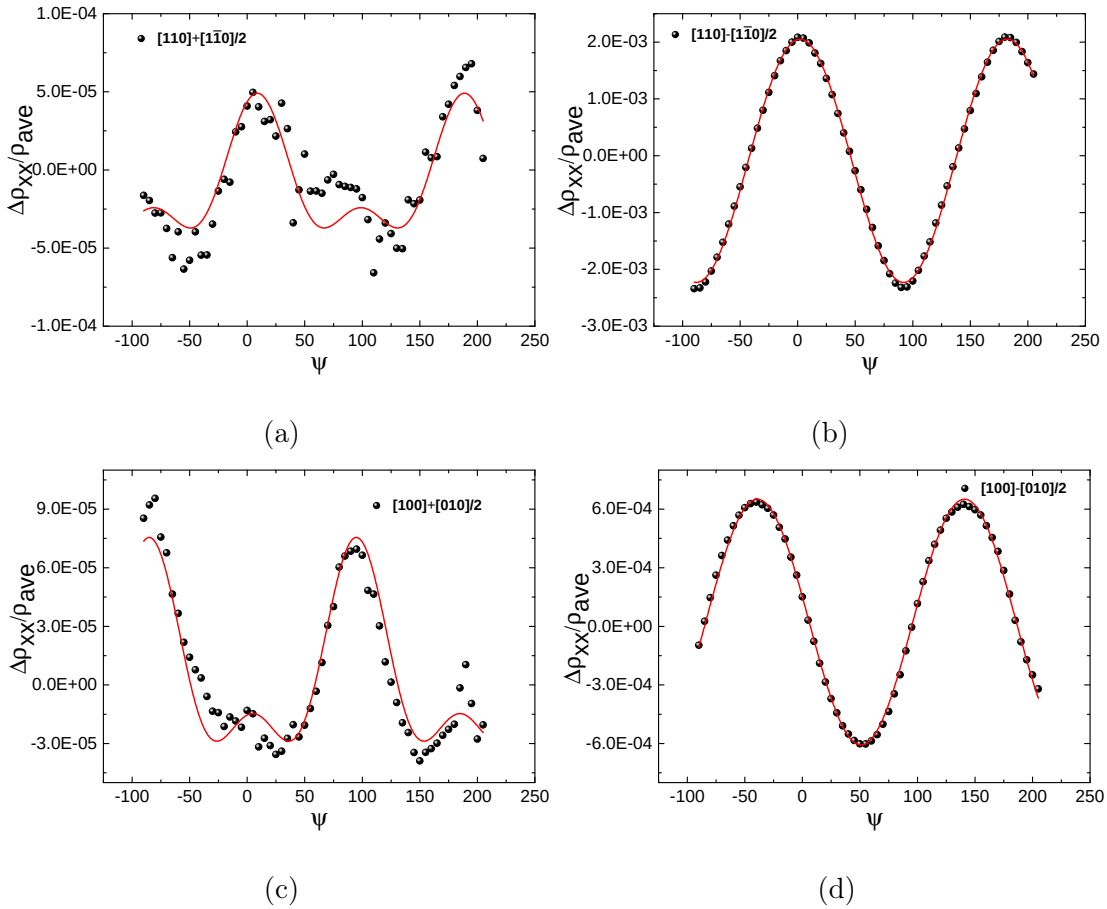

Figure 6.3: Shows the fitting to the longitudinal AMR data of sample S534 using the method described in the above section. (a) and (c) depends on $\cos 2\psi$ and $\cos 4\psi$ and gives the crystalline components C_C and C_U. (b) and (d) depends on $\cos 2\psi$ and gives the non-crystalline components C_I and $C_{I,C}$.

The origin of the dependence of electric resistance of magnetic metals on the direction of magnetisation is often associated with the interplay between the spin-orbit interaction and the magnetisation. The AMR of a crystalline material has various contributions which are each associated with different symmetries. The crystalline terms associated with the AMR are due to the band warping effects which reflect the underlying crystal symmetry [188, 215]. Hence, the trend observed for crystalline anisotropies for samples with varying Ga concentration can be compared with the pattern for the crystalline coefficients obtained from magneto-transport measurements. Figure 6.4 (a) and (b) shows the cubic crystalline coefficient (C_C) obtained from the magneto-transport measurements and the cubic anisotropy constant obtained from the SQUID magnetometry measurements up to Ga concentration of 18%, respectively. Above 18% Ga, the magnetocrystalline anisotropy coefficients were zero within experimental uncertainty. The inset in figure 6.4 shows the cubic crystalline coefficients for all the samples discussed in table 3.1. By comparing both the graphs, it can be observed that the cubic magnetocrystalline coefficients and magnetocrystalline anisotropy constants follow a similar pattern. The cubic magnetocrystalline coefficient decreases as the Ga concentration is increased as expected. From the XRD measurements in section 4.2.1 we observe that the crystal quality reduces with the increase in the Ga concentration, comparing the data with the cubic crystalline coefficient it can be concluded that the cubic magnetocrystalline AMR coefficient reduces with the reduction in the crystal quality.

Similarly, figure 6.5 (a) and (b) shows the uniaxial crystalline coefficient (C_U) obtained from the magneto-transport measurements and the uniaxial anisotropy constant obtained from the SQUID magnetometry measurements, respectively. The inset in figure 6.5 shows the uniaxial crystalline coefficients for all the samples discussed in table 3.1 excluding sample S535. The uniaxial crystalline coefficient replicates the pattern followed by the uniaxial anisotropy constant with change in Ga concentration. As the Ga concentration is increased in Galfenol thin films, the uniaxial crystalline coefficient increases and then saturates.

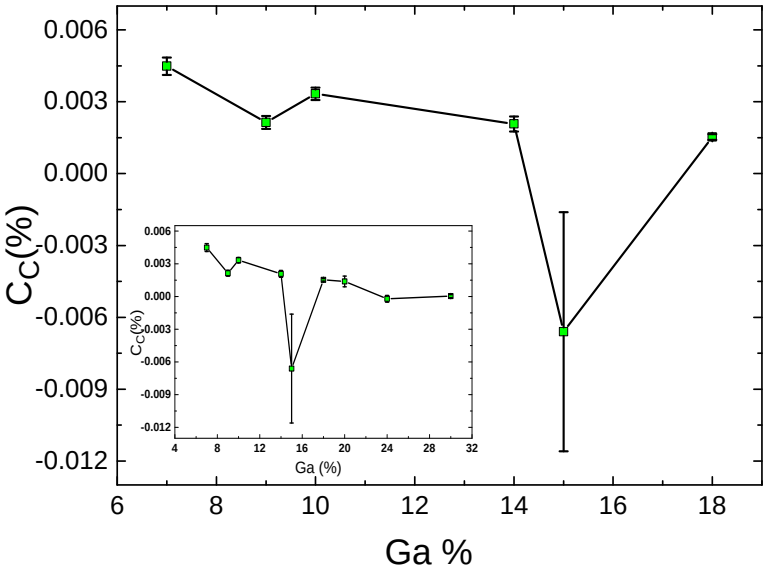

(a)

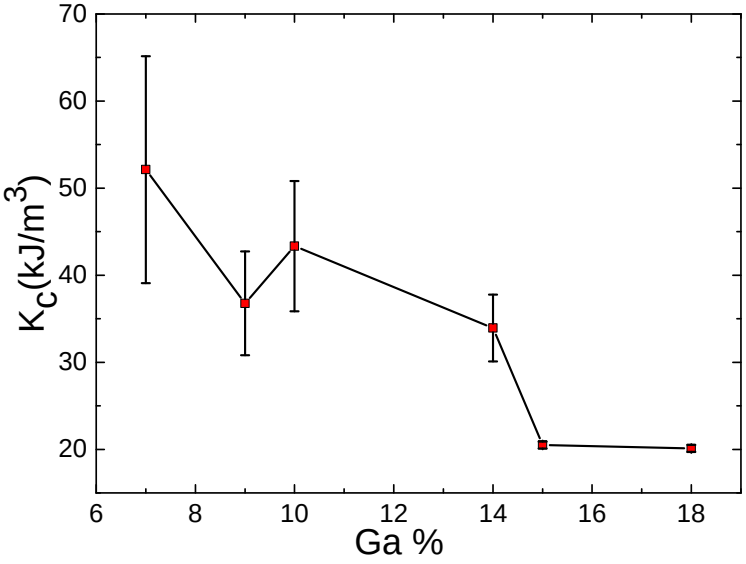

(b)

Figure 6.4: Shows comparison of the (a) cubic magnetocrystalline coefficient (C_C) obtained by fitting to the longitudinal AMR and (b) the cubic crystalline anisotropy constants (K_C) for samples with varying Ga concentration. The inset in (a) shows the cubic crystalline coefficient for all samples discussed in table 3.1 except sample S535.

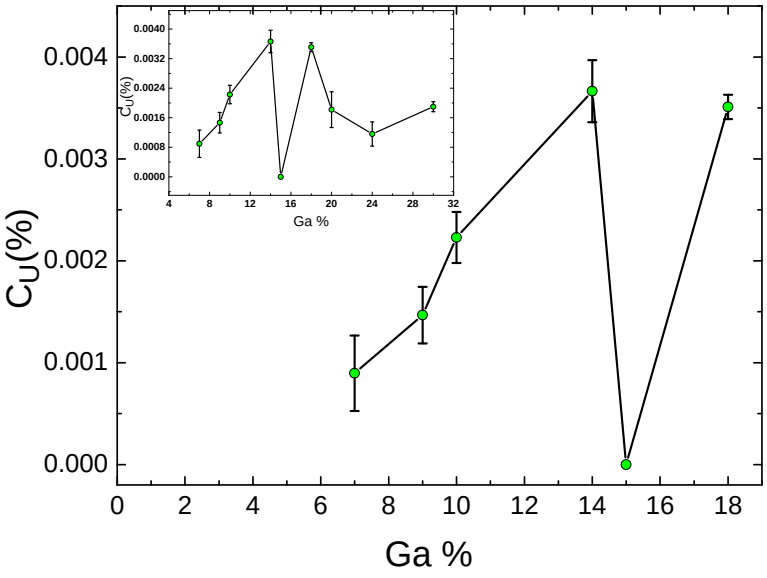

(a)

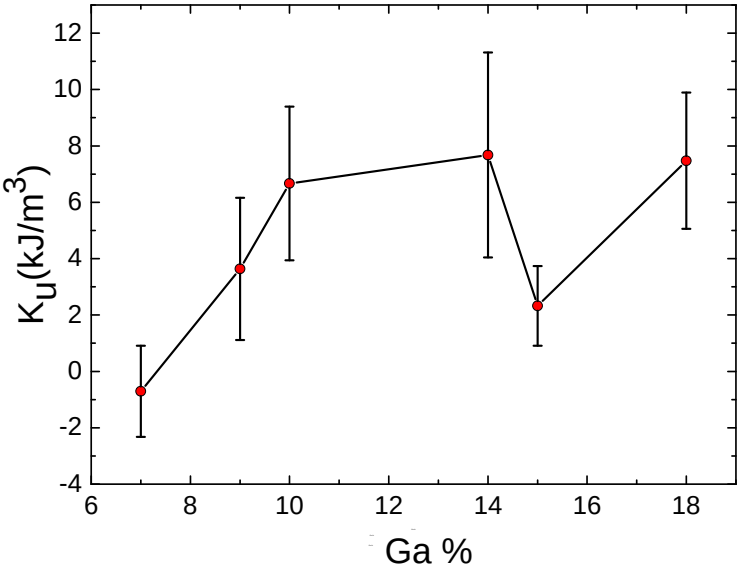

(b)

Figure 6.5: Shows comparison of the (a) uniaxial crystalline coefficient (C_U) obtained by fitting to the longitudinal AMR and (b) the uniaxial crystalline anisotropy constants (K_U) for samples with varying Ga concentration. The inset in (a) shows the uniaxial crystalline coefficient for all samples discussed in table 3.1 except sample S535.

Non-crystalline AMR is governed only by the angle between the magnetisation and the current contradictory to the crystalline AMR which is governed by the orientation with respect to the crystallographic axes. Non-crystalline component of the AMR arises from the breaking of the symmetry by choosing a specific current direction and spin-orbit interaction. In reference, [216], the underline physical mechanism of the non-crystalline AMR was presented. Non-crystalline AMR is ruled by a mechanism in which anisotropic Fermi velocities occur because of the distortion of Fermi surfaces from the spherical shape therefore, indicating an anisotropic scattering rate. This can happen either due to anisotropic wave function or anisotropic scatterers. The magnetisation thus induces a magneto-transport anisotropy via the spin-orbit interaction present at the group velocities of the exchange-split Fermi surfaces. Figure 6.6 (a) and (b) shows the non-crystalline coefficient (C_I) and the coefficient due to the crossing between the crystalline and non-crystalline contribution ($C_{I,C}$) towards AMR respectively. The inset in both the graphs presents the values of the coefficients for all the samples discussed in table 3.1 excluding sample S535. This was done to have consistency in the representation of the data. As can be seen from the graph 6.6 (a), as the Ga concentration increases the non-crystalline coefficient (C_I) increases as well. Figure 6.6 (b) represents the cross term ($C_{I,C}$), it decreases with the increase in Ga concentration. There is a significant contribution from the crossed cubic crystalline/non-crystalline term towards the AMR. These effects are due to the interplay of the crystalline and non-crystalline components. The errors on these measurements are reasonably small indicating that the measurements are reliable. In section 4.2.1, it has been already established that crystal quality reduces over the addition of Ga impurities. In contrary to the observation of the C_C, the C_I increases with the increase in the Ga concentration, establishing the fact the resistance increases with increase in the impurities.

For the isotropic samples, C_U is a non-zero value, however smaller than those compared with the C_U value for the anisotropic samples. Since uniaxial crystalline coefficient (C_U) gets its contribution from the uniaxial anisotropy, which is an interface phenomenon, therefore, its impact reduces for isotropic samples but never entirely drops down to zero. Cubic crystalline coefficient (C_C) however

drops down to zero within experimental error for isotropic samples because of the loss in crystallinity due to the increase in Ga concentration. This could be reconfirmed from the XRD measurements in section 4.2.1 where the crystallinity of the samples decreased with the increase in Ga concentration, and the isotropic samples did not show any sample peak. C_I gives a non-zero value and $C_{I,C}$ drops down to zero within experimental error respectively for the isotropic samples.

From figure 6.6, the longitudinal AMR is dominated by the non-crystalline $\cos 2\phi$ and $\sin 2\phi$ part, being of the order of magnitude higher than the crystalline contribution of $\cos 4\phi$ from cubic anisotropy. C_I and $C_{I,C}$ are of a similar magnitude.

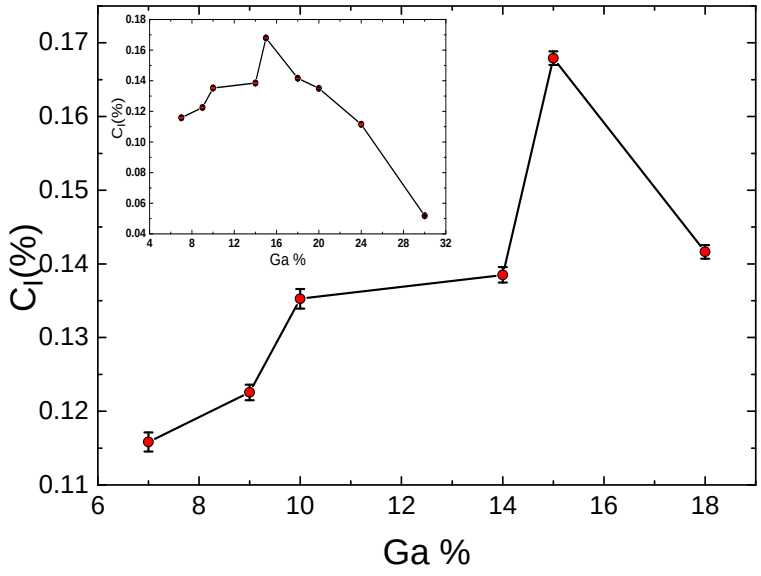

(a)

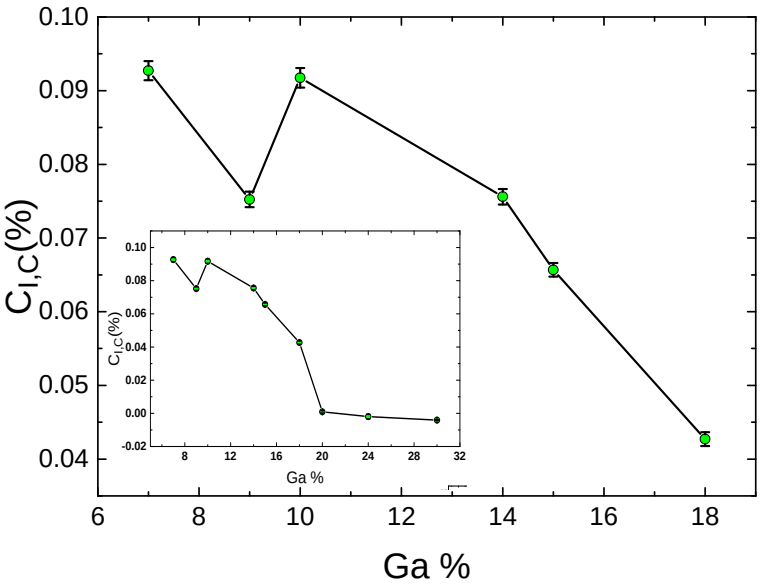

(b)

Figure 6.6: Shows the non-crystalline coefficients (a) C_I and the cross-term (b) $C_{I,C}$. The inset shows the non-crystalline coefficients for all samples discussed in table 3.1 except sample S535.

6.2 Magneto-transport measurements of $Fe_{79}Ga_{21}$ thin films with varying film thickness

Magneto-transport measurements were performed at room temperature on $Fe_{79}Ga_{21}$ thin films with increasing film thickness varying between 5 nm to 95 nm grown on GaAs(001) substrates. The extracted crystalline AMR coefficients for the samples were then compared with the pattern followed by the anisotropy constants extracted from the SQUID magnetometry measurement.

Figure 6.7 shows an example of fitting of the combined experimental data with equation 6.6 for sample S643 (7.5 nm). The black solid points represent the experimental data, and the red line represents the fitting. Graphs 6.7 (b) and (d) gives a combination of two linear equation for C_I and $C_{I,C}$ coefficients, which was then extracted by solving the equations.

Figure 6.8 (a) and (b) shows the cubic magnetocrystalline coefficient (C_C) obtained from the magneto-transport measurements and the cubic anisotropy constant obtained from the SQUID magnetometry measurements, respectively. By analysing both the graphs, it was observed that both the graphs have a resembling pattern. The cubic crystalline AMR coefficient increases eventually saturating with the increase in the film thickness. In section 4.2.2, the XRD measurements revealed that the clarity of sample peak increases with an increase in the film thickness, indicating an increase in the crystal quality. This is then reflected in the crystalline AMR coefficients observed for the films. Crystalline AMR increases with an increase in crystal quality.

Likewise, the analysis for uniaxial crystalline AMR coefficient (C_U) is shown in figure 6.9 (a) and figure 6.9 (b)shows the uniaxial anisotropy constant obtained from the SQUID magnetometry measurements for the purpose of comparison. The uniaxial crystalline AMR coefficient replicates the pattern followed by the uniaxial anisotropy constant with change in film thickness. As the film thickness is increased in Galfenol thin films, the uniaxial crystalline AMR coefficient decreases first, but as the film continues to increase to 30 nm and above the uniaxial crystalline coefficient starts increasing again.

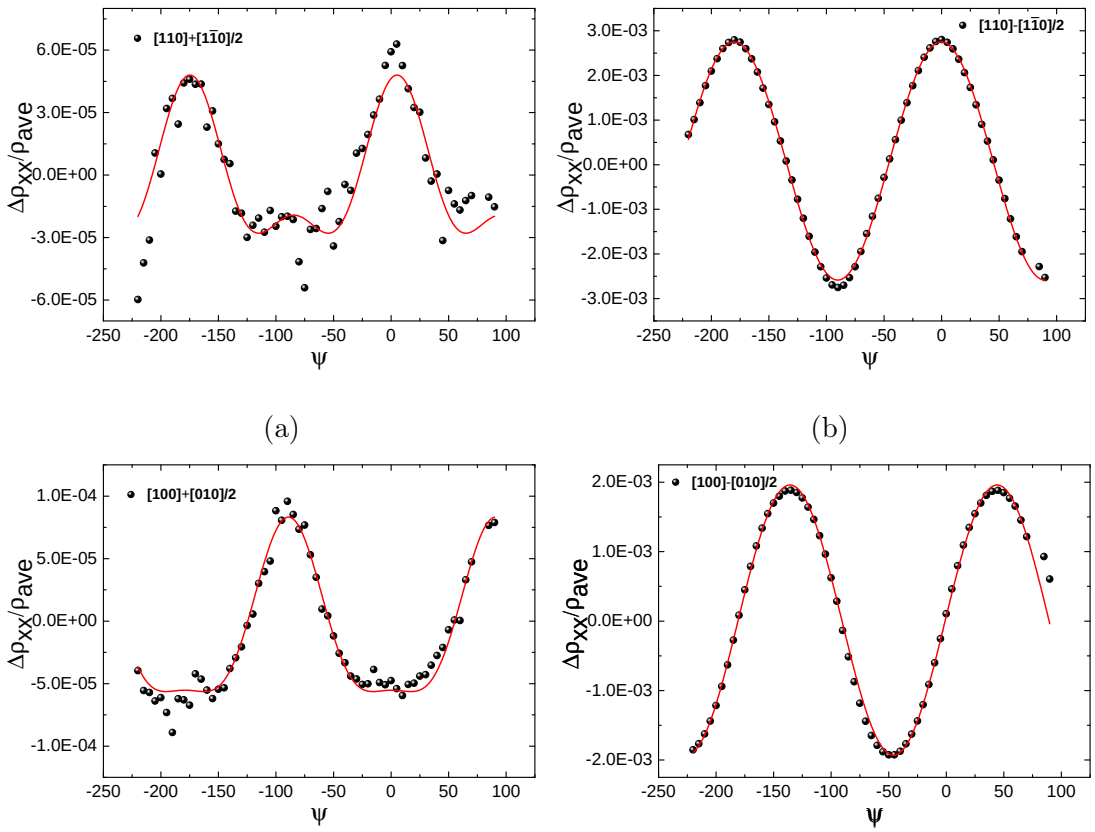

(a) (b)

(c) (d)

Figure 6.7: Shows the fitting to the longitudinal AMR data of sample S643 (7.5 nm) using the method described in the above section. (a) and (c) depends on $\cos 2\psi$ and $\cos 4\psi$ and gives the crystalline components C_C and C_U. (b) and (d) depends on $\cos 2\psi$ and gives the non-crystalline components C_I and $C_{I,C}$.

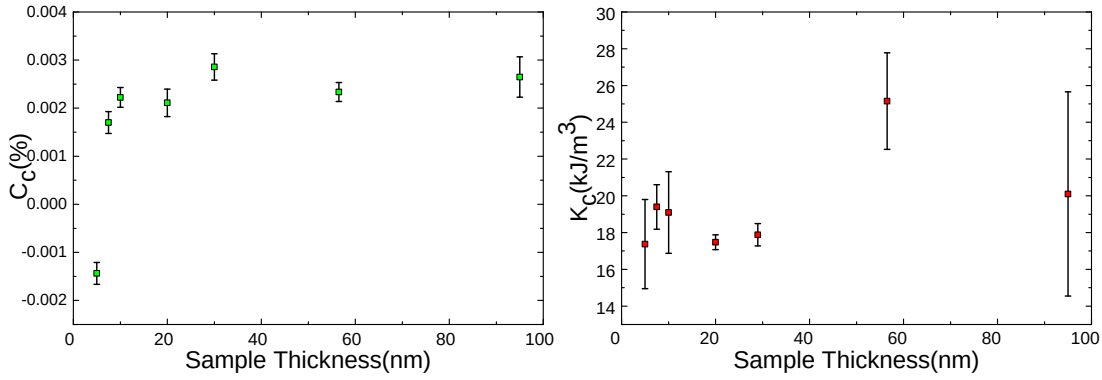

(a) (b)

Figure 6.8: Shows comparison of the (a) cubic magnetocrystalline coefficient (C_C) obtained by fitting to the longitudinal AMR and (b) the cubic crystalline anisotropy constants (K_C) for samples with varying film thickness.

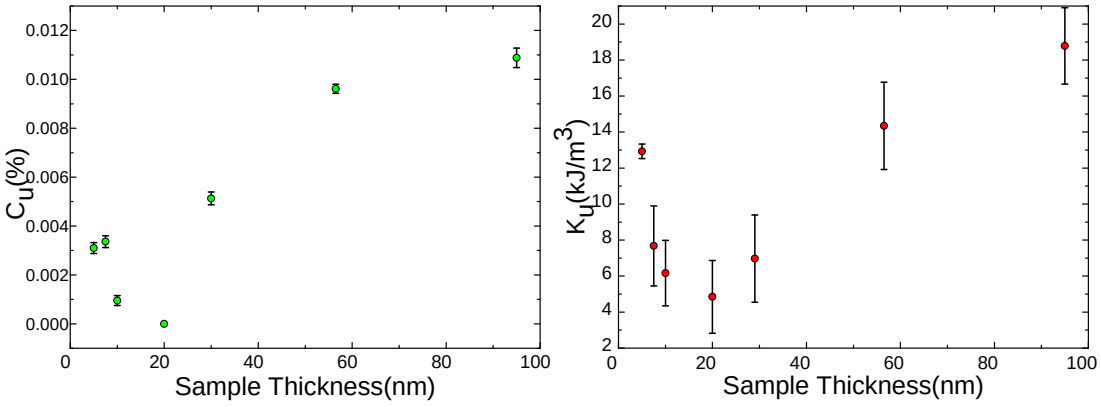

(a) (b)

Figure 6.9: Shows comparison of the (a) uniaxial crystalline AMR coefficient (C_U) obtained by fitting to the longitudinal AMR and (b) the uniaxial crystalline anisotropy constants (K_U) for samples with varying film thickness.

Figure 6.10 (a) and (b) shows the non-crystalline coefficient (C_I) and the coefficient due to the crossing between the crystalline and non-crystalline contribution ($C_{I,C}$) towards AMR respectively. As seen in the graph 6.10 (a), as the film thickness increases the non-crystalline coefficient increases as well but starts dropping as the film thickness gets to 56.5 nm and above. It is not possible to accurately identify the film thickness from which the coefficient starts decreasing due to lack of data between the film thickness of 30 nm and 56.5 nm. It was expected that thicker films will have higher non-crystalline AMR coefficient, which was the case for 30 nm thick sample, however it started decreasing after that, to establish a concrete answer more films with thickness in between 30 nm and 95 nm is required. Figure 6.10 (b) represents the cross term ($C_{I,C}$), it decreases with the increase in the film thickness with the exception for sample S645 with the film thickness of 95 nm.

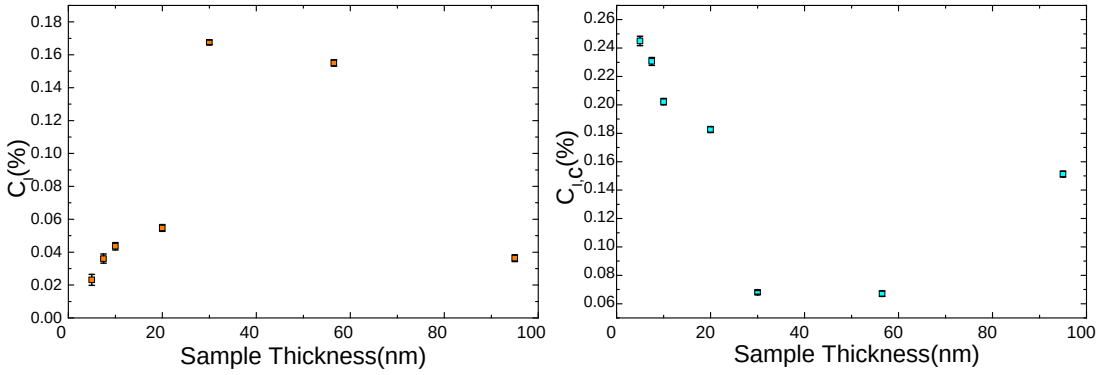

(a) (b)

Figure 6.10: Shows the non-crystalline coefficients (a) C_I and the cross-term (b) $C_{I,C}$ for samples with varying film thickness.

For Fe/GaAs(001) thin films in reference [211] have concluded that the AMR depends on the crystallographic direction of the current flow from there observations. The longitudinal resistivity (ρ_{xx}) for Fe/GaAs(110) thin films showed the largest difference between 0° and 90° which clearly agrees with what we have observed [212]. A systematic AMR study of five Fe/GaAs(110) films with thickness varying between 9 nm to 20 nm was done to extract the anisotropy constants using a first-order magnetisation-reorientation phase transition [217]. The increasing trend observed with the increase in film thickness for the cubic anisotropy constant agrees within reasonable boundaries of error with the trend observed for the samples discussed in this section. However, the uniaxial anisotropy constant increases with the increase in the film thickness in reference [217] disagreeing with the trend observed for the samples discussed in this section. The uniaxial crystalline coefficient decreases with the increase in the film thickness up to 20 nm and then starts increasing, since uniaxial anisotropy is an interface phenomenon a conclusive answer was difficult to draw.

6.3 Summary

This chapter presented measurements, analysis, and discussion of AMR in sputtered Galfenol thin films on GaAs(001) substrates, with varying Ga concentration as well as varying film thickness. Previous studies have shown that ferromagnetic materials not only have a non-crystalline AMR contribution that varies with the

angle between the magnetisation and current direction but also have crystalline AMR contributions that vary with the angle between magnetisation and crystalline axes that can be of considerable size. The motivation behind the study in this chapter was to understand the origins of the different AMR contributions and observe how they change with Ga concentration and film thickness as well as compare the trend with that concluded from SQUID magnetometry measurements.

The non-crystalline part comes from the lowering of the symmetry by imposing a current direction. The crystalline contributions have two parts one due to the cubic anisotropy along [100] and [010] directions and a uniaxial anisotropy along [110] direction. Union jacks were fabricated on the thin films such that current can be passed along the [100], [010], [110] and $[1\bar{1}0]$ crystallographic axes and the different AMR coefficients were extracted through magneto-transport measurements.

For both set of samples the non-crystalline component dominates the AMR. The cubic and uniaxial AMR coefficients for both the groups of samples tend to follow a similar trend as observed for the cubic and uniaxial anisotropies obtained from the SQUID magnetometry measurements within reasonable boundaries. The striking similarity is because the crystalline AMR contribution is due to the underlying crystal symmetry.

Chapter 7

Dynamic properties of $Fe_{100-x}Ga_x$ thin films with varying Ga concentration investigated by ferromagnetic resonance

In this chapter, the ferromagnetic resonance (FMR) measurements and the analysis conducted to obtain the magnetic parameters as a consequence of altering the Ga concentration in the samples is discussed. The FMR experiments were performed by Ms L. Clark under the supervision of Dr S. Cavill at the University of York, UK.

7.1 Magnetic anisotropy constants

The FMR experiments were performed using the vector network analyser based FMR set-up to investigate the magnetic static and dynamic properties of the samples with varying Ga concentration, as discussed in the previous sections. The magnetic field was applied between 0 T to 0.3 T at microwave frequencies ranging from 0 GHz to 20 GHz along different in-plane direction as the magnetic field is being rotated in steps of 5° with respect to the transmission axis parallel to the [110] crystallographic direction.

Sweeping the frequency across, the resonance frequency in a fixed magnetic

field gives rise to a characteristic Lorentzian absorption peak, as observed in figure 7.1. A coplanar waveplate (CPW) will have some losses as a function of the frequency, therefore the baseline of these measurements are usually not flat. This is then compensated by forcing the resonance to high frequencies beyond the VNA measurement range and recording the background or reference signal and subtracting it from the experimental data to flatten the baseline.

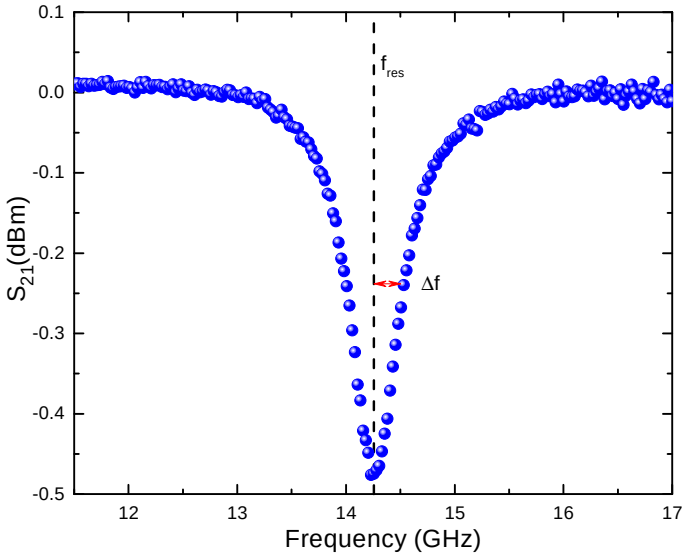

Figure 7.1: Shows a typical VNA-FMR linescan of S_{21} as a function of the applied frequency at a fixed magnetic field of 0.15 T for sample S536 along [110] direction with the baseline already been removed. The resonance frequency, f_{res} is given by the trough centre and the frequency linewidth, Δf given by the half-width at half maximum of the trough.

In order to extract the anisotropy constants, the resonance frequency at different azimuthal angles when a constant in-plane external field was applied were extracted for each sample from the S_{21} spectra (eq. 3.6). This was achieved by extracting line scans from the 2D array at a fixed field, then plotting the intensity data as a function of frequency and fitting the resulting absorption dip using an asymmetric Lorentzian function, given by equation 7.1. An asymmetric Lorentzian fit is appropriate since in a practical system, asymmetry can arise as a result of the coupling between the sample and the waveguide giving rise to the

mixing between the real and the imaginary susceptibility components [218, 219].

$$\chi^{'} \sin\alpha_i + \chi^{''} \cos\alpha_i = A\frac{\Delta f \cos\alpha_i + (f - f_{res})\sin\alpha_i}{\Delta f^2 + (f - f_{res})^2} + B \tag{7.1}$$

where $\chi^{'}$ and $\chi^{''}$ are the real and imaginary components of the AC susceptibility respectively, α_i is the mixing angle between the absorptive and dispersive components of the FMR signal, A and B are constants, Δf is the frequency linewidth given by the half-width at half maximum (HWHM) of the absorption lineshape, f is the applied frequency in GHz, and f_{res} is the resonance frequency in GHz.

By fitting the lineshape using the equation 7.1, resonance frequency(f_r) and linewidth can be extracted at a particular applied magnetic field. The magnetic parameters discussed in this thesis were extracted at the saturating applied magnetic field of 0.15 T, to ensure that all the magnetic moments are saturated along the direction of the applied magnetic field and all of them were resonating. From the asymmetric Lorentzian fit, as shown in figure 7.1, the resonance frequency is the trough, and the frequency linewidth is given by the half-width at half maximum of the trough. Example fitting of the lineshape using equation 7.1 is shown in figure 7.2. It shows FMR spectra along four different crystallographic directions [010], [100], [110], and [1$\bar{1}$0] at a fixed external magnetic field of 0.15 T for sample S536. The blue solid circle is the experimental data obtained from the FMR experiment, and the red coloured solid line is the asymmetric Lorentzian fit. During the FMR experiment, the [110] crystal direction of the sample was held parallel to the transmission axis for the first measurement and the sample was then rotated away from the transmission axis in steps of 5° to ± 90° to cover all possible crystallographic directions. Therefore as seen in figure 7.2, the FMR spectra along [110] direction have better signal to noise ratio in comparison to the other crystal directions. This ambiguity was introduced by the experimental set-up and cannot be improved by external factors.

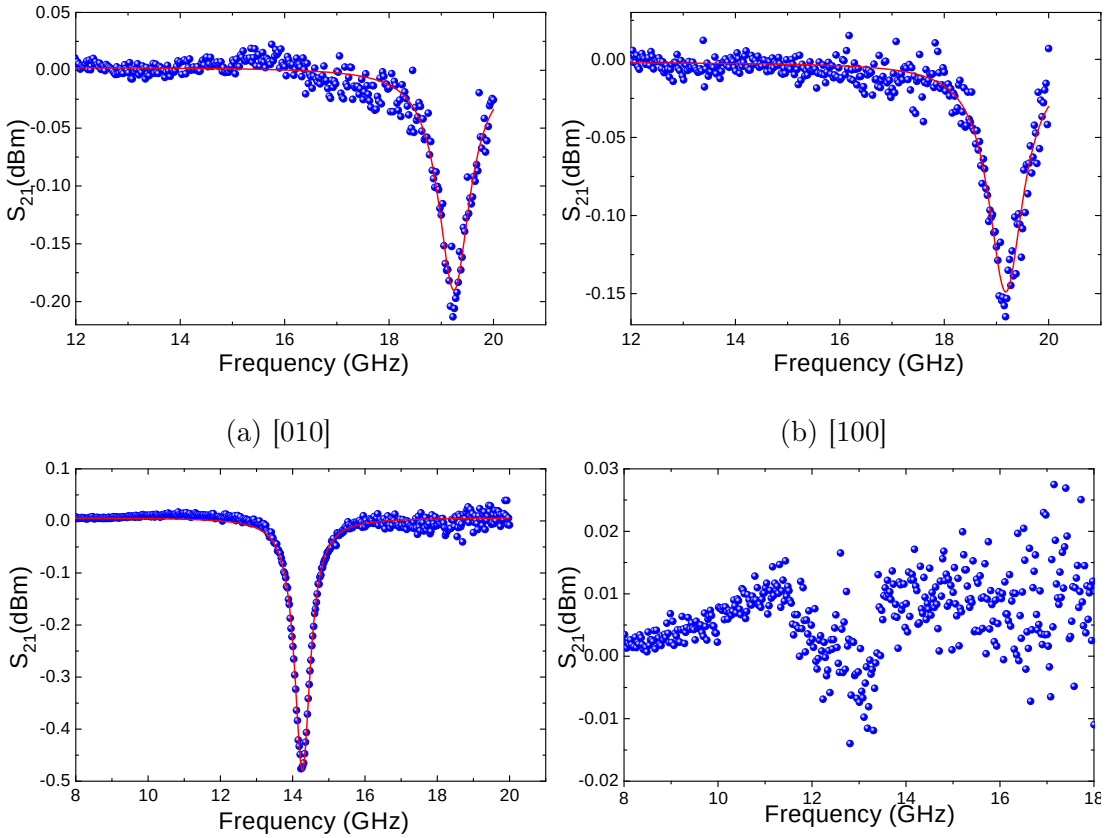

(a) [010] (b) [100]

(c) [110] (d) [1$\bar{1}$0]

Figure 7.2: FMR spectra for sample S536 at 0.15 T along different crystallographic direction (a)[010], (b)[100], (c)[110] and (d)[1$\bar{1}$0]. The lineshape is fitted using the asymmetric Lorentzian function to extract the resonance frequency. The solid blue points represent the experimental data, and the solid red line represents the fitting. The signal to noise ratio is better along the [110] direction since the sample was kept parallel to the transmission axis during the measurement along [110], as the angle deviates from the transmission axis the noise increases. Therefore, the FMR spectra along [1$\bar{1}$0] doesn't give a clear Lorentzian absorption peak hence the fitting was not possible along the [1$\bar{1}$0] crystal direction.

The extraction of the resonance frequency, f_{res}, as a function of the azimuthal angle, ϕ_M, facilitates the extraction of the in-plane anisotropy constants, K_u and K_c. For the samples with varying Ga composition, the values of the resonance frequency at different azimuthal angles achieved by rotating the sample in steps of 5° at a fixed magnetic field value of 0.15 T and the transmission axis only being parallel to the magnetic field for the measurement along [110] direction corresponding to 45° in the figure, were extracted and are shown in figure 7.3

(a) to (g). For samples with Ga concentration 20 % and higher, no anisotropy could be detected within the level of uncertainty allowed by the noise; therefore the FMR measurements for these samples have been excluded from any further analysis.

In figure 7.3, the peaks at 0° and 90° are represented by the [010] and [100] crystal direction and the troughs at −45°, 45° and 135° are represented by $[\bar{1}10]$, [110] and $[1\bar{1}0]$ respectively. There is a slight difference between the resonance frequency along [110] direction and $[\bar{1}10]$, $[1\bar{1}0]$ direction due to the uniaxial anisotropy present in the thin film. From the resonance frequency versus azimuthal angle plots, it can be observed that the epitaxially grown samples of $Fe_{100-x}Ga_x$ on GaAs with varying Ga concentration shows a four-fold cubic anisotropy along the easy axis and two-fold uniaxial anisotropy along [110] agreeing with the conclusion from section 5.1.

In order to extract the anisotropy constants and the saturation magnetisation, the resonance frequency extracted from the experimental data was fitted using the equation 7.2, previously discussed in section 3.3.2.

$$\begin{aligned}\left(\frac{\omega_{res}}{\gamma}\right)^2 &= [H_{ext}M_s\cos(\phi_H-\phi_M)\\ &\quad - H_u\cos^2(\phi_M-\phi_0)+\frac{1}{2}H_c\cos^2 2\theta_M+4\pi M_s]\\ &\quad \times[H_{ext}\cos(\phi_H-\phi_M)\\ &\quad - H_u\cos 2(\phi_M-\phi_0)+H_c\cos 4\phi_M]\end{aligned} \tag{7.2}$$

where ω_{res} is the angular resonance frequency, H_{ext} is the external applied magnetic field, M_s is the saturation magnetisation, θ_M is the polar angle, ϕ_M is the azimuthal angle, $H_u = 2K_u/M_s$ is the uniaxial anisotropy field, ϕ_0 is the angle between in-plane uniaxial easy axis, and the cubic easy axis and $H_c = 2K_c/M_s$ is the cubic anisotropy field. The resonance frequency variation with respect to the azimuthal angle for all the samples were fitted with the above equation 7.2 using the sum of least squares method, with the anisotropy fields and the saturation magnetisation constant as the free parameters. The fit to the resonance frequency at 0.15 T is represented by the red solid line and the resonance frequency extracted from the experimental data is represented by the blue points in figure 7.3 (a) to (g).

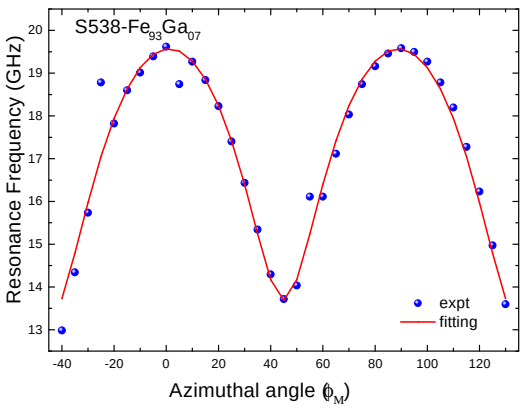
S538-Fe93Ga07
Resonance Frequency (GHz)
Azimuthal angle (ϕM)
expt
fitting

(a)

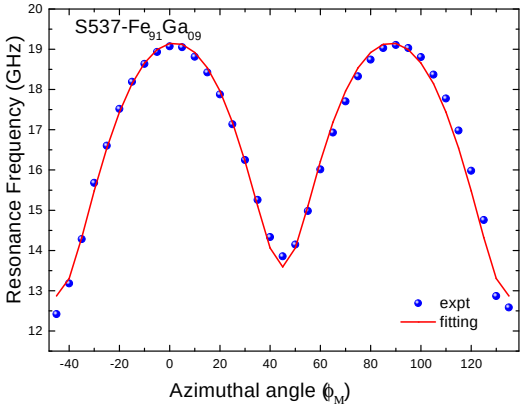
S537-Fe91Ga09
Resonance Frequency (GHz)
Azimuthal angle (ϕM)
expt
fitting

(b)

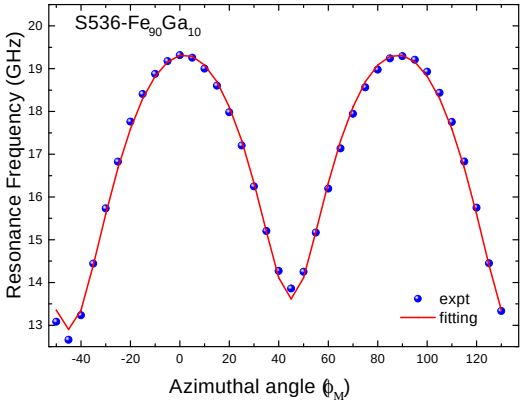
S536-Fe90Ga10
Resonance Frequency (GHz)
Azimuthal angle (ϕM)
expt
fitting

(c)

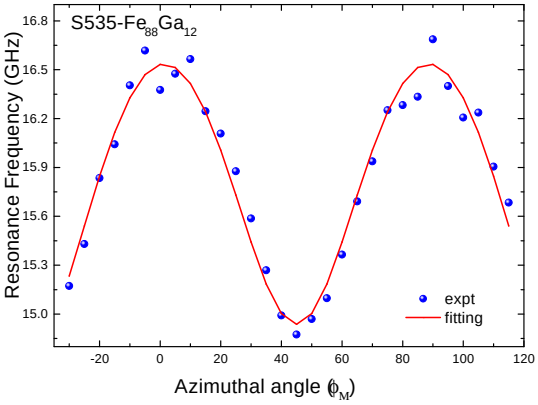
S535-Fe88Ga12
Resonance Frequency (GHz)
Azimuthal angle (ϕM)
expt
fitting

(d)

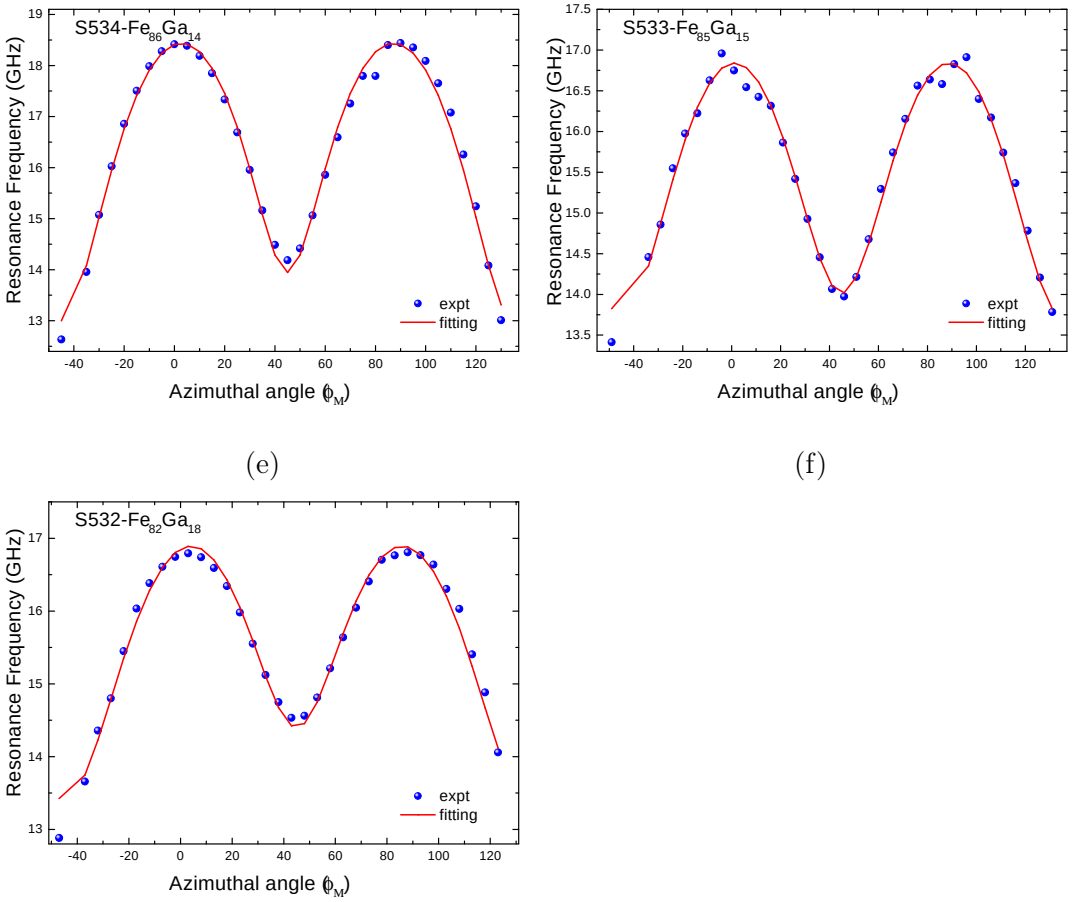

Figure 7.3: Fit to the angular resonance frequency at 0.15 T for the samples with varying Ga composition discussed in table 3.1. The resonance frequency extracted from the experimental data is represented by the blue points, and the solid red line represents the simulated fit to the experimental data. Anisotropy constants, K_u and K_c, as well as saturation magnetisation, M_s, were extracted from the fitting.

Table 7.1 enumerates the calculated values of the magnetic anisotropy constants, K_u and K_c, and the saturation magnetisation, M_s, along with the associated errors calculated by fitting the experimental data with the mathematical model as described above.

Sample name	% Ga	K_c (kJ/m^3)	K_u (kJ/m^3)	M_s ($\times 10^6 Am^{-1}$)
S532	18	20.5±0.5	6.3±0.5	1.5±0.1
S533	15	20.4±0.5	1.8±0.0	1.5±0.1
S534	14	35.7±0.7	5.9±0.1	1.6±0.2
S536	10	44.7±0.8	4.4±0.5	1.7±0.1
S537	9	43.4±0.8	4.4±0.0	1.7±0.2
S538	7	45.8±1.7	2.6± 0.0	1.8±0.4

Table 7.1: Extracted values of the cubic and uniaxial magnetocrystalline anisotropy constant in kJ/m^3 for $Fe_{100-x}Ga_x$ thin films. Extracted values of the saturation magnetisation are in Am^{-1}. The values were determined by fitting numerically simulated data with the experimental data obtained from ferromagnetic resonance experiment.

The magnetocrystalline anisotropies and the saturation magnetisation extracted by fitting the resonance frequency obtained from the FMR experiment with the mathematical model is compared with anisotropies and saturation magnetisation obtained from the SQUID experiment discussed in section 5.1. Figure 7.4 (a) and (b) gives a graphical comparison between the cubic and uniaxial constants extracted from FMR measurement and SQUID magnetometry. The blue triangular points represent the values extracted from FMR measurements, and the red points represent the values from the SQUID magnetometry. The values of the uniaxial and cubic anisotropies extracted from the SQUID magnetometry measurements discussed in section 5.1 substantiates the values obtained using ferromagnetic resonance experiment measurements within the boundaries of reasonable error. The error bars on the FMR measurements are reasonably small, indicating that the pattern observed for the cubic and uniaxial magnetocrystalline

constant values as the Ga concentration is varied are reliable. As the Ga concentration is increased the cubic anisotropy decreases eventually becoming entirely isotropic. Whereas, the uniaxial anisotropy constant increases with increase in Ga concentration.

Figure 7.4 (c) gives a graphical comparison between the saturation magnetisation extracted from FMR measurement and SQUID magnetometry. The saturation magnetisation decreases with the increase in Ga concentration. This trend agreed with previously observed trend for bulk Galfenol as well as polycrystalline thin films [220]. The saturation magnetisation values for SQUID magnetometry measurement are systematically lower than the values extracted from the FMR measurement. The reasonably smaller error bars on the saturation magnetisation extracted from the mathematical fitting of the resonance frequency indicates that this pattern is not imprecision in the fitting method and the pattern observed is reliable. In case of SQUID magnetometry since the saturation magnetisation is calculated using the volume of the sample, there is a possibility that the regions near the interfaces with the substrate (GaAs) and capping layer (Cr) may not be magnetic. This non-magnetic layer near the interfaces may be assumed to be within 0.5-2.0 nm. Hence, the SQUID measurements would systematically underestimate the magnetisation by $\approx$ 5-20%. Therefore, these process might have introduced a systematic error in the saturation magnetisation obtained from the SQUID measurements. Therefore, the numbers from the SQUID could be increased by 5% to account for a possible magnetically dead layer at the GaAs/FeGa interface. Figure 7.4 (d) shows the dead layer present near the interfaces.

In a study on epitaxial thin films of Fe-Ga grown on GaAs(001) using molecular beam epitaxy, the saturation magnetisation decreased from 1371 to 1105 kA/m with increasing Ga concentration from 10.5 to 24.3 % at room temperature [221]. Similar decreasing trend in saturation magnetisation was observed for our samples as well. Kellogg *et al*. reported a saturation magnetisation of 1265 kA/m for single crystal $Fe_{81}Ga_{19}$ [222]. A saturation magnetisation of 765 kA/m in the $Fe_{75}Ga_{25}$ thin film on GaAs (001) was observed by Erve *et al* [223].

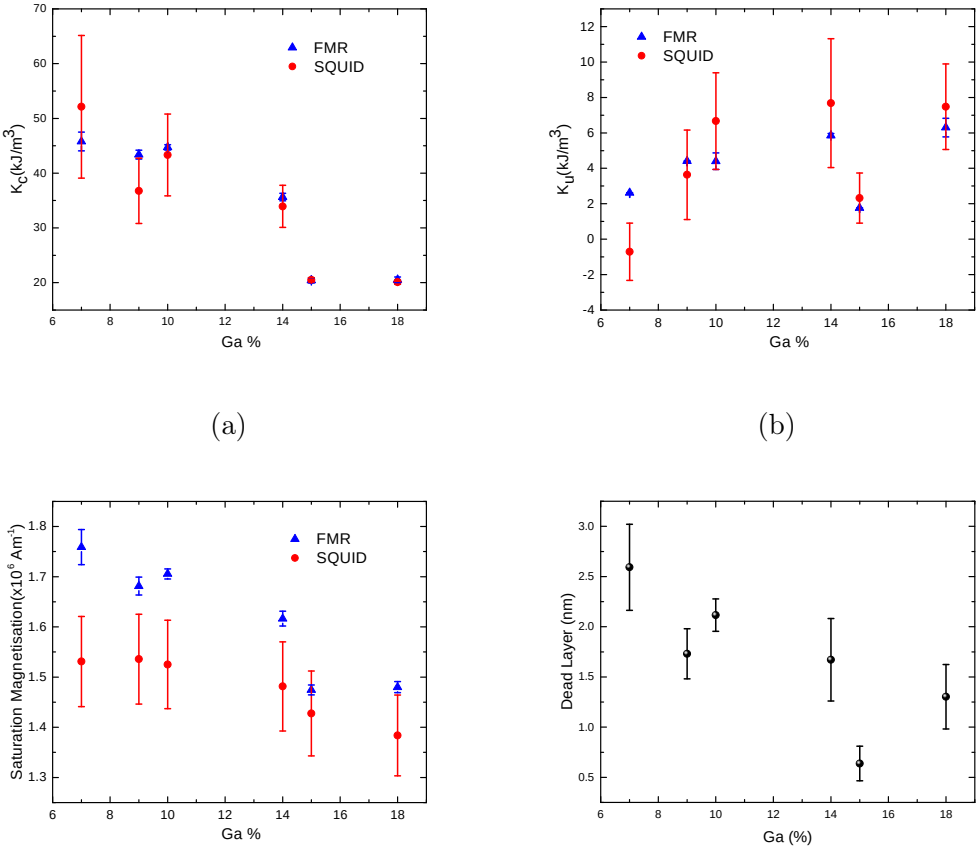

Figure 7.4: Shows a comparison between the magnetic parameters extracted from FMR measurements and SQUID magnetometry (a) cubic anisotropy constant, (b) uniaxial anisotropy constant, and (c) saturation magnetisation. The blue triangular points represent the values extracted from FMR measurements, and the red points represent the values from the SQUID magnetometry. Figure (d) shows the non-magnetic dead layer near the interfaces.

7.2 Dynamic parameters

In order to understand and investigate the magnetisation dynamics in ferromagnetic thin films, the regularly used parameter is the field linewidth. The field linewidth (ΔH) of the ferromagnetic resonance can be linked to the magnetic damping in the sample, hence extracting ΔH from the lineshape as a function of the rf frequency, the damping within the system can be quantified. This gives insight into different spin relaxation and scattering processes involved in a magnetic system exposed to varying rf signal in a magnetic film.

ΔH can be extracted using the same procedure described in section 7.1. This is achieved by extracting lineshape at a fixed frequency, then plotting the intensity data as a function of field and fitting the absorption dip to the asymmetric Lorentzian. Figure 7.5 shows an example of the asymmetric Lorentzian fit to the resonance dip at 15 GHz. The blue points represent the experimental data, and the red line represents the Lorentzian fitting. The half-width at half maximum of the absorption lineshape gives ΔH.

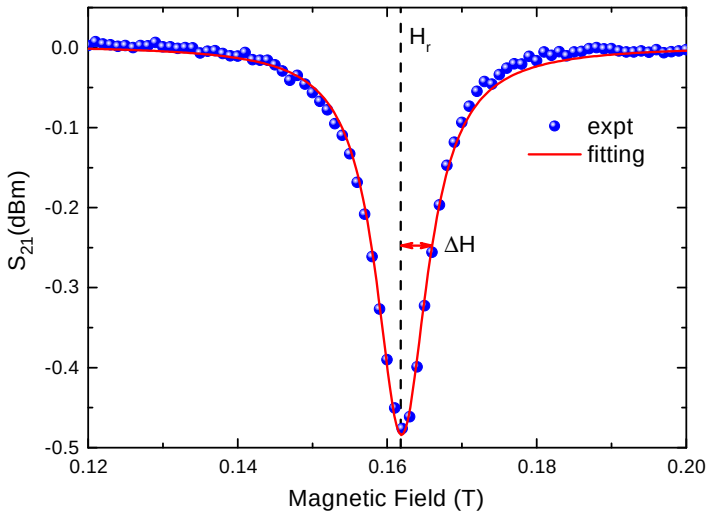

Figure 7.5: FMR spectra for sample S536 at 15 GHz along [110] crystallographic direction. The lineshape is fitted using the asymmetric Lorentzian function to extract the resonance frequency. The solid blue points represent the experimental data, and the solid red line represents the fitting.

For the purpose of extracting the damping in the system, the linewidths were extracted as a function of frequency. Assuming the relationship between the field linewidth and frequency is linear, fitting the data to equation 7.3 discussed in section 3.3.2 yields the Gilbert damping parameter (α) as well as the extrinsic damping parameter (ΔH_0). Otherwise, if the trend has a curvature, the two-magnon scattering parameter can be included to quantify the dominant damping mechanism. The field linewidth is given by;

$$\Delta H = \Delta H_0 + \frac{2\alpha\omega_{res}}{\gamma} \frac{1}{\cos\left(\phi_H - \phi_M\right)} \tag{7.3}$$

where ϕ_H is the angle between the applied magnetic field and the easy axis of the sample, ϕ_M is the azimuthal angle. However, since a high saturating magnetic field is applied during FMR measurements, ϕ_H and ϕ_M are assumed to be in the same direction; therefore, $\cos\left(\phi_H - \phi_M\right)$ becomes 1.

The linewidths determined from the Lorentzian fits at varying rf frequency for all the samples along [110] have been shown in figure 7.6 (a) to (f). In the plots, the blue solid points represent the experimentally extracted linewidth, and the red lines represent the fitting. The linewidths were extracted only along the [110] crystal direction. Since the transmission line was parallel to [110] direction, the extracted linewidths had the best signal to noise ratio in comparison to the other crystal direction. The fitting was done for rf frequencies 10 GHz and higher frequencies up to which it gave the best signal to noise ratio. Linear fit using equation 7.3 seems to be the most suitable option for fitting to the experimental data with the exception of S538 sample. The fit to figure 7.6 (b) to (f) seems reasonable within the boundaries of error.

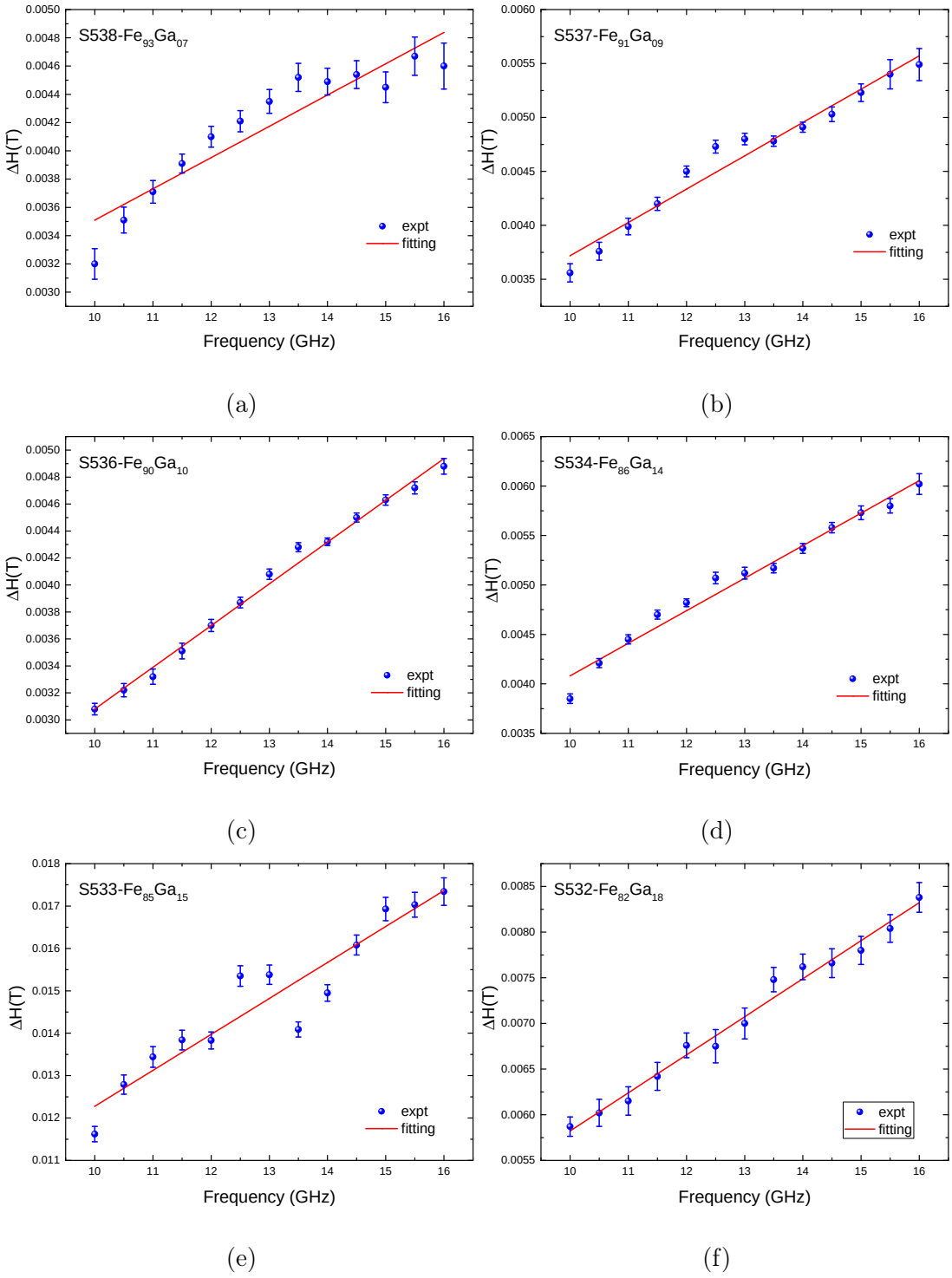

Figure 7.6: Field linewidth for samples with magnetic field along [110] direction. The experimental values are represented by the blue solid points, and the fitting is represented by the red lines. The Gilbert damping and the extrinsic damping are obtained from the fit.

The linear fits to the experimental field linewidths yield the intrinsic damping parameter (Gilbert damping) as well as the extrinsic damping parameter. Table 7.2 gives the intrinsic and extrinsic damping parameters along with the associated errors for all the anisotropic samples with varying Ga composition discussed in this thesis.

Sample name	% Ga	Gilbert damping ($\times 10^{-3}$)	Extrinsic damping ($\times 10^{-3}$ T)
S532	18	11.7±1.0	1.7±0.4
S533	15	23.8±5.4	3.8±2.6
S534	14	9.2±1.0	0.8±0.5
S536	10	8.7±0.5	-0.01±0.2
S537	9	8.7±1.1	0.6±0.5
S538	7	6.2±1.6	1.3± 0.8

Table 7.2: Table showing the extracted values of the intrinsic damping or Gilbert damping and the extrinsic damping by fitting the field linewidth with the mathematical model for the samples with varying Ga composition.

Typically, the Gilbert damping for Fe is ≈ 0.002 [224], and the Gilbert damping for epitaxial $Fe_{81}Ga_{19}$ has been reported previously as 0.017 [2]. Phenomenologically, the damping term exists to bring the system to equilibrium; hence the value of α determines how quickly or slowly a system will attain equilibrium. Therefore, measuring the damping within a material is critical to be used in practical spintronic based devices. The Gilbert damping parameter for sample S532 ($Fe_{82}Ga_{18}$) is comparable to what was reported previously within the reasonable boundaries of error.

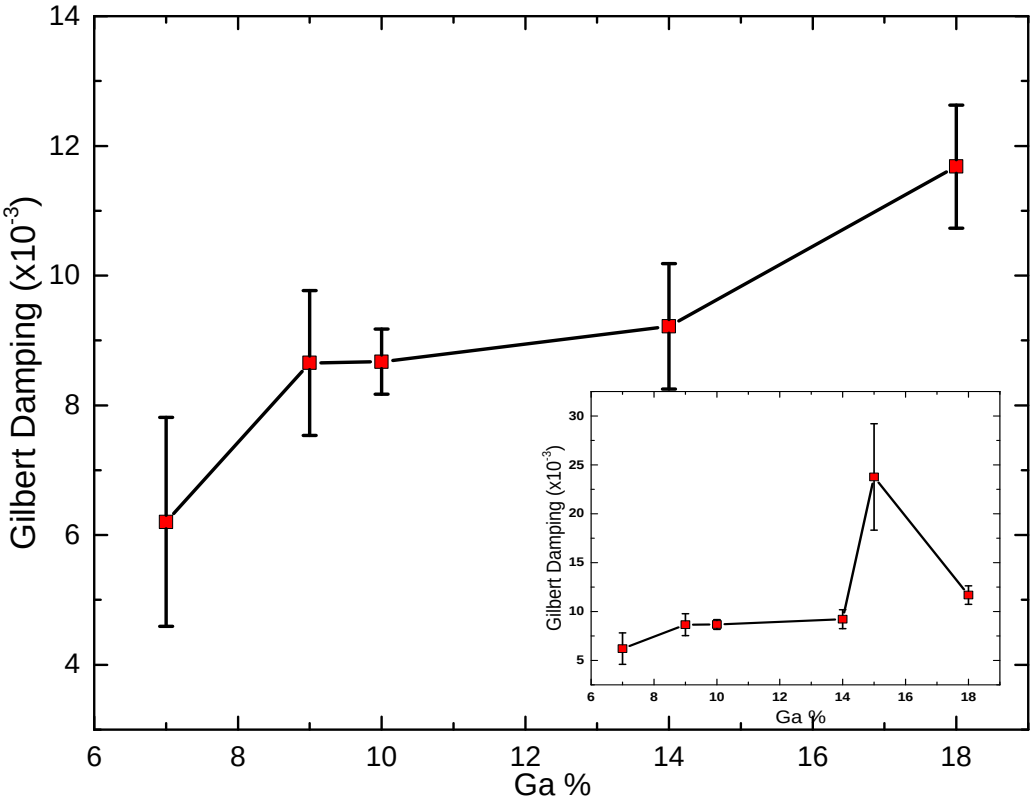

Figure 7.7: Shows the values of the intrinsic or Gilbert damping obtained by fitting the field linewidth with the mathematical model as a function of Ga concentration. The inset shows the plot when S533 is included and was removed from the main graph purely to show a clear trend as plotted against Ga concentration.

Figure 7.7 shows the plot of Gilbert damping as a function of Ga concentration extracted by fitting the field linewidth. As the Ga concentration increases, the Gilbert damping gradually increases. It has been previously reported that the intrinsic damping is affected by the Ga concentration in Galfenol samples, as the Ga concentration increases the intrinsic damping increases [142]. Since the Gilbert damping term originates from spin-orbit coupling [171], adding a second element Ga increases the intrinsic damping. In section 4.2.1 it has already been established that as the Ga concentration was gradually increased the crystallinity of the films tend to reduce. As the Ga concentration is increased the ordering in the films reduces, which is reflected in the increase in the Gilbert damping parameter. However, the Gilbert damping parameter may also be affected by surface morphology; therefore, a definitive answer cannot be presumed.

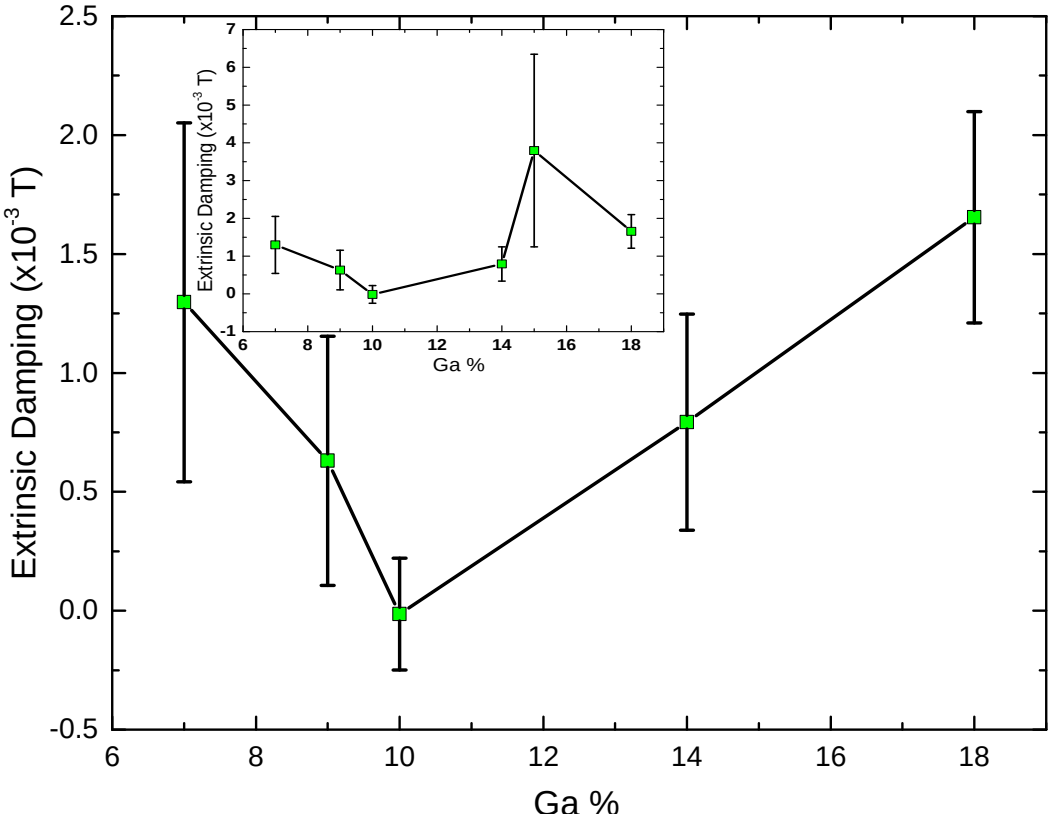

Figure 7.8: Shows the values of the extrinsic damping obtained by fitting the field linewidth with the mathematical model as a function of Ga concentration. The inset shows the plot when S533 is included and was removed from the main graph to keep a similarity between the extrinsic and intrinsic damping representation.

Figure 7.8 shows the plot of extrinsic damping as a function of Ga concentration given by the intercept of the field linewidth. Extrinsic damping effects are primarily the outcome of interactions with the structural defects. The extrinsic damping decreases initially up to 10 % Ga concentration after which it starts increasing. Non-linearity in the damping arises from extrinsic damping effects, primarily due to two magnon scattering in the sample; however, the field linewidths mentioned in this thesis were fairly linear; so it can be concluded that the extrinsic damping is caused by the inhomogeneity within the structure of the magnetic films.

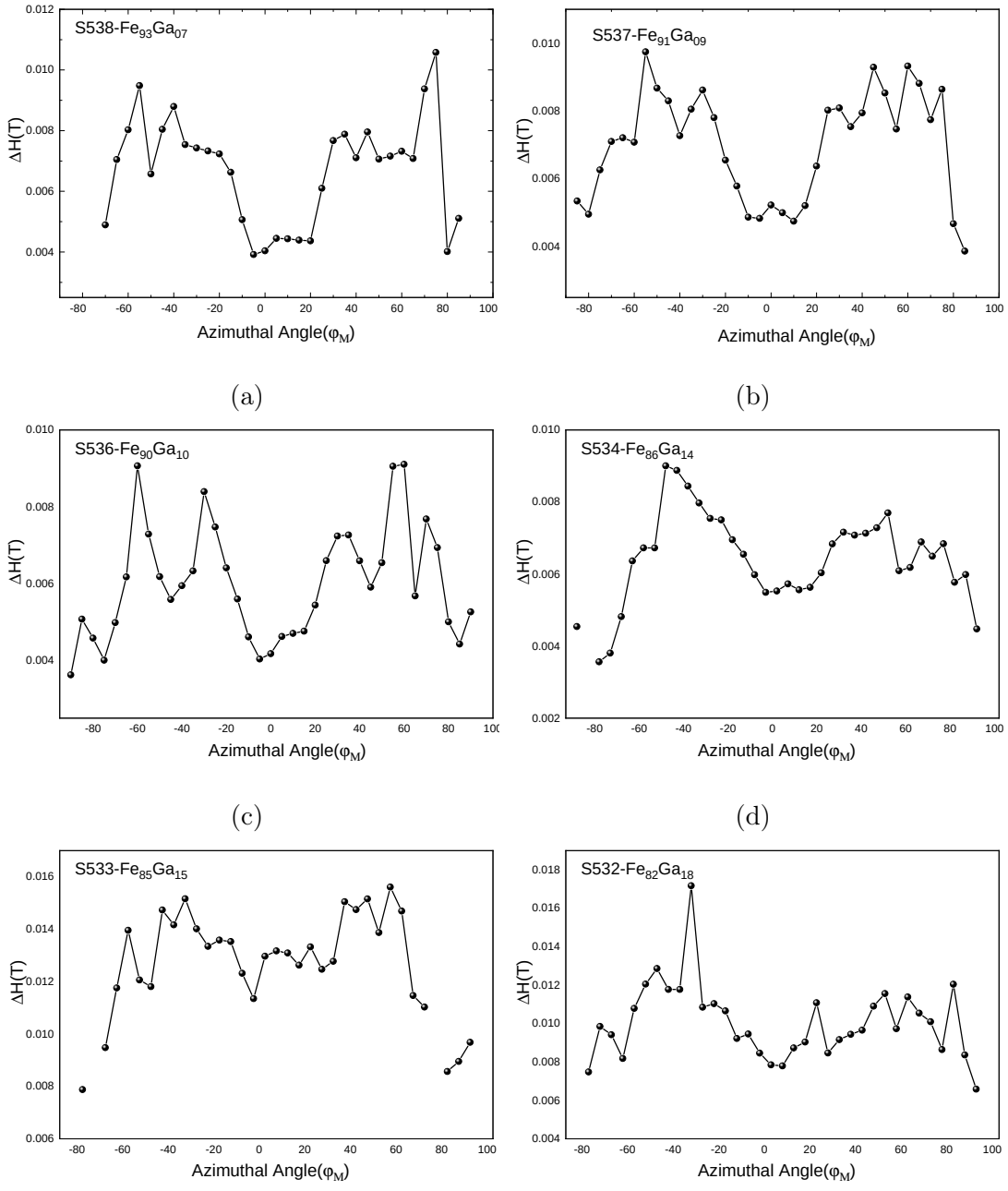

Figure 7.9: Field linewidth versus the azimuthal angle for the samples with varying Ga composition discussed in table 3.1. The field linewidths were extracted at 15 GHz frequency. Some of the points near to the hard axis $[1\bar{1}0]$ are missing because the linescan S_{21} was noisy and a fit to the Lorentzian was not possible.

Figure 7.9 shows the plot of the field linewidth as a function of the azimuthal angle at 15 GHz frequency. The linewidths were extracted by fitting the linescans to the asymmetric Lorentzian. As reported in reference [165], if the contribution of Gilbert damping towards the linewidth when plotted as a function of the

azimuthal angle is considered alone, a linear line parallel to the x-axis is obtained. Whereas, when the two-magnon scattering was included, the in-plane angular dependency of the FMR linewidth showed a fourfold symmetry. From figure 7.9, it clearly shows that the Gilbert mechanism alone is not sufficient to describe the relaxation within the films, so we can expect to have some two-magnon scattering contribution as well during the relaxation process. However, since the signal to noise was low, it was challenging to fit the in-plane angular dependency of linewidth. Therefore, only the Gilbert damping parameters have been extracted in the earlier sections, and a conclusive answer towards the two-magnon scattering could not be drawn.

7.3 Summary

In summary, this chapter examined the static and magnetic properties of $Fe_{100-x}Ga_x$ thin films grown on GaAs substrates with varying Ga composition discussed in table 3.1 using the measurements obtained from ferromagnetic resonance experiment. The saturation magnetisation, cubic and uniaxial anisotropy constants obtained from the FMR experiments were compared with the anisotropy constants and saturation magnetisation obtained from the SQUID magnetometry measurements. The dynamic properties like Gilbert damping and extrinsic damping were also extracted as a function of Ga concentration.

The static properties were obtained by fitting the resonance frequency as a function of in-plane angular dependency. The values of the uniaxial and cubic anisotropies extracted from the ferromagnetic resonance experiment verify the values obtained from the SQUID magnetometry measurements within the boundaries of reasonable error. The error bars on the FMR measurements are reasonably small comparing to those obtained from the SQUID magnetometry measurements. However, the saturation magnetisation values obtained from the SQUID magnetometry measurement are systematically lower in value than those extracted from the FMR measurement possibly due to a systematic error introduced during the process of extracting saturation magnetisation from the SQUID measurements. Gilbert damping and extrinsic damping are the two dynamic

parameters that were extracted from the field linewidths obtained from the ferromagnetic resonance experiment. The Gilbert damping showed an increasing trend with the increase in the Ga concentration and the extrinsic damping decreases initially up to 10 % Ga concentration after which it starts increasing. There could be a possible contribution from the two-magnon scattering towards the damping; however, due to poor signal to noise ratio fitting was not possible. Hence, a conclusive answer could not be drawn.

Chapter 8

Conclusion

In this thesis, a combination of structural characterisation techniques including XRD, XRR, XPS and magnetic characterisation techniques including SQUID magnetometry, ferromagnetic resonance and magneto-transport were employed to investigate the structural and magnetic properties (both static and dynamic) of Galfenol thin films deposited using sputter deposition onto GaAs(001) substrates. These measurements were done for two sets of samples, first by varying the Ga concentration in 26.20 nm thick $Fe_{100-x}Ga_x$ films with $07 \leq x \leq 30$, secondly by varying the film thickness (t) for $Fe_{79}Ga_{21}$ films between $5\,\text{nm} \leq t \leq 95\,\text{nm}$. The work presented in this thesis gives a comprehensive study about the structural and magnetic properties of the epitaxially grown Galfenol thin films.

Chapter 4 began by presenting the fundamental structural characterisation of the sputtered grown epitaxial thin films of $Fe_{100-x}Ga_x$ with $07 \leq x \leq 30$. XRR was used to determine the thickness of the films grown as compared with the expected thickness from the calibration during the sputtered growth. The actual thickness estimated from XRR for the samples with varying Ga composition was systematically slightly higher than what was expected. The interface roughness between the film and the substrate was below 2 nm for most of the samples, which was expected from epitaxially grown samples. The density of the samples varied over the range of samples reaching a maximum of 8.02 ± 0.07 g/cm^3 as compared to the density of Fe (7.83 g/cm^3). Next, the XRD was used to determine the lattice parameter along the growth direction and the crystallite size of the thin films. The XRD results also showed a good epitaxial and crystalline growth

for the samples with lower Ga concentration, however with the increase in the Ga concentration in the thin films the sample peak slowly became insignificant indicating that the crystallinity reduced with the increase in the impurities. The final stage of structural properties analysis on these samples was done using XPS to determine the composition of these films. From analysing two samples with extreme Ga composition, it was confirmed that the thin films had good agreement with what was expected.

In Chapter 5, SQUID magnetometry was used to determine the magnetocrystalline anisotropy constants of these samples. The samples were found to have cubic magnetic anisotropy along [100]/[010] direction and a weak uniaxial anisotropy along [110] direction and a hard axis along $[1\bar{1}0]$ crystalline direction. For Ga concentration up to 18% there is a clear distinction between the axes representing cubic anisotropy and uniaxial anisotropy. But, for Ga concentration 20% and above the sample becomes entirely isotropic, which was consistent with the lack of crystallinity for the higher Ga concentration samples. For lower Ga concentration the hysteresis loops indicated a strong cubic anisotropy along [100]/[010] direction which reduces with the increase in the Ga concentration, which was consistent with the values extracted for the cubic anisotropy constant by fitting the hysteresis loops with the mathematically modelled magnetisation loops. The uniaxial anisotropy increased initially with the increase in the Ga concentration, ultimately saturating upon a further increase in Ga concentration. The coercive field was also determined to have an increasing trend with the increase in Ga concentration which we attribute to the increased number of pinning sites due to impurities.

The AMR of these samples were investigated in chapter 6 through field rotation measurement and passing current along the four in-plane crystalline axes. The AMR was decomposed to four different contributions with corresponding unique symmetries. The non-crystalline contribution dominates the AMR as expected for a metallic ferromagnet. The cubic and uniaxial AMR crystalline coefficient followed a similar pattern as the magnetocrystalline anisotropy constants obtained for the samples using the SQUID magnetometry hysteresis loops. For the samples with Ga concentration above 18%, the magnetocrystalline anisotropy

coefficients were zero within the experimental uncertainty being consistent with the disappearing XRD sample peaks.

Chapter 7 presents the dynamic magnetic properties of these samples. FMR was performed on these samples at different GHz frequencies alongside a field rotation measurement in order to determine the Gilbert damping parameter. The Gilbert or the intrinsic damping increased with the increase in Ga concentration, which was consistent with the previously reported pattern. The Gilbert damping parameter was also comparable to the previously reported value [142]. Although there could have been a two-magnon scattering contribution to the relaxation process, it was challenging to perform a fitting on the extracted values due to low signal to noise ratio. The magnetocrystalline anisotropy coefficients were also determined by fitting the angular resonance frequency with the mathematical model. These coefficients were later compared with those obtained using the SQUID magnetometry. The determined values of both the cubic and uniaxial anisotropy were comparable to those previously obtained from the hysteresis loops. However, the error bars on the values obtained from SQUID magnetometry were comparatively larger to those from FMR measurement. One of the possible reason could be an underestimation of the magnetisation due to non-magnetic interfaces at the substrate and the capping layer.

Similarly, a comprehensive study of the Galfenol films with varying film thickness was studied. Thin films with composition $Fe_{79}Ga_{21}$ films and thickness (t) ranging between $5\,\text{nm} \leq t \leq 95\,\text{nm}$ were grown on GaAs(001) substrate. In chapter 4, the structural properties of these samples were studied. It began with the determination of the thickness of these samples using XRR. The thickness of the thinner samples was close to the expected thickness from the growth. The thickness of the thicker samples deviated from the expected thickness because of the prolonged deposition conditions. XRD was performed to determine the lattice parameter along the growth direction and the crystallite size of the films. From the XRD, the epitaxial and crystalline growth of the samples could be confirmed. The lattice parameter determined was comparable with the previously reported value. The sample peak for the thinner samples was not distinguishable because of the low signal to noise ratio.

Chapter 5 continued with the determination of the magnetocrystalline anisotropy constant of the samples using the SQUID magnetometry. All the samples were found to have cubic magnetic anisotropy favouring the [100]/[010] axes and a weaker uniaxial anisotropy along [110] crystalline direction. The cubic crystalline anisotropy increases with the increase in the film thickness with a peak for the 56.5 nm sample, which is in accordant with the sample peaks observed for the samples using the XRD measurement. The uniaxial anisotropy, on the other hand, decreased with an increase in the film thickness being the lowest for 20 nm thick sample and again started increasing for thicker samples associated with the interface phenomenon between the sample and the GaAs(001) substrate.

The electrical properties using the magneto-transport measurements were investigated in chapter 6. The samples were studied using field rotation and analytical fitting by enabling the current to flow along the four in-plane crystalline axes. As discussed earlier, the AMR was established to have four different contributions with unique symmetries. The non-crystalline term dominated the AMR contribution. The non-crystalline coefficient increases with the increase in the film thickness but starts dropping for thicker samples (56.5 nm and above). The crystalline AMR coefficients were compared with the magnetocrystalline constants extracted from the hysteresis loops obtained by SQUID magnetometry. The pattern observed for both the measurements were in good agreement with each other.

Galfenol being such a versatile magnetostrictive material with a wide range of applications has been a centre of attraction for a long period. Up until now, the focus has been on bulk and polycrystalline thin films of Galfenol. There are few works concerning sputtered grown epitaxial thin films [2, 85]. Because these films are epitaxial and sputtered grown, it makes them more economical with the easier and less time-consuming growth process. There are some areas which could be further explored as a continuation to work presented in this thesis. One could attempt to vary the thickness of these films with a gradual increase in film thickness between 30 nm to 95 nm and study the magnetic properties. There were some interesting deviation for thicker samples which could be further explored. Even increasing the thickness further could reveal some interesting results and

evaluate when does the thin film approach the bulk state. FMR measurements as a function of thickness could reveal some interesting magneto-dynamic properties. Further these epitaxial layers could be investigated for strain-induced microwave magnetisation dynamics as a function of Ga composition and film thickness, and exhibit some intriguing results with prospective of applications. The magnetostriction properties of epitaxial thin films of Galfenol as a function of Ga composition and thickness can be monitored by the change in the magnetic anisotropy in response to an applied strain (i.e. the Villari effect). A more direct approach for measurement of magnetostriction could be attempted by using a cantilever beam magnetometer.

References

[1] A E Clark, K B Hathaway, M Wun-Fogle, JB Restorff, Thomas A Lograsso, VM Keppens, G Petculescu, and RA Taylor. Extraordinary magnetoelasticity and lattice softening in bcc fe-ga alloys. *Journal of Applied Physics*, 93(10):8621–8623, 2003.

[2] DE Parkes, LR Shelford, P Wadley, V Holỳ, M Wang, AT Hindmarch, G Van Der Laan, RP Campion, KW Edmonds, SA Cavill, and *et al.* Magnetostrictive thin films for microwave spintronics. *Scientific reports*, 3:2220, 2013.

[3] Susmita Kamila. Introduction, classification and applications of smart materials: an overview. *American Journal of Applied Sciences*, 10(8):876, 2013.

[4] Mel Schwartz. *Smart materials*. CRC press, 2008.

[5] HS Tzou, H-J Lee, and SM Arnold. Smart materials, precision sensors/actuators, smart structures, and structronic systems. *Mechanics of Advanced Materials and Structures*, 11(4-5):367–393, 2004.

[6] James Prescott Joule. Xvii. on the effects of magnetism upon the dimensions of iron and steel bars. *The London, Edinburgh, and Dublin Philosophical Magazine and Journal of Science*, 30(199):76–87, 1847.

[7] Bernard Dennis Cullity and Chad D Graham. *Introduction to magnetic materials*. John Wiley & Sons, 2011.

[8] EW Lee and MA Asgar. The magnetostriction of nickel. *Proceedings of*

the Royal Society of London. A. Mathematical and Physical Sciences, 326 (1564):73–85, 1971.

[9] RC Hall. Single crystal anisotropy and magnetostriction constants of several ferromagnetic materials including alloys of nife, sife, alfe, coni, and cofe. *Journal of Applied Physics*, 30(6):816–819, 1959.

[10] Eric W Lee. Magnetostriction and magnetomechanical effects. *Reports on progress in physics*, 18(1):184, 1955.

[11] E Villari. Ueber die aenderungen des magnetischen moments, welche der zug und das hindurchleiten eines galvanischen stroms in einem stabe von stahl oder eisen hervorbringen. *Annalen der Physik*, 202(9):87–122, 1865.

[12] G Wiedemann. Über die torsion und die beziehung derselben zum magnetismus. *Pogg. Ann*, 106:161–201, 1860.

[13] DV Malyugin. On the theory of wiedemann effects. *Journal of magnetism and magnetic materials*, 97(1-3):193–197, 1991.

[14] Cu Matteucci. Recherches expérimentales sur les phénomènes électromagnétiques développés par la torsion. *Ann. Chim. Phys*, 53:385–417, 1858.

[15] Rick Allen Kellogg. *The Delta-E effect in Terfenol-D and its application in a tunable mechanical resonator*. PhD thesis, Iowa State Universitytest data are examined to quantify the variability in ..., 2000.

[16] WF Barrett. On the alterations in the dimensions of the magnetic metals by the act of magnetisation. *Nature*, 26:585–586, 1882.

[17] R Grössinger, R Sato Turtelli, and N Mehmood. Materials with high magnetostriction. In *IOP Conference Series: Materials Science and Engineering*, volume 60, page 012002. IOP Publishing, 2014.

[18] Robert C O'Handley. *Modern magnetic materials: principles and applications*. Wiley, New York, NY, 2000. URL `http://cds.cern.ch/record/2131967`.

[19] Michael E McHenry and David E Laughlin. Magnetic properties of metals and alloys. In *Physical Metallurgy*, pages 1881–2008. Elsevier, 2014.

[20] A Eo Clark. Magnetostrictive rare earth-fe2 compounds. *Handbook of ferromagnetic materials*, 1:531–589, 1980.

[21] AE Clark, BF DeSavage, and R Bozorth. Anomalous thermal expansion and magnetostriction of single-crystal dysprosium. *Physical Review*, 138 (1A):A216, 1965.

[22] WC Thoburn, S Legvold, and FH Spedding. Magnetic properties of terbium metal. *Physical Review*, 112(1):56, 1958.

[23] JJ Rhyne and S Legvold. Magnetostriction of tb single crystals. *Physical Review*, 138(2A):A507, 1965.

[24] NC Koon, CM Williams, and BN Das. Giant magnetostriction materials. *Journal of magnetism and magnetic materials*, 100(1-3):173–185, 1991.

[25] AE t Clark and HS Belson. Giant room-temperature magnetostrictions in tb fe 2 and dy fe 2. *Physical Review B*, 5(9):3642, 1972.

[26] LARS Sandlund, MIRKA Fahlander, TORD Cedell, AE Clark, JB Restorff, and M Wun-Fogle. Magnetostriction, elastic moduli, and coupling factors of composite terfenol-d. *Journal of Applied Physics*, 75(10):5656–5658, 1994.

[27] Mel Goodfriend, John Sewell, and Cal Jones. Application of a magnetostrictive alloy, terfenol-d to direct control of hydraulic valves. *SAE transactions*, pages 364–369, 1990.

[28] Rick A Kellogg and Alison B Flatau. Stress-strain relationship in terfenol-d. In *Smart Structures and Materials 2001: Smart Structures and Integrated Systems*, volume 4327, pages 541–549. International Society for Optics and Photonics, 2001.

[29] Arthur E Clark, Marilyn Wun-Fogle, James B Restorff, Thomas A Lograsso, and James R Cullen. Effect of quenching on the magnetostriction on fe/sub

1-x/ga/sub x/(0.13 x< 0.21). *IEEE Transactions on Magnetics*, 37(4):2678–2680, 2001.

[30] Rick Allen Kellogg. Development and modeling of iron-gallium alloys. 2003.

[31] RA Kellogg, AM Russell, TA Lograsso, AB Flatau, AE Clark, and M Wun-Fogle. Tensile properties of magnetostrictive iron–gallium alloys. *Acta materialia*, 52(17):5043–5050, 2004.

[32] E Klokholm and JA Aboaf. The saturation magnetostriction of permalloy films. *Journal of Applied Physics*, 52(3):2474–2476, 1981.

[33] RM Bozorth and JG Walker. Magnetic crystal anisotropy and magnetostriction of iron-nickel alloys. *Physical Review*, 89(3):624, 1953.

[34] Mark B Moffett, Arthur E Clark, Marilyn Wun-Fogle, Jan Linberg, Joseph P Teter, and Elizabeth A McLaughlin. Characterization of terfenol-d for magnetostrictive transducers. *The Journal of the Acoustical Society of America*, 89(3):1448–1455, 1991.

[35] Laurent Daniel and Nicolas Galopin. A constitutive law for magnetostrictive materials and its application to terfenol-d single and polycrystals. *The European Physical Journal Applied Physics*, 42(2):153–159, 2008.

[36] Jayasimha Atulasimha and Alison B Flatau. A review of magnetostrictive iron–gallium alloys. *Smart Materials and Structures*, 20(4):043001, 2011.

[37] Jaehwan Kim and Jaekyun Doo. Magnetostrictive self-moving cell linear motor. *Mechatronics*, 13(7):739–753, 2003.

[38] Seok-Jun Moon, Chae-Wook Lim, Byung-Hyun Kim, and Youngjin Park. Structural vibration control using linear magnetostrictive actuators. *Journal of Sound and Vibration*, 302(4-5):875–891, 2007.

[39] Tianli Zhang, Chengbao Jiang, Hu Zhang, and Huibin Xu. Giant magnetostrictive actuators for active vibration control. *Smart materials and structures*, 13(3):473, 2004.

[40] Zhaoshu Yang, Zhongbo He, Dongwei Li, Guangming Xue, and Xu Cui. Hydraulic amplifier design and its application to direct drive valve based on magnetostrictive actuator. *Sensors and Actuators A: Physical*, 216:52–63, 2014.

[41] Suryarghya Chakrabarti and Marcelo J Dapino. Design and modeling of a hydraulically amplified magnetostrictive actuator for automotive engine mounts. In *Industrial and Commercial Applications of Smart Structures Technologies 2010*, volume 7645, page 76450G. International Society for Optics and Photonics, 2010.

[42] John E Miesner and Joseph P Teter. Piezoelectric/magnetostrictive resonant inchworm motor. In *Smart Structures and Materials 1994: Smart Structures and Intelligent Systems*, volume 2190, pages 520–527. International Society for Optics and Photonics, 1994.

[43] Jaehwan Kim, Hyang-Ki Kim, and Seung-Bok Choi. A hybrid inchworm linear motor. *Mechatronics*, 12(4):525–542, 2002.

[44] C Visone and C Serpico. Hysteresis operators for the modeling of magnetostrictive materials. *Physica B: Condensed Matter*, 306(1-4):78–83, 2001.

[45] L Gros, G Reyne, C Body, and G Meunier. Strong coupling magneto mechanical methods applied to model heavy magnetostrictive actuators. *IEEE Transactions on magnetics*, 34(5):3150–3153, 1998.

[46] Göran Engdahl and Anders Bergqvist. Loss simulations in magnetostrictive actuators. *Journal of applied physics*, 79(8):4689–4691, 1996.

[47] Mauro Zucca, Paolo E Roccato, Oriano Bottauscio, and Cinzia Beatrice. Analysis of losses in a magnetostrictive device under dynamic supply conditions. *IEEE Transactions on Magnetics*, 46(2):183–186, 2010.

[48] CH Joshi. Compact magnetostrictive actuators and linear motors. In *Conference Actuator*, 2000.

[49] Becky Jones and Chen Liang. Magnetostriction: revealing the unknown. *IEEE Aerospace and Electronic Systems Magazine*, 11(3):3–6, 1996.

[50] Marcelo J Dapino and *et al.* On magnetostrictive materials and their use in adaptive structures. *Structural Engineering and Mechanics*, 17(3-4):303–330, 2004.

[51] JM Vranish, DP Naik, JB Restorff, and JP Teter. Magnetostrictive direct drive rotary motor development. *IEEE Transactions on Magnetics*, 27(6): 5355–5357, 1991.

[52] James H Goldie, Michael J Gerver, Jerome E Kiley, and John R Swenbeck. Observations and theory of terfenol-d inchworm motors. In *Smart Structures and Materials 1998: Smart Structures and Integrated Systems*, volume 3329, pages 780–785. International Society for Optics and Photonics, 1998.

[53] Aldo Boglietti, Andrea Cavagnino, Alberto Tenconi, Silvio Vaschetto, and Politecnico di Torino. The safety critical electric machines and drives in the more electric aircraft: A survey. In *2009 35th Annual Conference of IEEE Industrial Electronics*, pages 2587–2594. IEEE, 2009.

[54] SC Trenter, AD Walmsley, G Landini, and JM Shippen. Assessment of the ultrasonic dental scaler insert. *Medical engineering & physics*, 24(2): 139–144, 2002.

[55] HA Chowdhury, Saiful Amri Mazlan, and Abdul Ghani Olabi. Implementation of magnetostrictive material terfenol-d in cng fuel injection actuation. In *Advanced Materials Research*, volume 47, pages 630–633. Trans Tech Publ, 2008.

[56] Jian-Jun Zhou, Yu-sheng Wang, Xia Wang, Ai-hua Meng, and Yu-liang Pan. Design of a flat-panel loudspeaker with giant magnetostrictive exciters. In *2008 Symposium on Piezoelectricity, Acoustic Waves, and Device Applications*, pages 528–532. IEEE, 2008.

[57] Mohammad Reza Karafi and Soroush Korivand. Design and fabrication of a novel vibration-assisted drilling tool using a torsional magnetostrictive transducer. *The International Journal of Advanced Manufacturing Technology*, 102(5-8):2095–2106, 2019.

[58] VI Aksinin, VV Apollonov, VI Borodin, AS Brynskikh, SA Chetkin, SV Murav'ev, VV Ostanin, and GV Vdovin. Spring-type magnetostriction actuator based on the wiedemam effect. *Sensors and Actuators A: Physical*, 21(1-3):236–242, 1990.

[59] JA Granath. Instrumentation applications of inverse-wiedemann effect. *Journal of Applied Physics*, 31(5):S178–S180, 1960.

[60] Frederick T Calkins and Alison B Flatau. Terfenol-d sensor design and optimization. In *NOISE CON*, pages 373–382. Noise control Foundation, 1997.

[61] R Chung, R Weber, and DC Jiles. A terfenol based magnetostrictive diode laser magnetometer. *IEEE transactions on magnetics*, 27(6):5358–5360, 1991.

[62] É Du. Tremolet de lacheisserie, magnetostriction: Theory and applications of magnetoelasticity, 1993.

[63] Ralph C Fenn and Michael J Gerver. Passive damping and velocity sensing using magnetostrictive transduction. In *Smart Structures and Materials 1994: Smart Structures and Intelligent Systems*, volume 2190, pages 216–227. International Society for Optics and Photonics, 1994.

[64] William J Fleming. Magnetostrictive torque sensors-comparison of branch, cross, and solenoidal designs. *SAE transactions*, pages 393–420, 1990.

[65] E Hristoforou and RE Reilly. Displacement sensors using soft magnetostrictive alloys. *IEEE transactions on magnetics*, 30(5):2728–2733, 1994.

[66] T Klinger, H Pfutzner, P Schonhuber, K Hoffmann, and N Bachl. Magnetostrictive amorphous sensor for biomedical monitoring. *IEEE transactions on magnetics*, 28(5):2400–2402, 1992.

[67] Russell G May and Richard O Claus. In-situ fiber optic sensor for composite cure monitoring through characterization of resin viscoelasticity. In *Nondestructive Evaluation for Process Control in Manufacturing*, volume 2948, pages 24–34. International Society for Optics and Photonics, 1996.

[68] Dave Nyce. Magnetostriction-based linear position sensors. *Sensors-the Journal of Applied Sensing Technology*, 11(4):22–26, 1994.

[69] Ljubiša Ristić. *Sensor technology and devices*. Artech House on Demand, 1994.

[70] Robert J Weber and David Jiles. *A Terfenol-D based magnetostrictive diode laser magnetometer*. Center for Advanced Technology Development, Iowa State University, 1992.

[71] SR White and RG Albers. Magnetostrictive tagging of composite materials for structural health monitoring. *USACERL Final Technical Paper*, 1996.

[72] T Worthington, P Calcagno, L Romankiw, and D Thompson. A magnetoacoustic keyboard. *IEEE Transactions on Magnetics*, 15(6):1797–1799, 1979.

[73] Zhangxian Deng and Marcelo J Dapino. Review of magnetostrictive vibration energy harvesters. *Smart Materials and Structures*, 26(10):103001, 2017.

[74] Fumio Narita and Marina Fox. A review on piezoelectric, magnetostrictive, and magnetoelectric materials and device technologies for energy harvesting applications. *Advanced Engineering Materials*, 20(5):1700743, 2018.

[75] Yang Bai, Heli Jantunen, and Jari Juuti. Energy harvesting research: the road from single source to multisource. *Advanced materials*, 30(34):1707271, 2018.

[76] Gary Backman, Ben Lawton, and Nicola A Morley. Magnetostrictive energy harvesting: Materials and design study. *IEEE Transactions on Magnetics*, 55(7):1–6, 2019.

[77] Toshiyuki Ueno and Sotoshi Yamada. Performance of energy harvester using iron–gallium alloy in free vibration. *IEEE transactions on magnetics*, 47(10):2407–2409, 2011.

[78] NH Duc, K Mackay, J Betz, and D Givord. Giant magnetostriction in amorphous (tb1- x dy x)(fe0. 45co0. 55) y films. *Journal of applied physics*, 79(2):973–977, 1996.

[79] F Schatz, M Hirscher, M Schnell, G Flik, and H Kronmüller. Magnetic anisotropy and giant magnetostriction of amorphous tbdyfe films. *Journal of applied physics*, 76(9):5380–5382, 1994.

[80] Sang Ho Lim, YS Choi, SH Han, HJ Kim, T Shima, and H Fujimori. Magnetostriction of sm–fe and sm–fe–b thin films fabricated by rf magnetron sputtering. *Journal of magnetism and magnetic materials*, 189(1):1–7, 1998.

[81] Eckhard Quandt and Alfred Ludwig. Magnetostrictive actuation in microsystems. *Sensors and Actuators A: Physical*, 81(1-3):275–280, 2000.

[82] E Quandt, A Ludwig, J Betz, K Mackay, and D Givord. Giant magnetostrictive spring magnet type multilayers. *Journal of applied physics*, 81 (8):5420–5422, 1997.

[83] Claude Chappert, Albert Fert, and Frédéric Nguyen Van Dau. The emergence of spin electronics in data storage. In *Nanoscience And Technology: A Collection of Reviews from Nature Journals*, pages 147–157. World Scientific, 2010.

[84] Russell P Cowburn. Change of direction. *Nature materials*, 6(4):255–256, 2007.

[85] DE Parkes, SA Cavill, AT Hindmarch, P Wadley, F McGee, CR Staddon, KW Edmonds, RP Campion, BL Gallagher, and AW Rushforth. Non-volatile voltage control of magnetization and magnetic domain walls in magnetostrictive epitaxial thin films. *Applied Physics Letters*, 101(7):072402, 2012.

[86] AW Rushforth, E De Ranieri, J Zemen, J Wunderlich, KW Edmonds, CS King, E Ahmad, RP Campion, CT Foxon, BL Gallagher, and *et al.* Voltage control of magnetocrystalline anisotropy in ferromagnetic-

semiconductor-piezoelectric hybrid structures. *Physical Review B*, 78(8): 085314, 2008.

[87] Ayan K Biswas, Supriyo Bandyopadhyay, and Jayasimha Atulasimha. Energy-efficient magnetoelastic non-volatile memory. *Applied Physics Letters*, 104(23):232403, 2014.

[88] William Thomson. Xxxi. the bakerian lecture.-on the electro-dynamic qualities of metals. *Philosophical Transactions of the Royal Society of London*, (146):649–751, 1856.

[89] Ching Tsang, M-M Chen, and Tadashi Yogi. Gigabit-density magnetic recording. *Proceedings of the IEEE*, 81(9):1344–1359, 1993.

[90] Stuart Parkin, Xin Jiang, Christian Kaiser, Alex Panchula, Kevin Roche, and Mahesh Samant. Magnetically engineered spintronic sensors and memory. *Proceedings of the IEEE*, 91(5):661–680, 2003.

[91] Ching Tsang, Tsann Lin, Scott MacDonald, Mustafa Pinarbasi, Neil Robertson, Hugo Santini, Mary Doerner, Tim Reith, Lang Vo, Tom Diola, and *et al.* 5 gb/in/sup 2/recording demonstration with conventional amr dual element heads and thin film disks. *IEEE Transactions on Magnetics*, 33(5):2866–2871, 1997.

[92] Grünberg Binasch, Peter Grünberg, F Saurenbach, and W Zinn. Enhanced magnetoresistance in layered magnetic structures with antiferromagnetic interlayer exchange. *Physical review B*, 39(7):4828, 1989.

[93] Albert Fert. Nobel lecture: Origin, development, and future of spintronics. *Reviews of modern physics*, 80(4):1517, 2008.

[94] Peter A Grünberg. Nobel lecture: From spin waves to giant magnetoresistance and beyond. *Reviews of Modern Physics*, 80(4):1531, 2008.

[95] Nevill Francis Mott. The electrical conductivity of transition metals. *Proceedings of the Royal Society of London. Series A-Mathematical and Physical Sciences*, 153(880):699–717, 1936.

[96] Nevill F Mott. Electrons in transition metals. *Advances in Physics*, 13(51): 325–422, 1964.

[97] IA Campbell, A Fert, and R Pomeroy. Evidence for two current conduction iron. *Philosophical Magazine*, 15(137):977–983, 1967.

[98] A Fert and IA Campbell. Two-current conduction in nickel. *Physical Review Letters*, 21(16):1190, 1968.

[99] Bernard Dieny, Virgil S Speriosu, Serhat Metin, Stuart SP Parkin, Bruce A Gurney, Peter Baumgart, and Dennis R Wilhoit. Magnetotransport properties of magnetically soft spin-valve structures. *Journal of Applied Physics*, 69(8):4774–4779, 1991.

[100] Ching Tsang, Robert E Fontana, Tsann Lin, David E Heim, Virgil S Speriosu, Bruce A Gurney, and Mason L Williams. Design, fabrication and testing of spin-valve read heads for high density recording. *IEEE Transactions on Magnetics*, 30(6):3801–3806, 1994.

[101] Sining Mao, Yonghua Chen, Feng Liu, Xingfu Chen, Bin Xu, Puling Lu, Mohammed Patwari, Haiwen Xi, Clif Chang, Brad Miller, and *et al.* Commercial tmr heads for hard disk drives: characterization and extendibility at 300 gbit 2. *IEEE transactions on magnetics*, 42(2):97–102, 2006.

[102] Jagadeesh S Moodera and George Mathon. Spin polarized tunneling in ferromagnetic junctions. *Journal of magnetism and magnetic materials*, 200(1-3):248–273, 1999.

[103] JM Slaughter. Materials for magnetoresistive random access memory. *Annual Review of Materials Research*, 39:277–296, 2009.

[104] HJ Zhu, M Ramsteiner, H Kostial, M Wassermeier, H-P Schönherr, and KH Ploog. Room-temperature spin injection from fe into gaas. *Physical Review Letters*, 87(1):016601, 2001.

[105] Aubrey T Hanbicki, BT Jonker, Grigorios Itskos, G Kioseoglou, and A Petrou. Efficient electrical spin injection from a magnetic metal/tun-

nel barrier contact into a semiconductor. *Applied Physics Letters*, 80(7): 1240–1242, 2002.

[106] A Hirohata, SJ Steinmueller, WS Cho, YB Xu, CM Guertler, G Wastlbauer, JAC Bland, and SN Holmes. Ballistic spin filtering across ferromagnet/semiconductor interfaces at room temperature. *Physical Review B*, 66 (3):035330, 2002.

[107] Arthur E Clark, James B Restorff, Marilyn Wun-Fogle, Thomas A Lograsso, and Deborah L Schlagel. Magnetostrictive properties of body-centered cubic fe-ga and fe-ga-al alloys. *IEEE Transactions on Magnetics*, 36(5):3238–3240, 2000.

[108] JR Cullen, AE Clark, M Wun-Fogle, JB Restorff, and TA Lograsso. Magnetoelasticity of fe–ga and fe–al alloys. *Journal of Magnetism and Magnetic Materials*, 226:948–949, 2001.

[109] Qingsong Xing, Y Du, RJ McQueeney, and TA Lograsso. Structural investigations of fe–ga alloys: phase relations and magnetostrictive behavior. *Acta Materialia*, 56(16):4536–4546, 2008.

[110] JX Cao, YN Zhang, WJ Ouyang, and RQ Wu. Large magnetostriction of fe 1- x ge x and its electronic origin: Density functional study. *Physical Review B*, 80(10):104414, 2009.

[111] Y Du, Mianliang Huang, S Chang, Deborah L Schlagel, Thomas A Lograsso, and Robert J McQueeney. Relation between ga ordering and magnetostriction of fe-ga alloys studied by x-ray diffuse scattering. *Physical Review B*, 81(5):054432, 2010.

[112] G Petculescu, KL Ledet, Mianliang Huang, Thomas A Lograsso, YN Zhang, RQ Wu, M Wun-Fogle, JB Restorff, AE Clark, and KB Hathaway. Magnetostriction, elasticity, and d03 phase stability in fe–ga and fe–ga–ge alloys. *Journal of Applied Physics*, 109(7):07A904, 2011.

[113] Hui Wang, YN Zhang, Teng Yang, ZD Zhang, LZ Sun, and RQ Wu. Ab

initio studies of the effect of nanoclusters on magnetostriction of fe 1- x ga x alloys. *Applied Physics Letters*, 97(26):262505, 2010.

[114] YN Zhang, JX Cao, and RQ Wu. Rigid band model for prediction of magnetostriction of iron-gallium alloys. *Applied Physics Letters*, 96(6):062508, 2010.

[115] Hu Cao, Peter M Gehring, Christopher P Devreugd, JA Rodriguez-Rivera, J Li, and D Viehland. Role of nanoscale precipitates on the enhanced magnetostriction of heat-treated galfenol (fe 1- x ga x) alloys. *Physical review letters*, 102(12):127201, 2009.

[116] MP Ruffoni, S Pascarelli, R Grössinger, R Sato Turtelli, C Bormio-Nunes, and RF Pettifer. Direct measurement of intrinsic atomic scale magnetostriction. *Physical review letters*, 101(14):147202, 2008.

[117] AG Khachaturyan and D Viehland. Structurally heterogeneous model of extrinsic magnetostriction for fe-ga and similar magnetic alloys: Part i. decomposition and confined displacive transformation. *Metallurgical and Materials Transactions A*, 38(13):2308–2316, 2007.

[118] Wei-Feng Rao and Armen G Khachaturyan. Phase field theory of proper displacive phase transformations: Structural anisotropy and directional flexibility, a vector model, and the transformation kinetics. *Acta materialia*, 59(11):4494–4503, 2011.

[119] Yangkun He, Chengbao Jiang, Wei Wu, Bin Wang, Huiping Duan, Hui Wang, Tianli Zhang, Jingmin Wang, Jinghua Liu, Zaoli Zhang, and *et al.* Giant heterogeneous magnetostriction in fe–ga alloys: effect of trace element doping. *Acta Materialia*, 109:177–186, 2016.

[120] Hui Wang, YN Zhang, RQ Wu, LZ Sun, DS Xu, and ZD Zhang. Understanding strong magnetostriction in fe 100- x ga x alloys. *Scientific reports*, 3:3521, 2013.

[121] AE Clark, M Wun-Fogle, JB Restorff, Thomas A Lograsso, and

G Petculescu. Magnetostriction and elasticity of body centered cubic fe 100- x be x alloys. *Journal of applied physics*, 95(11):6942–6944, 2004.

[122] G Petculescu, KB Hathaway, Thomas A Lograsso, M Wun-Fogle, and AE Clark. Magnetic field dependence of galfenol elastic properties. *Journal of Applied Physics*, 97(10):10M315, 2005.

[123] Manfred Wuttig, Liyang Dai, and James Cullen. Elasticity and magnetoelasticity of fe-ga solid solutions. *Applied Physics Letters*, 80(7):1135–1137, 2002.

[124] TA Lograsso, AR Ross, DL Schlagel, AE Clark, and M Wun-Fogle. Structural transformations in quenched fe–ga alloys. *Journal of Alloys and Compounds*, 350(1-2):95–101, 2003.

[125] Ruqian Wu. Origin of large magnetostriction in fega alloys. *Journal of Applied Physics*, 91(10):7358–7360, 2002.

[126] Gottfried Wastlbauer and J Anthony C Bland*. Structural and magnetic properties of ultrathin epitaxial fe films on gaas (001) and related semiconductor substrates. *Advances in physics*, 54(2):137–219, 2005.

[127] Mike RJ Gibbs. Materials optimization for magnetic mems. *IEEE transactions on magnetics*, 43(6):2666–2671, 2007.

[128] RA Dunlap, NC Deschamps, RE Mar, and SP Farrell. Mössbauer effect studies of fe100- xgax films prepared by combinatorial methods. *Journal of Physics: Condensed Matter*, 18(20):4907, 2006.

[129] A Javed, NA Morley, and MRJ Gibbs. Structure, magnetic and magnetostrictive properties of as-deposited fe–ga thin films. *Journal of magnetism and magnetic materials*, 321(18):2877–2882, 2009.

[130] Jason R Hattrick-Simpers, Dwight Hunter, Corneliu M Craciunescu, Kyu Sung Jang, Makoto Murakami, James Cullen, Manfred Wuttig, Ichiro Takeuchi, Samuel E Lofland, Leonid Benderksy, and *et al.* Combinatorial investigation of magnetostriction in fe–ga and fe–ga–al. *Applied Physics Letters*, 93(10):102507, 2008.

[131] A Javed, T Szumiata, NA Morley, and MRJ Gibbs. An investigation of the effect of structural order on magnetostriction and magnetic behavior of fe–ga alloy thin films. *Acta Materialia*, 58(11):4003–4011, 2010.

[132] NA Morley, A Javed, and MRJ Gibbs. Effect of a forming field on the magnetic and structural properties of thin fe–ga films. *Journal of Applied Physics*, 105(7):07A912, 2009.

[133] Katarzyna Brzózka, Michał Gawroński, Małgorzata Gzik-Szumiata, Athar Javed, Nicola A Morley, and Mike RJ Gibbs. Mössbauer study of vacuum annealed fe100-xgax (10≤ x≤ 35) thin films.

[134] Lalitha Raveendran Nivedita, Valiveti Venkata Siva Kumar, Kandasami Asokan, and Ramasamy Thangavelu Rajendrakumar. Growth and magnetic properties of rf sputtered fe-ga thin films. *Materials Research*, 18(5):946–952, 2015.

[135] A Butera, J Gómez, JA Barnard, and JL Weston. Magnetic anisotropy in fe81ga19/mgo (1 0 0) films sputtered at different powers. *Physica B: Condensed Matter*, 384(1-2):262–264, 2006.

[136] A Butera, J Gómez, JL Weston, and JA Barnard. Growth and magnetic characterization of epitaxial fe 81 ga 19/ mgo (100) thin films. *Journal of applied physics*, 98(3):033901, 2005.

[137] Yasushi Endo, Yasuyuki Kawabe, Takamichi Miyazaki, and Yutaka Shimada. Effect of ga composition on the static and dynamic magnetic properties of fe100-xgax films (18.5≤ x≤ 33.4). *Journal of Magnetism and Magnetic Materials*, 487:165323, 2019.

[138] A Javed, NA Morley, and MRJ Gibbs. Thickness dependence of magnetic and structural properties in fe 80 ga 20 thin films. *Journal of Applied Physics*, 107(9):09A944, 2010.

[139] Daniel B Gopman, Vimal Sampath, Hasnain Ahmad, Supriyo Bandyopadhyay, and Jayasimha Atulasimha. Static and dynamic magnetic properties

of sputtered fe–ga thin films. *IEEE transactions on magnetics*, 53(11):1–4, 2017.

[140] Yasushi Endo, Takumi Sakai, Takamichi Miyazaki, and Yutaka Shimada. Effect of film thickness on the high frequency magnetic properties of polycrystalline fe–ga films. *IEEE Transactions on Magnetics*, 53(11):1–5, 2017.

[141] Julian Dean, MT Bryan, NA Morley, G Hrkac, A Javed, MRJ Gibbs, and DA Allwood. Numerical study of the effective magnetocrystalline anisotropy and magnetostriction in polycrystalline fega films. *Journal of Applied Physics*, 110(4):043902, 2011.

[142] Bijoy K Kuanr, RE Camley, Z Celinski, Adam McClure, and Yves Idzerda. Single crystal fe1- xgax thin films for monolithic microwave devices. *Journal of Applied Physics*, 115(17):17C112, 2014.

[143] Stephen Blundell. Magnetism in condensed matter, 2003.

[144] B. D. Cullity and C. D. Graham. *Introduction to Magnetic Materials*. Wiley-IEEE Press, 2 edition, 2008. ISBN 0471477419, 9780471477419.

[145] Charles Kittel. *Introduction to Solid State Physics*. Wiley, 8 edition, 2004. ISBN 9780471415268. URL `http://www.amazon.com/Introduction-Solid-Physics-Charles-Kittel/dp/047141526X/ref=dp_ob_title_bk`.

[146] Michael Farle. Ferromagnetic resonance of ultrathin metallic layers. *Reports on Progress in Physics*, 61:755, 01 1999. doi: 10.1088/0034-4885/61/7/001.

[147] Mathias Getzlaff. *Fundamentals of magnetism*. Springer Science & Business Media, 2007.

[148] B Heinrich, T Monchesky, and R Urban. Role of interfaces in higher order angular terms of magnetic anisotropies: ultrathin film structures. *Journal of magnetism and magnetic materials*, 236(3):339–346, 2001.

[149] MT Johnson, PJH Bloemen, FJA Den Broeder, and JJ De Vries. Magnetic anisotropy in metallic multilayers. *Reports on Progress in Physics*, 59(11): 1409, 1996.

[150] Alex Hubert and Rudolf Schäfer. *Magnetic domains: the analysis of magnetic microstructures*. Springer Science & Business Media, 2008.

[151] EC Stoner and EP Wohlfarth. Philos. trans. r. soc. london, ser. a. *A mechanism of magnetic hysteresis in heterogeneous alloys*, 240:599–642, 1948.

[152] C Tannous and J Gieraltowski. The stoner-wohlfarth model of ferromagnetism: Static properties. *arXiv: physics/0607118*.

[153] Neil W Ashcroft and N David Mermin. Solid state physics (saunders college, philadelphia, 1976). *Appendix N*, 2010.

[154] AE Berkowitz, JR Mitchell, MJ Carey, AP Young, Shufeng Zhang, FE Spada, FT Parker, A Hutten, and G Thomas. Giant magnetoresistance in heterogeneous cu-co alloys. *Physical Review Letters*, 68(25):3745, 1992.

[155] Thomas L Gilbert. A phenomenological theory of damping in ferromagnetic materials. *IEEE Transactions on Magnetics*, 40(6):3443–3449, 2004.

[156] M Lakshmanan. The fascinating world of the landau–lifshitz–gilbert equation: an overview. *Philosophical Transactions of the Royal Society A: Mathematical, Physical and Engineering Sciences*, 369(1939):1280–1300, 2011.

[157] Bretislav Heinrich and J Anthony C Bland. *Ultrathin magnetic structures II: Measurement techniques and novel magnetic properties*, volume 2. Springer Science & Business Media, 2006.

[158] C Bilzer, T Devolder, P Crozat, C Chappert, S Cardoso, and PP Freitas. Vector network analyzer ferromagnetic resonance of thin films on coplanar waveguides: Comparison of different evaluation methods. *Journal of applied physics*, 101(7):074505, 2007.

[159] Charles Kittel. On the theory of ferromagnetic resonance absorption. *Physical Review*, 73(2):155, 1948.

[160] D Fang, H Kurebayashi, J Wunderlich, K Vỳbornỳ, Liviu P Zârbo, RP Campion, A Casiraghi, BL Gallagher, T Jungwirth, and AJ Fergu-

son. Spin–orbit-driven ferromagnetic resonance. *Nature nanotechnology*, 6 (7):413, 2011.

[161] J Smit and HG Beljers. Philips res. rep. 10, 113 (1955). *Google Scholar CAS*, 1957.

[162] J Smith and HG Beljers. Ferromagnetic resonance absorption in bafe12o19, a highly anisotropic crystal. *Phillips Res. Rep*, 10(2):113–130, 1955.

[163] SV Vonsovskii. *Ferromagnetic resonance: the phenomenon of resonant absorption of a high-frequency magnetic field in ferromagnetic substances*. Elsevier, 2016.

[164] H Suhl. Ferromagnetic resonance in nickel ferrite between one and two kilomegacycles. *Physical Review*, 97(2):555, 1955.

[165] Kh Zakeri, J Lindner, I Barsukov, R Meckenstock, M Farle, U Von Hörsten, H Wende, W Keune, J Rocker, SS Kalarickal, and *et al.* Spin dynamics in ferromagnets: Gilbert damping and two-magnon scattering. *Physical Review B*, 76(10):104416, 2007.

[166] Shufeng Zhang and Z Li. Roles of nonequilibrium conduction electrons on the magnetization dynamics of ferromagnets. *Physical Review Letters*, 93 (12):127204, 2004.

[167] K Lenz, H Wende, W Kuch, K Baberschke, Kálmán Nagy, and András Jánossy. Two-magnon scattering and viscous gilbert damping in ultrathin ferromagnets. *Physical Review B*, 73(14):144424, 2006.

[168] Georg Woltersdorf, Matthias Buess, B Heinrich, and CH Back. Time resolved magnetization dynamics of ultrathin fe (001) films: Spin-pumping and two-magnon scattering. *Physical review letters*, 95(3):037401, 2005.

[169] E Šimánek and B Heinrich. Gilbert damping in magnetic multilayers. *Physical Review B*, 67(14):144418, 2003.

[170] V Korenman and RE Prange. Anomalous damping of spin waves in magnetic metals. *Physical Review B*, 6(7):2769, 1972.

[171] Mark C Hickey and Jagadeesh S Moodera. Origin of intrinsic gilbert damping. *Physical review letters*, 102(13):137601, 2009.

[172] V Kamberskỳ. On ferromagnetic resonance damping in metals. *Czechoslovak Journal of Physics B*, 26(12):1366–1383, 1976.

[173] J Kuneš and V Kamberskỳ. First-principles investigation of the damping of fast magnetization precession in ferromagnetic 3 d metals. *Physical Review B*, 65(21):212411, 2002.

[174] Olle Eriksson, Anders Bergman, Lars Bergqvist, and Johan Hellsvik. *Atomistic spin dynamics: foundations and applications*. Oxford university press, 2017.

[175] A Layadi. A theoretical investigation of ferromagnetic resonance linewidth and damping constants in coupled trilayer and spin valve systems. *AIP Advances*, 5(5):057113, 2015.

[176] Rodrigo Arias and DL Mills. Extrinsic contributions to the ferromagnetic resonance response of ultrathin films. *Physical review B*, 60(10):7395, 1999.

[177] Robert E Camley, Zbigniew Celinski, and Robert L Stamps. *Magnetism of Surfaces, Interfaces, and Nanoscale Materials*. Elsevier, 2015.

[178] Rosa A Lukaszew. *Handbook of nanomagnetism: applications and tools*. CRC Press, 2015.

[179] Mario Norberto Baibich, Jean Marc Broto, Albert Fert, F Nguyen Van Dau, Frédéric Petroff, P Etienne, G Creuzet, A Friederich, and J Chazelas. Giant magnetoresistance of (001) fe/(001) cr magnetic superlattices. *Physical review letters*, 61(21):2472, 1988.

[180] H Dery, P Dalal, LJ Sham, and *et al.* Spin-based logic in semiconductors for reconfigurable large-scale circuits. *Nature*, 447(7144):573, 2007.

[181] PP Freitas, R Ferreira, S Cardoso, and F Cardoso. Magnetoresistive sensors. *Journal of Physics: Condensed Matter*, 19(16):165221, 2007.

[182] EH Hall. On a new action of the jia19flet onz electric currents. *American Journal of Mathematics*, 2(3):287–292, 1879.

[183] Naoto Nagaosa, Jairo Sinova, Shigeki Onoda, Allan H MacDonald, and Nai Phuan Ong. Anomalous hall effect. *Reviews of modern physics*, 82(2): 1539, 2010.

[184] Jerome M Lavine. Alternate current apparatus for measuring the ordinary hall coefficient of ferromagnetic metals and semiconductors. *Review of Scientific Instruments*, 29(11):970–976, 1958.

[185] Emerson M Pugh. Hall effect and the magnetic properties of some ferromagnetic materials. *Physical Review*, 36(9):1503, 1930.

[186] William Thomson. Xix. on the electro-dynamic qualities of metals:—effects of magnetization on the electric conductivity of nickel and of iron. *Proceedings of the Royal Society of London*, (8):546–550, 1857.

[187] IA Campbell, A Fert, and O Jaoul. The spontaneous resistivity anisotropy in Ni-based alloys. *Journal of Physics C: Solid State Physics*, 3(1S):S95, 1970.

[188] AW Rushforth, K Vỳbornỳ, CS King, KW Edmonds, RP Campion, CT Foxon, J Wunderlich, AC Irvine, P Vašek, V Novák, and *et al.* Anisotropic magnetoresistance components in (Ga,Mn)As. *Physical Review Letters*, 99(14):147207, 2007.

[189] Shinya Osakabe and Sadao Adachi. Study of GaAs(001) surfaces treated in aqueous HCl solutions. *Japanese Journal of Applied Physics, Part 1: Regular Papers and Short Notes and Review Papers*, 36(12 A):7119–7125, 1997. ISSN 00214922.

[190] J Crites, W Snodgrass, and L Luu. Dynamics of Surface Treatments and Pre-Cleans for High Volume Wafer Manufacturing. In *Proceedings of CS ManTech Conference 2015*, pages 87–90, 2015.

[191] Lalitha Raveendran Nivedita, Valiveti Venkata Siva Kumar, Kandasami Asokan, and Ramasamy Thangavelu Rajendrakumar. Growth and Magnetic Properties of RF Sputtered Fe-Ga Thin Films. *Materials Research*, 18(5):946–952, 2015. doi: 10.1590/1516-1439.349014. URL http://dx.doi.org/10.1590/1516-1439.349014.

[192] M K Ryu, S H Lee, M S Jang, G N Panin, and T W Kang. Postgrowth annealing effect on structural and optical properties of ZnO films grown on GaAs substrates by the radio frequency magnetron sputtering technique. *Journal of Applied Physics*, 92(1):154–158, 2002. ISSN 00218979. doi: 10.1063/1.1483371. URL https://doi.org/10.1063/1.1483371.

[193] R L Fagaly. Superconducting quantum interference device instruments and applications. In *Review of Scientific Instruments*, volume 77, page 101101, 2006. ISBN 1011012006. doi: 10.1063/1.2354545. URL https://doi.org/10.1063/1.2354545.

[194] J. M L Beaujour, A D Kent, D W Abraham, and J Z Sun. Ferromagnetic resonance study of polycrystalline Fe1-x Vx alloy thin films. *Journal of Applied Physics*, 103(7):7–519, 2008. ISSN 00218979. doi: 10.1063/1.2830648. URL https://doi.org/10.1063/1.2830648.

[195] H. Suhl. Ferromagnetic resonance in nickel ferrite between one and two kilomegacycles. *Phys. Rev.*, 97:555–557, Jan 1955. doi: 10.1103/PhysRev.97.555.2. URL https://link.aps.org/doi/10.1103/PhysRev.97.555.2.

[196] HL Luo. Lattice parameters of iron-rich iron-gallium alloys. *AIME MET SOC TRANS*, 239(1):119–120, 1967.

[197] JM Borrego, JS Blazquez, CF Conde, A Conde, and S Roth. Structural ordering and magnetic properties of arc-melted fega alloys. *Intermetallics*, 15(2):193–200, 2007.

[198] JC Vickerman and AJ Swift. Secondary ion mass spectrometry—the surface mass spectrometry. *Surface analysis—the principal techniques. Wiley, Chichester*, 1997.

[199] Tery L Barr and ESCA Modern. The principles and practice of x-ray photoelectron spectroscopy. *CRC, Boca Raton, FL*, page 11, 1994.

[200] Gerhard Ertl and Jürgen Küppers. *Low energy electrons and surface chemistry*. Vch Weinheim, 1985.

[201] JJ Krebs, BT Jonker, and GA Prinz. Properties of fe single-crystal films grown on (100) gaas by molecular-beam epitaxy. *Journal of applied physics*, 61(7):2596–2599, 1987.

[202] E Arenholz, G van der Laan, A McClure, and Y Idzerda. Electronic and magnetic structure of ga x fe 1- x thin films. *Physical review B*, 82(18): 180405, 2010.

[203] T Khmelevska, S Khmelevskyi, and Peter Mohn. Magnetism and structural ordering on a bcc lattice for highly magnetostrictive fe–ga alloys: A coherent potential approximation study. *Journal of Applied Physics*, 103(7):073911, 2008.

[204] Zheng Lei, Jiang Cheng-Bao, Shang Jia-Xiang, and Xu Hui-Bin. First principles study on the magnetocrystalline anisotropy of fe–ga magnetostrictive alloys. *Chinese Physics B*, 18(4):1647, 2009.

[205] F Bensch, R Moosbühler, and G Bayreuther. Onset of magnetic anisotropy in epitaxial fe films on gaas (001). *Journal of applied physics*, 91(10):8754–8756, 2002.

[206] O Thomas, Q Shen, Philippe Schieffer, N Tournerie, and Bruno Lépine. Interplay between anisotropic strain relaxation and uniaxial interface magnetic anisotropy in epitaxial fe films on (001) gaas. *Physical Review Letters*, 90(1):017205, 2003.

[207] M Brockmann, M Zölfl, S Miethaner, and G Bayreuther. In-plane volume and interface magnetic anisotropies in epitaxial fe films on gaas (0 0 1). *Journal of magnetism and magnetic materials*, 198:384–386, 1999.

[208] R Zuberek, K Fronc, A Szewczyk, MU Gutowska, H Szymczak, and MRJ Gibbs. Thickness dependence of magnetic anisotropy and magnetoelastic

constants in epitaxial fe/gaas (001) thin films. *Czechoslovak journal of physics*, 52(1):A169–A172, 2002.

[209] M Gester, C Daboo, RJ Hicken, SJ Gray, A Ercole, and JA C Bland. Continuous evolution of the in-plane magnetic anisotropies with thickness in epitaxial fe films. *Journal of applied physics*, 80(1):347–355, 1996.

[210] RJ Hicken, DEP Eley, M Gester, SJ Gray, C Daboo, AJR Ives, and JAC Bland. Brillouin light scattering studies of magnetic anisotropy in epitaxial fe/gaas films. *Journal of magnetism and magnetic materials*, 145(3):278–292, 1995.

[211] Thomas Hupfauer, A Matos-Abiague, Martin Gmitra, Fritz Schiller, Josef Loher, Dominique Bougeard, Christian H Back, Jaroslav Fabian, and Dieter Weiss. Emergence of spin–orbit fields in magnetotransport of quasi-two-dimensional iron on gallium arsenide. *Nature communications*, 6(1):1–6, 2015.

[212] FL Zeng, C Zhou, MW Jia, D Shi, Y Huo, W Zhang, and YZ Wu. Strong current-direction dependence of anisotropic magnetoresistance in single crystalline fe/gaas (1 1 0) films. *Journal of Magnetism and Magnetic Materials*, 499:166204, 2020.

[213] R Ramos, SK Arora, and IV Shvets. Anomalous anisotropic magnetoresistance in epitaxial fe 3 o 4 thin films on mgo (001). *Physical Review B*, 78 (21):214402, 2008.

[214] Z Ding, JX Li, J Zhu, TP Ma, C Won, and YZ Wu. Three-dimensional mapping of the anisotropic magnetoresistance in fe3o4 single crystal thin films. *Journal of Applied Physics*, 113(17):17B103, 2013.

[215] AW Rushforth, K Výborný, CS King, KW Edmonds, RP Campion, CT Foxon, J Wunderlich, AC Irvine, V Novák, K Olejník, and *et al.* The origin and control of the sources of amr in (ga, mn) as devices. *Journal of Magnetism and Magnetic Materials*, 321(8):1001–1008, 2009.

[216] Karel Vỳbornỳ, Jan Kučera, Jairo Sinova, AW Rushforth, BL Gallagher, and T Jungwirth. Microscopic mechanism of the noncrystalline anisotropic magnetoresistance in (ga, mn) as. *Physical Review B*, 80(16):165204, 2009.

[217] KT Riggs, E Dan Dahlberg, and GA Prinz. First-order magnetic-field-induced phase transition in epitaxial iron films studied by magnetoresistance. *Physical Review B*, 41(10):7088, 1990.

[218] Sangita S Kalarickal, Pavol Krivosik, Mingzhong Wu, Carl E Patton, Michael L Schneider, Pavel Kabos, Thomas J Silva, and John P Nibarger. Ferromagnetic resonance linewidth in metallic thin films: Comparison of measurement methods. *Journal of Applied Physics*, 99(9):093909, 2006.

[219] G Woltersdorf. Spin-pumping and two-magnon scattering in magnetic multilayers phd thesis simon fraser university, 2004.

[220] Nobuo Kawamiya, Kengo Adachi, and Yoji Nakamura. Magnetic properties and mössabauer investigations of fe-ga alloys. *Journal of the Physical Society of Japan*, 33(5):1318–1327, 1972.

[221] Duong Anh Tuan, Dang Duc Dung, Vo Thanh Son, Yooleemi Shin, and Sunglae Cho. Magnetism and transport properties of epitaxial fe–ga thin films on gaas (001). *Journal of Applied Physics*, 111(7):07C517, 2012.

[222] RA Kellogg, Alison B Flatau, AE Clark, M Wun-Fogle, and Thomas A Lograsso. Temperature and stress dependencies of the magnetic and magnetostrictive properties of fe 0.81 ga 0.19. *Journal of applied physics*, 91 (10):7821–7823, 2002.

[223] OMJ van 't Erve, CH Li, G Kioseoglou, AT Hanbicki, M Osofsky, S-F Cheng, and BT Jonker. Epitaxial growth and electrical spin injection from fe (1- x) ga x (001) films on al ga as/ ga as (001) heterostructures. *Applied Physics Letters*, 91(12):122515, 2007.

[224] C Scheck, L Cheng, I Barsukov, Z Frait, and WE Bailey. Low relaxation rate in epitaxial vanadium-doped ultrathin iron films. *Physical review letters*, 98(11):117601, 2007.

Appendix A

SQUID Magnetometry fitting

The uniaxial and cubic anisotropy constants of the samples discussed in this thesis were extracted from the hysteresis loops obtained by SQUID experiment at room temperature using a mathematical fitting model discussed in section 3.3.1. This appendix contains the loops fitted to the SQUID data in chapter 5. The black points represent the experimental data, and the red line shows the fitted curve in all the graphs below.

A.0.1 $Fe_{100-x}Ga_x$ thin films with varying Ga concentration.

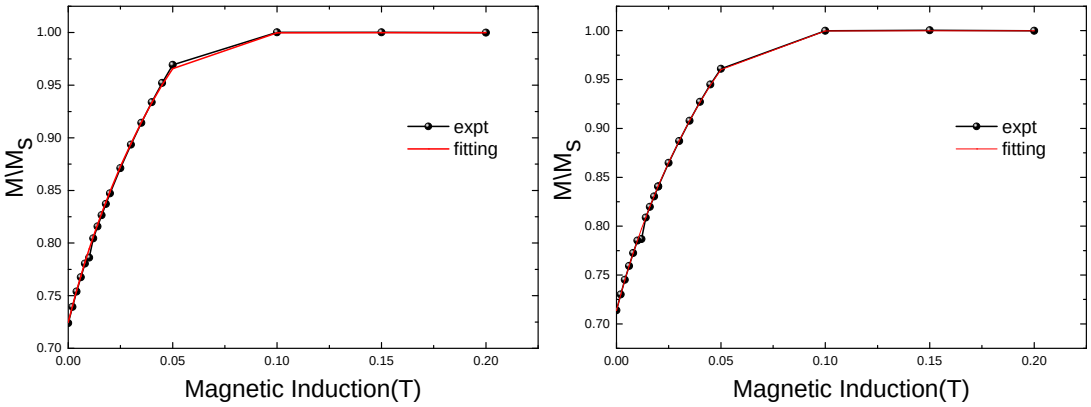

(a) [110] (b) [1$\bar{1}$0]

Figure A.1: Demonstrates the fitting between simulated data and experimental data collected using a SQUID magnetometer for sample $Fe_{93}Ga_{07}$ along (a) [110] and (b) [1$\bar{1}$0] crystalline direction.

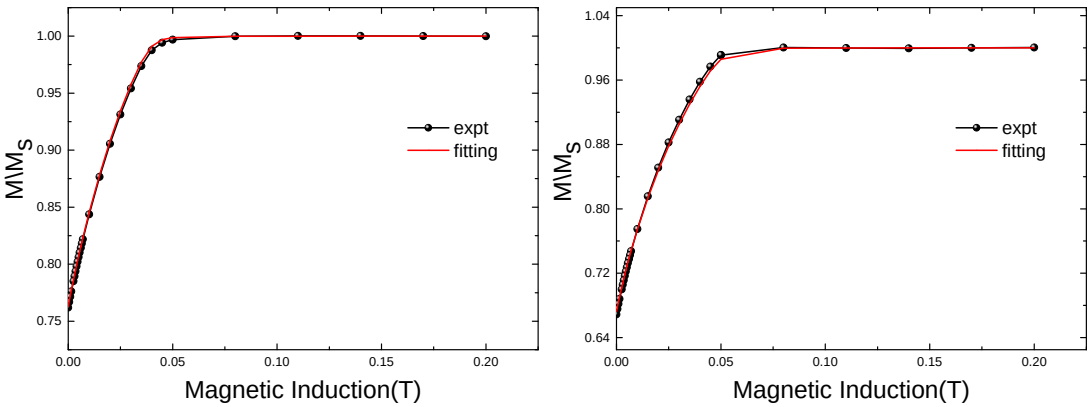

(a) [110] (b) [1$\bar{1}$0]

Figure A.2: Demonstrates the fitting between simulated data and experimental data collected using a SQUID magnetometer for sample $Fe_{91}Ga_{09}$ along (a) [110] and (b) [1$\bar{1}$0] crystalline direction.

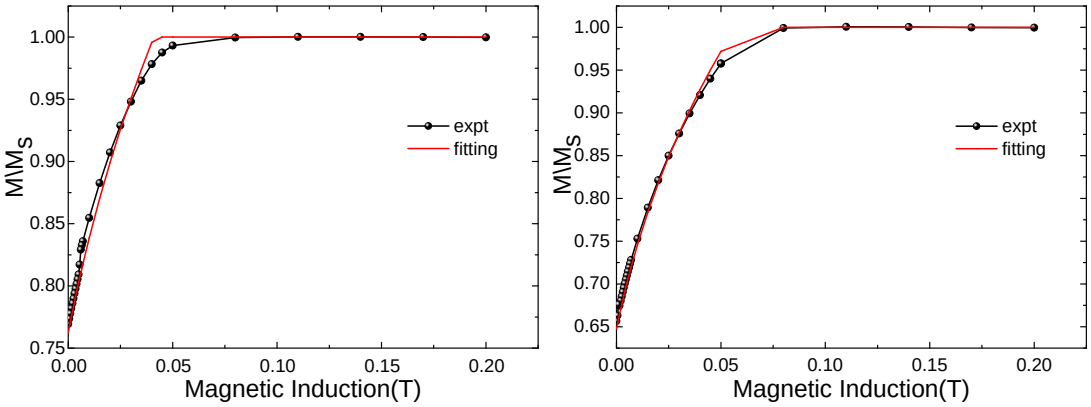

(a) [110] (b) [1$\bar{1}$0]

Figure A.3: Demonstrates the fitting between simulated data and experimental data collected using a SQUID magnetometer for sample $Fe_{90}Ga_{10}$ along (a) [110] and (b) [1$\bar{1}$0] crystalline direction.

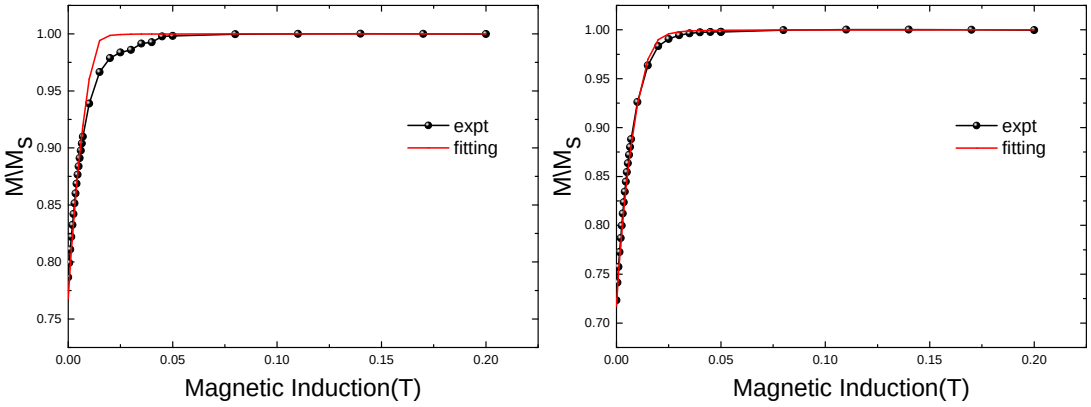

(a) [110] (b) [1$\bar{1}$0]

Figure A.4: Demonstrates the fitting between simulated data and experimental data collected using a SQUID magnetometer for sample $Fe_{88}Ga_{12}$ along (a) [110] and (b) [1$\bar{1}$0] crystalline direction.

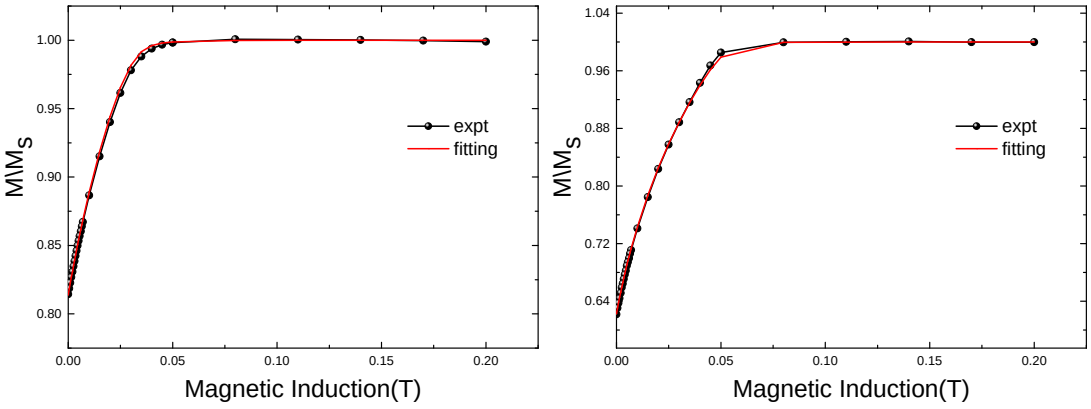

(a) [110] (b) [$1\bar{1}0$]

Figure A.5: Demonstrates the fitting between simulated data and experimental data collected using a SQUID magnetometer for sample $Fe_{86}Ga_{14}$ along (a) [110] and (b) [$1\bar{1}0$] crystalline direction.

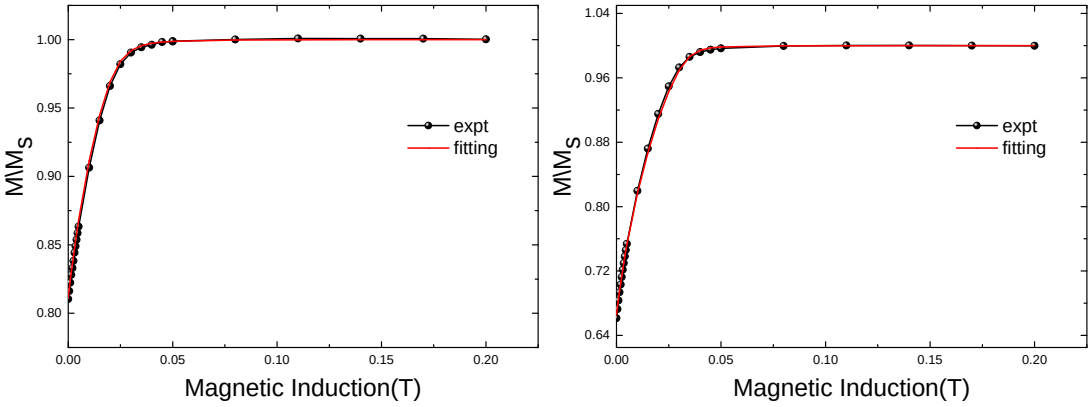

(a) [110] (b) [$1\bar{1}0$]

Figure A.6: Demonstrates the fitting between simulated data and experimental data collected using a SQUID magnetometer for sample $Fe_{85}Ga_{15}$ along (a) [110] and (b) [$1\bar{1}0$] crystalline direction.

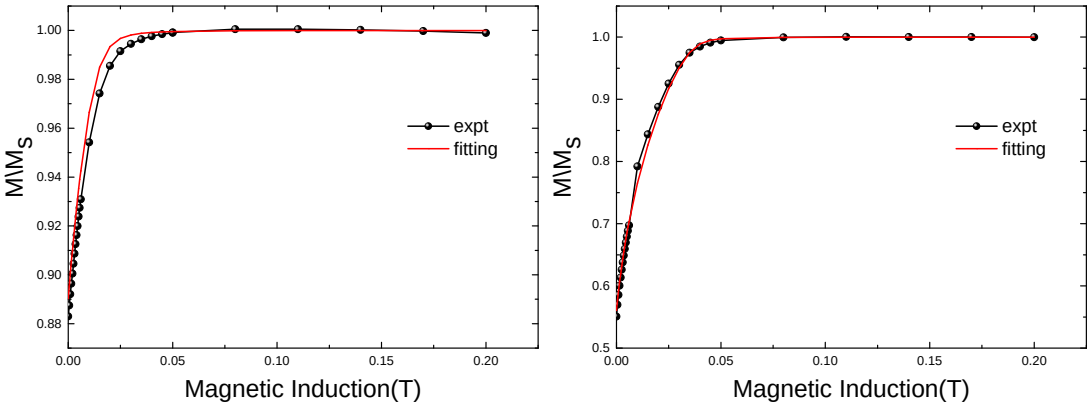

(a) [110] (b) [1$\bar{1}$0]

Figure A.7: Demonstrates the fitting between simulated data and experimental data collected using a SQUID magnetometer for sample $Fe_{82}Ga_{18}$ along (a) [110] and (b) [1$\bar{1}$0] crystalline direction.

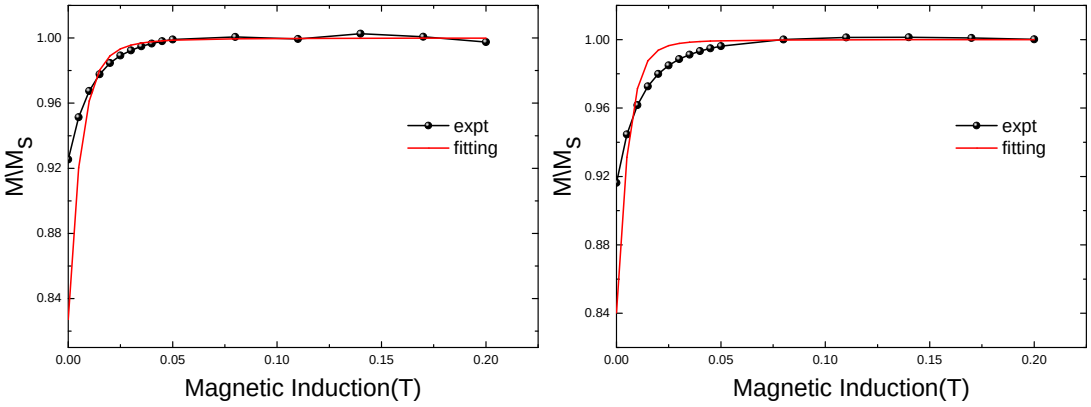

(a) [110] (b) [1$\bar{1}$0]

Figure A.8: Demonstrates the fitting between simulated data and experimental data collected using a SQUID magnetometer for sample $Fe_{80}Ga_{20}$ along (a) [110] and (b) [1$\bar{1}$0] crystalline direction.

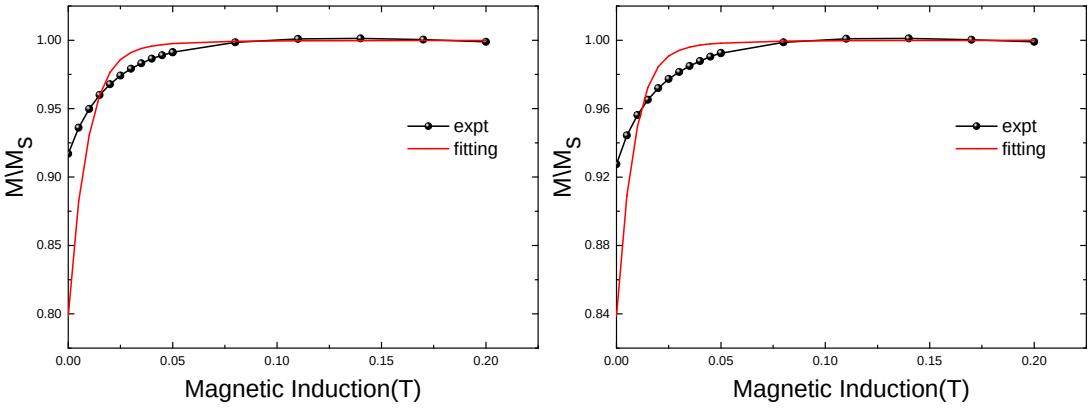

(a) [110] (b) [1$\bar{1}$0]

Figure A.9: Demonstrates the fitting between simulated data and experimental data collected using a SQUID magnetometer for sample $Fe_{76}Ga_{24}$ along (a) [110] and (b) [1$\bar{1}$0] crystalline direction.

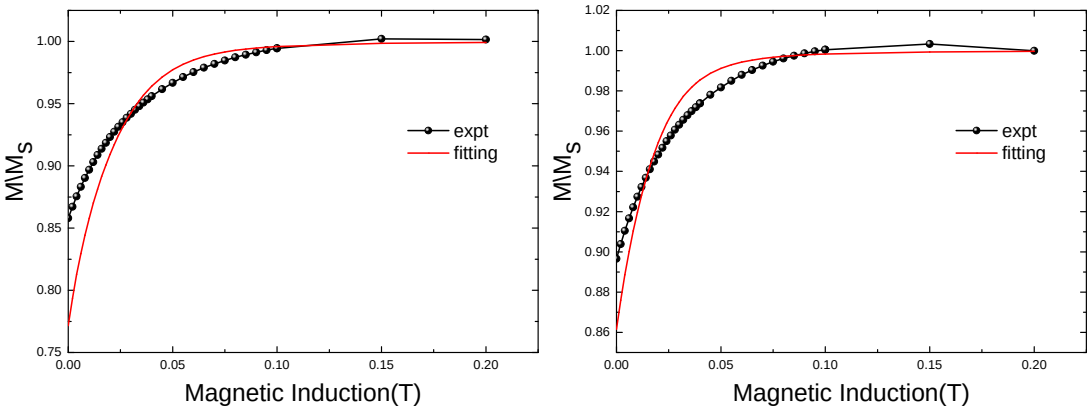

(a) [110] (b) [1$\bar{1}$0]

Figure A.10: Demonstrates the fitting between simulated data and experimental data collected using a SQUID magnetometer for sample $Fe_{70}Ga_{30}$ along (a) [110] and (b) [1$\bar{1}$0] crystalline direction.

A.0.2 $Fe_{79}Ga_{21}$ thin films with varying film thickness.

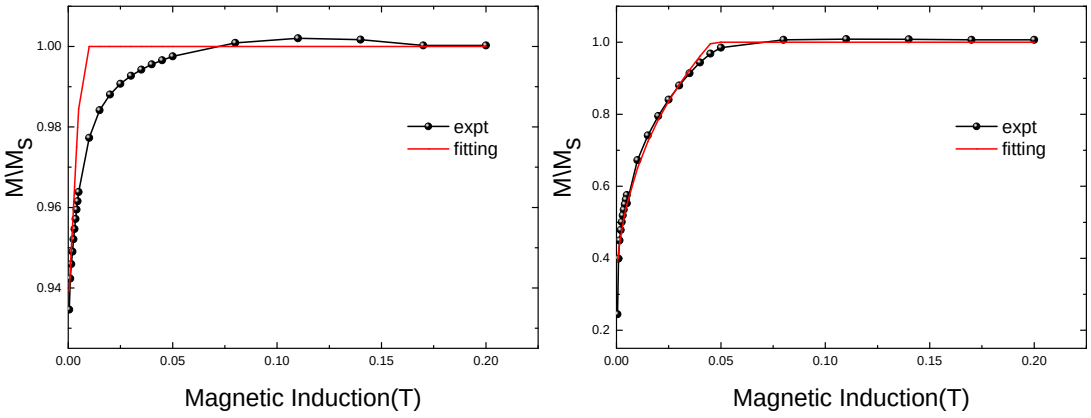

(a) [110] (b) [1$\bar{1}$0]

Figure A.11: Demonstrates the fitting between simulated data and experimental data collected using a SQUID magnetometer for sample $Fe_{79}Ga_{21}$ with 5 nm film thickness along (a) [110] and (b) [1$\bar{1}$0] crystalline direction.

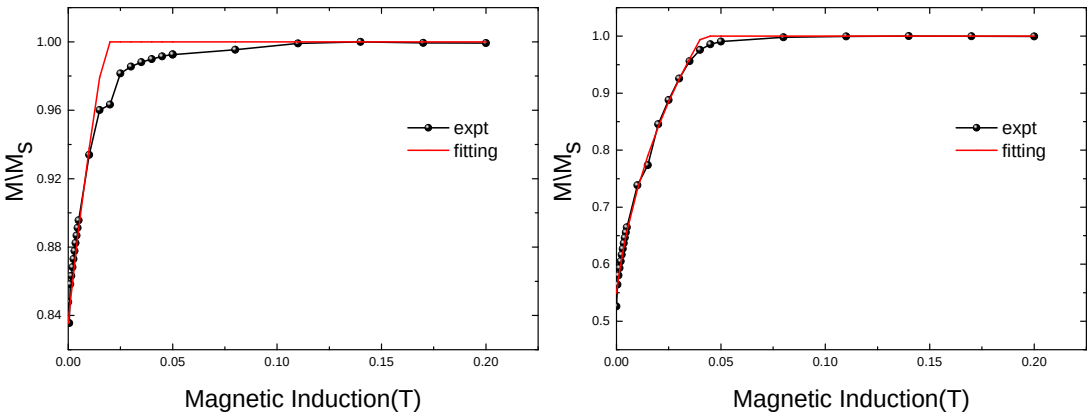

(a) [110] (b) [1$\bar{1}$0]

Figure A.12: Demonstrates the fitting between simulated data and experimental data collected using a SQUID magnetometer for sample $Fe_{79}Ga_{21}$ with 7.5 nm film thickness along (a) [110] and (b) [1$\bar{1}$0] crystalline direction.

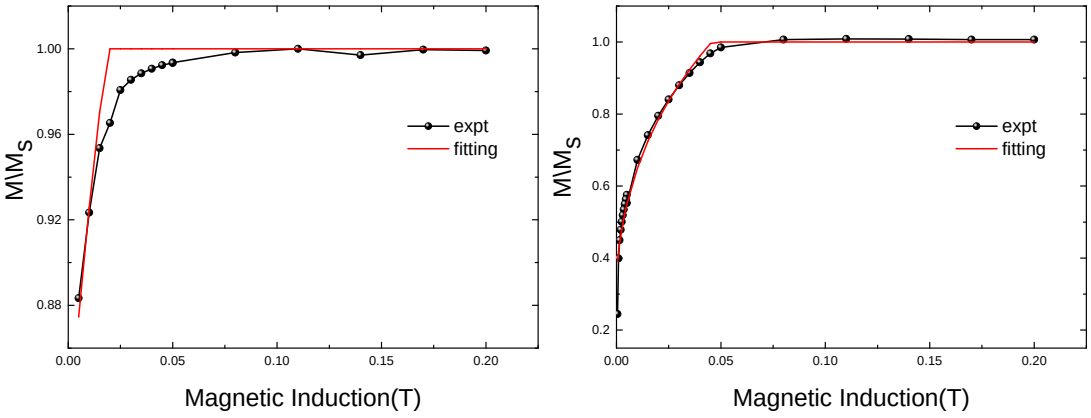

(a) [110] (b) [1$\bar{1}$0]

Figure A.13: Demonstrates the fitting between simulated data and experimental data collected using a SQUID magnetometer for sample $Fe_{79}Ga_{21}$ with 10 nm film thickness along (a) [110] and (b) [1$\bar{1}$0] crystalline direction.

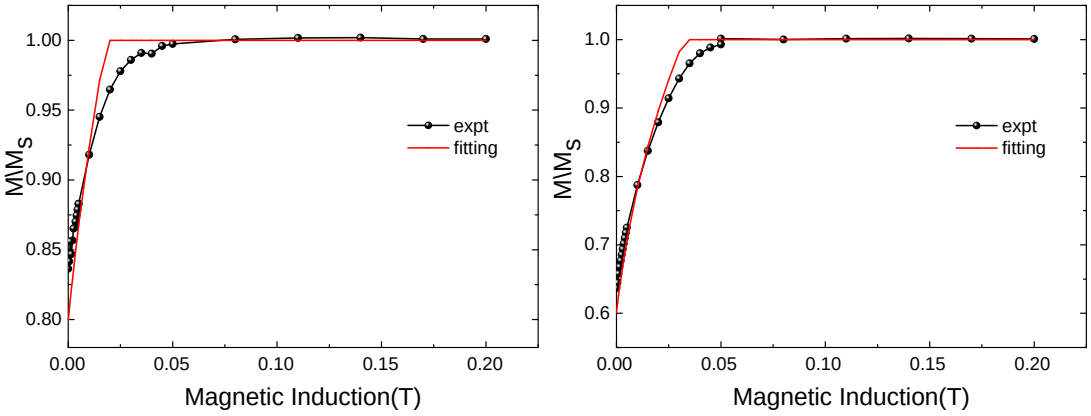

(a) [110] (b) [1$\bar{1}$0]

Figure A.14: Demonstrates the fitting between simulated data and experimental data collected using a SQUID magnetometer for sample $Fe_{79}Ga_{21}$ with 20 nm film thickness along (a) [110] and (b) [1$\bar{1}$0] crystalline direction.

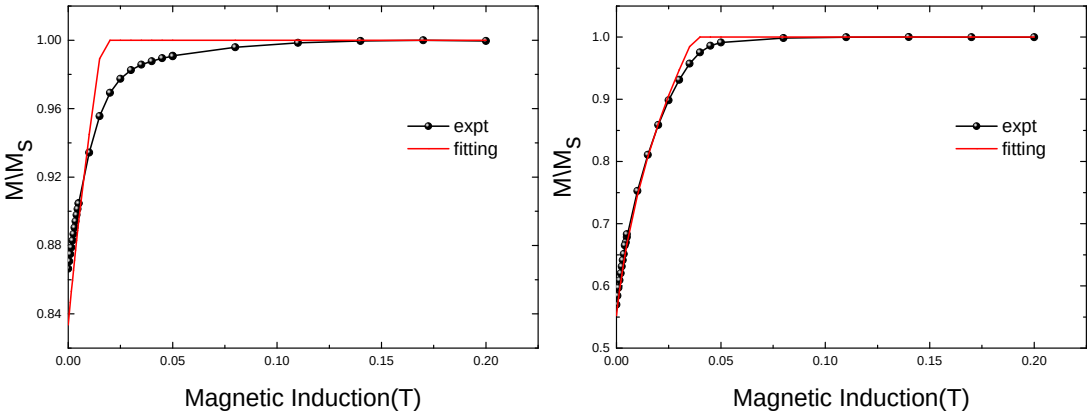

(a) [110] (b) [1$\bar{1}$0]

Figure A.15: Demonstrates the fitting between simulated data and experimental data collected using a SQUID magnetometer for sample $Fe_{79}Ga_{21}$ with 29 nm film thickness along (a) [110] and (b) [1$\bar{1}$0] crystalline direction.

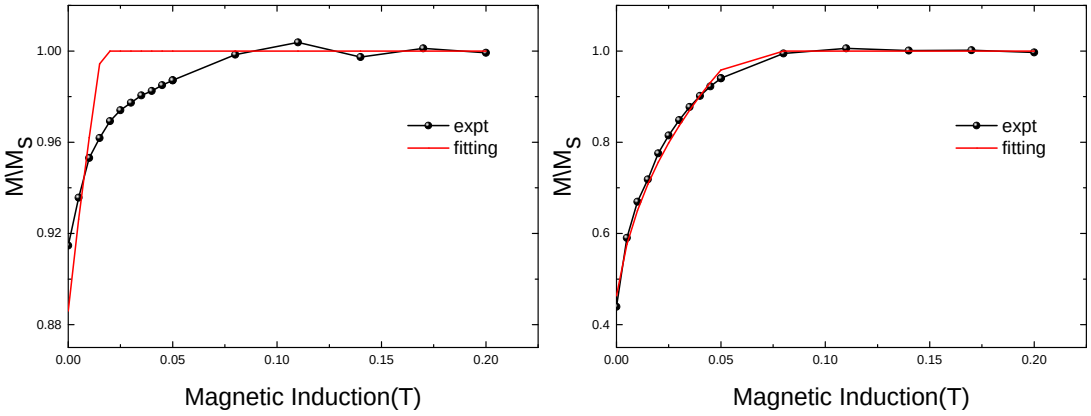

(a) [110] (b) [1$\bar{1}$0]

Figure A.16: Demonstrates the fitting between simulated data and experimental data collected using a SQUID magnetometer for sample $Fe_{79}Ga_{21}$ with 56.5 nm film thickness along (a) [110] and (b) [1$\bar{1}$0] crystalline direction.

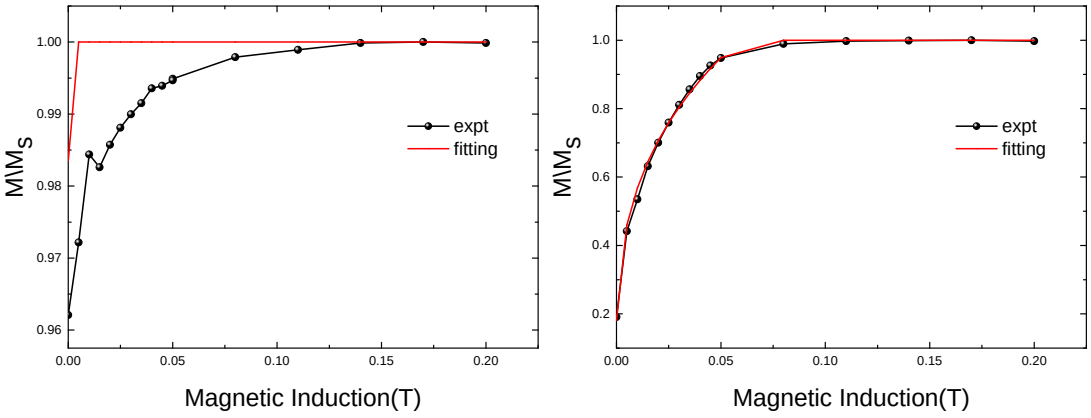

(a) [110] (b) [1$\bar{1}$0]

Figure A.17: Demonstrates the fitting between simulated data and experimental data collected using a SQUID magnetometer for sample $Fe_{79}Ga_{21}$ with 95 nm film thickness along (a) [110] and (b) [1$\bar{1}$0] crystalline direction.